

University of Nottingham
UK | CHINA | MALAYSIA

The Fluid and Thermal Dynamics of Rimming Flows with Boundary Slip

by
Jonathon Michael Paul Nicholson

Thesis submitted to the University of Nottingham for the degree of Doctor of Philosophy

August 2019

Abstract

This thesis intends to provide the reader with a detailed understanding of the current research into aero-engine bearing chambers, providing a description of their function and importance to the aerospace industry. The bearing chambers are a complex component where there is a chaotic mix of oil droplets, splashing, heating and geometric complexities which makes conventional analysis techniques costly to implement. The aim of this research is to describe the important physical effects pertinent to the rotational flow found in bearing chambers within a mathematical modelling strategy.

In developing a mathematical model of the flow inside a bearing chamber, it is useful to simplify the geometry. This geometry is a stationary horizontal cylinder. The model includes effects that are specifically important to the bearing chamber. These effects can relate to the film's inertia or internal pressure which are normally ignored due to the scale of problem under investigation. The proposed model utilises an averaging method of the governing equations, known as depth-averaging, which provides a reasonable estimation of the temporally averaged flow with significant reductions in both time and costs associated with simulations. This method contains the key mechanisms of the film, as well as introducing a new effect that has not been previously considered. This is an effect known as fluid slip, which is typically associated to either; small scale flows, of which the bearing chamber flows can be, or certain texturing methods which can also induce this flow behaviour. This phenomenon is investigated under a variety of flow configurations using the microscopic effects to generate macro scale changes. The thorough exploration of these changes is the main aim of this thesis.

The model is shown to be a well posed extension to classical lubrication theory, which includes both wall slip and inertia. The inertial effects lead to a series of transitional profiles between a stagnating pool and the uniformly distributed film. The film behaviour with fluid slip was shown to create flow recirculation and to have multiple steady profiles in a non-unique solution region. The impact of slip during high levels of inertia is minimal, but in moderate to low levels the imposed surface slip is significant as a flow control technique.

The effect of fluid slip on the film temperatures is relatively small in com-

parison to thermal convection, which has a direct effect on temperature. When thermal convection is of equal or greater strength relative to conduction, there is a significant increase in the amount of heat contained within the fluid. The main effect of slip is to accelerate the film, which in turn amplifies the rate of convection.

The physical characteristics have been thoroughly detailed, with an emphasis on which values are most important in determining the film profile. Minor variations in these values can lead to drastic deviation from the expected behaviour and necessitates a mindfulness of the temporal problem at large.

Importantly, the quantification of the slip condition is discussed in depth. This includes the range of slip scales that are expected with examples of the structures thought to produce sustainable slip. The most important findings of this thesis are contained in the analysis of the different scales of slip on flows which are characteristic of the bearing chamber.

Acknowledgements

I would like to acknowledge the support by the Engineering and Physical Sciences Research Council of the United Kingdom through the scholarship provided by the Industrial CASE Account for the University of Nottingham, grant number EP/M507519/1. I would also like to thank Rolls-Royce PLC for its financial and technical support as part of the Industrial CASE Award.

I am grateful for the continued support and hard work of my supervisors, Dr Antonino La Rocca, Dr Donald Giddings, Dr Outi Tammisola and Dr Stephen Hibberd, who have all been invaluable over my years spent at the University of Nottingham for both my development and backing during my Ph.D. Appreciation is also due to Dr Edward Kay, his guidance and insight has been influential in supporting my Ph.D. and helped in solving many frustrating problems.

Special thanks must go to my mentor, the late Professor Henry Power. His guidance and insight helped me in appreciating the beauty and the elegance of mathematics. His character has had a profound and continued impact on me.

I am thankful to my friends and colleagues whom I have had the pleasure of meeting and have each made my time at the University of Nottingham such an enjoyable and unique experience, providing both a happy distraction and supportive ear.

To my family, especially my brother, Alex, my mother, Tracey and my grandma, Marilyn, their encouraging love and support throughout my life has been a strong foundation to help me keep going and strive for more, without which I would not have succeeded otherwise. This thesis is also in tribute to my late grandad, Maurice Roy Newman, he continues to inspire me and cultivated my passion in pursuing the rewarding path as an engineer. Last, but not least, I will forever be indebted to Cat, thank you for your love and patience, you have kept me sane in trying times and able to achieve my ambitions.

Jonathon M. P. Nicholson
Nottingham, August 27th, 2019.

Contents

Abstract i

Acknowledgements iii

Contents vii

Nomenclature viii

List of Publications xii

List of Figures xxiv

List of Tables xxv

1 Introduction 1

1.1 The Role of the Aero-Engine Bearing Chamber 1

1.2 Aims and Objectives 7

1.3 Methodology of the Thesis 7

1.4 Overview of the Thesis 10

2 Literature Review 12

2.1 Current Models of the Bearing Chamber 12

2.2 Rimming Flows and Related Studies 18

2.2.1 The Classic Analysis of Rotating Flows 18

2.2.2 Including Significant Internal Pressure Gradients within Thin Films 23

2.2.3 Modelling the Presence of Fluid Surface Tension 24

2.2.4 Introduction of Fluid Inertia in Modelling Strategies . . . 27

2.2.5 Experimental Investigations of Rimming and Coating Flows 30

2.2.6 Flows Coating the Cylinder Exterior Surface 32

2.2.7 The Depth-Averaged Method 33

2.2.8 The Thermal Effects Found in Thin Films 36

2.3 Notable Contributions into Investigating Planar Flows 38
2.4 Surface Coatings and Alternate Substrates in Flow Control 41
2.4.1 The Modelling of Air Lubricated Bearings 47
2.4.2 Porous Substrates and the Matching Boundary Conditions 49
2.5 Chapter Summary 51

3 Mathematical Formulation 53
3.1 Introduction to the Two-Phase Governing and Boundary Equations 54
3.2 The Rimming Flow Equations in Cylindrical Coordinates 56
3.3 Scaling into a Non-Dimensional System 60
3.4 The Thin Film Approximation 64
3.5 Depth-Averaging of the Governing Equations 67
3.6 Introducing Polynomial Functions for Velocity and Temperature . 69
3.7 Numerical Methods 76
3.7.1 Spatial Discretisation 76
3.7.2 Temporal Discretisation 79
3.7.3 Programming the Algorithms 79
3.7.4 Computational Resources 80
3.7.5 Solver Convergence 80
3.8 Chapter Summary 81

4 Isothermal Thin Film Rimming Flow Driven by Surface Shear 82
4.1 Film Profiles within Classical Lubrication Theory Framework . . . 82
4.2 Film Profiles in Comparison to Classical Lubrication Theory . . . 86
4.3 Stronger Gravitational Effects with Negligible Inertia 86
4.4 The Balancing of Slip and Gravity 88
4.5 Transitioning to Smooth Solutions with Inertia 91
4.6 Determining the Presence of Non-Unique Solution Branches . . . 98
4.7 The Effect of Larger Slip Lengths on a Controlled Fluid Volume with Increasing Reynolds Numbers 102
4.8 Chapter Summary 108

5 Surface Driven Non-Isothermal Thin Film Rimming Flow 110
5.1 Outlining the Non-Isothermal Model without Slip 111
5.2 Impact of the Surface Heat Transfer Coefficient and Slip Length on Film Temperatures 113
5.3 Influence of Convection on the Thermal Profiles 116
5.4 Combined effect of Inertia and Convection on Temperatures both with and without Slip 119

5.5 Development of Shock Solutions with Inertial and Thermal Convective Effects . . . 126
5.6 Localised Thermal Effects Across a Heated Patch . . . 128
5.6.1 Heating a Section of the Rising Wall . . . 129
5.6.2 Films Being Heated at the Falling Wall . . . 130
5.6.3 Symmetrical Heating at the Cylinder Base . . . 130
5.6.4 Localised Heating Effects on the Mean Temperatures . . . 133
5.7 Chapter Summary . . . 133

6 Physical Applications and Comparative Films 136
6.1 Modelling the Physical Flow Features and Chamber Conditions . 136
6.2 Comparative Study to Existing Rimming Flows . . . 138
6.2.1 Obtaining Smooth Rimming Flows . . . 140
6.2.2 Development of Deep Recirculating Pools . . . 143
6.3 Smooth Solutions with a Strong Driving Shear . . . 152
6.3.1 Importance of Fluid Density on Attainable Films . . . 152
6.3.2 Solutions with Changing Film Speeds . . . 156
6.3.3 How Viscosity Affects the Observable Film Profiles . . . 156
6.3.4 Film Profiles with Varying Characteristic Film Heights . . 158
6.3.5 Effects of Cylinder Size on Film Profiles . . . 161
6.3.6 How the Driving Surface Shear Affects Flow Rotation . . . 164
6.3.7 How Slip Effects a Strongly Driven Film . . . 166
6.4 A Weakly Driven Film without Fluid Pooling . . . 168
6.4.1 Surface Stabilisation for Various Surface Tension Coefficients . . . 170
6.4.2 Importance of Fluid Density in Determining the Film Profile 172
6.4.3 The Effect of Viscosity with Weak Surface Shear . . . 174
6.4.4 Effect of Characteristic Thickness on Stable Film Structures . . . 176
6.4.5 Variation to the Cylinder Radius and Resulting Solutions . 177
6.4.6 The Effect of the Slip Condition on the Weakly Supported Film . . . 179
6.5 Chapter Summary . . . 183

7 Conclusions 184

A Cylindrical Coordinate Identities 188

B The Free Surface Boundary Conditions 190
B.1 Conservation of Interface Mass . . . 190

B.2 Conservation of Momentum at the Interface 192
B.3 Conservation of Energy at the Interface 195
B.4 Expansion of Stress Boundary Condition 197

Nomenclature

This nomenclature list contains the variables used within this thesis and their definition, however all necessary terms will be locally defined at their introduction for the section in which they appear including those denoting functions.

Characteristic Values of the Oil Film

ρ	The oil density, in kg/m^3.
μ	The dynamic viscosity, in Ns/m^2.
ν	Kinematic viscosity, measured in m^2/s.
σ	The surface tension coefficient, in N/m.
h_0	The characteristic value of the film depth, measured in m.
r_0	A characteristic radius of the bearing chamber, in m.
U_0	Typical film speeds within the bearing chamber, measured in m/s.
k^*	The oil thermal conductivity, in W/mK.
γ^*	The free surface heat transfer coefficient, in W/Km^2.
c_p	The specific heat capacity of the oil, in J/kgK.
φ	The thermal diffusivity of the oil, in m^2/s.

Dimensional Variables

r^*	Radial coordinate measurement, in m.
θ^*	Azimuthal angle, measured in degrees, $^\circ$.
t^*	Time, measured in s.
$\mathbf{g}\left(\theta^*, r^*\right)$	Gravitational field, acting vertically downwards at $9.81m/s^2$.

$h^*(\theta^*, r^*, t^*)$	Film depth, in m.
$u_r^*(\theta^*, r^*, t^*)$	Radial velocity component, measured in m/s.
$u_\theta^*(\theta^*, r^*, t^*)$	Azimuthal velocity component, measured in m/s.
τ_a^*	Applied surface shear, measured in N/m^2.
$P^*(\theta^*, r^*, t^*)$	Film pressure field as a function of (θ^*, r^*, t^*), measured in N/m^2.
P_a^*	Atmospheric pressure from core gas flow, measured in N/m^2.
κ^*	The dimensional surface curvature of the fluid free surface, measured in m^{-1}.
$l_s^*(\theta^*)$	Slip length, measured in m.
ξ^*	Shear rate of fluid, taken as the gradient of the velocity, measured in s^{-1}.
Π^*	Function used in defining normal to the film free surface.
H^*	Function defining the location of the free surface.
$T^*(\theta^*, r^*, t^*)$	The film temperature, as a function of (θ^*, r^*, t^*), in $^\circ C$.
T_a^*	Temperature of core gas flow, measured in $^\circ C$.
T_w^*	The characteristic wall temperature, measured in $^\circ C$ and the hottest part of the chamber.

Dimensionless Variables

y	Radial coordinate measurement from the wall, non-dimensional.
s	Azimuthal coordinate, measured anti-clockwise from the vertical downwards and dimensionless.
t	Time, as a dimensionless variable.
$h(s, y, t)$	Film height, non-dimensional.
$v(s, y, t)$	Radial velocity field as a dimensionless function of (s, y, t).
$u(s, y, t)$	Azimuthal velocity field as a dimensionless function of (s, y, t).
τ_a	The dimensionless applied surface shear stress.

$P(s, y, t)$	Pressure field within the film, as a function of (s, y, t) having been scaled by the dynamic pressure field.
P_a	The non-dimensional atmospheric pressure applied at the free surface.
κ	The surface curvature of the fluid free surface as a dimensionless function.
$l_s(s)$	The non-dimensional slip length as a function of (s) acting on the wall.
Π	The dimensionless factor when defining the normal to the film free surface.
H	A dimensionless function which defines the free surface location.
$T(s, y, t)$	Film temperature field, as a non-dimensional function of (s, y, t).
T_a	Dimensionless temperature for the air phase.
T_w	Dimensionless wall temperature of the cylinder.

Key Dimensionless Parameters

ε	A small parameter, measuring the ratio between the height and length scales of the film.
Re	The Reynolds number, as a measure of the inertial and viscous forces.
Re^*	The reduced Reynolds number, a scaled version of the Reynolds number by ε.
λ	A measure between the gravitational and viscous forces.
Ca	The capillary number, a measure of the surface tension and viscous drag effects.
Bi	The Biot number, as a ratio between the heat transfer external and internally to the film.
Pe	The Péclet number, measuring the ratio of thermal advective and diffusive effects.
Pe^*	The reduced Péclet number, as a scaled Péclet number by the small parameter ε.

Other Symbols

$\hat{r}$	Radial unit vector, taken as normal to the cylinder wall.
$\hat{\theta}$	Azimuthal unit vector, taken as tangential to the cylinder wall.
Γ^*	Stress tensor, formed from the summation of $\left(\hat{r}, \hat{\theta}\right)$ contributions.
c	Domain bunching parameter, with $c = 1$ creating a near-uniform domain, and $c > 1$ creating a clustered mesh.
N	Number of nodes within domain, typically in the 1000s.

List of Publications

Published

J. M. P. Nicholson, H. Power, O. Tammisola, S. Hibberd, E. D. Kay, *Fluid dynamics of the slip boundary condition for isothermal rimming flow with moderate inertial effects*, Physics of Fluids, **31**, 033602, (2019).

Forthcoming

J. M. P. Nicholson, A. La Rocca, D. Giddings, O. Tammisola, E. D. Kay, *On the non-isothermal thin film modelling of partial slip rimming flows*, Journal of Fluid Mechanics, Submitted 2020.

Conference Presentations

J. M. P. Nicholson, A. La Rocca, D. Giddings, O. Tammisola, E. D. Kay, *Thin Film Flow with Partial Slip in Non-Isothermal Rimming Flow.* American Physical Society's Division of Fluid Dynamics, 71st Annual Meeting, (2018), Atlanta, USA.

J. M. P. Nicholson, A. La Rocca, D. Giddings, O. Tammisola, E. D. Kay, *On non-isothermal thin film rimming flows with partial slip.* UK Fluids Conference, (2018), Manchester, UK.

Guest Presentations

J. M. P. Nicholson, *On the development of oil films in the bearing chambers of aero-engines.* (2018) University of Palermo, Italy.

List of Figures

1.1 The main supporting structure of a Rolls-Royce Trent series engine. This photograph is produced with the permission of Rolls-Royce plc, copyright © Rolls-Royce plc. 2020. 2
1.2 The closed cycle of oil for the Rolls-Royce Trent 500 engine. This photograph is produced with the permission of Rolls-Royce plc, copyright © Rolls-Royce plc. 2020. 3
1.3 A cross section view of the bearing chamber, showing the concentric shafts of the HP and IP systems, where oil droplets coalesce on the wall of the bearing chamber. 5

2.1 The typical streamlines around the sharp and rounded sump lips. Republished with permission of American Society of Mechanical Engineers, from Scavenge Flow in a Bearing Chamber With Tangential Sump Off-Take, B. Chandra, S. H. Collicott and J. H. Munson, 135, 3, 2013; permission conveyed through Copyright Clearance Center, Inc. 16
2.2 The porous insert (a) and perforated plate (b) used in the experimental investigation of bearing chamber flows by Chandra and Simmons. This photograph is produced with the permission of Rolls-Royce plc, copyright © Rolls-Royce plc. 2020. 17
2.3 Four typical flow profiles found when studying rimming flows which depend upon the associated driving force, with the stagnant pool in (a), a wetting flow with significant pooling (b), a transitional flow subject to a surface shock with capillary ripples (c) and the uniform rimming flow in (d). 19

2.4 The axial features known as "shark's-teeth", showing the formation along the entire cylinder length (a), the transient form (b), the typical cusp formation and corresponding flow field (c). The swirl patterns captured around the peak formations were presented by Thoroddsen and Mahdevan, illuminating the pathlines and vortices in (d). Reprinted by permission from Springer Nature Customer Service Centre GmbH: Springer Nature, Experiments in Fluids, Experimental study of coating flows in a partially-filled horizontally Rotating cylinder, S. T. Thoroddsen and L. Mahadevan, 23, 1997. Reprinted from Physics of Fluids, 8, S10, S. T. Thoroddsen and L. Mahadevan, Shark-Teeth Pattern in Coating Flow Inside a Horizontally Rotating Cylinder, 1996, with the permission of AIP Publishing. 27

2.5 Some examples of the other axial variations which were found by Thoroddsen and Mahadevan, given as; A stable "fish-like" pattern as the dimples from "shark's-teeth" are extruded into longer axial patterns in (a), equispaced curtains of fluid around the cylinder in (b) and hydroplaning droplets exiting a bubbly front shown in (c). Reprinted by permission from Springer Nature Customer Service Centre GmbH: Springer Nature, Experiments in Fluids, Experimental study of coating flows in a partially-filled horizontally Rotating cylinder, S. T. Thoroddsen and L. Mahadevan, 23, 1997. 29

2.6 A representation of the three distinct velocity profiles, obeying the no-slip condition (a), the partial slip condition (b) and the stagnant layer hypothesis (c). 42

2.7 Atomic force microscope measurements of surface roughness (a), densely packed pillars on a surface (b) and sparsely packed pillars (c) as described in the work by Lee et al. . The probe radius is given as R, with w denoting the pillar width, h as the feature height and λ as the frequency of the structure. Reprinted from Advances in Colloid and Interface Science, 210, T. Lee, E. Charrault and C. Neto, Interfacial slip on rough, patterned and soft surfaces: A review of experiments and simulations, 21-38, Copyright 2014, with permission from Elsevier. 44

2.8 A design of a super hydrophobic surface to develop large scale surface slip. 46

2.9 Suspended water droplets on top of a super-hydrophobic surface, using narrow ridges spaced 45 μm apart which are 15 μm wide, with a side view (a) and top down view in (b) as reported by Rothstein. Republished with permission of Annual Reviews, Inc., from Slip on Superhydrophobic Surfaces, J. P. Rothstein, 42, 2009; permission conveyed through Copyright Clearance Center, Inc. 47

3.1 Two-dimensional representation of bearing chamber and cylindrical coordinate system. 57
3.2 A demonstration of a quadratic function modelling complex recirculation regions of the velocity field for a typical pooling film. The *red* lines denote the calculated azimuthal velocity profile at each *blue* point, having been normalised to the maximum film velocity. 70
3.3 The numerical convergence of a fourth order finite difference scheme in *red* and the numerical scheme of this thesis in *black* in approximating the derivative of $e^{cos(x)}$. 77

4.1 The effect of slip length, l_s on the critical film values under classical lubrication theory, as calculated from (4.1) with h_c in (a), q_c in (b) and A_c in (c). 85
4.2 The three possible regimes of sub-critical (a), critical (b) and super-critical (c) film profiles for; $\lambda = 1$, $\tau = 1$, $l_s = 0$, $Re^* = 30$, $\varepsilon = 10^{-2}$, $Ca = 10^{-3}$. The unbounded solutions are shown in parts (a) and (b), while the non-physical region is shown in part (c). With *dotted* lines indicating solutions to (4.1) and *solid* lines as solutions to the coupled equations of (3.113), (3.61) and (3.60). 87
4.3 Profiles for increasing gravitational forces for; $\tau = 1$, $\varepsilon = 0.1$, $Re^* = 10^{-3}$, $Ca = 0.1$, $A = 0.1$ and $l_s = 0.01$. With the coloured lines given as *orange* for $\lambda = 1$, *blue* for $\lambda = 2$, *black* for $\lambda = 3$, *green* for $\lambda = 5$ and *red* for $\lambda = 10$. 88
4.4 Streamlines of pooled and smooth solutions, for $\lambda = 1$ in (a) and $\lambda = 3$ in (b), showing the fluid recirculation of the solutions presented in figure 4.3. 89
4.5 Changes to gravity dominate flows due to slip, for $\varepsilon = 0.01$, $Re^* = 0$, $Ca = 10^{-3}$, $A = 0.1$. Where λ is 1 in (a), 2 in (b), 5 in (c) and 10 in (d). Coloured lines represent $l_s = 0.01$ in *blue*, $l_s = 0.1$ in *green* and $l_s = 1$ in *red*. 90

4.6 Effect of increasing Re^* with and without slip: $l_s = 0$ *blue* and $l_s = 0.01$ *green*, $l_s = 0.1$ in *orange* and *red* for $l_s = 0.2$, with $\tau = 1$, $\lambda = 1$, $Ca = 10^{-3}$, $\varepsilon = 10^{-2}$ and $A/A_c = 1.073$. The points correspond to: $Re^* = 0.01$, $Re^* = 1.8$, $Re^* = 5$, $Re^* = 10$, $Re^* = 15$, $Re^* = 20$ and $Re^* = 100$, with solutions found in figures 4.7 and 4.8. 92

4.7 The effect of inertia on the slip boundary condition from figure 4.6, for $\tau = 1$, $\lambda = 1$, $Ca = 10^{-3}$, $\varepsilon = 10^{-2}$ and $A/A_c = 1.073$. With $Re^* = 0.01$ in (a), $Re^* = 1.8$ in (b), (c) with $Re^* = 5$, (d) with $Re^* = 10$, $Re^* = 15$ in (e) and (f) with $Re^* = 100$ for $l_s = 0$. . . . 94

4.8 Effect of the slip boundary condition and inertia with $l_s = 0.2$ from figure 4.6. Where the reduced Reynolds number of (a) is $Re^* = 0.01$, (b) with $Re^* = 1.8$, (c) with $Re^* = 5$, (d) with $Re^* = 10$ and $Re^* = 20$ and $Re^* = 100$ in (e) and (f). With $\tau = 1$, $\lambda = 1$, $Ca = 10^{-3}$, $\varepsilon = 10^{-2}$ and $A/A_c = 1.073$. 95

4.9 The changing film profiles due to fluid slip at different levels of inertia as detailed in figure 4.6, where the parameters are given as $\tau = 1$, $\lambda = 1$, $Ca = 10^{-3}$, $\varepsilon = 10^{-2}$ and $A/A_c = 1.073$. The values of Re^* are; 0.01 in (a), 1.8 in (b), 5 in (c), 10 in (d), 15 in (e) and 100 in (f). The slip lengths are given by the coloured lines; *red* for $l_s = 0$, *green* for $l_s = 0.01$, *blue* for $l_s = 0.1$ and *orange* for $l_s = 0.2$. 97

4.10 Parameter space q/q_c against A/A_c for smooth solutions transitioning to deep pooling solutions with wall slip. For; $Re^* = 1$, $\tau = 1$, $\lambda = 1$, $Ca = 10^{-3}$, $\varepsilon = 10^{-2}$. With $l_s = 0$ coloured in *blue* and dashed *red* representing $l_s = 0.5$. The films at each point can be found in figure 4.11 and figure 4.12 for the no-slip and slip cases respectively. The insert is the magnification of the slip line for $s \in [0.9, 1.1]$. 100

4.11 Film profiles of results represented in figure 4.10 for no-slip, detailing the transition films of points (a), (b), (c) and (d). 101

4.12 Profiles from figure 4.10 with $l_s = 0.5$, for the films at points (e), (f), (g), (h), (i), (j) and (k). 103

4.13 The effect of increasing Re^* on a fixed filling fraction $A = 0.013494$ with the no-slip condition. With $\tau = 1$, $\lambda = 1$, $Ca = 10^{-3}$ and $\varepsilon = 10^{-2}$. The reduced Reynolds number of each panel is given as; 0.01 in (a), 1.8 in (b), 5 in (c), 10 in (d), 15 in (e) and 20 in (f). . 104

4.14 The effect of moderate slip length, $l_s = 0.01$ for a fixed filling fraction $A = 0.013494$ for increasing Re^*. In each panel, the reduced Reynolds number is given as 0.01, 1.8, 5, 10, 15 and 20 in (a), (b), (c), (d), (e) and (f) respectively. The remaining flow parameters are; $\tau = 1$, $\lambda = 1$, $Ca = 10^{-3}$ and $\varepsilon = 10^{-2}$. 106

4.15 Effect of inertia for a constant filling fraction $A = 0.013494$ with large slip, $l_s = 0.1$ condition. Where the parameters are given as $\lambda = 1$, $\tau = 1$, $\varepsilon = 10^{-2}$ and $Ca = 10^{-3}$. With $Re^* = 0.01$ in (a), (b) $Re^* = 1.8$, $Re^* = 5$ in (c), $Re^* = 10$ in (d), $Re^* = 15$ in (e) and $Re^* = 20$ in (f). The *red* line in (d) indicating an unstable solution. 107

5.1 The typical film profiles for smooth (a), shock (d) and pooling (g) solutions using parameters from table 5.1. The temperature bar shows the uniform temperatures across all of these films. The velocity streamlines of each film show when recirculation occurs in panels (b), (e) and (h). The film profiles and the film temperatures have been plotted into a cylindrical representation in (c), (f) and (i) for each flow respectively. 112

5.2 The effect of different surface heat transfer rates and slip lengths on smooth and pooling films with weak thermal convection has been explored in this Section. In the first column $l_s = 0$ and $l_s = 0.1$ for the second. Panels (a) and (b) are with $B = 0.01$ while panels (c) and (d) have $B = 0.1$ respectively. The mean temperature lines in (e) and (f) are coloured for each Biot number and represented as; $B = 10^0$ with *red*, $B = 10^{-1}$ in *green*, $B = 10^{-2}$ with *blue* and $B = 10^{-6}$ with *orange*. 114

5.3 Panels (a) and (b) are with no-slip and for $B = 0.01$ and $B = 0.1$ respectively, while the second row is with $l_s = 0.1$ with the same Biot numbers. The Biot numbers of the last row of panels are; *red* is $B = 10^0$, *green* represents $B = 10^{-1}$, *blue* shows $B = 10^{-2}$ and $B = 10^{-6}$ is given by *orange* for the mean temperature $\bar{T}$. 115

5.4 The influence of slip length, l_s on the fixed volume smooth films of (a) and (b), and on the pooled films (c) and (d) for Biot numbers $B = 0.01$ and $B = 0.1$ in (a), (c) and (b), (d) respectively. The slip lengths are indicated by the coloured lines; $l_s = 0$ in *red*, $l_s = 10^{-2}$ in *green*, $l_s = 10^{-1}$ by *blue* and $l_s = 5 \times 10^{-1}$ with *orange*. 116

5.5 The role of convection on smooth films, the first column is for $l_s = 0$ and $l_s = 0.1$ in the second column. Panels (a) - (c) are with $Pe^* = 0.01$, row two for $Pe^* = 1$, row three for $Pe^* = 5$ and the last row by $Pe^* = 10$. The third column is the mean temperatures for various slip lengths, with $l_s = 0$ given in *red*, $l_s = 10^{-2}$ in *green*, $l_s = 10^{-1}$ in *blue* and $l_s = 5 \times 10^{-1}$ coloured *orange*. 117

5.6 The role of convection on pooled films, the first column of panels are with $l_s = 0$ while $l_s = 0.1$ is for the second column of panels. The first row are for $Pe^* = 0.01$, the second row with $Pe^* = 1$, the third row is with $Pe^* = 5$ and $Pe^* = 10$ in panels (j), (k) and (l). The mean temperatures for various slip lengths in the third column are given by; *red* for $l_s = 0$, *green* for $l_s = 10^{-2}$, $l_s = 10^{-1}$ by *blue* and *orange* for $l_s = 5 \times 10^{-1}$. 118

5.7 Inertial and thermal convection on pooling films, for the no-slip case. The Péclet number, Pe^* is given as 0.01, 1, 5 and 10 for columns one, two three and four respectively. The magnitude of inertia by the Reynolds number, $Re^* = 0.1$ in row one, $Re^* = 1$ for row two, $Re^* = 5$ for row three and $Re^* = 10$ in row four. The last row of panels are for $Re^* = 100$. 122

5.8 Inertial and thermal convection on pooling films, for $l_s = 0.1$ and $A = 1.987\varepsilon$. The Reynolds number of row one is $Re^* = 0.1$, increasing to $Re^* = 100$ in the last row, row two has $Re^* = 1$, row three is with $Re^* = 5$ and row four has $Re^* = 10$. The Péclet number, Pe^* increases between each column, from 0.01, to 10, with columns two and three having $Pe^* = 1$ and $Pe^* = 5$ respectively. . 123

5.9 Comparing the role of slip on the mean temperature fields from figure 5.7 and figure 5.8, for $l_s = 0$ in *blue* and $l_s = 0.1$ in *red*. The increasing inertia between each row from $Re^* = 0.1$ to $Re^* = 100$ and Péclet number from Pe^* and $Pe^* = 10$ are equal to figures 5.7 and 5.8. 125

5.10 The shock solution, with the Péclet number $Pe^* = 0.1$ in column one and $Pe^* = 10$ in column two while the mean temperatures for several Péclet numbers are in panels (c), (f), (i) and (l). The Reynolds number for each row is given as 0.1, 1, 5, 10 and 100 respectively. The varying Péclet numbers in column three are coloured as $Pe^* = 0.1$ in *red*, $Pe^* = 1$ in *green*, $Pe^* = 5$ in *blue* and $Pe^* = 5$ coloured in *orange*. 127

5.11 The step functions for defining the rising *red*, central *orange* and falling *blue* wall locally heated sections. 128

5.12 Thermal convection and partial slip on the rising wall heated patch, with Pe^* given in increments of 0.1, 1, 5 and 10 for each row from top down respectively. The temperature profiles in column one are for no-slip and column two for $l_s = 0.1$. The third column is the cylindrically mapped temperature profiles with $l_s = 0.1$. 129

5.13 The falling wall heated patch with increasing thermal convection and partial slip. The temperature profiles in panels (a) - (d) are for no-slip and panels (e) - (h) for $l_s = 0.1$. The increasing thermal convection down each row is given by $Pe^* = 0.1$, 1, 5 and 10 respectively with the slip solutions reconstructed as cylindrical flow in column three. 131

5.14 The localised heating of the cylinder base, the reconstructed cylinders in panels (m) - (p) are with $l_s = 0.1$. The Péclet number increases across columns one to four at intervals $Pe^* = 0.1$, $Pe^* = 1$, $Pe^* = 5$ and $Pe^* = 10$ respectively. The no-slip condition has been applied for panels (a) - (d) while panels (e) - (h) have a partial slip condition with $l_s = 0.1$. 132

5.15 The effect of thermal convection and partial slip on the rising wall heated patch, with Pe^* given in increments of 0.1, 1, 5 and 10 for each row. The columns represent the rising, central and falling wall scenarios respectively. The temperature profiles in row one are for no-slip and row two for $l_s = 0.1$. The mean temperature profiles are for no-slip *red* and $l_s = 0.1$ *blue*. 134

6.1 The film height profiles of the smooth film found in the work of Kakimpa et al. [1] and those calculated with the current model for a range of surface tension coefficients using the parameters of table 6.2. The *blue* line is with $\sigma = 0.0245\,N/m$ and $\sigma = 0.5\,N/m$ is in *red* (which is perfectly under the *blue* line), while those of Kakimpa et al. are denoted by $\diamond$. 141

6.2 The calculated forces within the films when $\sigma = 0.0245\,N/m$ and $\sigma = 0.5\,N/m$ in (a) and (b) respectively. The contributing forces are denoted by *blue* for gravity, *green* for viscosity, *red* for inertia, *orange* for surface tension and *black* for hydrostatic pressure, which is consistently used throughout this Chapter. 142

6.3 A comparison between the films by Kakimpa et al. [1], denoted in *orange* for $\sigma = 0.5\,N/m$ and *blue* for $\sigma = 0.0245\,N/m$ and the film profiles calculated using the parameters of table 6.2. Where the surface tension coefficients for $\sigma = 0.5\,N/m$ in *green* and $\sigma = 0.0245\,N/m$ in *red*. Close up of film height profiles preceding the fluid pool, highlighting the differences between the range of σ values tested. 144

6.4 The forces found within the films for $\sigma = 0.0245\,N/m$ in (a) and $\sigma = 0.5\,N/m$ in (b), from the films of figure 6.1. The lines are calculated for inertia, viscosity, hydrostatic pressure, surface tension and gravity, given as *red*, *green*, *black*, *orange* and *blue* respectively. 145

6.5 The effect of adding centrifugal effects from inertia and pressure on the film profile for $\sigma = 0.0245\,N/m$ in (a), where the full inertial effects are plotted in *red* and the simplified inertial terms are coloured in *blue*. The absolute percentage error between the films with and without centrifugal effects is given in (b). 147

6.6 The calculated contributions of inertia in the pooling film of figure 6.5, having been normalised to only the inertial effects. The *red* line gives the total inertial contribution, *orange* gives the contribution for the convective terms, *blue* and *green* are for the centrifugal pressure and the centrifugal inertial contributions respectively. . . 148

6.7 How the pooling film changes depending on the surface tension coefficients, where $\sigma = 0.0245\,N/m$ is given by *blue*, $\sigma = 0.1\,N/m$ in *green*, $\sigma = 0.3\,N/m$ with *orange* and $\sigma = 0.5\,N/m$ with *red*. These films are closely investigated in figure 6.8. 148

6.8 Close views at the film in front of and receding from the fluid pool of figure 6.7 in part (a) and (b) respectively to highlight the effect of surface tension, for *blue* with $\sigma = 0.0245\,N/m$, *green* as $\sigma = 0.1\,N/m$, *orange* for $\sigma = 0.3\,N/m$ and $\sigma = 0.5\,N/m$ in *red*. . . 149

6.9 A comparison of the obtained solutions between the numerical solver using an *upwind* and a *central* difference method in gradient calculations. Where the upwind solutions to $\sigma = 0.5\,N/m$ and $\sigma = 0.0245\,N/m$ are given by *red* and *orange* lines, and solutions using the central scheme are given as dashed *green* and *blue* lines. 150

6.10 The absolute percentage error between the *upwind* and *central* differencing schemes of Matlab's *fsolve* for calculating the pooling film. The *red* line denotes the error in the results for $\sigma = 0.5\,N/m$ and the *blue* line is for $\sigma = 0.0245\,N/m$. 151

6.11 The uniform and centrally clustered meshes, showing the obtained solutions for the pooling film in (a), with *orange* for the uniform mesh while *blue* is on the clustered mesh. The spacing between each node across the domain is shown in (b), where *orange* is for $N = 5,000$ and *blue* is for $N = 3,750$. 153
6.12 The influence of the fluid density, ρ on the smooth solution characterised by table 6.2. The solution profiles for each value of the fluid density is given as *orange* for $730\,kg/m^3$, *blue* for $930\,kg/m^3$, *black* for $950\,kg/m^3$, *green* for $1000\,kg/m^3$ and *red* for $1500\,kg/m^3$. 154
6.13 With inertia, hydrostatic pressure, surface tension, viscosity and gravity plotted as *red*, *black*, *orange*, *green* and *blue* respectively, the change in forces from figure 6.12 with different values of ρ, with $700\,kg/m^3$ in (a), $930\,kg/m^3$ in (b) and $1500\,kg/m^3$ in (c). 155
6.14 The resulting film profiles for various film speeds, denoted by U_0 of the smooth film, with *orange* for $0.1305\,m/s$, *blue* at $0.261\,m/s$, *black* having $U_0 = 0.512\,m/s$, *green* with $U_0 = 1.024\,m/s$ and *red* for $2\,m/s$. 156
6.15 The effective forces of figure 6.14, with inertia (*red*), hydrostatic pressure (*black*), viscosity (*green*), gravity (*blue*) and surface tension (*orange*). The characteristic velocities of each panel are $0.1305\,m/s$ in (a), $0.512\,m/s$ in (b), and $2\,m/s$ for (c). 157
6.16 The film profiles that develop with changes to the fluid viscosity μ for a smooth solution, with $0.001\,Ns/m^2$ in *orange*, $0.002\,Ns/m^2$ in *blue*, $0.00483\,Ns/m^2$ in *black*, $0.0075Ns/m^2$ in *green* and *red* for $0.01\,Ns/m^2$. 158
6.17 The contributing forces found for changes to the fluid viscosity of figure 6.16, specifically those of $0.001\,Ns/m^2$ in (a), $0.00483\,Ns/m^2$ in (b) and $0.01\,Ns/m^2$ for (c). The lines represent the effect of inertia, viscosity, gravity, hydrostatic pressure, and surface tension calculated at each node, given as *red*, *green*, *blue*, *black* and *orange*. 159
6.18 With changes to the characteristic film height h_0, the resulting film profiles and shown for $1\,mm$ in *red*, $0.7\,mm$ in *green*, $0.55\,mm$ in *black*, *blue* for $0.05\,mm$ and $0.01\,mm$ as *orange*. 161
6.19 The effective force of inertia (in *red*), gravity (in *blue*), viscosity (in *green*), hydrostatic pressure (in *black*) and surface tension (in *orange*) for the films where $h_0 = 0.01\,mm$ in (a), $h_0 = 0.55\,mm$ in panel (b) and $h_0 = 1\,mm$ in (c). 162

6.20 The influence that the cylinder radius, r_0 has on the smooth solutions, for $r_0 = 1\,m$ represented by the *orange*, $0.5\,m$ in *blue*, $0.11\,m$ in *black*, $r_0 = 0.05\,m$ with the *green* line and $0.01\,m$ with *red*. . . . 163

6.21 A graph detailing the forces found within the fluid film for the cylinder radius, r_0, where (a) is for $0.01\,m$, (b) for $0.11\,m$ and in (c), $r_0 = 1\,m$. The relevant forces are given as hydrostatic pressure in *black*, surface tension in *orange*, gravity and viscosity in *blue* and *green* respectively and inertia in *red*. 165

6.22 Effect of the applied driving shear force τ_a^* at the surface, and the sensitivity the film profiles to the strength of the driving surface shear with a fixed fluid volume. Where $\tau_a^* = 2\,N/m^2$ in *orange*, $3\,N/m^2$ in *blue*, *black* for $4.5\,N/m^2$, *green* for $9\,N/m^2$ and $18\,N/m^2$ is in *red*. 166

6.23 Forces for changing τ_a^*. With inertia in *red*, gravity in *blue*, viscosity in *green*, hydrostatic pressure in *black* and surface tension in *orange*. Where (a), (b), (c) and (d) are for solutions to $\tau_a^* = 2\,N/m^2$, $4.5\,N/m^2$, $9\,N/m^2$ and $18\,N/m^2$. 167

6.24 The importance of the slip length, measured in m on the film profile of the strongly driven flow. The lines correspond to no-slip *red*, $l_s^* = 0.00001\,m = 10\,\mu m$ in *green*, $l_s^* = 0.00005\,m = 50\,\mu m$ in *black*, $l_s^* = 0.0001\,m = 100\,\mu m$ in *blue* and $l_s^* = 0.0002\,m = 200\,\mu m$ is depicted in *orange*. 168

6.25 The effect of the five modelled forces of gravity (in *blue*), hydrostatic pressure (in *black*), inertia (in *red*), surface tension (in *orange*) and viscosity (in *green*) found in the films of figure 6.24. With $l_s^* = 0\,\mu m$ in (a), $l_s^* = 50\,\mu m$ in (b) and $l_s^* = 200\,\mu m$ in (c). 169

6.26 The effect of the surface tension coefficient, σ on the film profiles when a lower driving shear force of $\tau_a^* = 4.5\,N/m^2$, depicted for $\sigma = 0.0245\,N/m$ in *orange*, $0.25\,N/m$ in *blue*, $0.5\,N/m$ in *black*, $0.75\,N/m$ in *green* and $1\,N/m$ in *red*. 170

6.27 The typical forces found within a rimming flow, consisting of viscosity (*green*), surface tension (*orange*), inertia (*red*), hydrostatic pressure (*black*) and gravity (*blue*). The different panels represent new values of the surface tension coefficient, for $\sigma = 0.0245\,N/m$ in (a), $\sigma = 0.5\,N/m$ in (b) and $\sigma = 1\,N/m$ in (c) as shown in figure 6.26. 171

6.28 The effect of fluid density on the films now that a weaker driving shear force acts on the surface. The densities are equal to those of figure 6.12, with $\rho = 700\,kg/m^3$ given in *orange*, $\rho = 930\,kg/m^3$ in *blue*, $950\,kg/m^3$ coloured *black*, $1000\,kg/m^3$ in *green* and $1500\,kg/m^3$ in *red*. 172

6.29 The developing forces within the films of figure 6.28 for increasing density, ρ, for $\rho = 700\,kg/m^3$, $930\,kg/m^3$ and $1500\,kg/m^3$ in (a), (b) and (c) respectively. The coloured lines depict the effective value of gravity, hydrostatic pressure, inertia, surface tension and viscosity as *blue*, *black*, *red*, *orange* and *green* colours respectively. 173

6.30 Profiles for changes to the fluid viscosity μ, with parameters defined in table 6.2 but the driving shear force is only $4.5\,N/m^2$. With *orange* for $0.001\,Ns/m^2$, *blue* for $0.002\,Ns/m^2$, *black* for $0.00483\,Ns/m^2$, *green* for $0.0075\,Ns/m^2$ and *red* for $0.01\,Ns/m^2$. . 174

6.31 Outlines of five key forces found within the film profiles of figure 6.30, for changing dynamic viscosity, μ. With (a) mapping the forces for $\mu = 0.001\,Ns/m^2$, (b) for $\mu = 0.00483\,Ns/m^2$ and $\mu = 0.01\,Ns/m^2$ in (c). The five forces are denoted by the coloured lines, as surface tension in *orange*, inertia in *red*, gravity in *blue*, hydrostatic pressure in *black* and viscosity in *green*. 175

6.32 The effect of h_0 for the smooth solution defined in table 6.2 using the lower shear force of $\tau_a^* = 4.5\,N/m^2$. With the characteristic film heights h_0 given by a *green* line for $0.7\,mm$, *black* for $0.55\,mm$, *blue* for $0.05\,mm$ and *orange* for $h_0 = 0.01\,mm$. 176

6.33 The forces of the key films defined as $h_0 = 0.01\,mm$, $h_0 = 0.55\,mm$ and $h_0 = 0.7\,mm$ shown in (a), (b) and (c) respectively as films from figure 6.32. The calculated forces are shown in *red* (inertia), *blue* (gravity), *green* (viscosity), *black* (hydrostatic pressure) and *orange* (surface tension). 178

6.34 The changes to the film profiles with different cylinder radii, r_0 using $\tau_a^* = 4.5\,N/m^2$ and the other parameters of table 6.2, where *red* is for $r_0 = 0.01\,m$, *green* for $0.05\,m$, *black* for $0.11\,m$, *blue* for $r_0 = 0.5\,m$ and *orange* for $r_0 = 1\,m$. 179

6.35 Visualisation of the forces found within films where $r_0 = 0.01\,m$, $r_0 = 0.11\,m$ and $r_0 = 1\,m$ in panels (a), (b) and (c) respectively for the films of figure 6.34, where the coloured lines are given as *black* for hydrostatic pressure, *blue* for gravity, *green* for viscosity, *red* for inertia and *orange* for surface tension. 180

6.36 The effect that longer slip lengths, including the no-slip condition, have on the resulting film profiles. Where the parameters are defined in table 6.2 with the reduced shear rate of $\tau_a^* = 4.5\,N/m^2$, with $l_s^* = 0\,\mu m$ in *red*, $l_s^* = 10\,\mu m$ in *green*, $l_s^* = 50\,\mu m$ in *black*, $l_s^* = 100\,\mu m$ in *blue* and the largest slip length of $200\,\mu m$ in *orange*. 181

6.37 The forces found within the film profiles of figure 6.36, for the no-slip case in (a), $l_s^* = 50\,\mu m$ in (b) and $l_s^* = 200\,\mu m$ in (c). The forces are represented as surface tension in *orange*, viscosity in *green*, inertia in *red*, gravity in *blue* and hydrostatic pressure in *black*.182

B.1 A pillbox volume which encompasses a volume within and external to the film interface. 191

List of Tables

4.1 The effects of increasing slip length, l_s on the critical film values, h_c, q_c and A_c. 84

5.1 Parameters for establishing a smooth or pooled solution. 113

6.1 Key dimensional film parameters as described by Kakimpa et al. [1] to create a smooth or pooling film. 139
6.2 Dimensionless parameters table for establishing either a smooth or pooled solution according to table 6.1. 140
6.3 The dimensionless parameters and calculated filling fractions for changing h_0 to establish a smooth solution which is consistent in volume to those presented in table 6.2. 160
6.4 The changed non-dimensional parameters for establishing a smooth solution which are dependent upon r_0, with the remaining parameters given in table 6.2. 163

Chapter 1

Introduction

1.1 The Role of the Aero-Engine Bearing Chamber

This thesis is motivated by the oil films that are found in the bearing chambers of aero-engines. These oil films are used for the dual purpose of being a lubricant and coolant in the transmission systems. Therefore, the study of a non-isothermal rotating flow is important for analysing the flows of the bearing chamber.

The efficiency of gas turbine engines may be improved significantly by increasing the combustion temperature. However, this means the surrounding components will be substantially hotter unless the cooling systems are able to handle the additional thermal load. These components include; the rotating parts (e.g. the engine shafts, gears and bearings), the stationary core and the mounting components which have been highlighted in figure 1.1.

These roller bearings which align and support the shafts that mount the fan, compressor and turbine stages of the engine are housed within bearing chambers. These chambers are used to isolate the oil flow from leaking into other areas of the aero-engine. This is the structure of the Rolls-Royce Trent series engines, shown in figure 1.1 and is representative of typical aero-engine configurations.

The oil is used in a self-contained cycle, to be recirculated through the oil fed bearings of the four typical bearing chambers: located between the High-Pressure (HP) and Intermediate-Pressure (IP) stages, the tail bearing, the front bearing and the internal gearbox.

The complete cycle is illustrated in figure 1.2, where the oil feed injection sites into the bearings have been indicated. The oil leaks out of the bearings as droplets, which coalesce as a thin film on the enclosing chambers due to the centrifugal forces. The dispersion of droplets within the rotating airflow is a chaotic two-phase system, which adds a large amount of mass and momentum into

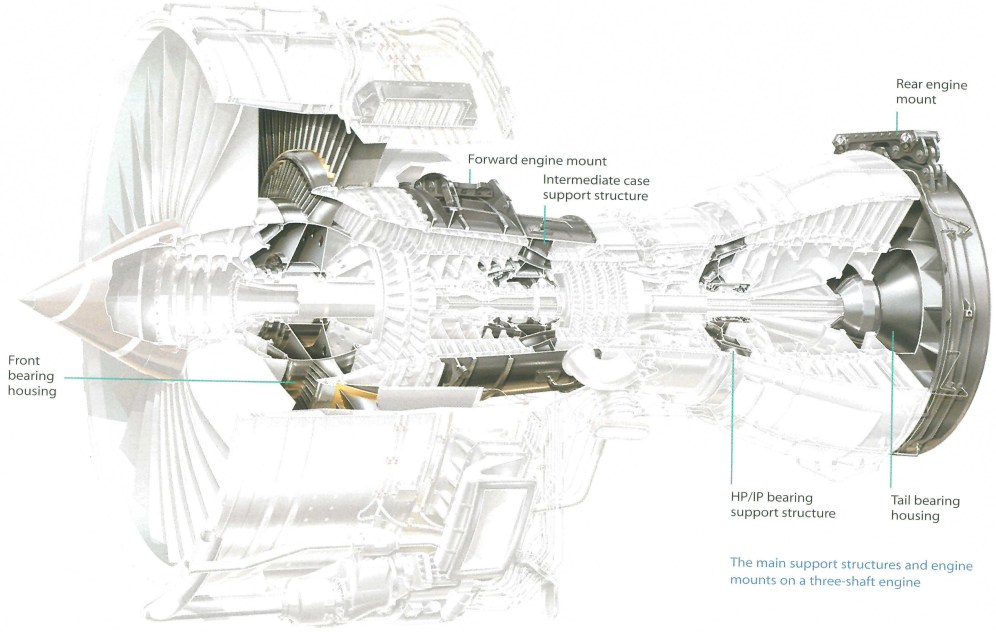


Figure 1.1: The main supporting structure of a Rolls-Royce Trent series engine. This photograph is produced with the permission of Rolls-Royce plc, copyright © Rolls-Royce plc. 2020.

the film at the surface. The airflow is driven by the high rotation speeds of the concentric engine shafts and leads to a strong air shear acting on the film surface, this shearing effect is also known as windage. The closed cycle is created as oil is drawn through a sump in the chamber base and regenerated through a series of filters and coolers before being fed back into the bearings. These coolers are heat exchangers between the heated oil and cold fuel of the aero-engine, preventing the freezing of and improving the combustion performance of, the fuel while cooling the oil.

This cooled oil is reintroduced to the bearings and subsequently the chamber to prevent the excessive heating of the oil by the walls. The temperature of the airflow through the chamber is somewhere between that of the cooled oil droplets and the heated chamber walls. The oil and air are contained by several pressurised seals that create a positive pressure in the chamber. The bulk of the oil is extracted through the sump, found at the beginning of the scavenge return system which is depicted in figure 1.2. However, a small amount of oil will leak through the vents that recycle the airflow and must be separated before it can be recycled back into the system.

The proximity of the HP-IP chamber to the combustion stage means this chamber is the hottest of the four chambers, due to the higher burning temperatures which increases the thermal load of the oil in this chamber. The ability to maintain

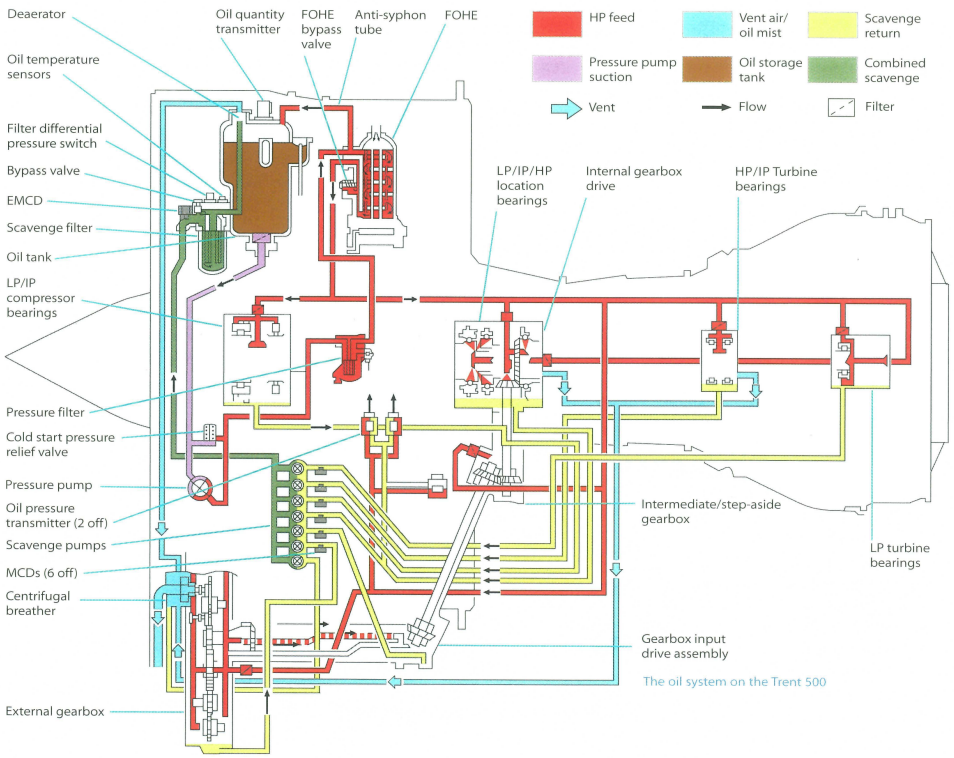


Figure 1.2: The closed cycle of oil for the Rolls-Royce Trent 500 engine. This photograph is produced with the permission of Rolls-Royce plc, copyright © Rolls-Royce plc. 2020.

the oils physical properties are important, however at higher temperatures the oil is likely to degrade or in severe cases may begin coking or can even ignite. Avoiding these negative situations is a key concern to engineers, who need to predict the behaviour of the oil in the chamber to monitor both the temperatures and residence times of the flow constituents. Therefore, an extended residence time is likely to accelerate the degradation of the oil, this can shorten the oil life cycle or lead to more severe issues over time. The cross section of a typical HP-IP chamber is shown in figure 1.3, showing where the oil droplets may enter and accumulate on the chamber wall. Interestingly, the concentric hollow design of the HP-IP chamber also means the two systems can rotate in opposing directions at a different speeds.

There are various flow structures of oil that can be formed from the escaping flow off the bearings into the bearing chambers. These can be fast moving filaments, bubbles of entrapped air within a film, droplets or flowing film across the hot wall structures. It is this flowing film structure that this work is most interested in.

The oil flow of the bearing chamber necessitates a number of physical effects to be described, of particular importance is the inertial forces being significant, contrary to the classical lubrication theory explanation; shallow films with decreasing film heights also have increasingly small Reynolds numbers and therefore have negligible inertia. However, the operating conditions of the aero-engine shafts of $5,000\ RPM$ to $15,000\ RPM$ mean film speeds may be sufficient such that inertia is also significant. This consideration means realistic models should include inertia to leading order, as the Reynolds numbers of $O(100)$ are feasible, which means the other consideration of thermal convection may be of leading order due to the film speed.

The oil films of the chamber vary for each aero-engine design and their operating speeds; however, the oil is typically only millimetres or micrometres in depth. At the macro-scale the currently accepted theory is that the velocity of a fluid in contact with a solid surface will be zero, which is commonly referred to as the no-slip condition. There is research into flows that are comparable in size or smaller than those of the bearing chamber where experimental measurements show the flow is not stationary at the wall. This non-zero velocity is known as fluid slip and is generally modelled as a partial slip condition. The partial slip condition is an equation which links the fluid velocity and shear rate at the surface, using a proportional constant which is known as the slip length. Studies have been able to measure this slip length in narrow flows. However, these have relied on either very precise measurements or have been inferred by correlation techniques. These methods are both susceptible to significant errors as the slip lengths can be just nanometres in size. However, there are studies which have reported significantly

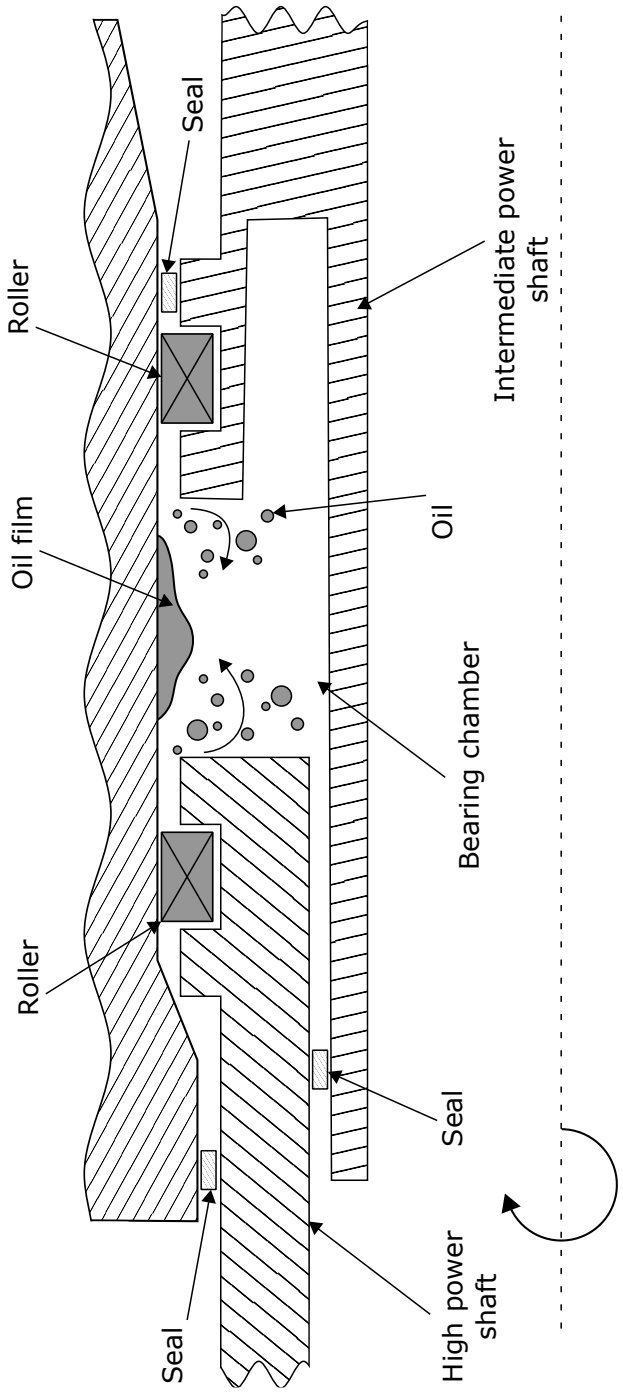


Figure 1.3: A cross section view of the bearing chamber, showing the concentric shafts of the HP and IP systems, where oil droplets coalesce on the wall of the bearing chamber.

larger slip lengths for flows which are relatively thick.

This is an area of research that is growing, though experimental studies have indicated some chemical coatings and structural patterns appear to generate significant slip. While the exact reason for slip is not currently known, a review of the background literature suggests that it may be possible to achieve up to hundreds of micrometres of slip. Many of the treatments typically make the surface repel the fluid, which is generally water, this repelling effect is believed to be the cause of fluid slip at the surface. This inherent ability of surfaces to repel water classifies them as being hydrophobic, while the ability to attract water means a surface is hydrophilic. Hydrophilic surfaces are not believed to cause slip.

The idea of using hydrophobic surfaces is due to this effect being observed in nature, specifically the lotus leaf. These leaves have unique properties which mean they strongly repel water as part of a self-cleaning mechanism and are deemed to be ultra-hydrophobic. There are numerous similar examples where engineers have used phenomenon found in nature to influence their designs. This is because nature has been able to optimise over many generations, creating efficient structures and effects to evolve and survive. One example is the honeycomb structure which forms beehives and is found throughout the aerospace sector, this is due to the structure's combination of being both light weight and high strength. The drag reduction that arises due to the pattern and texture of shark scales is one more instance where natural designs are being studied by researchers.

The surfaces which are most likely to be used in the bearing chamber will be from micro-structures on the surface. Machining these structures are expected to be costly due to the methods needed to achieve the precision necessary for stable slip. Therefore, alternative methods will be needed for commercial use. One possible method is with additive manufacturing, as it is now possible to fabricate complex metal components. A recent example of this is from Siemens AG [2], who were able to create and test a gas turbine engine using turbine blades produced by additive manufacturing. As the turbine blades are thought to be one of the most complex and demanding structures in an engine, this achievement marks a significant milestone for additive manufacturing. It is anticipated that over the next few decades the technology will continue to progress and it will be possible to fabricate the surfaces needed to produce fluid slip.

The core idea of this thesis is that the surface of the bearing chamber may be modified to sustain a large fluid slip. This is likely to involve using additive manufacturing to construct the chamber so that it incorporates the necessary intricate designs. However, before funding can be sourced to manufacture these chambers, it is necessary to determine if slip has a significant effect on the flow of the bearing chamber as this is not yet known. This thesis is consequently set

out to begin answering the specific question of if fluid slip has a significant effect on how the oil flow may act in the bearing chamber. This is completed by using a dependable model of the oil flow that can reveal the intricate fluid dynamics and prevailing thermodynamics throughout the chamber to assess how the flow changes due to slip.

1.2 Aims and Objectives

The aim of this research is to investigate the behaviour of the oil flows found within the bearing chambers of aeroengines, which allows for the identification of the pertinent physical effects and model representative flows.

The specific objectives which are presented in this thesis are:

- to develop a model which represents the flow of oil inside the bearing chamber as a rimming flow.
- to carry out studies with partial slip on the wall and assess the impact on the fluid dynamics of the flow.
- to assess the changes to the thermodynamics of the thin film when partial slip acts on the wall.
- to highlight that the value of the characteristic parameters are important considerations for modelling applications.
- to demonstrate for characteristic values typical for the bearing chamber and with slip lengths equal to lengths of slip measured in experiments that slip has a significant impact on the film.

1.3 Methodology of the Thesis

The aero-engine bearing chamber is a multiphase flow of predominantly air and oil, amongst other constituents, which encompasses numerous complex phenomena that occur as each phase interacts with each other. This complexity is compounded in the bearing chamber as the bolts, connectors, seals and the varying speeds of the shafts also interact with the oil system. The progress of Computational Fluid Dynamics (CFD) on modelling multiphase flows has been significant since its commercialisation, whilst geometric features can now be resolved with complex meshing algorithms. However, these can be time consuming to set up and simulate, therefore a simple representative case will be used which can swiftly assess the flow characteristics and addresses this issue. A second concern is that CFD models

assume all necessary physics have been appropriately included. Although this thesis explores physical behaviour that has been previously undocumented for the bearing chamber and rimming flow. Specifically, the physical behaviour at the interface between the fluid and solid surface is investigated, as studies have detailed multiple mechanisms that may produce a type of slip behaviour.

The first step in the methodology of this thesis is to make several assumptions about the oil flow within the bearing chamber, many of these are to make the modelling strategy easier and to limit the scope of the study. The first assumption is that the bearing chamber contains a small volume of oil that may coat the entire chamber walls by a thin film. The second assumption is the inner shaft is rotating fast enough that the core air flow will be travelling with enough velocity that it creates a shear force on the oil surface. This force is assumed to be strong enough that the oil will be driven to completely coat the chamber walls as a thin film.

The chamber geometry is a very complex structure which includes bearings, ports and seals. There are ways to detail the chamber with commercial software, but these complexities make understanding the importance of physical effects difficult to determine. It is therefore prudent to use a simpler geometry, which can be described as a stationary horizontal cylinder. The rotating flow inside a cylinder is commonly referred to as a rimming flow and is therefore the topic of study in this thesis.

The chambers include a sump to extract the oil that is being continuously injected into the bearings, however for the work of this thesis neither the sump nor the oil droplets have been included. While the flows vary axially, for the work of this thesis there is an assumption of axial homogeneity per unit length. This means the problem under investigation is only two-dimensional.

There are several physical effects in the flow of oil which are assumed to be significant, notably these are gravity, hydrostatic pressure, inertia, surface tension and viscosity. The review of existing literature on thin film models and flows within the bearing chamber have verified this assumption.

The last assumption is related to how fluid interacts on the cylinder wall and the investigation into this forms the bulk of this research. At the macro-scale, this interaction is typically described by the no-slip condition which states that the velocity of fluids in contact with the surface is zero. However, studies have indicated that if the layer of fluid is small enough, this description may no longer be accurate. Another description of this effect is known as the partial slip condition, where the fluid velocity at the wall is related to the fluid shear by a proportional constant known as the slip length. There have also been studies on surfaces which have been treated with specific chemicals or built with certain patterns that may

produce a similar effect. The surface attributes which create this flow behaviour have not been fully defined, however experimental results have measured this slip length. Therefore, the last assumption is either that the size of the flow or that the design of the chamber walls satisfies the criteria that partial slip will occur.

The mathematical model of the oil film is derived from the conservation of mass, momentum and energy equations using a two-dimensional cylindrical coordinate system. The film of oil has two boundaries which are located at the cylinder wall and the interface between the fluid and air flow. Equations which conserve the mass, momentum and energy at the air interface have been derived to provide suitable boundary conditions, along with the kinematic boundary condition at the interface. Two of the boundary conditions at the wall are the no-penetration condition and the equation to model the wall temperature. The last boundary condition describes the flow velocity at the wall, using a generalised Navier slip model, in this instance velocity is related to the fluid shear rate as defined by slip length. These equations are non-dimensionalised using appropriately defined non-dimensional parameters. This includes the capillary, Reynolds and Péclet numbers which are a common step in developing mathematical models.

The assumption that the walls are coated in a thin layer of oil means the characteristic height and cylinder radius may be expressed as a small parameter, ε. Each term of the equations may be expressed as an order of this small parameter, this allows for terms to be grouped to zero order (leading), first order and even higher orders of ε. The governing equations may be simplified by taking a thin-film approximation to retain only leading and first order terms, this approach has been presented in many studies which have been reviewed in Chapter 2. However, some higher order terms which may be removed by the thin-film approximation are necessary effects when modelling the bearing chamber. These effects are predominantly those of inertia, surface tension and thermal convection. Therefore, the Reynolds and Péclet numbers which describe the inertial and convective effects are deemed to be large enough that the terms may be equal to a leading order term. The higher order terms of surface tension are known to approach values equal to leading order terms in the presence of surface discontinuities and are therefore retained in the model. This treatment of the governing equations has been shown in the study of other flow configurations, including the rimming flow and planar flow problems which has been reviewed in Chapter 2.

The study of open channel and waterway flows have concluded that inertial effects are important as the Reynolds number is relatively large. These hydraulic applications are typically assumed to be either one-dimensional or planar as the components of the vertical velocity are relatively small. The vertical velocity in the rimming flow problem is also small as the film is typically smooth. Making

it sensible to use techniques for hydraulic studies which include inertia to also include inertia for rimming flows. One of these techniques is the depth-averaging method and can be used to model high Reynolds number flows. This method uses the boundaries of the flow, in this case the cylinder wall and interface at the air, to integrate the governing equations over the entire fluid depth. This reduces the dimensionality of the governing equations to now being one-dimensional, having introduced two new variables to replace the temperature and velocity fields. These variables are known as the mean temperature and flow flux and are the integral of the temperature and velocity fields across the film depth. While the mean variables contain no two-dimensional information on either the temperature or velocity, reconstruction of these fields can be done by an *a priori* selection of the field profile. In this thesis the profile is taken to be a parabolic polynomial with a dependency on the radial distance from the cylinder wall, this is in keeping with analytical solutions to Stokes flow. The polynomial coefficients are calculated from the boundary conditions and definitions of the mean flow variables. The interpreted velocity and temperature fields from the parabolic polynomials may provide the necessary details to determine the presence of any regions with flow recirculation or high temperatures.

The mathematical model is implemented in a numerical model by discretising the spatial domain with a pseudo-spectral method and using an implicit time stepping scheme. The numerical model is implemented within a specialised program within MathWorks MATLAB software package, where the depth-averaged governing equations are linearized and then solved. The solutions provide approximations to the mean variables and reconstructs the temperature and velocity fields for a given non-dimensional parameter set ready for analysis.

1.4 Overview of the Thesis

This first Chapter gives a brief overview of the motivations behind the research and introduces the aims and objectives that have guided this thesis. The key assumptions which have formed the basis of the work are also outlined, along with aspects of the methodology which has been used for this study.

Chapter 2 contains the background literature on both experimental and theoretical studies on the topic of bearing chamber flows, to help highlight the current understanding of fluid effects and determine which are most applicable to this thesis. The wide body of literature on the related area of rimming flows and thin film models are also reviewed. A review of the lesser explored area of surfaces which are linked to an effect known as fluid slip is accumulated, where the surfaces have been treated by either special chemicals or structures.

The mathematical model of this thesis is formulated in Chapter 3, where the complex bearing chamber flow has been developed into a time-averaged rotating flow within a horizontal cylinder. Several non-dimensional parameters are also introduced to gauge the relative strengths of the various physical effects in fluid flows and defines the regime the model is intended for. The method of depth-averaging the governing equations is presented in detail and the numerical method used to solve the problem is presented with a discussion on both the numerical validity and testing benchmarks.

The analysis of isothermal films covered in Chapter 4 details a rich variety of flow scenarios relevant to the wider problem of rimming flows. Chapter 5 contains results and draws some conclusions of the role fluid slip can have in controlling the temperatures within films coating the cylinder walls, while Chapter 6 analyses flows relevant to the bearing chamber and gives an in-depth overview of each characteristic value. Chapter 6 additionally sets out the main findings of this research by assessing the varying levels of slip reported in the background literature and the corresponding impact these have on the film.

The closing statements of Chapter 7 presents the core conclusions from each Chapter and gives several potential topics where the work can be expanded in future studies. The Appendices contains some useful mathematical identities and the derivation of the boundary conditions at the free surface.

Chapter 2

Literature Review

The work within this thesis may be applicable to both the aero-engine bearing chamber application and other related problems of industry. Relevant literature related to the mathematical formulation and rimming flow problem is categorised into distinct sections: the modelling of thin-film flows pertinent to rimming flows; the integral approach from hydraulic theory; thermal effects of thin films; the role of surface coatings and substrates in flow control and the models of bearing chambers.

2.1 Current Models of the Bearing Chamber

There is significant research focusing specifically on the films within bearing chambers. The Karlsruhe Institute of Technology (KIT) in Germany has produced a quantitative assessment of bearing chamber flows, having conceived a practical rig that can replicate a broad range of operating conditions experienced in aero-engines. One of these assessments has been the use of ultrasonic instruments to locate the film surface in the bearing chamber, where Wittig et al. [3] were able to measure the film thickness. They found that the film thickness was dependent upon the speed of the rotating cylinders and was found to be between $0.7\,mm$ and $5\,mm$ in depth. This measurement technique is useful as it is both non-reactive to the fluid and may be adapted for other geometries. From readings of thermocouples spaced throughout the chamber, a model using the finite element method was used in characterising the heat transfer coefficients of the wall, which may be used to infer the thermal load within the chamber. The driving force was from a rapidly rotating shaft concentric to the test chamber, with an operational speed up to $16,000\,RPM$, which had a gap of $28\,mm$ between the rotating and stationary cylinders according to Glahn and Wittig [4], who used the same apparatus.

The flow of the bearing chamber was monitored by fibre optic laser Doppler velocimetery by Glahn and Wittig [4], where measurements of all operating

conditions gave rise to corrective terms which were added to a simple model of balancing the gravitational and viscous forces. These terms were empirical correlations which include additional gravitational forces and eddy viscosities when modelling the laminar and turbulent flows that were reported, which depended upon the operational conditions. The films were measured to be approximately $2\,mm$ in thickness and is additional evidence that the scale of the bearing chamber films is small. This assessment of the experimental data and models was developed further in the prediction of heat transfer in a simple mathematical formulation by several existing models. It is worth noting that this analytical approach was a good compromise, but under-predicted trends by nearly $40\,\%$ of the experimental data, though further refinement is possible by including correlations of turbulent Prandtl number, which measures the ratio of momentum and thermal diffusivity.

The work by Rolls-Royce plc is significant in developing the models for oil films within the bearing chamber, with an integral approach to the bearing chamber presented by Chew [5] to model the oil films driven by a rapidly rotating inner cylinder with large Reynolds numbers signifying inertial effects, which improves on the previous works by Wittig et al. [3] and Glahn and Wittig [4]. The works of Chew [5], Wittig et al. [3] and Glahn and Wittig [4] all assumed that the radial pressure gradients within the film are sufficiently small as the small film thickness means that they can be treated as negligible. The surface tension of the film at the interface between the fluid and air was treated as being negligible. The model Chew develops is not completely conclusive due to differences when evaluated with the experimental data. These differences may be attributed to the reliance on specific correlations which depend on if the fluid is being treated as either a laminar or turbulent flow. These corrective factors which describe the flow are dependent on being in either the laminar or turbulent regimes and limits the generalisation of the model to all regimes. However, it is possible to formulate a model which composes a more generalised approach for both laminar and turbulent flows, shown in the thesis of Kay [6] and developed within this thesis.

Gorse et al. [7] also used laser Doppler velocimetry and capacitance probes at the KIT to measure the velocity profiles and film thickness by indirect and direct measurements respectively. The minimum film thickness reported was $0.5\,mm$ and depended on both the rotation speed of the inner shaft and the volume flow rate of oil into the chamber and had a maximum thickness of $1.5\,mm$ indicating the films are of micro-scale characteristically. Predictions of the driving shear force created by the fast air flow over the film was calculated as an assumed constant value ranging between $2\,N/m^2$ and $20\,N/m^2$ depending upon the rotation speed of the rotor.

A stability analysis used by Noakes et al. [8] was based on the idea that bearing chamber flows operate at such high speeds that the effect from gravity is negligible. The results suggest that the axial disturbances in their three-dimensional model are the most unstable, known as ring instability in their general study of both rimming and coating flows. They also discussed the difficulty in comparing their model as the operational regime was yet uncharted for either rimming or coating flows, most notably for the cylinder size being around $0.1\,m$ while the rotational speed is in excess of $9,000\,RPM$, giving a cylinder speed of $100\,m/s$.

The first example of using an integral approach for the rimming flow problem can be found in the works of Chew [5]. A second example can be found in the works by Farrall et al. [9]. This later integral model compared well with the experimental data collected by the KIT, where flow profiles were approximated with a reasonable level of accuracy. The methodology involved a two stage process which mixed a CFD package to track the dispersion of oil droplets through the chamber and interaction with the film surface, the results at the interface were then transferred into a boundary condition for the integral model of the film that had been developed previously. The two-dimensional model was able to account for several traits including gravity, surface shear and importantly the transfer of mass and momentum by impinging oil droplets into the film.

A study on the aero-engine bearing chamber by Guoding et al. [10] created a distribution function that modelled the momentum transfer and mass deposition of the oil droplets onto the wall. As expected, with a significant reduction in the driving force, by reducing the speed of the rotor, the film that was sustained around the chamber walls shrank substantially. The model predicted larger films than expected but remained in good agreement with experimental results. The ability of modelling droplet impacts onto the surface of a coating film was further explored by Noakes et al. [11], where only mass transfer of droplets was considered in a continuous droplet distribution into the film surface and no momentum was imparted into the film. The formation of steep fronts were observed in the steady state films, where fluid mass is added at an equivalent rate to the extraction rate, which are associated with hindering the heat transfer of the film, but which can be suppressed by a smaller Bond number, defined as $Bo = \Delta\rho g L^2/\sigma$. This suppression is due to surface tension acting to smooth the steep fronts, which are linked to the pools found in rimming flows. If the droplet spatial distribution is not uniform, and deposits a significant portion of mass on the falling cylinder side, this leads to a secondary jump in the film profile forming. It may be possible that strategies can be found to specify the delivery of oil droplets and locate sinks for extraction in order to eliminate the flow recirculation found in aero-engine bearing chambers.

The depth-averaged model by Wang et al. [12] was a single equation where the continuity and momentum equations had been coupled together in a mathematical formulation. This model included many physical mechanisms within the film, most notably, gravity, pressure, surface shear stress, surface tension and the interaction of droplets. The model compared qualitatively to the work by Chew [5] in the prediction of film heights and velocities. The model by Wang et al. was implemented into commercialised CFD codes and was able to reproduce stable, smooth solutions. A drawback of this was the inability to account for shock and pool solutions which are stable. This was due to retaining terms that are up to first order only and simplification of the inertial terms according to Kakimpa et al. [1].

With a droplet injector opposite to the extraction sump, Chandra et al. [13] created an acrylic rig to capture the importance of the sump design on the flow conditions. The importance of the sump was an aspect of the work by Guoding et al. [10], who had investigated if the sump location or design were important. The lip attachments that were mounted to the front of the sump were based on previous models as either sharp or rounded lips, shown in figure 2.1. The sharp lip is linked to a separation region, which generates flow recirculation within the outlet channel and inhibits the drainage which also causes a stagnation point within the chamber, and these are all problematic features in maintaining the oil. With a curved surface on the underside of the lip, the separation region may be eliminated, though a stagnation point is present in the region of the tip as the flow is splintered into either flowing through the outlet channel or the main chamber. Unfortunately, neither design of the tangential sump was able to eliminate the recirculating regions from forming, even with a larger outlet channel size, which showed limitations to the performance. An altogether different design of the sump which showed promise was presented which reduced the volume of fluid contained instantaneously within the chamber up to moderate shaft speeds, where the residence volume may be used as an indication of the chamber performance.

The ability to model the flow within the bearing chamber by thin film models was furthered by Kay et al. [14] for isothermal and later for non-isothermal films by Kay et al. [15] in the rimming flows characteristic of the bearing chamber. The flow was assumed to be axially uniform and the fluid coated the cylinder walls. Importantly, the full terms of inertia are retained within the thin film limits due to the assumption that the film will have a moderate Reynolds number. This is due to the bearing chamber operating conditions and was shown to be important in their first study. Their later work highlighted the role that thermal convection plays by including the full thermal convective terms to a leading order formulation. The addition of droplet effects where mass and momentum were

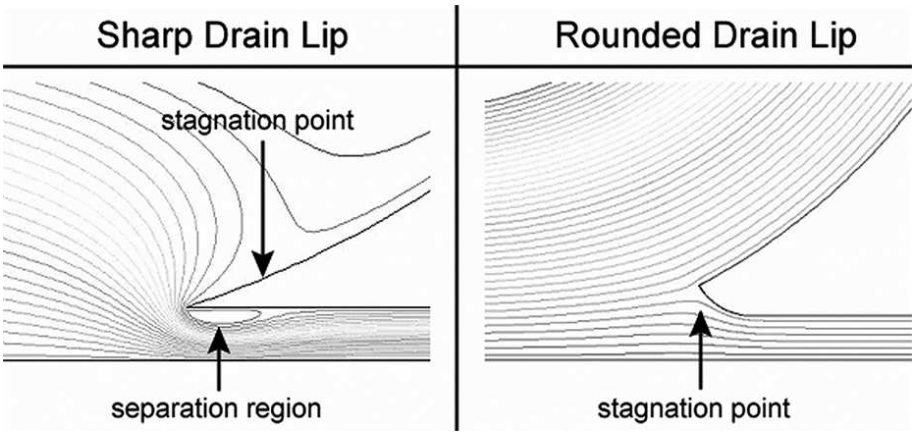


Figure 2.1: The typical streamlines around the sharp and rounded sump lips. Republished with permission of American Society of Mechanical Engineers, from Scavenge Flow in a Bearing Chamber With Tangential Sump Off-Take, B. Chandra, S. H. Collicott and J. H. Munson, 135, 3, 2013; permission conveyed through Copyright Clearance Center, Inc.

transferred to the film were also studied by Kay et al. [16]. They specifically added the transfer of energy that may occur if the fluid droplets are at a different temperature as they enter the film. The thin film models of Kay et al. [16] were found to be a reliable method to capture the average instance of flow within the rotating flow when driven by air shear, where the chaotic nature of the potentially turbulent flow is averaged over time. This means that the characteristic flow values of the subsequent work by Kakimpa et al. [1] will fluctuate throughout the chamber, which adds complexity in studying the physical phenomena. The depth-averaged model of Kakimpa et al. [1] was shown to measure well against the experimental data of Tirumkudulu and Acrivos [17]. However, the use of surface tension coefficients in some previous works were linked to non-physical waves from capillary forces to relax the numerical calculations necessary. These surface waves incur a high computational cost to avoid under-sampling issues related to the small wavelengths of the capillary waves. This ability to reduce the computational requirements by depth-averaging is also mentioned in Kakimpa et al. [18], as a method which is both relatively cheap and rapid in assessing preliminary designs of bearing chambers and can approximate both the film dynamics and core gas flow.

Unlike the modern thin film models for bearing chamber flows, Adeniyi et al. [19] created a model within the ANSYS FLUENT software. The oil input feed was modelled as both a continuous axial slot and as distinct holes for injection sites on the outer wall, with nearly complete wetting only occurring in the continuous slot simulations. If the oil is injected from distinct holes into the chamber, the flow can

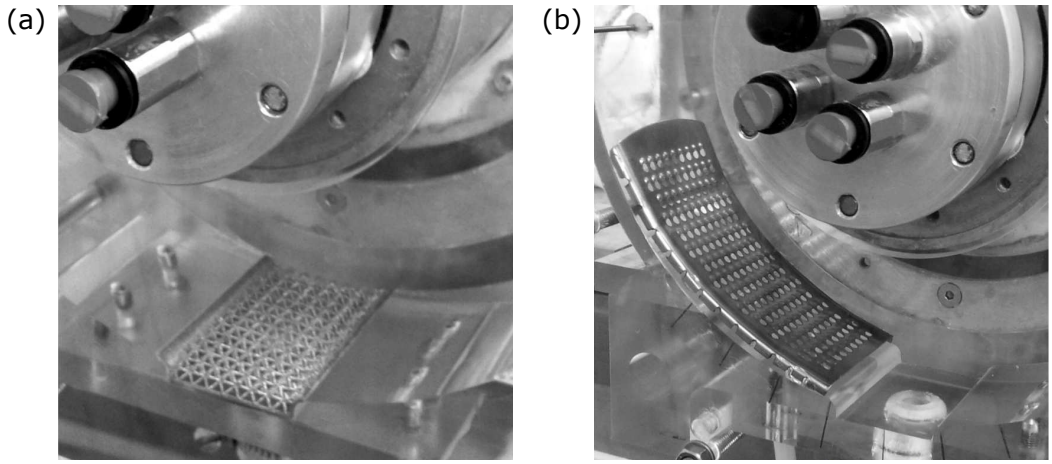


Figure 2.2: The porous insert (a) and perforated plate (b) used in the experimental investigation of bearing chamber flows by Chandra and Simmons. This photograph is produced with the permission of Rolls-Royce plc, copyright © Rolls-Royce plc. 2020.

be almost half the thickness of the single slot case so it must be considered when modelling the three-dimensional flow that simplifications for modelling complexity will no longer represent the real world case of the bearing chamber.

The splattering of oil droplets onto the chamber walls by oil shedding from the bearings of the aero-engine were validated in computational and experimental studies by Sun et al. [20]. The droplets of fluid were injected into the chamber by jetting fluid onto a rotating disk that ejected droplets with both radial and azimuthal momentum and the film was extracted via a simple sump at the chamber base. While showing good agreement with the experimental data, the general formulae were suitable for a number of geometric and operating conditions using 14 criteria to identify the flow.

Chandra and Simmons [21] tested a number of sumps to improve the flow within the bearing chamber by a measure of the instantaneous residence volume of fluid for evaluating the sump performance, similar to that of Chandra et al. [13]. An optimised geometry for the sump, similar to the Rolls-Royce AE3007 sump was targeted in Chandra and Simmons [21] as an option to reduce the volume of fluid trapped within the chamber. This new sump design is referred to as the optimised shallow sump. When operating with a rotating inlet distributor which seeded the chamber with oil droplets, the optimised shallow sump was shown to be beneficial over a simple sump outlet. However, when using a simple film generator to create a continuous film around the chamber, the optimised sump was found to have worse behaviour for the flow than the simple sump according to the instantaneous residence volumes.

This thesis explores the idea that the chamber may be designed in a way

that changes the interaction of the oil with the surface. Part of this idea stems from the knowledge that a porous surface, even in the equivalent scale to the film thickness may improve the flow dynamics. This was shown by Chandra and Simmons [21] for a porous insert and offered significant improvements in both droplet and continuous film generated flows, as shown in figure 2.2. Despite the porosity and permeability of the insert not being stated, the performance of the insert showed good overall performance while not being the best for any single case and covered only a limited area over the outlet. These results show that a porous material can be beneficial for the chamber and there are suitable materials which can be used in the bearing chamber. There are several interesting designs which were explored in this study, one of these was a perforated plate which is shown in figure 2.2.

2.2 Rimming Flows and Related Studies

This Section describes many of the approaches used by previous authors into modelling a thin film of fluid. The rotating flow within the cylinder is an important topic to discuss as they are relevant to the flows in the bearing chamber. This review starts with the earliest studies which outlined the topic and explores the wider literature including recent publications.

2.2.1 The Classic Analysis of Rotating Flows

The oil flow within the bearing chamber can be described as a thin fluid film, with the topic of models for thin films being the focus of a substantial number of studies in recent decades. The geometry of a partially filled horizontal cylinder is also representative of the chamber geometry, omitting the intricacies that the components of the chamber such as the seals and fastenings may add. Accordingly, the details of modelling strategies for thin fluid films and those of flows around a horizontal cylinder are examined in this thesis. The distinction between the flow internal to a cylinder, known as rimming flow and those external to the cylinder, known as coating flow is appropriate at this point.

A rimming flow problem is described as a volume of fluid within a cylinder that does not saturate the cylinder, driven by either the rotation of the cylinder or by shear at the inner interface by an air flow to the extent that fluid may form a coating layer around the entire inner surface. Dependent upon the strength of the driving forces and the quantity of fluid contained within a cylinder, there are typically four recognisable scenarios that may form according to sources including Chatterjee et al. [22] and Johnson [23]. Examples of these flows have been

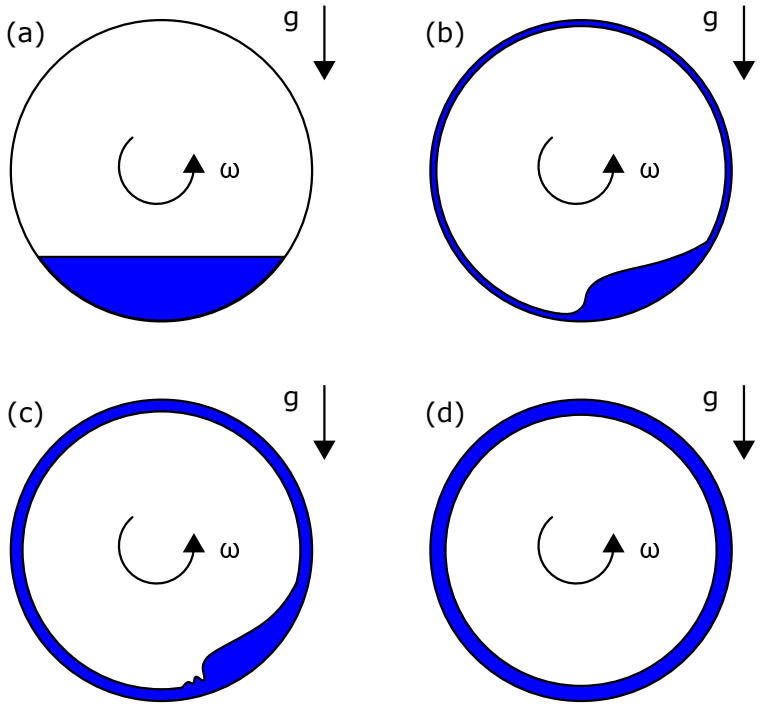


Figure 2.3: Four typical flow profiles found when studying rimming flows which depend upon the associated driving force, with the stagnant pool in (a), a wetting flow with significant pooling (b), a transitional flow subject to a surface shock with capillary ripples (c) and the uniform rimming flow in (d).

portrayed in figure 2.3 and are explained in the following paragraph.

One of the more frequently observed cases is where fluid is evenly dispersed throughout, creating a film which has a height that is uniform, or relatively constant around the entire cylinder. These uniform films are typically generated by either a fast rotation rate of the cylinder or strong shearing force of the airflow imparted upon the fluid or a compounding combination of both factors and are shown in part (d) of figure 2.3. However, if the cylinder is stationary or slowly rotating or there is a stagnating air flow, the fluid will form a pool under the influence of gravity because the driving strength is insufficient to overcome gravity and dry out of the cylinder wall occurs, shown in figure 2.3 part (a). Within this fluid pool, the aspect of a recirculating flow becomes important as the velocity may turn against the direction of the flow, as shown in figure 2.3. This can be detrimental in maintaining the conditions of oil in the bearing chambers. Between these two cases there are other types of films; an example is shown in figure 2.3 part (b). This is where a pool of fluid forms near the cylinder base and a thin layer of liquid is pulled onto the wall. This is due the airflow or cylinder rotation drawing fluid from the pool and prevents the chamber from de-wetting. Another example is when the driving force is stronger, and results in the large fluid body

appearing on the upstream cylinder wall as in figure 2.3 (c), which will still contain a degree of either flow reversal or stagnation.

The study of rotating flows that coat the containing walls is prevalent across a number of industries beyond those of aero-engines, examples of which can be found in powder rotational moulding using reactive polymers by Agbessi et al. [24], oscillating tidal water behaviour across sea beds that deposit sand constituents for sediment infused water flows by Dyakova et al. [25], the synthesis of ceramic coatings by reactive powders coating the inner surface of steel tubing by Menekse et al. [26], rotocasting by either reactive or thermoplastic powders by Nguyen et al. [27], single and continuous multi-shot rotational moulding of polymers by Oglia et al. [28], cream separators for the production of milk products by Ruschak and Scriven [29] or in rotating heat pipes by Singaram et al. [30].

The work of Ruschak and Scriven [29] treats the flow around a cylinder as a solid body rather than a shifting flow. This assumption can be made if the gravitational effects approach zero, the cylinder radius approaches infinity or if the cylinder rotation rate tends to infinity and means the fluid is uniform around the cylinder. However, if the effect of gravity is larger or the cylinder speed slows, the surface of the flow will start to deviate from the uniform profile. Their work used a regular perturbation method to deviate from the rigid-body flow to calculate where the film thickness changes. The location of the maximum thickness was always found to be on the opposite side of the cylinder to the minimum thickness and this was in the upper quadrant of the rising side.

However, there are situations where the driving force, typically from the cylinder rotation means a rigid body approach is not suitable. The earliest work on flows within a cylinder where they are not treated as a rigid body was done by Johnson [23]. This work used the lubrication approximation to model the flow, which implies that the characteristic thickness of the flow is significantly smaller than the length scale. Johnson derived an equation for rimming flow to $O(\epsilon)$, with ϵ being the ratio of film thickness and cylinder radius and is subsequently small. Though the cylinder is filled with air, Johnson assumed that any effects of this gas were negligible and made the same assumption about any effects from the flow inertia or surface tension being negligible. This assumption that inertia is negligible or very small is a common feature of works using lubrication theory, as the small ratio between the film thickness and length scale implies that the Reynolds number is also small. The equation Johnson established was a balance between the effects of gravity and viscosity in a rotating cylinder partially filled with fluid. This is commonly known as the flux equation, which determines the volume flux of the fluid moving within the chamber. The internal hydrostatic pressure within a fluid will increase with added depth, however the fluid was assumed to be very narrow.

This assumption means that the pressure difference between the top and bottom of the film may be negligible, so pressure will be constant within the film. It could be inferred by the results of the flux equation that reverse flow may occur. This is because points in the film where flow stagnation occurs were calculated, although these results were beyond the modelling capabilities of the presented flux equation.

Prior to the work of Johnson, the paper by Moffatt [31] has been the foundation for all subsequent studies. Moffatt first presented a lubrication model for a coating flow around a cylinder which resulted in the flux equation, describing the flow rate within the cylinder. Instabilities of the flow were shown to evolve into a series of sections separated by a liquid ring that can carry "lobes" of fluid along the axial dimension from the experimental studies of a rotating cylinder. The previously mentioned flux equation was also arrived at within the lubrication theory for coating flows, showing a dependence on the rotation rate that leads to a critical mass which can be sustained in a steady flow. It was also inferred that with the unstable features of the liquid rings which collect fluid as axial patterns, as depicted in figure 2.5, that surface tension may play a significant role when determining their final shape.

The inclusion of inertia in the modelling of rimming flows was presented by Orr and Scriven [32] who showed a finite element analysis of the governing equations was an effective modelling strategy. Their work solved the full Navier-Stokes equations, so they were able to retain the full effects of the inertia of the fluid. The interaction of the forces is a complex system and suggests that in only limiting cases can effects be disregarded. The expectation that fluid will drain from a rotating cylinder when coating the surface if the driving force is reduced was explored by Preziosi and Joseph [33]. Their work documented some of the known axial features as mentioned previously, the most notable being in rimming flow where the entrapped air layer becomes segmented by rings of fluid that cascade from the cylinder wall. This axial behaviour of fluid collecting along the cylinder also occurred with coating flows, showing undulations occurring along the cylinder length.

There are three solutions to the cubic flux equation for the film height for a given volume flux. Normally, at least one of these solutions will be a real physical profile that is approximately smooth across the domain. There is another solution that is likely to be unbounded and non-physical. This solution branch exists above the local maxima of the film, which is on the lower quadrant of the rising wall. However, there is an upper limit to maintaining the real physical solution across the domain and this is related to the volume flux. As the volume flux gets larger, the smooth physical solution begins to form a local maximum depth on

the rising wall of the cylinder. The unbounded physical solution also approaches the bounded physical curve with increasing flux until they eventually connect at the maximum point of the bounded solution. The value of the volume flux when this connection happens is referred to as the critical volume flux. While the single bounded physical solution with the connected unbounded solution is known as the critical film, the maximum depth of this solution is known as the critical film height.

If the value of the volume flux is increased beyond this critical value, the location where the solution branches connect will begin to form a region in the domain with no physical solution. The size of this region increases with greater volume flux and two distinct solution branches now exist in the domain. This presents a significant limitation of lubrication theory in modelling a pool of fluid in the cylinder as a discontinuous jump is necessary to bridge this region. Films which have this discontinuous jump are known as a shock solution, which is where a sharp change in the film height occurs.

While the shock solution was suggested by Johnson [23], O'Brien and Gath [34] explored the limitation of the shock solution. Their work confirmed the criteria of Johnson for the locations where the discontinuities occur and developed a simple expression to be able to determine if a shock were to occur on the film. The shock solution was linked to the total fluid volume contained within the cylinder. While some solutions are expected to be non-physical, it was expected that a shock solution may occur in the lower quadrant on the cylinder wall where fluid is rising upwards. The existence of a shock solution was also shown by Benilov et al. [35] in the absence of surface tension, forming a sharp peak on the film surface. However, the sharp solutions were stabilised by surface tension, acting to regularise the instability which eliminated any physically meaningless solutions. The role that surface tension plays in rimming flows is detailed later in this thesis.

Configurations of the possible shock solutions that may occur in rimming flow are presented by Villegas-Díaz et al. [36] using kinematic wave theory. The three configurations are; a shock solution occurring on the lower quadrant of the falling wall, on the lower quadrant of the rising side or as a dual state where a shock is present in the lower quadrants of both the rising and falling walls. The combination of driving factors was the cause of shock locations occurring at alternate locations of the cylinder.

2.2.2 Including Significant Internal Pressure Gradients within Thin Films

A typical assumption when using the lubrication theory is the pressure differential within the film is negligible due to the film being thin. The study by Tirumkudulu and Acrivos [17] showed film solutions may have a discontinuous region, this is where the film height changes abruptly. This discontinuous region is important, as it means that the assumption that the pressure gradients are small is no longer valid as there is a jump in the hydrostatic pressure. This jump in the hydrostatic pressure is predicted to strengthen the back flow that can occur and was previously discussed by both Moffatt [31] and Johnson [23]. Therefore, Tirumkudulu and Acrivos retained a simple hydrostatic pressure term with the thin film approximation to model a pressure jump. This additional term in the model allowed Tirumkudulu and Acrivos to calculate solutions which were representative of their own experimental results and the experimental data that had been presented earlier in the works of Melo [37]. The lubrication model which is extended to include hydrostatic pressure gradients can form a film profile with a deep fluid pool around the base of the cylinder, due to gravity. A narrow film of fluid is drawn from the pool across the cylinder as a complete wetting flow. Within the deep pool a recirculation zone appears where fluid overturns against the cylinder rotation. This maintained assumption was that the film is still sufficiently thin that both inertia and surface tension are still negligible in the lubrication theory limits.

The lubrication theory models indicate there is a maximum volume of fluid that can be sustained as a coating or rimming flow. This was first mentioned by Moffatt [31] where a sharp corner occurs at a maximum local thickness for a critically loaded cylinder. This peak was absent in the work by Wilson et al. [38] as a higher order model was shown to have smoothed profiles for the critical solutions of both rimming and coating flows. The higher order terms, which included pressure, were dominant over those at leading order in the region of the sharp peak. These terms lead to a smoothing of the profile, which alter the critical loading volume to be higher than Moffatt's. The model formulation with higher order terms also assumed the surface tension effects were small, while experimental results have shown surface tension may become significant.

Further to this concept of including hydrostatic pressure as an important force in modelling rimming flow, Acrivos and Jin [39] investigated the stability of the extended lubrication equation of Tirumkudulu and Acrivos [17]. While the model was shown to be stable if surface tension is neglected, if surface tension was to be included in the extended lubrication model, the films would be more stable to

two-dimensional disturbances.

An interesting instability was reported by Benilov et al. [40], where unstable solutions may develop as a perturbation on the film surface, which, due to gravity, increases the perturbation amplitude until a large size is reached then a drop of fluid can detach from the film and descend from the cylinder ceiling. These instabilities are also investigated by Benilov et al. [41] where both azimuthal and axial hydrostatic pressure terms are included in their model of the lubrication approximation. The asymptotic analysis of the surface instability can describe the initial stage of the surface perturbation that forms into detached droplets, however the limits of the lubrication theory would be broken and invalidated.

The work of Villegas-Díaz et al. [36] furthered the modelling of rimming flows within the lubrication theory framework, but rather than only the rotation rate of the horizontal cylinder acting as a driving force of the flow, a constant surface traction force may be imposed on the free surface of the fluid. Their analysis assumed a hydrostatic pressure, with zero pressure at the interface for defining various combinations of the driving forces, which will be discussed in further detail later.

2.2.3 Modelling the Presence of Fluid Surface Tension

There are several early studies which have built upon the lubrication theory model of Johnson [23]. The original models of gravitational and viscous effects now include the effects of hydrostatic pressure. This has been justified as there may be a significant change in the film depth, which means these terms are important. However, for these films where there is a significant change in the film depth, studies including those by Acrivos and Jin [39] and Benliov et al. [35] suggest that surface tension may be significant. The analysis by Wilson et al. [38] also concluded that surface tension effects may be a significant factor in the experimental results. It is thought that surface tension may be a significant factor on the stability of flows.

Benilov et al. [40] conducted a harmonic analysis of a lubrication model which contained higher order terms. While they cite harmonic solutions are not a completely reliable indicator for solution stability, they reported systems where the disturbances eventually blew up in a finite time and are therefore unstable. These unstable solutions behaved in a similar way to the instabilities found in nonlinear media and were consequently deemed to be explosive in nature. As surface tension is generally stabilising, Benilov et al. [42] included terms which represented surface tension and showed that the explosive instabilities were eliminated and solutions were completely stable. However, some solutions instead became unstable as a

result of including surface tension for a particular parameter range.

The smoothing of the shock features for a flow which can be driven by both cylinder rotation or air shear were explored by Villegas-Díaz et al. [43], using higher order terms from gravity or surface tension. The three previously mentioned compositions of shock structures were shown to be smoothed by surface tension, appearing instead as a sharp front with a narrow trough and peak neighbouring the pool, these are known as capillary ripples. The strength of the surface tension coefficient has a profound impact on the flow profiles, with low capillary numbers leading to an almost smooth film. The higher order gravitational terms were also shown to provide a stabilising effect for the shock solutions. When the stabilising effects of surface tension and high order gravity were included, multiple shock fronts were found to exist in the cylinder. The stability of the film structure around and above the critical volume flux were also investigated using this model to find regions where shocks occur. Their findings showed that with only surface shear a singular shock which may appear anywhere on the film. However, the multiple shock solutions were limited to existing only in the descending lower quadrant.

Benilov et al. [44] focused solely on the effects of surface tension extending the lubrication approximation with the absence of hydrostatic pressure effects. A dependency on the film volume and weak to zero surface tension created five characteristic flow types, known as the continuous, shock, near-critical, super critical and strongly super critical flows where the film height approaches the cylinder radius in size. While the formulation excluded the hydrostatic pressure effects that have been used to model flow recirculation as an extension of lubrication theory, the model was able to predict the thin coating flow and deep pooling fluid with a recirculating flow. The flow streamlines highlight how the flow drives the fluid along the cylinder wall and underneath the recirculating region, while in the shear driven flow of Kay et al. [14] the recirculation region will be underneath the bulk flow motion as a result of the different driving forces and stationary cylinder.

A three-dimensional analysis on the stability of rimming flows was used by Aggarwal and Tiwari [45] in the lubrication limits to first order with surface tension. The undulations known as "shark's-teeth" were shown to form as the flow collapses due to the influence from axial perturbations. If the viscosity of the fluid is sufficiently high in comparison to the gravitational forces, the film was shown to be stable due to strong viscous stresses supporting the film.

If surface tension is absent, Benilov et al. [46] state that a stable shock may only occur in the lower quadrant of the rising wall in a leading order lubrication approximation analysis. However, if surface tension effects are considered sufficiently strong, the region where a stable shock can form expands as the potential

region where unstable shocks, which overturn, contracts to a narrower region.

Evans et al. [47] investigated how the effects of gravity, surface tension and viscosity affected the flow on the outer surface of the rotating cylinder. Their lubrication theory model showed that surface tension is generally a minor factor for most of the flow conditions. However, if the rotation speed is either fast or slow, there is a small localised region where the surface tension effects are significant. Surface tension was shown to be a crucial force in supporting a mass of liquid that hangs off the cylinder surface as a pendant shaped droplet. Furthering their research on coating flows with surface tension, Evans et al. [48] created a three-dimensional lubrication theory model to explore the axial features of coating flows. The three-dimensional simulations showed that droplets of fluid form which are suspended from the underside of the cylinder. These were found at slow cylinder speeds and were validated against a simple experiment. They also found several other features including long fingers of entrained fluid.

An important piece of work in the study of rimming flows is presented in the work of Ashmore et al. [49] who investigated a broad range of flow conditions analytically. The primary focus was how varying strengths of the surface tension coefficient will change the profiles of the flow dependant upon the ratio of the relative strength between those of gravity and viscous forces of the flow. The classifications of the gravitational to viscous forces were in three distinctive sets, defined using a parameter λ, which measures the relative strength of gravity to viscous effects, and the typical profiles if either surface tension or that of first order gravitational terms or both are included. The most typical class of flow is where the gravitational and viscous forces are relatively equivalent in strength, $\lambda \leqslant 2$ which results in a predominantly smooth film that is largely uniform in fluid thickness around the cylinder surface, and therefore surface tension is unimportant due to the minimal gradients of the surface variation. If the viscous force is weaker, $2 \leqslant \lambda \leqslant 5$, gravitational effects are more notable and result in an accumulation of fluid toward the cylinder base though a thick film of fluid still coats the chamber. For an almost inviscid flow, $\lambda \geqslant 5$, gravity is the dominant factor and here surface tension is important as there is a strong tendency for fluid to accumulate at the base of the cylinder. One of the features that arises due to surface tension was termed the "dimple" that develops in front of the sudden change in film depth that occurs at the entrance of the pool, which is a common feature where surface tension is concerned for smoothing a film against sharp transitions in the film surface.

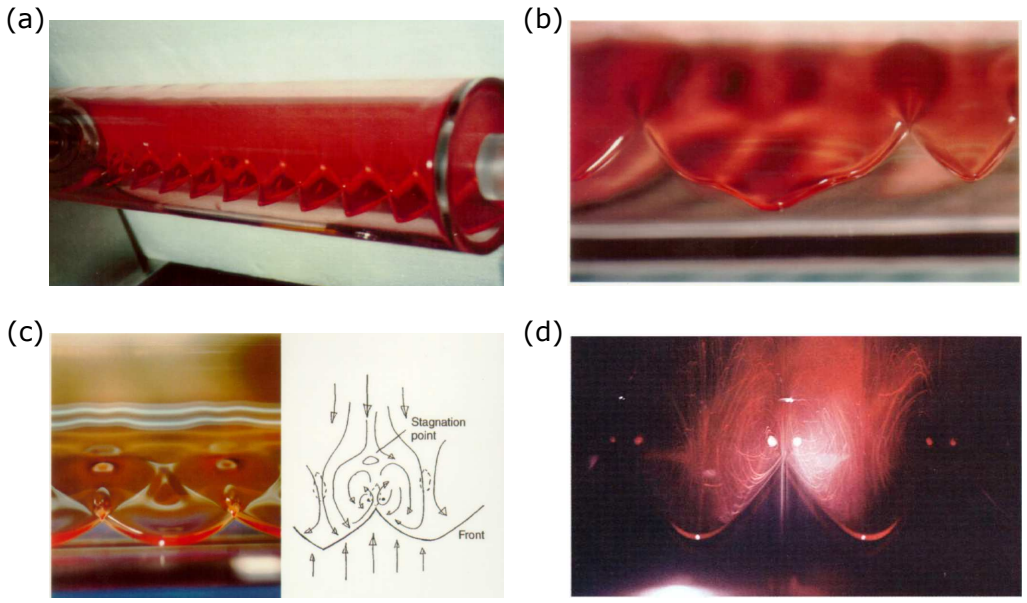


Figure 2.4: The axial features known as "shark's-teeth", showing the formation along the entire cylinder length (a), the transient form (b), the typical cusp formation and corresponding flow field (c). The swirl patterns captured around the peak formations were presented by Thoroddsen and Mahdevan, illuminating the pathlines and vortices in (d). Reprinted by permission from Springer Nature Customer Service Centre GmbH: Springer Nature, Experiments in Fluids, Experimental study of coating flows in a partially-filled horizontally Rotating cylinder, S. T. Thoroddsen and L. Mahadevan, 23, 1997. Reprinted from Physics of Fluids, 8, S10, S. T. Thoroddsen and L. Mahadevan, Shark-Teeth Pattern in Coating Flow Inside a Horizontally Rotating Cylinder, 1996, with the permission of AIP Publishing.

2.2.4 Introduction of Fluid Inertia in Modelling Strategies

One of the main assumptions for lubrication theory is that the film is sufficiently thin, which means the Reynolds number that describes the strength of inertia is characteristically small and may therefore be neglected. This assumption is typical when the flow is moving slowly because of the cylinder rotation being slow. This was one of the assumptions used by Moffatt [31], Johnson [23] and Melo [37]. However, there are situations where the angular velocity and fluid properties mean the Reynolds numbers are very large. An example of this is found in the work of Thoroddsen and Mahadevan [50], the high speeds and properties of the diluted glycerine and water mixture meant Reynolds numbers were calculated in excess of $20,000$ and inertia is no longer negligible even with the assumption of the thin film.

Hosoi and Mahadevan [51] derived an asymptotic equation which was able to model three-dimensional rimming flow. Their work investigated the effects of including inertia and surface tension with the use of a modified lubrication

theory, where the higher order terms were retained. The azimuthal velocity was approximated by a cubic profile and high order polynomial corrections. They showed that inertia was a significant factor on the shape of the film and instability onset. They were able to observe local ridge formations which are characteristically similar to those found in planar flows, which are explored later in Section 2.3. Their results were in agreement with the results by Thoroddsen and Mahadevan [50], where it was shown that axial instabilities ultimately developed as a stationary axial pattern of sharp peaks like those of "shark's-teeth", which are shown in figure 2.4. The destabilising effect of inertia was also shown by Benilov and O'Brien [52] with a leading order lubrication model. The higher order terms for inertia, surface tension, gravity and hydrostatic pressure were included as correcting terms. Their asymptotic expansion of the governing equations and harmonic analysis showed hydrostatic pressure does not cause instability, while surface tension causes only weak instability. Inertia was found to always cause instabilities in the flow as expected due to the non-linear behaviour of inertia. By creating an instability criterion, it was shown that the instability effect of surface tension is relatively weak in comparison to inertia. In fact, surface tension may stabilise the flow. Aggarwal and Tiwari [45] discussed how viscous effects may be able to inhibit the instabilities. This was shown earlier by Benilov and O'Brien [52], where they found viscous effects lengthen the characteristic time scale of instability growth. The instability would take millions of years to develop and is therefore irrelevant. The parameter space of the stable and unstable regions is dependent on the strength of inertia, surface tension and the size of the film. It was also found that a thicker film can be stabilising.

The stabilisation offered by surface tension was further explored by Benilov [53], as solutions which were unstable due to inertia were stabilised if the wavelength of the disturbance is short, while if the wavelength is on a similar scale or larger to the cylinder radius, surface tension acted instead as a destabilising effect. While surface tension was destabilising under certain conditions, inertia has a stronger effect on the flow.

Noakes et al. [54] derived a first order model in ε which included both inertial and surface tension effects for rimming flows and coating flows. Their approach in using multiple-timescale analysis led to an evolution equation which allows greater flexibility in both the velocity scaling and parameter regimes. However, solving these equations was explicitly proposed for future work. This work was a development on the previous study of Noakes et al. [8], where surface tension effects had been excluded.

A model to first order was presented by Pougatch and Frigaard [55] for viscous and gravitational forces, in which leading order terms of surface tension and inertia

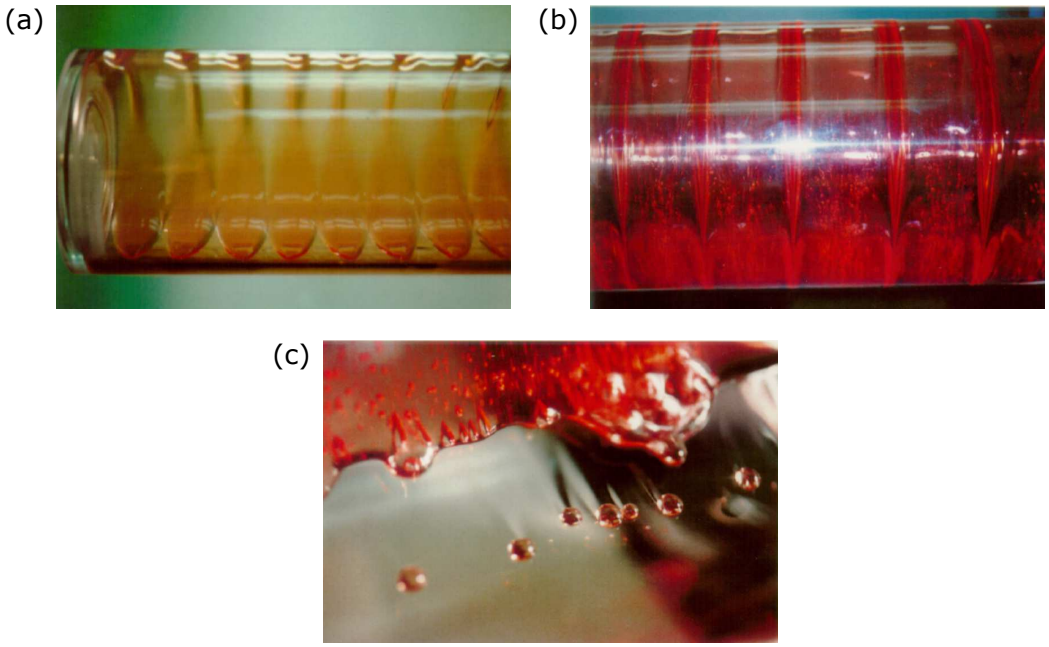


Figure 2.5: Some examples of the other axial variations which were found by Thoroddsen and Mahadevan, given as; A stable "fish-like" pattern as the dimples from "shark's-teeth" are extruded into longer axial patterns in (a), equispaced curtains of fluid around the cylinder in (b) and hydroplaning droplets exiting a bubbly front shown in (c). Reprinted by permission from Springer Nature Customer Service Centre GmbH: Springer Nature, Experiments in Fluids, Experimental study of coating flows in a partially-filled horizontally Rotating cylinder, S. T. Thoroddsen and L. Mahadevan, 23, 1997.

were also included in a three-dimensional formulation of flow inside a rotating cylinder. Contrary to the previously mentioned stabilising effects that surface tension typically has on inertia, it was found to frequently destabilise the flow. Equally, while inertia has been typically found to act as a solely destabilising term, it was counter intuitively stabilising the flow, though this was dependent on the fluid having a strong surface tension compared to the force of gravity. Features of the three-dimensional flow included rings of fluid that occur periodically across the cylinder axis with fluid accumulating on the lower quadrant of the rising wall.

The instability of inertia may be suppressed, if the rotating cylinder is sufficiently small such that the instability can be sufficiently stabilised by surface tension according to Benilov and Lapin [56], where solutions to the full Navier-Stokes equations were formulated. This was due to the violation of the requirements for a lubrication theory model. If the film is smooth, the flow was found to be unstable, while if a shock was present the disturbances can be absorbed by the shock.

An idea to include the non-linearity of inertia in rimming flows by using an integral approach by Kay et al. [14] allowed for a model to span between the smooth and pooled solutions dependent upon the inertial strength of the film. Further to the unique solutions presented by the addition of moderate inertia which satisfies the thin film assumption, a correction factor of surface friction which reduced the volume flux of fluid if the roughness factor increased as the flow resistance is also increased.

A parameter map for the onset of the axial features of rimming flows by Chatterjee et al. [22] presents a series of experimental values and shows a distinct correlation where four flow types are expected to form. These flows are of the smooth annular flow, shown as a smooth three-dimensional rimming flow, a "shark's-teeth" flow as shown by Thoroddsen and Mahadevan [50], hanging pendants of fluid or as a pool of fluid around the cylinder base. The Reynolds numbers of the problem ranged from 500 to $3,600$ and can be considered moderate even if the thin film limit is assumed.

2.2.5 Experimental Investigations of Rimming and Coating Flows

There have been a significant number of works which have focused on creating a reliable model for the rotating flows which can be found on the internal and external surfaces of a cylinder. However, these models fundamentally require physical data to be validated against, so experimental works like that by Thoroddsen and Mahadevan [57] are invaluable sources of information. The experimental works

have shown there are three-dimensional flow features which are unique to rimming flows. An example is the "shark's-teeth" pattern that was shown by Thoroddsen and Mahadevan [57], which has been presented in figure 2.4 alongside several other flow features. Unfortunately, while there have been experimental investigations for flows where the cylinder rotation is the driving force and for the aero-engine bearing chamber, there are few rimming flow studies where the flow has been powered by surface shear of the air interface.

The work by Thoroddsen and Mahadevan [57] was an early work of a slowly rotating cylinder that was filled with fluid of up to 5.5 % of the cylinder's volume. Using a technique to illuminate the flow that had been seeded with microscopic particles, they showed a recirculation vortex around the axial undulations; where these undulations were named "shark's-teeth", due to the distinct profiles they developed. These "shark's-teeth" undulations were further explored in detail in the later paper of Thoroddsen and Mahadevan [50]. This later paper observed that the frequency and size of the "shark's-teeth" were linked to the cylinder rotation rate and thought to be a feature like the viscous fingering instability which is connected to surface tension. While these undulations are typically transient and therefore unstable, the time scales of the transient state were sufficiently long to be treated as being in a quasi-stable state. In addition to the unique "shark's-teeth" patterns, among several flow features that they reported are the curtains or sheets that formed axially along the cylinder, an example of this can be found in figure 2.5. These curtains are where fluid cascades from the rising wall into sheets of fluid which are uniformly spaced in the span wise direction. These sheets are similar to the fluid curtains reported by Balmer [58]. Interestingly, the sheets of fluid reported by Balmer were present for a variety of geometric prisms including the cylinder.

Recently, a study by Chatterjee et al. [22] tested annular flows which may have a slight inclination. They were able to recreate the classic rimming flow with a uniform thickness, which in three-dimensions is also known as an annular flow. By adjusting the cylinder speed, they were able to chart the parameter space from a stationary pool up until the flow was a smooth annular flow. Profiles between these two cases showed that pendants formed on the film surface and the "shark's-teeth" comparable to those reported by Thoroddsen and Mahadevan [50].

The topic of rotating flows applies to an extensive range of applications, a review of which can be found in Seiden and Thomas [59] who detail both the homogeneous liquid flows, diluted and dense particulate flows.

Melo [37] showed that dependent upon the fluid volume contained within a cylinder and the rotation rate of said cylinder, a series of bumps will develop on the film from an initial flat front on the film surface. These bumps appear

as a sinusoidal series along the axial direction that may collapse with adjacent bumps to create a quasiperiodic pattern along the wave front. This flat wave front is the shock structure previously described, appearing uniformly in the axial direction is therefore similar to the two-dimensional flow, but converted into a full three-dimensional solution accordingly.

2.2.6 Flows Coating the Cylinder Exterior Surface

There is a close relationship between the flow on the outside and on the inside of a cylinder, though many studies have studied only one type of flow. There are works which have studied both the internal and external flows in conjunction due to the similarities between the flow internal and external to the cylinder, these are the works of Wilson et al. [38], Noakes et al. [54], Lopes et al. [60] and Leslie et al. [61].

With a lubrication approximation of the flow around a cylinder, Duffy and Wilson [62] showed that the shock solutions of rimming flows, where a jump in the film surface occurs, cannot appear on a coating flow. The distinction between coating and rimming flows are when higher order effects like those of surface tension are included. The curtain flows, where fluid is continuously fed onto the cylinder with an equivalent volume of fluid draining from the cylinder, the stabilising terms of hydrostatic pressure and surface tension are not considered in their model as higher order terms are absent.

Kelmanson [63] made an asymptotic expansion, which included inertia and surface tension in a thorough piece of work on the coating flow problem, with comprehensive review of the supporting literature. As expected of inertia, instabilities of the centrifugal forces caused unstable flows to form above a critical Reynolds number for the problem. This critical limit of the Reynolds number was dependent on the value of the surface tension, with a broad spectrum of small and large surface tension coefficients being considered.

The question of using a patterned rotating cylinder was explored by Sahu and Kumar [64] wherein a sinusoidal pattern on the exterior of the cylinder influenced the coating flow around the rotating prism. With an asymptotic expansion, the solutions admitted profiles where droplets hanging toward the base due to gravity that correlate to the frequency of the sinusoidal surface profile in the number of droplets are found. The scale of the rotating cylinder may be an avenue to control the flow and how the droplets or rings of fluid may form.

The work of Evans et al. [47] detailed the role of balancing the forces, focusing on the study of the coating flow problem and summarising a number of experimental systems that have been used for the coating flow problem, where a scope of

fluids from water to golden syrup or SAE grade 50 engine oil have been sampled.

2.2.7 The Depth-Averaged Method

The Navier-Stokes governing equations are a well known set of differential equations that are known to be cumbersome when solving analytically. It is therefore usual to see authors who have used a combination of either mathematical manipulation of the governing equations to simplify the problem or an approximation method which will only estimate the flow values. It is possible to directly solve the governing equations for rimming flow, as in the work by Benilov et al. [46] who investigated rimming flows with a finite element solver built within the Multiphysics package of the COMSOL software. While their work neglected inertia, it is possible to include inertia in most CFD simulations now. However, the non-linearity of inertia in two and especially in three-dimensional problems are expensive to solve.

The method found in hydraulics theory, known as depth-averaging is based upon the idea of using mean variables of the flow fields, namely velocity and temperature to facilitate a reduction of the dimensionality of the problem and therefore the reduced computational cost previously mentioned. One of the earliest works on using mean flow values was by Antoine de Chézy who was tasked with analysing the flow of the Yvette river in France according to Herschel [65]. At this point in 1775, the Navier-Stokes equations had not been created, so Chézy set about the task without the familiar conservation of fluid momentum equations, by using a coefficient as a correctional factor that accounts for frictional effects, appropriately named the Chézy coefficient. This simplification of the river stream served to be accurate in the context of modelling the river flow.

A series of equations, called the Saint-Venant equations were derived by the technique of depth-averaging the Navier-Stokes equations by Adhémar Jean Claude Barré de Saint-Venant [66], also known as the shallow-water wave equations. This approach is based on the premise that the film height is significantly smaller than the length scale of the flow, thereby satisfying the long wavelength approximation. By integrating the velocity field across the entire fluid depth, a mean flow speed is created that forms a fundamental part of the depth-averaging method.

The technique of depth averaging the governing equations for fluid flows has been used for rimming flows and planar flows with the approximation of the thin film limit. Benney [67] developed the method of using depth-averaging for planar flows, where a single evolution equation to calculate the film thickness was constructed under the limitation that the film is thin. This early work has faced criticisms on how the solutions can predict non-physical wave profiles for an increasing wave amplitude by Nguyen and Balakotaiah [68] or that singularities

develop in finite time by Scheid et al. [69].

Gribben et al. [70] used the Pohlhausen technique (a momentum integral technique to assume the form of the velocity profile) to integrate the velocity field. This method is applicable to several geometries including vertical planar flows or around cylinders as a draining coating flow. Their work is an early variant of the integral approach to the governing equations that were shown to have a good accuracy for pure hydrodynamic flows. If the flow is non-isothermal, as is the case in the circuit boards where a planar flow acts as a coolant of the electrical devices, Recktenwald and Butler [71] solved the momentum and energy equations and used depth-averaging to present a solvable system of equations using the mean flux and mean temperatures. The ability to simplify the governing equations presents a method to improve the performance of CFD software while maintaining a good accuracy to the flow problem without the excessive cost of fully solving the Navier-Stokes equations. The use of depth-averaging to analyse non-isothermal planar flows was also used by Costa and Macedonio [72], where they were investigating how lava flows propagate following a volcanic eruption. Their main conclusions were that depth-averaging has the potential to forecast flows with enough accuracy and importantly, faster than the full three-dimensional analysis.

The work by Nguyen and Balakotaiah [68] used an integral approach to solve falling fluid films in comparison to the previous formulations, known as the Shkadov model, the Kapitza boundary layer model, the Nakaya model and the long wave equation. These models differ in their treatment of the governing equations; the Shkadov model uses an integral boundary layer method with a velocity assumption in deriving a two-equation model, the Kapitza boundary layer model is a first order boundary layer model of the simplified Navier-Stokes equations, the Nakaya model is a third order long wave approximation and the long wave equation model uses a perturbation expansion method to only first order. Their integral approach creates a mass and momentum equation to be solved as a coupled set of equations with the mean quantities introduced from integrating the velocity field and assuming a parabolic profile, and is similar to the formulation of this thesis and that of Kay [6].

An improvement over the model by Shkadov who introduced the local flow rate, or mean flux of the film was formulated by Ruyer-Quil and Manneville [73] to be an adaptable approach for both the non-linear regime and critical behaviours of inclined planar flows. The ability to introduce the mean flow quantities were in good agreement with direct numerical simulations and asymptotic analysis of the complete Navier-Stokes equations. However, limitations gave a finite time instability that caused solutions to blow up, so a modification was later presented

by Ruyer-Quil and Manneville [74] with viscous dispersion to map solutions within the strongly non-linear regime. Their notion was that solutions to fluid flows can be accurately represented by an approach using only mean values up to an intermediary Reynolds number.

It is in the thesis of Kay [6] that the technique of depth-averaging the governing equations can be found in the study of non-isothermal films found within stationary cylinders. The papers generated during Kay's PhD in collaboration with Hibberd and Power [14, 15] are good benchmarks for the capability of using the mean flow values for solutions to the rimming flow problem.

By capturing the non-linear effects of inertia by depth averaging, Sivapuratharasu et al. [75] found a series of unique surface waves that included two and three tier solutions on an inclined plane. These structures were not predicted if inertial terms are absent, showing the need for fuller models to appropriately map the complex fluid dynamics present even within the thin film limits.

Lopes et al. [60] modelled both rimming and coating flows with the Stokes equations (assuming no inertial forces) while those of surface tension are kept with a full expression of the free surface curvature, which is typically reduced by approximation. Their work uses a gradient dynamics approach to resolve film profiles with an assumed quadratic velocity profile for the flow, while their work showed good agreement to solutions of the Stokes equations, completion of the model to include inertia or three-dimensional effects are still a matter of ongoing research to be applicable.

A good formulation that applies to inclined planar flows can be found in the work by Benilov [76] where a parabolic profile is remarkably accurate to those of solving the Stokes equations both qualitatively and quantitatively. Another type of depth-averaging technique can be found in the work by Kay et al. [77], where an inclined planar flow is separated into multiple imaginary fluid films. These imaginary layers are then integrated across in a similar fashion to that when depth-averaging, using matching boundary conditions between layers, higher order profiles can be represented as a series of quadratic profiles which can improve the models performance.

The integration of the velocity field creates a loss of the information about the velocity profile, so an *a priori* use of a suitable equation that may closely match the typical flow shape is needed. A general expansion polynomial with the thin film limit is a suitable base, though the order of the polynomial involves knowledge of previous works and suitability to the problem. A linear profile is known to be insufficient to model the flow, however there have been studies where a quadratic profile is sufficient in a number of circumstances. First, if the Reynolds number is small such that the Navier-Stokes equations can be reduced to those of Stokes

flow, the flow velocity has an analytical solution that is quadratic in nature, and has been used by Kay et al. [14] or Sivaouratharasu et al. [75] when including inertial effects. When using an expression to model surface roughness using the Chézy model, Kay et al. [14] used a cubic velocity profile while Gribben et al. [70] used a quartic profile.

2.2.8 The Thermal Effects Found in Thin Films

The fluid system of the aero-engines for this thesis requires non-isothermal films to be modelled. There is a diverse range of studies which focus on the various thermal effects of thin films, though some cases are not relevant as they are beyond the current scope of this thesis. The thermal effects reviewed are summarised into three distinct sources; thermal convection of the fluid, Marangoni effects of the surface (localised changes to the surface tension coefficient as a function of temperature), also known as thermocapillary forces and lastly the role of thermoviscosity for changing temperatures of the fluid. Two of these thermal effects are not included in the model, these are the thermoviscous and Marangoni effects. These assumptions are based on aero-engine oils operating in a stage where the changes to viscosity with temperature are small and as this Section shows studies for how to implement Marangoni effects, they are outside the current scope of work in this thesis.

The draining flow off a horizontal cylinder by Reisfeld and Bankoff [78] showed that thermocapillary forces amplify the gravitational effects, causing an increase to the flow drainage on a heated cylinder, while the reverse occurred if the cylinder was cooled and fluid was confined onto the cylinder. The stabilising role of surface tension effects from the thermocapillary forces may also be sufficient to overcome axial disturbances.

The Marangoni stresses that arise by fluctuations of the surface tension for flow down a vertically inclined cylinder may initiate an unstable flow which can develop as either droplets or complete film rupture according to Ding et al. [79]. This limiting factor of the Marangoni effects on the flow stability was also discussed by Burmistrova [80], where a critical Marangoni number for a sustainable flow was dependent upon the strength of inertia, however, this model assumed gravity as negligible.

Leslie et al. [81] developed a mathematical model to include the physical change that occurs with fluid viscosity if there is a change in the fluid temperature, modelled as an exponential relationship for the thermoviscosity. Part of their work included the cylinder being either heated or cooled. When the cylinder was heated, a thickening of the coating film on the outer surface was found. This is because

the positive thermoviscosity causes a slowdown of the flow and subsequently increases the capacity of the fluid loading on the cylinder. The film gets thinner if the cylinder is actively cooled, due to the increase in the flow velocity as the inhibition of viscosity is reduced. This change in fluid loading is similar for flows where gravity is weak and a thick film can be held around the cylinder. A later comprehensive extension to the study of thermoviscous coating flows also included rimming flows in the absence of inertial effects by Leslie et al. [82], with short reviews of the thermal effects also contained within these works by Leslie et al. [81, 82].

The thesis of Kay [6] focused on both the isothermal and the non-isothermal effects that occur in rimming flows. This research was the foundation to the paper by Kay et al. [15], which outlined the role that thermal convective effects have on the temperature profile. This study was a development of the earlier isothermal work of Kay et al. [14] where the film of fluid is driven by a strong shear at the film surface and not the normal rotation of the cylinder. Their work showed that for classic lubrication theory, (negligible inertia, surface tension and hydrostatic pressure, meaning the film does not contain any discontinuities), that even strong thermal convection has a negligible effect on the temperatures as the film is smooth. However, by retaining the effects of hydrostatic pressure and surface tension so that pools of fluid can be formed, thermal convection has a significant effect on the temperature profile. Their depth-averaging technique for the energy equation was compared with analytical solutions for a planar flow and was found to be in good agreement with each other. However, there were discrepancies with the solutions when this was applied to the rimming flow problem.

Kumawat and Tiwari [83] derived a thin film model to first order and included inertia and Marangoni effects at the surface. Their model included a linear variation of the surface tension coefficient which was dependent on the surface temperature and found that for a heated cylinder, a stable film can form due to the Marangoni effects at the surface. Along with the thermocapillary effects being able to stabilise against inertia, the surface tension gradients were also stabilising to axial perturbations. While the region of minimal film depth is dominated by the forces of gravity and viscous drag, the importance of higher order effects in local regions is clear.

These Marangoni stresses arose from the gradients of the surface tension due to the thermocapillarity and variation in surface temperature, while Marangoni forces can also occur if an insoluble surfactant is present that can lead to a variation in the concentration which creates these Marangoni stresses, as in the study by Kumawat and Tiwari [84]. The concept that the isothermal Marangoni stresses may stabilise the film against the instabilities of inertia was demonstrated, with a

model for first and leading order thin film approximation of viscosity and gravity while other terms were taken at first order only. The dampening of the oscillations from the inertial instability are part of the stabilising effects when Marangoni stresses are included.

An experiment by Chatterjee et al. [85] was conceived to determine the heat transfer coefficients for a flow within a horizontal rotating pipe, where an applied heat flux permeates into the pipe while fluid is cycled axially along the cylinder by a continuous feed inlet. The heat transfer coefficients were measured to be between $200\,W/m^2K$ and $1,500\,W/m^2K$ with a dependency on the flow rate of fluid, heat flux into the pipe and the rotation rate of the cylinder. The speed of the cylinder was linked to the development of the axial features including smooth "shark's-teeth" and pendants which will change the interface and compliments the mixing of fluid in the cylinder. The experiment was repeated with a pipe that was slightly inclined at a small angle of between $3\,^\circ$ and $6\,^\circ$ and shown to reduce the heat transfer coefficient in comparison to those calculated for a horizontal pipe. This reduction in the heat transfer coefficient to $200\,W/m^2K$ and $600\,W/m^2K$ was attributed to the pool becoming shallower as the inclination is increased and the contained volume of fluid decreased even with the constant fluid influx according to Chatterjee et al. [86].

Kumawat and Tiwari [87] explored the stability of a thermoviscous fluid within a rotating pipe with thermocapillarity for exponential viscosity and linear surface tension relationships to the film temperature. While their formulation excluded both inertia and thermal convection, their results showed that a destabilising effect occurs for higher Marangoni stresses if the cylinder walls are externally heated and that thermoviscosity also destabilises the film but only when the cylinder is cooled. The stability of the film for a heated cylinder arises from thermoviscous forces, and when the cylinder is cooled it is in the thermocapillarity that stability emanates.

2.3 Notable Contributions into Investigating Planar Flows

The use of the thin film approximation can be found in many studies which focused on the rotating flows both internally and externally to a cylinder, there are also many models with a similar assumption for planar flows. These planar flows range between a horizontal, vertical and an inclined plate at some degree between the horizontal and vertical. A review of many of the early works on these thin planar flows, and some coating flow models, can be found in the work

of Oron, Davis and Bankoff [88]. This review covers a broad range of topics in modelling thin films, with developments to include the effects and problems where surface tension, gravity, thermocapillarity and temperature dependent viscosity can be relevant. Since this review, many good studies have been published that investigate a number of effects which are included in this Section. The later review by Craster and Matar [89] covers a range of biological, engineering, geophysical and nano to macro scale flows, with a significant number of effects that have been incorporated in thin film models for both fluid mechanics and thermodynamics.

Many inclined flows can assume the driving force is predominantly due to gravity pulling on the fluid, however Shuaib et al. [90] investigated the role that a surface shear has on the developing surface waves with negligible inertia, by solving the Stokes equations. From an initially steep profile, the wave structures are shown to relax or compress in width depending on a number of factors, including both the downstream and upstream conditions and the inclination angle, though these structures develop transiently and appear as smooth travelling waves over time. This applied shear that is tangential to the surface is also the origin of flow in the flat flow of Tang et al. [91], with a constant air shear directly applied to the film, and requires a velocity condition to become a well posed problem.

The effect of localised heating has been investigated by Miladinova et al. [92], which causes thermocapillary instability of the film for a film flow down an inclined plane. The stabilising effect of hydrostatic pressure, as found for rimming flows, also appears to inhibit the effect of the thermocapillarity. The main effect is limited to influence the shape of the surface waves by the local change to the surface tension coefficient. A separate study by Kalliadasis et al. [93] for an inclined plate showed that Marangoni stresses are balanced by gravity, where a lower limit of the Marangoni number exists in which solutions are stable, but above which led to increasingly unstable films. This work also introduces the notion of the Newton's law of cooling at the interface between the fluid and air phases. An inclined planar flow was studied by Kalliadasis et al. [94] using an extension of the longwave approximation to include both Marangoni effects and moderate Reynolds numbers of $O(1)$. They used a Shkadov integral-boundary-layer approach with an assumed parabolic velocity profile. The instability of thermocapillarity is further confirmed and amplifies the typical hydrodynamic instability, with the angle of inclination also increasing the film instability. A detailed numerical simulation of flow behaviour over a prescribed temperature of a local region was used by Frank [95], using the method of particles to include both Marangoni effects and thermoviscosity of the fluid when solving the full three-dimensional system of equations for an inclined surface. The periodic axial undulations that have been observed experimentally were also captured numerically, with insight into the

internal flow structures due to the full three-dimensional analysis.

The difference in flow behaviour when including Marangoni stresses is detailed by Thiele and Knobloch [96], where the Newton's law of cooling can also be found, the hydrostatic pressure and gravitational effects are included while the inertial and evaporative effects of the heated film are negligible. Dependent upon the inclination angle, the film creates periodic droplets and local film dryout as a consequence, if the surface is inclined these stationary droplets transition into a sliding state. Interestingly, if the inclination angle is sufficiently large, the surface waves that are typical of inclined flows are analogous to those presented by moderate inertia, though the applicability is limited to a certain range of films. This formation of droplets was also shown in the work by Liu et al. [97] for flow down a vertically suspended fibre, as the Marangoni stresses cause the film surface to break up into droplets that will cascade under the influence of gravity, with the droplet size being linked to the Marangoni number. The flow down a vertical fibre was also explored by Ding et al. [79], with confirmation of the droplet formation and rupture of the film surface by using direct numerical simulations of the heated film.

The deformation of a film surface by thermocapillarity was investigated by Kabov et al. [98], where a three-dimensional numerical analysis presented a number of surface wave formations depending upon the submerged local structures that directly heat the film. As expected, the Marangoni stresses on the surface due to the local fluid heating causes a range of waves and ridges to form with an accompanying trench in the downwards flow that can be detrimental in maintaining a continuous flow.

The integral approach for falling films was developed by Trevelyan and Kalliadasis [99], to improve on the integral-boundary-layer approximation of Kalliadasis et al. [93] for understanding the effect of both thermocapillary effects by a Galerkin projection of the velocity field which corrects the critical flow limits. While this work assumes a fixed temperature via a Dirichlet boundary condition, as with many non-isothermal works, Frank and Kabov [100] defined a heat flux input into the film instead, under the notion that the fluid temperature at a heated wall will depend on many factors which are unknown. The numerical results were shown to be in good agreement with experimental studies where the axial undulations appear periodic, with a connection to structure width and the strength of the Marangoni number.

The direct application of either the wall temperature or heat flux by Dirichlet or Neumann boundary conditions has featured in many works, however Gambaryan-Roisman [101] developed a long-wave model where the substrate is directly heated and modelled with a fluctuating thermal conductivity which can represent com-

posite or graded materials. This fluctuation of the substrate temperature causes non-uniform temperature gradients at the surface which lead to strong Marangoni stresses and evaporative effects which deform the film, with the intention being to create a passively controlled thin film flow.

The heat flux boundary condition is also used by Gatapova and Kabov [102], where the liquid film is driven downwards on an inclined plane with moderate Reynolds and Péclet numbers to account for convective effects. The resulting thermocapillary deformation due to variation in the film surface temperature causes a thinning of the film downstream of the heated patch and a surface bump which boarders upstream to the patch. An additional feature is in modelling the evaporative effects of fluid when subject to heating effects, which drastically changes the temperatures and Marangoni forces through the film.

The localised heating effect has also been modelled with the lubrication theory framework, where flow down an inclined plate contacts a narrow heating element which causes Marangoni stresses at the flow surface which are amplified by the presence of insoluble surfactants, found in the work by Ding and Wong [103]. These surfactants were able to change the surface tension coefficient of the fluid to become a stabilising factor, and a means of increasing the surface tension coefficient beyond the value of the base fluid.

2.4 Surface Coatings and Alternate Substrates in Flow Control

The true behaviour of a fluid on a solid surface has been studied extensively since the 18th century, with experimental and theoretical models often in strong contrast to each other with no consensus on how to describe the boundary condition appropriately. Typically, the behaviour of how a fluid interacts at solid surfaces has long been described by the no-slip condition since as early as 1738, where Daniel Bernoulli linked the velocity of a substrate that supports a fluid flow to be the fluid velocity according to Lauga et al. [104]. However, Neto et al. [105] discussed how the engineer Claude-Louis Navier had theorised that a liquid may slip across a solid surface, while encountering an opposing force to the fluid velocity that arises from friction and is relative to the surface velocity. The description of partial slip by Navier was founded upon a quantifying constant known as the slip length, l_s^* which is the distance across the interface for the liquid velocity to be extrapolated to zero, as in figure 2.6. If the slip length is reported as being 10 μm in length or longer, it is treated as a large slip for this thesis.

The fluid boundary condition at the surface has been proposed as being one

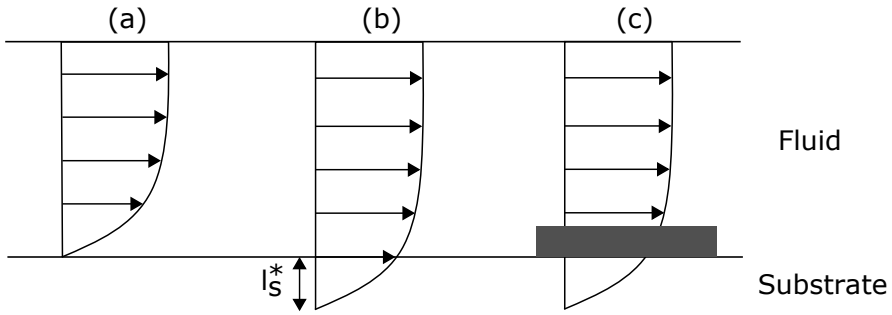


Figure 2.6: A representation of the three distinct velocity profiles, obeying the no-slip condition (a), the partial slip condition (b) and the stagnant layer hypothesis (c).

of four typical variations; a stagnant layer, a complete surface slip, the partial slip which we are interested in and the no-slip condition. The description of the stagnant layer involves a thin layer of fluid connected on the solid surface, allowing the majority of the fluid mass to slip over the static layer as in figure 2.6.

These competing ideas have been under intense scrutiny since their inception according to Neto et al. [105], with George Stokes being commissioned by the Royal Academy of Science to determine the true nature of the interface. The conclusion was that the no-slip condition of Daniel Bernoulli was eventually favoured over the partial slip condition of Claude-Louis Navier. To the frustration of Stokes, the disagreements between theory and experiments hampered his decision and this was compounded further by the support of the no-slip condition being legitimate in subsequent years and is the source of its popularity in modern day fluid dynamics.

This acceptance of the no-slip condition is determined by empirical knowledge, with the experimental techniques required to distinguish the occurrence of slip being beyond those available for the period. With the rapid rise in technology, these constraints have been slowly lifted as nanoscale methods have developed to investigate the phenomena of biological surfaces and fabricate intricate surfaces. This has revitalised investigations into clarifying the boundary condition of the fluid and solid interface, with techniques such as microscopic particle image velocimetry, which captures images of travelling tracers, or surface force apparatus that gauge drainage forces having been used to calculate liquid slip lengths. A good review of the available experimental techniques to determine if fluid slip occurs can be found in the work by Neto et al. [105], with reviews in the advances to understanding the slip condition within the works of Granick et al. [106] and Eijkel [107].

Typically, surfaces which have garnered most interest in observing the presence of fluid slip have been for hydrophobic and hydrophilic surfaces, where for example the lotus leaf is classified as a hydrophobic surface that repels water. In highly

precise micro channels down to $1\,\mu m$ with chemical treatments, Choi et al. [108] had nanometer uncertainties in their equipment for measuring the channel which were insufficient to measure if slip occurs on the hydrophilic coating, while $30\,nm$ slip lengths were measured on the hydrophobic surface. Cottin-Bizonne et al. [109] also investigated the hydrophilic and hydrophobic coatings using dynamic surface force apparatus for water and glycerol, with the no-slip boundary condition likewise found on their hydrophilic surface. The hydrophobic surface however, had significant fluid slip, with an observable slip length up to $100\,nm$. They conjectured that slip is found on hydrophobic surfaces as there will be nano-bubbles of entrapped air on the surface will reduce the surface contact and lead to slip. Early work on a hydrophobic surface by Schnell [110] measured a pressure difference between glass capillary tubes due to treatment by dimethyldichlorosilane creating a hydrophobic layer.

Molecular dynamic simulations of hydrophilic and hydrophobic surfaces by Ho et al. [111] showed that fluid slip could occur if hydrophilic surfaces have been carefully manufactured, easing the migration of water molecules between adsorption sites on the surface. The associated difficulty of creating these dense adsorption sites has meant that slip is typically only connected to hydrophobic surfaces and may largely be coincidental. This notion that a strongly non-wetting surface of a hydrophobic coating may have a relatively low slip length is mentioned by Cottin-Bizonne et al. [112], being also associated with the geometric features of the surface for fluid drag reduction by partial slip.

The full theory of how fluid slip occurs on a solid surface has not been fully established due to complex interactions at the surface, a good review on the effects such as surface roughness and wettability and how they are anticipated to cause fluid slip can be found in Lauga et al. [104].

The influence of surface roughness on the slip length was explored by Bonaccurso et al. [113], with the molecular scale roughness increasing the degree of slip, which may be applicable to systems where surface roughness is on an equivalent scale. The study at a molecular scale is synonymous with fluid slip, with the brief review by Hu and Granick [114] showing the role that molecular dynamic simulations have in predicting the onset of fluid slip. Contrary to this, Lauga et al. [104] state surface roughness will decrease the slip length.

Ajaev [115] designed a solid surface to investigate film rupture, where thin grooves were mathematically modelled with small pockets of trapped air beneath a layer of liquid. A limiting factor of the arrangements of the thin grooves was the instability that developed on films dependent on the groove width and film thickness, inhibiting their application without a suitably steady film. To model atomically smooth walls, Priezjev's [116] work with molecular dynamic

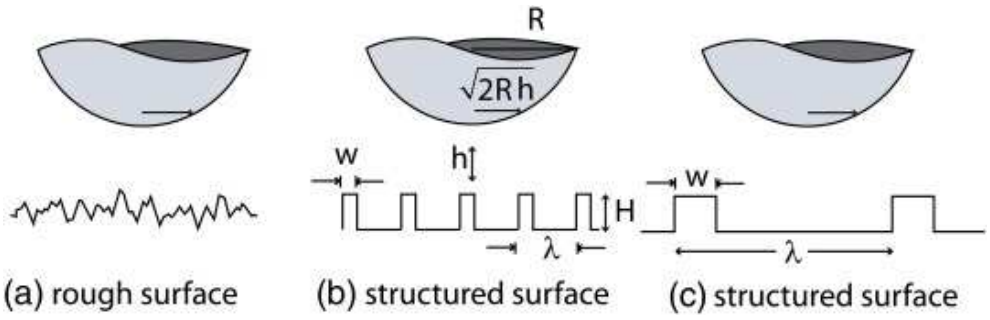


Figure 2.7: Atomic force microscope measurements of surface roughness (a), densely packed pillars on a surface (b) and sparsely packed pillars (c) as described in the work by Lee et al. . The probe radius is given as R, with w denoting the pillar width, h as the feature height and λ as the frequency of the structure. Reprinted from Advances in Colloid and Interface Science, 210, T. Lee, E. Charrault and C. Neto, Interfacial slip on rough, patterned and soft surfaces: A review of experiments and simulations, 21-38, Copyright 2014, with permission from Elsevier.

simulations showed how a strong fluid shear rate increased the measured slip length in proportion to the shear increase. Richardson [117] argues that a viscous fluid flow across a surface will obey the no-slip condition at macroscopic scale due to surface roughness, concluding how no-slip can be expected at all scales due to resistive forces to fluid motion. The works of Zhu and Granick [118, 119] perceive that simple Newtonian fluids will slip on molecularly smooth surfaces, speculating that bubble nucleation of the surface may be the causing factor for fluid slippage which will be inhibited by notably rough surfaces. Spikes and Granick [120] worked with nano to microscale Newtonian liquids using surface force apparatus on smooth mica surfaces, with the complete wetting of the mica leading to a slip length in the order of $1\,\mu m$.

It was speculated by Lee et al. [121], that a super-hydrophobic surface will lead to significantly longer slip lengths in comparison to hydrophobic surfaces, and that by altering the surface features with polymer brushes, fluid slip may occur. The theory of super-hydrophobic surfaces is that gaseous pockets can be trapped under the liquid layer. A super-hydrophobic coating can consist of a surface patterned with microscale posts and ridges or chemical coatings, with the main difference to hydrophobic surfaces being the strength of which they repel water. These super-hydrophobic surfaces are reputed to have large microscale slip, and in the works by Ou et al. [122] were reported to have a measured slip length of $20\,\mu m$.

The role of micro structures were further shown to develop fluid slip by Tretheway and Meinhart [123] when $30\,\mu m$ channels were coated with a hydrophobic coating of octadecyltrichlorosilane. Changes to the flow velocity indicate a

slip length of $1\,\mu m$, due to a 10 % change in the free stream velocity using particle image velocimetry.

Large scale slip was presented by Nieto et al. [124] for a creeping flow with both linear and non-linear slip models, where recirculation of the flow can be completely dampened by a large slip length. Their approach was to use an integral formulation to include the partial slip condition in their model formulation of concentric rotating cylinders for Couette flow. The partial slip condition was the Thompson and Troian non-linear slip model, appropriately named after the fundamental works of Thompson and Troian [125]. This non-linear condition was devised by Thompson and Troian from analysis of molecular dynamic simulations of a Newtonian fluid. Their generalised condition is applicable at shear rates which are much higher than the maximum allowable shear rate of the Navier slip condition. Using this Thompson and Troian condition, Nieto et al. were able to predict flow behaviour which had not been previously reported. Couette flow with the Thompson and Troian condition has also been explored by Power et al. [126], with the presented boundary condition forming a significant part of this thesis. The application of the slip boundary condition has also been presented in the work of Nieto et al. [127] and Nieto et al. [128] for microscale Couette and planar flows, with large slip lengths relative to the flow length scales presented. The use of the Thompson and Troian nonlinear boundary condition was also presented by Matthews and Hill [129], where the ratio between a flow surface and volume is significant so surface related effects may be dominant. Their work highlighted the mathematical formulation of the non-linear condition on three well known flows of pipe, channel and annulus flows and how they can be obtained with careful selection of the proportionality constant of the linear slip condition. The theoretical non-linear slip condition of Thompson and Troian was also used by Zhoi et al. [130] for nanoscale films. Zhoi et al. showed that the slip length was dependent on the flow shear rate and the role that fluid shear has on the slip condition.

The usefulness of slip for lubrication has been previously explored, with an experimental and numerical analysis by Pit et al. [131] for a hexadecane oil and stearic acid coated surface in a demonstration of slip for Newtonian fluids to nanometer scale. Later developments by Pit et al. [132] for hexadecane oil showed that slip occurs on hydrocarbon surfaces, however increased surface roughness actually countered slip. In determining nanometer scale surface slip, Baudry et al. [133] also showed a measurable difference between hydrophobic and hydrophilic planar surfaces in drainage by surface force apparatus, accounted for by a slip velocity at the boundary. The surface force apparatus was also used to measure nanometer scale slip on a smooth hydrophobic surface by Bonaccurso et al. [134].

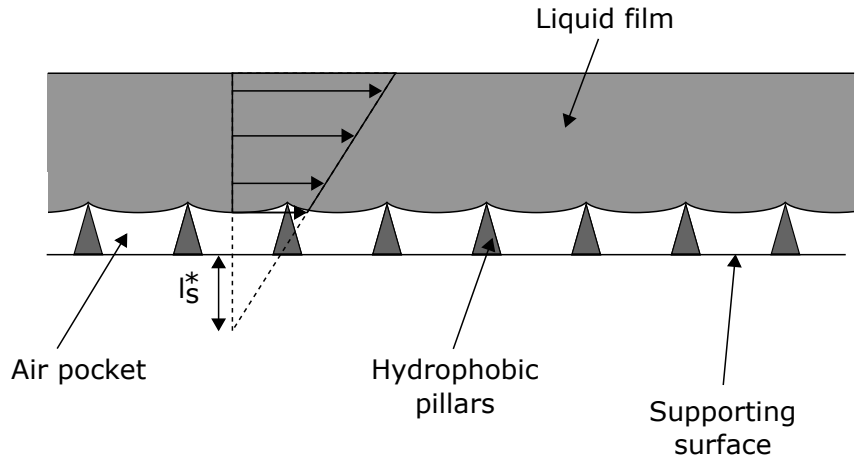


Figure 2.8: A design of a super hydrophobic surface to develop large scale surface slip.

If an idealised super-hydrophobic surface can be fabricated by using trapped gas pockets to develop large scale slip, as in Ybert et al. [135], the predictions of possible slip lengths are in excess of $100\,\mu m$. The idealised structure can be fabricated by cylindrical pillars around $50\,nm$ in diameter spaced $5\,\mu m$ apart that trap a gas phase to support the liquid flow. The hindering factor for developing super-hydrophobic surfaces is the stability of the trapped gas due to dissipation or impregnation of fluid into the air pockets. A design concept for developing a super-hydrophobic surface that may induce large scale slip is presented by Choi and Kim [136], where a gas layer between prisms acts to support a liquid film, described as a nano-turf shown in figure 2.8. The design was tested on the surface of rotating disks for Couette flow, resulting in slip lengths of $20\,\mu m$ to $50\,\mu m$ dependent on the working fluid.

Willmott and Tallon [137] used a torsional ultrasonic oscillator to measure the existence of fluid slip. However, with an experimental accuracy of $60\,nm$, their results gave confirmation that fluid slip does not occur and is in contradiction to the previous works cited. Vinogradova [138] reviewed hydrophobic surfaces in support of the slip condition, posturing that qualitative methods exist that may quantify the presence of slip. However, three major causes of error are due to the surface roughness, inhomogeneity and surface tension which may lead to slip disassociation with hydrophobic surfaces, as shown for example by Richardson [117]. Deviations from Reynolds theory for liquid drainage between two surfaces can be explained by fluid slip according to Vinogradova [139], which may originate from a decrease in viscosity in a layer near to the wall due to nucleation of dissolved gas from a hydrophobic surface. A model that calculates the hydrodynamic drag force with a correction factor allowing for slip of a surface is presented by Vinogradova

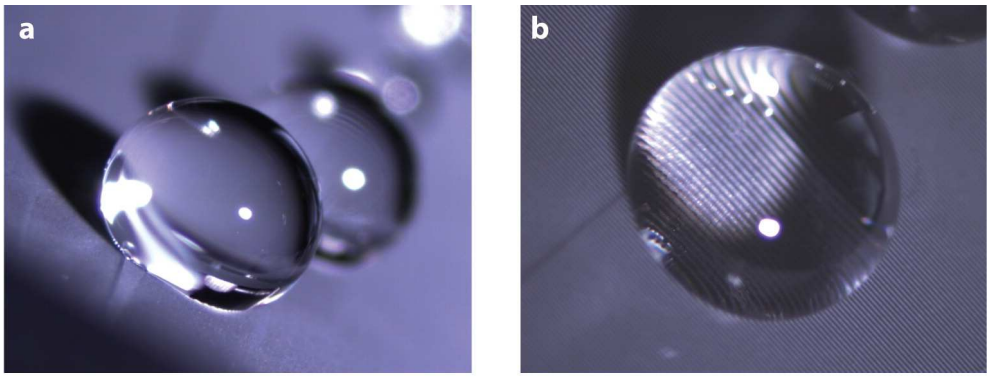


Figure 2.9: Suspended water droplets on top of a super-hydrophobic surface, using narrow ridges spaced 45 μm apart which are 15 μm wide, with a side view (a) and top down view in (b) as reported by Rothstein. Republished with permission of Annual Reviews, Inc., from Slip on Superhydrophobic Surfaces, J. P. Rothstein, 42, 2009; permission conveyed through Copyright Clearance Center, Inc.

[138] and used in many studies to calculate the apparent slip length of a surface, such as in the work of Craig et al. [140] who used atomic force microscopy to measure slip lengths of 20 nm and showed a discrepancy between experimental and theoretical results. Measurements of nanoscale slip lengths of 125 nm by Honig et al. [141] showed good correlation between the experimental results using atomic force microscopy and the model of Vinogradova [138] for gas flows.

A review of super-hydrophobic surfaces and the benefits to fluid systems, an example being fluid transport being enhanced by a reduction in the drag coefficient, is given by Rothstein [142]. This review further confirms the concept that surface roughness and material hydrophobicity are linked in the creation of liquid slip at large scale, where the fluid is suspended upon a gas and connected by the surface peaks as shown in figure 2.9.

While the majority of the previously mentioned works focused on water and oils for the working fluid, Churaev et al. [143] studied the slip phenomena for mercury within thin capillary tubes. The predicted flow rate of the micro tubes differed by 10 % when corrected for a partial slip condition with a length of 70 nm to the measured rates. The work of Maali and Bhushan [144] gives a short review of super hydrophobic surfaces and provides measurements of slip effects, where 20 μm of surface slip has been calculated from a fluid drag reduction of 40 %.

2.4.1 The Modelling of Air Lubricated Bearings

Similarities are found between modelling liquid films and studies of gases, where there is a comparable length scale to the small parameter of the thin film approximation, known as the Knudsen number according to Bailey et al. [145].

The Knudsen number is defined as the ratio between the mean free path of the gas molecules and the characteristic length scale of the problem, outlining when important effects of the flow regime must be considered.

The separation between the static and rotating components of the stator and rotor in turbo machinery by thrust bearings is an example where the thin film approximation can be used to simplify the governing equations, as in the work of Bailey et al. [145]. The theory suggests that for a gas flow across a wall, a portion of molecules are reflected off the surface which creates a slipping flow on a scale comparable to the mean free path. The inclusion of slip was found to decrease the spacing between the rotor and stator as the film thickness reduces due to slip. This work was extended from planar thrust bearings to coned bearings, where slip also reduced the fluid thickness and gap of the bearing Bailey et al. [146]. A review of the slip condition for gas flows can be found in the work of Bailey et al. [147].

The use of air as a lubricating fluid of micro bearings produces an environment where slip may occur, with a length scale similar to the mean free path, Maureau et al. [148] show that slip can prevent fluid recirculation with increasing flow velocity.

In a similar vein to these air-lubricated bearings, Aurelian et al. [149] investigated hydrodynamic journal bearings with surface texturing and coatings to develop wall slip. The numerical study calculated slip lengths of $1.3\,\mu m$ that may reduce power loss of the bearings, showing the beneficial role slip may have on liquid systems. Barber et al. [150] construct the Maxwell definition of slip for a cylindrical geometry (the Maxwell slip condition defines a slip velocity relative to the mean free path), where the fluid drag is reduced by stronger slip. While, for Couette flow a comparison between the Maxwell model and an alternative model was tested by Myong et al. [151], where the alternative model was able to correctly predict the velocity fields inversion (reverse flow). The paper by Seo and Ducker [152] details how the Maxwell slip condition may alter gas flows and finds slip increases with fluid temperature, up to $590\,nm$, which may be otherwise used in flow control where geometry and fluids are fixed. The Maxwell's boundary slip condition is popular in studies of gas flows, such as Yuhong et al. [153] or Zhang et al. [154] who reviewed slip models applied to gas flows. The idea that flows can be altered by selectively treating surfaces to create fluid slipping surfaces is a key application where the slip condition may be important according to Seo and Ducker [152].

With planar flows, observations on molecularly smooth plates by Bowles and Ducker [155] showed how gas may slip across a surface by up to $480\,nm$, greater than the calculated slip observed over rough materials using atomic force

microscopy.

2.4.2 Porous Substrates and the Matching Boundary Conditions

The micro and nano structures, such as those of ridges or pillars previously have been significant features in creating hydrophobic surfaces that may lead to fluid slip and in a similar way micro pores found in porous materials may lead to fluid slip according to Javadpour et al. [156]. These micro pores have an apparent slip length of $250\,nm$ for liquid flow through a shale matrix, which increases the apparent permeability of the porous matrix. This observation of fluid slip with porous materials connects well to the studies that aimed to correlate fluid flow across porous substrates and formulate a suitable mathematical expression of the boundary condition. The key parameters in measuring porous materials are the permeability and porosity, where the porosity is given as the ratio between the volume of empty space and volume of solid material and the permeability equates to the resistance of fluid to flow through the material.

The concept of fluid moving across a porous material can be found in engineering applications, such as providing passive flow control, thermal insulation or in porous bearings. While the fluid flow within a porous matrix may be described by the well known Darcy or Brinkmann equations depending upon the flow parameters and free fluid may be described by a variation of the Navier-Stokes equations, the coupling of these equations is not as clearly defined, similar to the understanding of fluid slip at a solid surface. This is because the flow velocity will not be zero at the interface of the porous and free fluid regions, as flow can occur within the substrate.

Alazmi and Vafai [157] analyse five different interface conditions, including the well known Beavers and Joseph condition by Beavers and Joseph [158]. These conditions, are grouped into either a slip or no-slip category by Alazmi and Vafai [157], where slip acts as a proportionality constant to determine the velocity across the surface, using zero for the no-slip limit. For a porous cylinder, the fluid velocity at the interface of the porous material and free fluid will be greater than zero, similar to the partial slip condition described in Section 2.4.

The Beavers and Joseph condition, developed by Beavers and Joseph [158], is one of the more popular mathematical expressions for the boundary condition, examples being; the work of Zuo and Hoi [159] to couple the Navier-Stokes and Darcy flow, the experimental work of Taylor [160] whose results agreed well with those predicted, the work by Das et al. [161] to model groundwater hydrodynamics with good correlation to experimental results or in de Socio et al. [162] for flow

across a permeable slab. A model which coupled Stokes and Darcy flows was done by Shan and Zheng [163], where they used a partitioned time stepping algorithm to solve an uncoupled Stokes and Darcy sub-physics and sub-domain for each time step. Ross [164] derived a slip boundary condition in modelling a flow with negligible inertia across an isotropic medium, with similarities to that of the Beavers and Joseph condition.

A review of the Beavers and Joseph boundary condition by Auriault [165] who includes some of the alternatives and drawbacks to the Beavers and Joseph condition. The work of Nield [166] also provides context for the Beavers and Joseph boundary condition, noting that the no-slip condition has been previously used to describe flow across a porous surface in contrast to recent works where the interface velocity is greater than zero. Jones [167] offers a modification to the Beavers and Joseph condition, to represent the fluid slip across a spherical boundary in a more general structure.

Matching conditions were presented by Valdes-Parada et al. [168], which coupled the governing equations of each region directly with a stress jump across the interface. The two domain approach with matching conditions was in good agreement for the bulk flow, but lost information around the interface. Jager and Mikelic [169] provide a rigorous approach in the justification of Saffman's modification of the Beavers and Joseph slip condition by scaling with the permeability tensor rather than the permeability, with the velocity field approximately satisfying that of the Beavers and Joseph condition.

According to the study by Tan et al. [170], the porosity is linked to the coefficient of surface slip. High porosity materials have a larger slip length coefficient, as the inhibiting impact from the porous structure is weakened. The connection between porous and surface slip conditions is reported by Berg et al. [171], who observed $0.7\,\mu m$ of slip at the interface, with a list of previously quantified slip coefficients from nanometer to micrometer lengths.

An experiment of fluid flow across a series of perpendicular rods to create a permeable insert showed a high velocity at the interface of up to 40 % of the unimpeded flow speed due to slip, similarly a slower velocity of 13 % was calculated for a smaller porosity ratio by Nair and Sameen [172].

A slip length across a porous wall was measured to be between $0.024\,\mu m$ and $0.063\,\mu m$ by Chun-Yuan and Qin-Feng [173] for a porous surface coated with hydrophobic nano particles to induce surface slip and increase the flow capacity. The benefit of porous media on fluid flows is explored by Bruneau and Mortazavi [174], where drag reduction of up to 40 % was achieved by strategic placement of porous layers for flow around a solid body. Their model used a simple stress jump condition to model the flow behaviour, with the alternative Beavers and Joseph

condition also being mentioned.

2.5 Chapter Summary

This Chapter provides a review of the extensive background literature on the analysis of bearing chamber flows, with both experimental and theoretical studies detailing how oil flows behave within the chamber. The understanding and capabilities of modelling flow within bearing chambers has advanced to the stage where droplet impacts and three-dimensional analysis can be simulated. However, this analysis is computationally costly and if the relevant physics are not included the models will deviate from the real chamber. To reduce the computational cost, thin film models are typically used to give quick assessments of flow patterns, which are akin to rimming flows.

For bearing chambers, the necessary physical effects to be modelled are outlined within this Chapter from the literature. The viscous and gravitational effects are the most important effects of the rotating flows and are fundamental in all types of flow. The effects of hydrostatic pressure and surface tension have shown to be relatively significant in local regions where there are sudden changes in film depth, therefore these effects will also be included in the model. The speed of the fluid within the chamber is very high and indicates inertia will be significant, with studies having demonstrated that models including inertia have different film profiles. Therefore, the model will need to include moderate inertial effects to be suitable to represent the bearing chamber. There are several methods which can include all these effects in a thin film rimming flow model. However, the depth-averaging approach was shown to be an economical and robust method of formulating the Navier-Stokes equations and has consequently been used in this thesis.

The assessment of literature in both thin film models and bearing chambers flows has identified areas where there is insufficient knowledge from either a physical or mathematical viewpoint. Specifically, this relates to the small scales involved in the bearing chamber flows and there is a significant lack of studies into how the fluid will interact with the chamber wall.

From the literature of the fluid to surface interactions at small scales, it is strongly indicated that liquids will slip across a surface. At this time, a comprehensive understanding of the exact causes of slip has not been fully established and there has been difficulty in directly measuring this effect. However, the experimental evidence from the chemical coatings and structural patterns in the literature predict patterns may cause up to $200\,\mu m$ of slip.

The coupling of the slip condition to the rimming flow problem has not been

explored in any previous work and there is a distinct lack of knowledge on how this will alter the film performance. This research consequently explores the effects slip has on the film shapes and temperature profiles, determining the merits of developing surfaces which cause slip for bearing chambers and to some extent fills this gap in the knowledge.

Chapter 3

Mathematical Formulation

This Chapter presents the modelling strategies used within this thesis to include the higher order effects that have been discussed in Chapter 2 and are intended to be an accurate representation of the conditions expected in the bearing chamber. This Chapter consists of the governing equations, which are given in a more generalised form, alongside the boundary conditions which describe the fluid interactions at the chamber wall and the core air phase. These equations are then written in terms of the cylindrical coordinate system being used to represent a geometrically simplified chamber as a horizontal cylinder with axial uniformity resulting in a two-dimensional flow. In typical fashion when developing numerical models, the equations are scaled by a set of characteristic values and expressed by non-dimensional parameters which retain the important higher order effects including those of inertia and convection. This provides a readily solvable system of equations, which includes complex non-linear terms.

The governing equations are integrated across the film as a method to reduce the complexity by lowering the problem dimensionality, leading to four integro-differential equations which need to be solved. The final model of four governing equations is developed from the *a priori* selection of field profiles which are solvable by any typical numerical method, with the specific method used in this thesis described in section 3.7, based on a type of spectral method. The advantage of this model is the dramatic cost reduction in calculating film profiles, as full scale CFD models may take weeks on a high performance computer, while these equations can be solved within hours.

3.1 Introduction to the Two-Phase Governing and Boundary Equations

In considering the walls of the bearing chamber as a smooth solid surface, a film of liquid is assumed to fully coat the entire interior surface as shown in figure 3.1. The film only partially fills the cylinder volume. The chamber is modelled as a horizontal stationary cylinder to avoid the complexities that are present in the physical chamber such as bolts or seals which are beyond the scope of this thesis. These may be included in more conventional computational fluid dynamic models with high fidelity meshing strategies.

The equations introduced in this section are independent of the coordinate system of the bearing chamber geometry, which is introduced later in section 3.2. The oil film found within the bearing chamber is treated as a generalised incompressible Newtonian fluid, where the fluid density is denoted by ρ, the dynamic viscosity μ, where the kinematic viscosity is $\nu = \mu/\rho$ and thermal diffusivity $\varphi = k^*/\rho c_p$, with the thermal conductivity and specific heat capacity of the fluid given as k^* and c_p respectively. All of the fluid properties are treated as being constant values irrespective of the film conditions such as the temperature or pressure, as most aero-engine oils properties are essentially isothermal at operating conditions. The partially filled cylinder means that a phase of gas is found internal to the liquid phase with respect to the cylinder radius. In a bearing chamber operation, the fluid phase is accelerated from an otherwise stationary flow by the rotation of the concentric shafts and kept at a constant temperature T_a^*, where the use of superscript * denotes a dimensional variable. The terms $\mathbf{n}^*$ and $\mathbf{l}^*$ are known as the surface normal and surface tangential unit vectors, which are defined for a given coordinate system.

Assuming the high windage caused by the shaft rotation in the chamber maintains a constant air phase velocity, an applied constant surface shear stress, τ_a^* is prescribed on the fluid at the interface between the air and fluid phases, where the pressure of the air phase at the interface is given as P_a^* as the atmospheric pressure.

The film is described by the Navier-Stokes equations and conservation of energy equation, shown as the continuity equation (3.1), Navier-Stokes momentum equation (3.2) and balance of energy equation of (3.3) where there is no internal heat generation.

$$\nabla^* \cdot \mathbf{u}^* = 0, \tag{3.1}$$

$$\frac{D^*(\mathbf{u}^*)}{D^* t^*} = -\frac{1}{\rho}\nabla^* P^* + \nu \nabla^{*2}\mathbf{u}^* + \mathbf{g}^*, \tag{3.2}$$

$$\frac{D^*(T^*)}{D^* t^*} = \frac{k^*}{\rho c_p}\nabla^{*2} T^*, \tag{3.3}$$

where the variables $\mathbf{u}^*$ and T^* denote the velocity and temperature fields within the film, while the pressure field within the film is given as P^*. The gradient, divergence and Laplacian operators of ∇^*, $\nabla^* \cdot$ and ∇^{*2} are functions of the coordinate geometry, with the gravitational field, $\mathbf{g}^*$ also being a function of the coordinate system. The convective derivative term is defined, for a given function χ^* as

$$\frac{D^*\chi^*}{D^* t^*} \rightarrow \frac{\partial \chi^*}{\partial t^*} + \mathbf{u}^* \cdot \nabla^* \chi^*. \tag{3.4}$$

If a fluid flow is considered to only partially fill the domain that is being investigated, the surface of the liquid phase must be maintained and is typically treated as a material surface where particles at the surface are bound on the surface, shown as

$$\frac{D^*}{D^* t^*}(\psi^*) = \frac{D^*}{D^* t^*}(r^* - r_0 + h^*) = 0, \tag{3.5}$$

where $\psi^* \equiv 0$ and (3.5) being the well known kinematic condition of an interface. As there is no droplet behaviour being considered within the core air flow, the evaluation of the boundary conditions to ensure that the mass, momentum and energy of the fluid interface are mostly well described, and with Γ^*_{ij} being stress tensor, with the internal and external tensors being defined as Γ^*_{ij} and Γ^*_{aij} respectively, are given as

$$\mathbf{u}^* = \mathbf{U}^*, \tag{3.6}$$

$$\left(\Gamma^*_{ij} - \Gamma^*_{aij}\right) = -\sigma \kappa^* n_i, \tag{3.7}$$

$$k^* \nabla^* T^* \cdot \mathbf{n}^* = \gamma^* \left(T^*_a - T^*\right). \tag{3.8}$$

These equations introduce the variables of κ^* as the function of surface curvature as $\kappa^* = \nabla^* \cdot \mathbf{n}^*$, σ is a constant surface tension coefficient of the fluid, the interface speed being defined by $\mathbf{U}^*$, and γ^* is the heat transfer coefficient between the air and liquid phases of the interface, assuming a constant temperature T^*_a, irrespective of the heat flux. The derivation of these boundary conditions can be

found in Appendix B.

The boundary conditions at the wall are generally well known. Regarding the tangential flow velocity there is the typical no-slip condition which defines the tangential velocity at the wall. This is usually zero for the no-slip condition. There is also the no-penetration condition, which states the radial velocity at the wall must reduce to zero because the surface is impermeable. Finally, there needs to be an equation which defines the thermal condition of the fluid at the wall; this can either be directly defining the fluid temperature at the wall or specifying the rate of heat entering the fluid. For this thesis, the wall boundary conditions are given as

$$\mathbf{u}^* \cdot \mathbf{l}^* = \pm l_s^* \dot{\xi}, \tag{3.9}$$

$$\mathbf{u}^* \cdot \mathbf{n}^* = 0, \tag{3.10}$$

$$\mathbf{T}^* = T_w^*. \tag{3.11}$$

The slip boundary condition of (3.9) follows the assumption that the wall has been treated to create large slip in a manner similar to those outlined in Chapter 2. The shear rate of the fluid is given as $\dot{\xi}$ and is similar to the conditions proposed by Nieto et al. [124], Lee et al. [121] and Ou et al. [122]. The temperature of the cylinder wall is denoted by T_w^* and is assumed to be hotter than the air temperature T_a^*.

The equations presented in this section may be applied to a number of problems and geometries, though following the cylindrical coordinate identities which are given in the Appendix A, the flow equations are given in a cylindrical coordinate system as detailed in section 3.2.

3.2 The Rimming Flow Equations in Cylindrical Coordinates

In developing the mathematical model for the rotating flows similar to those found in the bearing chamber, a polar coordinate system for a stationary cylinder is introduced, with the azimuthal angle, θ^* measuring positively in an anticlockwise direction from the base as shown in figure 3.1. The cylinder has a typical radius which is defined as r_0 and the radial distance measured from the center is denoted by r^*. The film of fluid is described with both velocity and temperature fields, denoted by $\mathbf{u}^*$ and T^* respectively, while time is represented by t^*. The fluid is exposed to an atmospheric pressure from the core airflow within the chamber,

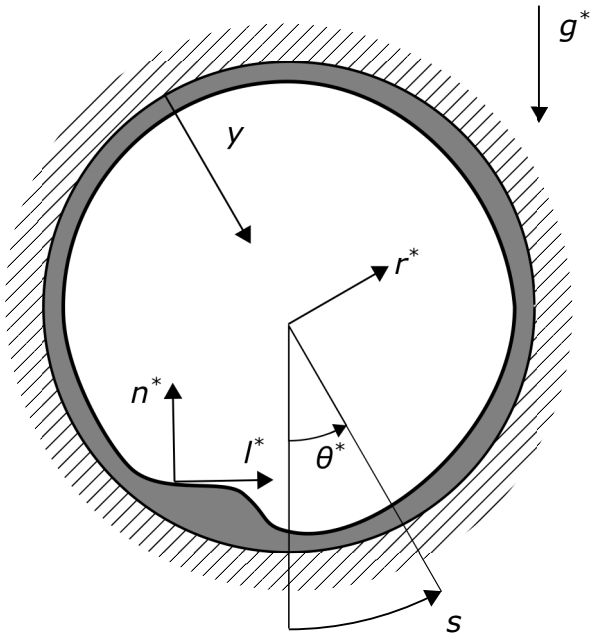


Figure 3.1: Two-dimensional representation of bearing chamber and cylindrical coordinate system.

given as P_a^* which acts on the film surface while the pressure field within the fluid is given by P^*. When investigating the non-isothermal films, it is important to describe the thermal conductivity of the fluid denoted with k^* and the specific heat capacity, c_p.

As introduced in section 3.1, the fluid is governed by the Navier-Stokes momentum, continuity and energy balance equations, with the gravitational field of the chamber, $\mathbf{g}^*$, in the chosen coordinate system is given as $\mathbf{g}^* = (g\cos\theta^*, -g\sin\theta^*)$. The unit tangential and unit normal vectors of the fluid surface are defined as $\mathbf{l}^* = l_r^*\hat{r} + l_\theta^*\hat{\theta}$ and $\mathbf{n}^* = n_r^*\hat{r} + n_\theta^*\hat{\theta}$ respectively ($\hat{r}$ and $\hat{\theta}$ are the radial and azimuthal unit vectors. The coefficients of the unit vectors l_r^*, l_θ^*, n_r^* and n_θ^* can be found in Appendix A). The velocity field for the film is given as both azimuthal and radial components as $\mathbf{u}^* = u_\theta^*\hat{\theta} + u_r^*\hat{r}$. Expressing the momentum equation of (3.2) into the cylindrical coordinates as illustrated in figure 3.1 leads to the separation of this governing equation into two components, defined as the radial momentum equation

$$\rho\left[\frac{\partial u_r^*}{\partial t^*} + u_r^*\frac{\partial u_r^*}{\partial r^*} + \frac{u_\theta^*}{r^*}\frac{\partial u_r^*}{\partial \theta^*} - \frac{u_\theta^{*2}}{r^*}\right] = -\frac{\partial P^*}{\partial r^*} + \mu\left[\frac{\partial^2 u_r^*}{\partial r^{*2}} + \frac{1}{r^*}\frac{\partial u_r^*}{\partial r^*} + \frac{1}{r^{*2}}\frac{\partial^2 u_r^*}{\partial \theta^{*2}} - \frac{u_r^*}{r^{*2}} - \frac{2}{r^{*2}}\frac{\partial u_\theta^*}{\partial \theta^*}\right] + \rho g\cos\theta^*, \quad (3.12)$$

and the azimuthal momentum equation

$$\rho\left[\frac{\partial u_\theta^*}{\partial t^*}+u_r^*\frac{\partial u_\theta^*}{\partial r^*}+\frac{u_\theta^*}{r^*}\frac{\partial u_\theta^*}{\partial \theta^*}+\frac{u_\theta^* u_r^*}{r^*}\right]=-\frac{1}{r^*}\frac{\partial P^*}{\partial \theta^*}$$
$$+\mu\left[\frac{\partial^2 u_\theta^*}{\partial r^{*2}}+\frac{1}{r^*}\frac{\partial u_\theta^*}{\partial r^*}+\frac{1}{r^{*2}}\frac{\partial^2 u_\theta^*}{\partial \theta^{*2}}-\frac{u_\theta^*}{r^{*2}}+\frac{2}{r^{*2}}\frac{\partial u_r^*}{\partial \theta^*}\right]-\rho g\sin\theta^*. \quad (3.13)$$

By expressing both the conservation of mass, or continuity equation (3.1) and the conservation of thermal energy equations (3.3) within the coordinate system, they may be written as

$$\frac{\partial u_r^*}{\partial r^*}+\frac{u_r^*}{r^*}+\frac{1}{r^*}\frac{\partial u_\theta^*}{\partial \theta^*}=0, \quad (3.14)$$

and

$$\frac{\partial T*}{\partial t^*}+u_r^*\frac{\partial T^*}{\partial r^*}+\frac{u_\theta^*}{r^*}\frac{\partial T^*}{\partial \theta^*}=k^*\left[\frac{\partial^2 T^*}{\partial r^{*2}}+\frac{1}{r^*}\frac{\partial T^*}{\partial r^*}+\frac{1}{r^{*2}}\frac{\partial^2 T^*}{\partial \theta^{*2}}\right]. \quad (3.15)$$

Between the film and stationary cylinder, there is an interface located at $r^*=r_0$ which requires conditions to describe the dynamics of the flow and thermal interactions of the fluid and wall as in (3.10) and (3.11) are imposed directly onto the fluid in the coordinate system as

$$u_r^*=0, \quad (3.16)$$

and

$$T^*=T_w^*. \quad (3.17)$$

The boundary condition to describe the azimuthal velocity arises from (3.9), which acts along the entire interface of the cylinder wall and fluid. The fluid shear, denoted by $\dot{\xi}$ is related to the fluid velocity at the wall by a proportional constant, known as the slip length, l_s^*. This slip length is equivalent to defining the apparent depth of penetration of the velocity field into the wall, as shown in figure 2.6. The fluid shear, $\dot{\xi}$ at $r^*=r_0$ on the solid wall is

$$\dot{\xi}=\frac{1}{r^*}\frac{\partial u_r^*}{\partial \theta^*}+r^*\frac{\partial}{\partial r^*}\left(\frac{u_\theta^*}{r^*}\right), \quad (3.18)$$

therefore, substitution of (3.18) into (3.9) and suitable use of the no-penetration condition of (3.16) leads to the equation for the azimuthal velocity on the cylinder as

$$u_\theta^* = -l_s^* \left[\frac{\partial u_\theta^*}{\partial r^*} - \frac{u_\theta^*}{r^*} \right]. \tag{3.19}$$

With a cylinder that is only partially filled with fluid, the kinematic condition of (3.5) is expressed in the cylindrical coordinate system as

$$\frac{\partial h^*}{\partial t^*} + u_r^* + \frac{u_\theta^*}{r^*} \frac{\partial h^*}{\partial \theta^*} = 0. \tag{3.20}$$

If the film is expected to experience a temperature difference across the surfaces of the fluid, such as between the heated fluid and cooled airflow, the generalized Newton's law of cooling as found in the works of Ding et al. [79] or Kay et al. [15] and given in (3.8) relates the heat flux of the interface to the temperature difference across the interface as

$$k^* \left(\frac{\partial T^*}{\partial r^*} + \frac{1}{H^{*2}} \frac{\partial h^*}{\partial \theta^*} \frac{\partial T^*}{\partial \theta^*} \right) = -\frac{\gamma^*}{\Pi^*} \left(T_a^* - T^* \right), \tag{3.21}$$

following the identities established within Appendix A.

With the stress tensors of the airflow and fluid, Γ_{aij}^* and Γ_{ij}^* given in Appendix B and detailed in the works by Kay et al. [14, 15] or Williams et al. [175] with an applied air shear, the conservation of momentum at the interface leads to the normal pressure and tangential shear stress equations

$$P_a^* = -\sigma\kappa^* + P^* - 2\mu\Pi^{*2} \left[\frac{\partial u_r^*}{\partial r^*} + \left(\frac{\partial u_\theta^*}{\partial r^*} - \frac{u_\theta^*}{r^*} + \frac{1}{r^*} \frac{\partial u_r^*}{\partial \theta^*} \right) \frac{1}{H^*} \frac{\partial h^*}{\partial \theta^*} + \left(\frac{1}{r^*} \frac{\partial u_\theta^*}{\partial \theta^*} + \frac{u_r^*}{r^*} \right) \left(\frac{1}{H^*} \frac{\partial h^*}{\partial \theta^*} \right)^2 \right], \tag{3.22}$$

$$\frac{\tau_a^*}{\Pi^{*2}} = \mu \left[\left(\frac{\partial u_\theta^*}{\partial r^*} - \frac{u_\theta^*}{r^*} + \frac{1}{r^*} \frac{\partial u_r^*}{\partial \theta^*} \right) \left(-1 - \left(\frac{1}{H^*} \frac{\partial h^*}{\partial \theta^*} \right)^2 \right) + \frac{2}{H^*} \frac{\partial h^*}{\partial \theta^*} \left(-\frac{\partial u_r^*}{\partial r^*} + \frac{1}{r^*} \frac{\partial u_\theta^*}{\partial \theta^*} + \frac{u_r^*}{r^*} \right) \right]. \tag{3.23}$$

The surface tension, σ acts relative to the film surface curvature, κ^* that is calculated from the divergence of the normal vector of the film interface, which is

$$\kappa^* = \frac{\partial n_r^*}{\partial r^*} + \frac{n_r^*}{r^*} + \frac{1}{r^*} \frac{\partial n_\theta^*}{\partial \theta^*}. \tag{3.24}$$

Expressing the normal vectors, the surface curvature at $r^* = r_0 - h^*$ is written as

$$\kappa^* = -\frac{\Pi^*}{r^*} + \frac{\Pi^{*3}}{r^{*4}}\left(\frac{\partial h^*}{\partial \theta^*}\right)^2 \frac{\partial^2 h^*}{\partial \theta^{*2}} + \frac{\Pi^{*3}}{r^{*5}}\left(\frac{\partial h^*}{\partial \theta^*}\right)^4 - \frac{\Pi^*}{r^{*3}}\left(\frac{\partial h^*}{\partial \theta^*}\right)^2 - \frac{\Pi^*}{r^{*2}}\frac{\partial^2 h^*}{\partial \theta^{*2}}. \quad (3.25)$$

An important parameter from the works of Ashmore et al. [49], that has been used as a small parameter is the filling fraction, A that quantifies the volume of fluid within the chamber and ensures that a consistent volume of fluid is investigated is found from the integral of the fluid volume across the domain

$$A = \frac{1}{\pi r_0}\int_{-\pi}^{\pi}\left(h^* - \frac{h^{*2}}{2r_0}\right)\, d\theta^*. \quad (3.26)$$

3.3 Scaling into a Non-Dimensional System

It is typical in developing mathematical models to remove the dimensions of the posed problem, therefore the equations are scaled from their physical representation into a more appropriate non-dimensional system. To do this, characteristic values are introduced which define typical values for the size of the cylinder radius that is analogous to the bearing chamber and film thickness, which are denoted as r_0 and h_0 respectively, while the film has a characteristic speed of the flow which is given as U_0. The coordinate system introduced in section 3.2 is transformed into a new system, which is defined as the new azimuthal location for $\theta^* = s$ while the radial coordinate is given by $r^* = r_0\left[1 - \varepsilon y\right]$, where the introduced variable y measures the radial distance from the wall. We introduce a new non-dimensional parameter known as the film aspect ratio,

$$\varepsilon = \frac{h_0}{r_0}, \quad (3.27)$$

which acts as a small parameter to aid in simplifying the mathematical problem by the thin-film assumption described in section 3.4. In order to retain the pressure field within the fluid, an effect which is expected to be important when sharp gradients are found in the film, the pressure P^* is scaled by the dynamic pressure of ρU_0^2. The inclusion of hydrostatic pressure effects are outlined in the works of Tirumkudulu and Acrivos [17], Ashmore et al. [49] and in the later works of Kay et al. [15]. These sharp gradients within the film are linked to regions in which stagnation or pooling of the working fluid occurs and are typically due to an insufficiently driven flow being overcome by gravitational effects. Alongside the non-dimensionalisation of the coordinate system and pressure fields, the components of the velocity field are scaled so that the radial velocity is scaled by $u_r^* = -\varepsilon U_0 v$ and the azimuthal component is scaled with $u_\theta^* = U_0 u$. A number

of other scalings are introduced to non-dimensionalise the remaining variables introduced in section 3.2, and are given as

$$\begin{aligned} t^* &= r_0 t/U_0, & \kappa^* &= \kappa/r_0, & l_s^* &= l_s h_0, \\ h^* &= h_0 h, & \tau_a^* &= \tau\mu U_0/h_0, & H^* &= H r_0. \end{aligned} \tag{3.28}$$

The slip length is a measure of the velocity field's impingement into the cylinder wall, and is therefore aptly scaled by the characteristic film height and infers that for a microscale film thickness, the slip length is therefore also microscale in size. In the work by Kakimpa et al. [1] who investigated bearing chamber films, the characteristic film is of several mm in thickness and if $l_s = 0.1$, the physical slip length corresponds to approximately $l_s^* \sim 100\mu m$.

The temperature field is non-dimensionalised by a characteristic temperature which is assumed to be the hottest point of the system, and is typically the temperature of the chamber wall temperature as being heated to a constant temperature.

These dimensional characteristic values can be collected into a set of dimensionless parameters that are useful in defining the conditions of the flow, one of the most notable is in the Reynolds number, Re, defined as

$$Re = \frac{\rho U_0 h_0}{\mu} = \frac{Inertial\ Forces}{Viscous\ Forces}. \tag{3.29}$$

When including the effects of surface tension, it is typical to use either the capillary number, Ca, or Weber number to non-dimensionalise the surface tension coefficient σ. In this work the capillary number is

$$Ca = \frac{\mu U_0}{\sigma} = \frac{Viscosity}{Surface\ Tension}, \tag{3.30}$$

and measures the viscous to surface tension effects. In determining the importance of the gravitational forces, λ is introduced as a scale of the gravitational to viscous forces as

$$\lambda = \frac{\rho g \left(h_0\right)^2}{\mu U_0} = \frac{Gravity}{Viscosity}, \tag{3.31}$$

which can be described as Re/Fr, with Fr given as the Froude number, defined as the ratio of inertia and gravity,

$$Fr = \frac{U_0^2}{g h_0} = \frac{Inertial\ Forces}{Gravity}. \tag{3.32}$$

In addition to the previous non-dimensional parameters which govern the isother-

mal flow, two more dimensionless parameters are defined to determine the thermodynamic properties of the film, these are the ratio between the heat transfer from convection of the fluid motion to that of conduction, known as the Péclet number

$$Pe = \frac{\rho c_p U_0 h_0}{k^*} = \frac{Advective\ Heat\ Transfer}{Diffusive\ Heat\ Transfer}, \tag{3.33}$$

and Biot number, B which relates the surface heat transfer rate to the conduction within the film, defined as

$$B = \frac{h_0 \gamma^*}{k^*} = \frac{External\ Convective\ Heat\ Transfer}{Internal\ Conductive\ Heat\ Transfer}. \tag{3.34}$$

By substitution of the newly introduced dimensionless variables and parameters, the continuity equation (3.14) can be written in dimensionless form as

$$\frac{\partial v}{\partial y}\left[1-\varepsilon y\right] - \varepsilon v + \frac{\partial u}{\partial s} = 0, \tag{3.35}$$

while the Navier-Stokes momentum equations of the radial and azimuthal components of (3.12) and (3.13) are expressed as the dimensionless radial momentum equation of

$$\begin{aligned}\varepsilon Re\left[-\varepsilon^2\frac{\partial v}{\partial t} - \varepsilon^2 v\frac{\partial v}{\partial y} - \frac{\varepsilon^2 u}{[1-\varepsilon y]}\frac{\partial v}{\partial s} - \frac{\varepsilon u^2}{[1-\varepsilon y]}\right] &= \varepsilon Re\frac{\partial P}{\partial y} - \varepsilon^2\frac{\partial^2 v}{\partial y^2} \\ + \frac{\varepsilon^3}{[1-\varepsilon y]}\frac{\partial v}{\partial y} - \varepsilon^4\frac{1}{[1-\varepsilon y]^2}\frac{\partial^2 v}{\partial s^2} + \frac{\varepsilon^4 v}{[1-\varepsilon y]^2} - \frac{2\varepsilon^3}{[1-\varepsilon y]^2}\frac{\partial u}{\partial s} + \varepsilon\lambda\cos s,\end{aligned} \tag{3.36}$$

and the azimuthal momentum equation

$$\begin{aligned}\varepsilon Re\left[\frac{\partial u}{\partial t} + v\frac{\partial u}{\partial y} + \frac{u}{[1-\varepsilon y]}\frac{\partial u}{\partial s} - \varepsilon\frac{uv}{[1-\varepsilon y]}\right] &= -\varepsilon Re\frac{1}{[1-\varepsilon y]}\frac{\partial P}{\partial s} + \frac{\partial^2 u}{\partial y^2} \\ - \frac{\varepsilon}{[1-\varepsilon y]}\frac{\partial u}{\partial y} + \frac{\varepsilon^2}{[1-\varepsilon y]^2}\frac{\partial^2 u}{\partial s^2} - \frac{\varepsilon^2 u}{[1-\varepsilon y]^2} - \frac{2\varepsilon^3}{[1-\varepsilon y]^2}\frac{\partial v}{\partial s} - \lambda\sin s.\end{aligned} \tag{3.37}$$

The energy equation of (3.15) is written as

$$\varepsilon Pe\left[\frac{\partial T}{\partial t} + v\frac{\partial T}{\partial y} + \frac{u}{[1-\varepsilon y]}\frac{\partial T}{\partial s}\right] = \frac{\partial^2 T}{\partial y^2} - \frac{\varepsilon}{[1-\varepsilon y]}\frac{\partial T}{\partial y} + \frac{\varepsilon^2}{[1-\varepsilon y]^2}\frac{\partial^2 T}{\partial s^2}. \tag{3.38}$$

The dimensionless boundary conditions at the free surface, now given at the location of $y = h$ of the kinematic surface condition of (3.20) and Newton's law of cooling (3.21) are

$$\frac{\partial h}{\partial t} - v + \frac{u}{H}\frac{\partial h}{\partial s} = 0, \tag{3.39}$$

$$\frac{\partial T}{\partial y} - \frac{\varepsilon^2}{H^2}\frac{\partial h}{\partial s}\frac{\partial T}{\partial s} = \frac{B}{\Pi}\left(T_a - T\right), \tag{3.40}$$

where the dimensionless values of Π and H are given as

$$\Pi = \left(1 + \left(\frac{\varepsilon h'}{1-\varepsilon h}\right)^2\right)^{-1/2}, \tag{3.41}$$

$$H = 1 - \varepsilon h. \tag{3.42}$$

Acting at the interface between the fluid and air phases, the components of the stress condition of (3.22) and (3.23) are written in dimensionless terms as

$$P_a = -\frac{\varepsilon}{ReCa}\kappa + P - \frac{2\Pi^2}{Re}\left[\varepsilon\frac{\partial v}{\partial y} - \left(\frac{\partial u}{\partial y} + \frac{\varepsilon u}{[1-\varepsilon y]} + \frac{\varepsilon^2}{[1-\varepsilon y]}\frac{\partial v}{\partial s}\right)\frac{\varepsilon}{H}\frac{\partial h}{\partial s} + \left(\frac{\varepsilon^3}{[1-\varepsilon y]}\frac{\partial u}{\partial s} - \frac{\varepsilon^4 v}{[1-\varepsilon y]}\right)\left(\frac{1}{H}\frac{\partial h}{\partial s}\right)^2\right], \tag{3.43}$$

$$\frac{\tau}{\Pi^2} = \left[\left(-\frac{\partial u}{\partial y} - \frac{\varepsilon u}{[1-\varepsilon y]} - \frac{\varepsilon^2}{[1-\varepsilon y]}\frac{\partial v}{\partial s}\right)\left(-1 - \left(\frac{\varepsilon}{H}\frac{\partial h}{\partial s}\right)^2\right) + \frac{2\varepsilon}{H}\frac{\partial h}{\partial s}\left(-\varepsilon\frac{\partial v}{\partial y} + \frac{\varepsilon}{[1-\varepsilon y]}\frac{\partial u}{\partial s} - \frac{\varepsilon^2 v}{[1-\varepsilon y]}\right)\right], \tag{3.44}$$

and curvature of the interface between the fluid and air flow, given by the function of (3.25) is non-dimensionalised as

$$\kappa = \frac{\Pi}{1-\varepsilon h}\left[-1 + \frac{\varepsilon^3\Pi^2}{(1-\varepsilon h)^3}\left(\frac{\partial h}{\partial s}\right)^2\frac{\partial^2 h}{\partial s^2} + \frac{\varepsilon^4\Pi^2}{(1-\varepsilon h)^4}\left(\frac{\partial h}{\partial s}\right)^4 - \frac{\varepsilon^2}{(1-\varepsilon h)^2}\left(\frac{\partial h}{\partial s}\right)^2 - \frac{\varepsilon}{(1-\varepsilon h)}\frac{\partial^2 h}{\partial s^2}\right]. \tag{3.45}$$

The equation of the filling fraction for the film of (3.26) is given as

$$\pi A = \varepsilon \int_{-\pi}^{\pi} \left(h - \frac{\varepsilon h^2}{2} \right) \, ds, \tag{3.46}$$

while the boundary conditions on the cylinder wall at $y = 0$ of (3.17), (3.16) and (3.19) for the prescribed wall temperature, no-penetration condition and slip boundary condition are also non-dimensionalised as

$$T = T_w, \tag{3.47}$$

$$v = 0, \tag{3.48}$$

$$u = l_s \left[\frac{\partial u}{\partial y} + \frac{\varepsilon u}{[1 - \varepsilon y]} \right]. \tag{3.49}$$

3.4 The Thin Film Approximation

In the bearing chambers of interest, the chamber is typically much larger in size than the oil film thickness found to coat the interior walls. Therefore, the characteristic radius r_0 of the cylinder is similar in size to that presented by Kakimpa et al. [1] and a film thickness is assumed to satisfy $\varepsilon \ll 1$, known as the thin film assumption. Along with the thin film approximation, the typical assumption is that many effects are likely to be negligible, notably those of inertia and thermal convection. However, situations arise where these assumptions are no longer suitable as the removed terms from the governing equations may be dominant in local regions. One example is in the highly sheared flows found in aero-engines according to Kay et al. [15] or Kakimpa et al. [1], where modest values of inertia and thermal convection may be found. In the interest of retaining the effects of moderate inertial and convective forces, the following regime is proposed

$$\begin{aligned} &\varepsilon \ll 1, && \varepsilon Re \sim O(1), \\ &\lambda \sim O(1), && \varepsilon Pe \sim O(1). \end{aligned} \tag{3.50}$$

As rimming flows are mainly a balance between the gravitational and viscous forces across the domain, the value of λ is therefore assumed to be leading order, $\lambda \sim O(1)$. The remaining terms approach zero, including those of inertia with $\varepsilon \ll 1$ when taken to $O(1)$, and forms the framework of the classical lubrication modelling for rimming flows, such as the work of Johnson [23]. Along with the removal of inertial terms, due to the assumed thickness of the film being sufficiently

narrow so that the inertial effects are negligible, the assumption of $\varepsilon \ll 1$ reduces the radial momentum equation of (3.36) to provide a function of the film pressure that is a constant. This constant pressure field is inadequate due to the hydrostatic effects within pooling films according to the work by Acrivos and Jin [39], where sharp pressure fluctuations are expected near locations with sudden variations in the film height which elevate the pressure terms to leading order locally. The terms of first order $O(\varepsilon)$ must be included to incorporate the $O(\varepsilon)$ gravitational terms in the formulation of the model so that the hydrostatic pressure gradients are retained. The inclusion of $O(\varepsilon)$ terms is to maintain consistency in modelling, and includes those of inertia at first order. The terms of higher order than $O(\varepsilon)$, found in the lateral thermal diffusion, at $O(\varepsilon^2)$ and those of surface tension at $O(\varepsilon^3)$ are due to the elevated spatial derivative terms only in local regions of sharp gradients, promoting these terms to be significant as either h' or $\bar{T}'$ are no longer insignificant, with the prime $'$ denoting a derivative with respect to s.

In this regime, the continuity equation of (3.35) is given exactly as

$$\frac{\partial v}{\partial y}\left[1-\varepsilon y\right]-\varepsilon v+\frac{\partial u}{\partial s}=0, \tag{3.51}$$

while the radial and azimuthal momentum equations (3.36) and (3.37) are reduced to

$$\varepsilon Re\left[-\frac{\varepsilon u^2}{\left[1-\varepsilon y\right]}\right]=\varepsilon Re\frac{\partial P}{\partial y}+\varepsilon\lambda\cos s+O\left(\varepsilon^2,\varepsilon^3 Re\right), \tag{3.52}$$

$$\begin{aligned}\varepsilon Re\left[\frac{\partial u}{\partial t}+v\frac{\partial u}{\partial y}+\frac{u}{\left[1-\varepsilon y\right]}\frac{\partial u}{\partial s}-\varepsilon\frac{uv}{\left[1-\varepsilon y\right]}\right]&=-\varepsilon Re\frac{1}{\left[1-\varepsilon y\right]}\frac{\partial P}{\partial s}\\&+\frac{\partial^2 u}{\partial y^2}-\frac{\varepsilon}{\left[1-\varepsilon y\right]}\frac{\partial u}{\partial y}+\frac{\varepsilon^2}{\left[1-\varepsilon y\right]^2}\frac{\partial^2 u}{\partial s^2}-\frac{\varepsilon^2 u}{\left[1-\varepsilon y\right]^2}-\lambda\sin s+O\left(\varepsilon^2,\varepsilon^3 Re\right).\end{aligned} \tag{3.53}$$

The energy equation of (3.38) is also given exactly as

$$\varepsilon Pe\left[\frac{\partial T}{\partial t}+v\frac{\partial T}{\partial y}+\frac{u}{\left[1-\varepsilon y\right]}\frac{\partial T}{\partial s}\right]=\frac{\partial^2 T}{\partial y^2}-\frac{\varepsilon}{\left[1-\varepsilon y\right]}\frac{\partial T}{\partial y}//+\frac{\varepsilon^2}{\left[1-\varepsilon y\right]^2}\frac{\partial^2 T}{\partial s^2}. \tag{3.54}$$

The boundary conditions at the cylinder surface of (3.47) and (3.48) remain identical for the thin film assumption, while the partial slip condition of (3.49) is reduced to become

$$u = l_s \left[\frac{\partial u}{\partial y} + \varepsilon u \right] + O\left(\varepsilon^2\right). \tag{3.55}$$

Similarly, by following the thin film approximation the free surface boundary conditions of the heat transfer equation (3.40) and kinematic condition at the free surface (3.39) yield

$$\frac{\partial T}{\partial y} = B\left(T_a - T\right) + O\left(\varepsilon^2\right), \tag{3.56}$$

$$\frac{\partial h}{\partial t}\left(1 - \varepsilon h\right) - v\left(1 - \varepsilon h\right) + u\frac{\partial h}{\partial s} = O\left(\varepsilon^2\right), \tag{3.57}$$

where the value of Π can be approximated to $\Pi \approx 1$ with a negative power binomial series, as Π will be multiplied by ε later in the formulation so all higher order terms have been neglected. The surface curvature (3.45) is also approximated by the thin film approximation and binomial expansion as $\kappa = -1 - \varepsilon\left(h'' + h\right)$, where the retention of $\varepsilon h''$ term is due to this term becoming considerable in developing pool or shock solutions according to Kay et al. [14], Ashmore et al. [49] and Benilov et al. [44]. This h'' will become a third order spatial derivative and is expected to act as the stabilizing surface tension term from the normal stress boundary condition (3.43), which in the thin film limit becomes

$$P_a \approx -\frac{\varepsilon\kappa}{ReCa} + P. \tag{3.58}$$

The driving shear force from the tangential stress condition (3.44), following the thin film limit is written as

$$\tau \approx \frac{\partial u}{\partial y} + \varepsilon u, \tag{3.59}$$

while the thin film approximation of (3.46) is simply

$$\pi A = \varepsilon \int_{-\pi}^{\pi} h \, ds + O\left(\varepsilon^2\right). \tag{3.60}$$

By calculating the filling fraction A, continuity of the film mass can be ensured when using a steady-state solver as a fixed volume of fluid can be safeguarded.

3.5 Depth-Averaging of the Governing Equations

The governing and boundary equations have been simplified by the thin film approximation, however there is another technique to aid in further simplifying the governing equations which involves the integration of the governing equations to reduce the dimensionality of the problem. This process is known as depth-averaging, and introduces a new type of quantity commonly called the mean field variables, good examples of which may be found in Nguyen and Balakotaiah [68] or Benilov [76] in the study of planar flows. The idea of integrating the equations is that by reducing the problem dimensionality, the computational costs associated with solving the governing equations are also reduced. This technique, known as depth-averaging or integral boundary layer method has been previously used in the exploration of rimming flows, see the works of Kakimpa et al. [1], Kay et al. [14] or Kay et al. [15].

The integration of (3.51) across the film from $y = 0$ to $y = h$ gives the depth-averaged continuity equation

$$(1 - \varepsilon h)\frac{\partial h}{\partial t} + \frac{\partial q}{\partial s} = O\left(\varepsilon^2\right), \tag{3.61}$$

where we have introduced one of the new mean film variables, denoted by q as a dimensionless volume flux per axial unit length of the cylinder, and can also be found in other works such as Moffatt [31] or Ashmore et al. [49] and is given as

$$\int_0^h u \, dy = q. \tag{3.62}$$

The radial momentum equation (3.52) is not integrated across the film depth, as an equation to model the variation in pressure through the film is still required. It is possible to integrate (3.52) and express this as a function which defines the pressure distribution radially across the film, this is given as

$$P(y) = \varepsilon \int_0^h u^2 \, dy - \varepsilon \int_0^y u^2 \, dy + P_a + \frac{\varepsilon}{ReCa}\kappa + \frac{\lambda \cos s \, [h - y]}{Re}, \tag{3.63}$$

where the normal stress condition of (3.58) is used to evaluate the integration constant. A useful identity can be formed from the continuity equation (3.51) and is given as

$$\frac{\partial}{\partial y}\left(\left[1-\varepsilon y\right]vu\right)+u\frac{\partial u}{\partial s}=\left(1-\varepsilon y\right)v\frac{\partial u}{\partial y}. \tag{3.64}$$

Using the pressure function of (3.63), the derivative function of (3.64), the normal stress condition (3.58) and kinematic condition (3.39), the depth-averaged azimuthal momentum equation of (3.53) can be evaluated with use of Leibniz rule of integration, and is henceforward referred to as the momentum equation is expressed as

$$\begin{aligned}\overbrace{\varepsilon Re\left[\tfrac{\partial}{\partial t}\int_0^h\left[\left(1-\varepsilon y\right)u\right]\,dy+\tfrac{\partial}{\partial s}\int_0^h u^2\,dy-\varepsilon\int_0^h uv\,dy\right]}^{\text{Inertia}}=\\ \overbrace{-\varepsilon^2 Re\left[\tfrac{\partial}{\partial s}\int_0^h\int_0^h u^2\,dy\,dy-\tfrac{\partial}{\partial s}\int_0^h\int_0^y u^2\,dy\,dy\right]}^{\text{Inertia}}+\overbrace{\tfrac{\varepsilon^3}{Ca}\left[h\tfrac{\partial^3 h}{\partial s^3}+h\tfrac{\partial h}{\partial s}\right]}^{\text{Surface Tension}}\\ \underbrace{-\varepsilon\left[\lambda\cos s h\tfrac{\partial h}{\partial s}-\lambda\sin s\tfrac{h^2}{2}\right]}_{\text{Hydrostatic Pressure}}+\underbrace{\left[\tfrac{\partial u}{\partial y}-\varepsilon y\tfrac{\partial u}{\partial y}\right]_0^h}_{\text{Viscosity}}-\underbrace{\left[h-\varepsilon\tfrac{h^2}{2}\right]\lambda\sin}_{\text{Gravity}}.\end{aligned} \tag{3.65}$$

The surface tension terms from (3.63) are retained, including those which are now at $O\left(\varepsilon^3\right)$, as mentioned in Kay et al. [14] or Kakimpa et al. [1], due to their reported stabilising effects, notably on the short wavelength perturbations that may occur when obtaining numerical solutions. With the substitution of the boundary conditions and functions prevalent on the various forces acting on the flow, (3.65) shows the contributions of the forces that have been added from the viscous and gravitational balance, with those of the pressure gradients, surface tension and inertia. The radial velocity, v can be inferred from the azimuthal velocity by integrating equation (3.51), leading to v as a function of the azimuthal velocity,

$$v=-\frac{\partial}{\partial s}\int u\,dy. \tag{3.66}$$

With the introduction of the volume flux, q as a mean parameter to represent the velocity field, the temperature field can also be expressed by the mean variable $\bar{T}$ which is defined as

$$\bar{T}=\frac{1}{h}\int_0^h T\,dy, \tag{3.67}$$

and is known as the mean film temperature, and is equivalent to the volume averaged temperature per axial unit length. Therefore, by integrating across the film depth, the depth-averaged energy equation of (3.54) is

$$\varepsilon Pe\left[\frac{\partial}{\partial t}\int_0^h \left[(1-\varepsilon y)\,T\right]\,dy+\frac{\partial}{\partial s}\int_0^h uT\,dy\right]=$$
$$\left[(1-\varepsilon y)\,\frac{\partial T}{\partial y}\right]_0^h+\varepsilon^2\frac{\partial^2}{\partial s^2}\int_0^h T\,dy-\varepsilon^2 T\frac{\partial^2 h}{\partial s^2}-2\varepsilon^2\frac{\partial T}{\partial s}\frac{\partial h}{\partial s}, \quad (3.68)$$

where the left hand side is the thermal convective terms and right hand side are thermal diffusive terms. The method of depth-averaging presents a useful technique for including complex non-linear terms like those of inertia and convection in a leading order model, by using mean parameters to eliminate some of the difficulty associated with solving the velocity fields with the non-linear inertial terms in numerical models. The caveat to this improvement in reducing the complexity of solving the Navier-Stokes equations is that while the velocity or temperature fields may be selected by *a priori* functions, the accuracy is reduced as a cost of not solving the full two-dimensional Navier-Stokes and energy equations.

3.6 Introducing Polynomial Functions for Velocity and Temperature

At this stage, the model has been reduced to a set of one-dimensional integro-differential equations, the depth-averaging method has substituted the velocity and temperature fields for mean values in the equations. However, it is helpful to observe flow recirculation and where high temperatures will occur to prevent oil degradation in the bearing chamber. Therefore, a method to approximate the velocity and temperature profiles is presented in this section by using a general leading and first order polynomial function which is defined as

$$u=\sum_{j=0}^{1}\varepsilon^j u^j = u^0+\varepsilon u^1, \quad (3.69)$$

$$T=\sum_{j=0}^{1}\varepsilon^j T^j = T^0+\varepsilon T^1. \quad (3.70)$$

The model is only given to $O(\varepsilon^2)$, so the fields functions are required to be only to $O(1)$ and $O(\varepsilon)$.

The order of the polynomial used in the literature has ranged from a quartic of Gribben et al. [70], a cubic of Kay et al. [14] or a quadratic expression as in Kay

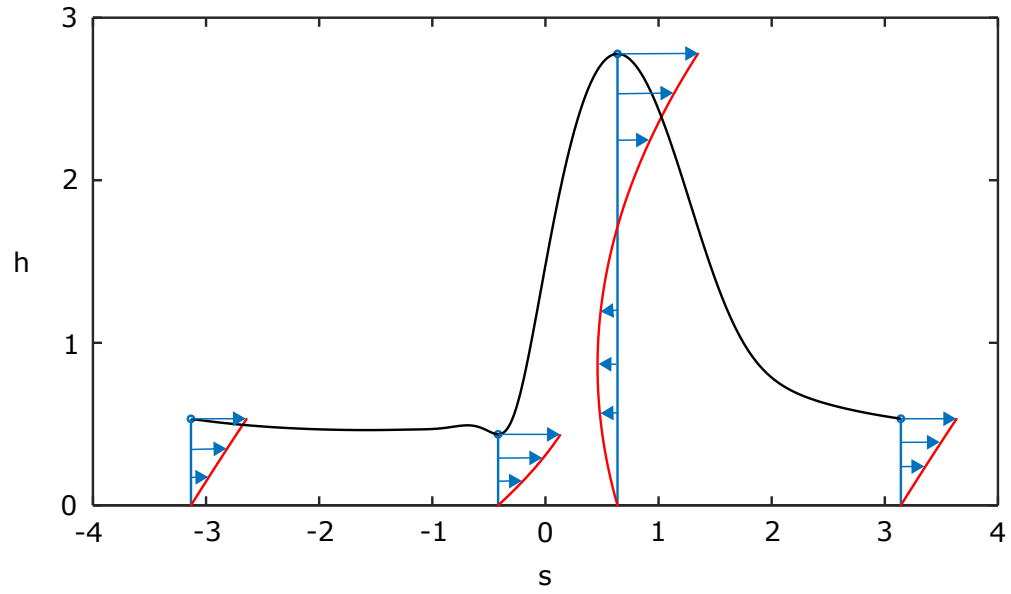


Figure 3.2: A demonstration of a quadratic function modelling complex recirculation regions of the velocity field for a typical pooling film. The *red* lines denote the calculated azimuthal velocity profile at each *blue* point, having been normalised to the maximum film velocity.

et al. [14] and Sivapuratharasu et al. [75] or Benilov [76]. In this work, quadratic profiles have been chosen as a suitable function to represent the temperature and velocity fields. This is because solutions to the Navier-Stokes equations with negligible inertia, known as Stokes flow, have analytical solutions with a parabolic profile. This quadratic assumption of the velocity profile is also found to be sufficient in modelling flow recirculation, with the azimuthal velocity components represented in figure 3.2 for a typical pooling film.

The $O(1)$ and $O(\varepsilon)$ coefficients of the quadratic profiles for velocity and temperature are

$$u^j = \sum_{i=0}^{2} a_i^j y^i = a_0^j + a_1^j y + a_2^j y^2, \tag{3.71}$$

$$T^j = \sum_{i=0}^{2} b_i^j y^i = b_0^j + b_1^j y + b_2^j y^2. \tag{3.72}$$

To evaluate the velocity polynomial, these coefficients may be found by establishing and solving a set of simultaneous equations which can be posed by the boundary conditions of (3.59) and (3.55) and the definition of the volume flux (3.62) at both leading and first order. At leading order, these equations are

$$u = l_s \left[\frac{\partial u^0}{\partial y} \right], \tag{3.73}$$

$$\tau = \frac{\partial u^0}{\partial y}, \tag{3.74}$$

$$q = \int_0^h u^0 \, dy, \tag{3.75}$$

while to first order they are given as

$$u^1 = l_s \left[\frac{\partial u^1}{\partial y} + u^0 \right], \tag{3.76}$$

$$0 = \frac{\partial u^1}{\partial y} + u^0 + u^1, \tag{3.77}$$

$$0 = \int_0^h u^1 \, dy. \tag{3.78}$$

The velocity coefficients, a_i^j to leading order of $j = 0$ can therefore be expressed as functions of τ, q, h and l_s as

$$a_0^0 = \frac{l_s \left(6q - \tau h^2\right)}{2h^2 + 6l_s h}, \tag{3.79}$$

$$a_1^0 = \frac{6q - \tau h^2}{2h^2 + 6l_s h}, \tag{3.80}$$

$$a_2^0 = \frac{3\tau h^3 + 6l_s \tau h - 6q}{4h^3 + 12l_s h^2}, \tag{3.81}$$

and the first order coefficients with $j = 1$

$$a_0^1 = \frac{l_s \left(\tau h^3 + 6qh + 36l_s q\right)}{8\left(h + 3l_s\right)^2}, \tag{3.82}$$

$$a_1^1 = \frac{\tau h^4 + 4\tau h^3 l_s + 12\tau h^2 l_s^2 + 6qh^2 + 12qhl_s - 72ql_s^2}{8h\left(h + 3l_s\right)^2}, \tag{3.83}$$

$$a_2^1 = -\frac{3\tau h^3 + 18\tau h^2 l_s + 36\tau h l_s^2 + 18qh + 72ql_s}{16\left(h^2 + 3l_s h\right)\left(h + 3l_s\right)}. \tag{3.84}$$

In a similar method of obtaining the coefficients to the velocity profile, the temperature coefficients are also solved by posing leading and first order expressions of the thermal conditions at the free surface (3.56) and at the wall (3.47), along

with the mean temperature definition (3.67), which at leading order is

$$T^0 = T_w, \tag{3.85}$$

$$B\left(T_a - T^0\right) = \frac{\partial T^0}{\partial y}, \tag{3.86}$$

with the mean temperature definition to create the three simultaneous equations

$$h\bar{T} = \int_0^h T^0 \, dy, \tag{3.87}$$

which are then solved to give the coefficients of b_i^j for $i = 0$ as

$$b_0^0 = T_w \tag{3.88}$$

$$b_1^0 = -\frac{12T_w - 12\bar{T} + 2BT_a h - 6B\bar{T}h + 4BT_w h}{Bh^2 + 4h} \tag{3.89}$$

$$b_2^0 = \frac{6T_w - 6\bar{T} + 3BT_a h - 6B\bar{T}h + 3BT_w h}{h\left(Bh^2 + 4h\right)}. \tag{3.90}$$

At a first order approximation, the thermal equations are

$$T^1 = 0, \tag{3.91}$$

$$-BT^1 = \frac{\partial T^1}{\partial y}, \tag{3.92}$$

$$0 = \int_0^h T^1 \, dy, \tag{3.93}$$

which are solved to give the coefficients to $O(\varepsilon)$

$$b_0^1 = b_1^1 = b_2^1 = 0, \tag{3.94}$$

and therefore leads to $T^1 = 0$.

Having defined the radial velocity in terms of the azimuthal velocity components in (3.66), it is appropriate to substitute (3.69) and the calculated coefficients of a_i^j from (3.79), (3.80) and (3.81) to obtain the leading order radial velocity

$$v^0 = -\frac{\partial}{\partial s}\left(a_0^0\right) y - \frac{\partial}{\partial s}\left(a_1^0\right)\frac{y^2}{2} - \frac{\partial}{\partial s}\left(a_2^0\right)\frac{y^3}{3}. \tag{3.95}$$

The terms which are higher than $O\left(\varepsilon^0\right)$ are shown to be raised to $O\left(\varepsilon^2\right)$ in (3.65)

and are therefore assumed to be negligible as part of the thin film limit (3.50). The derivative terms in (3.95) may be resolved analytically, previously shown in the work of Kay et al. [15]. However, they may also be resolved numerically and this is detailed later in section 3.7.

The momentum equation of (3.65) contains a number of integrals with functions of u and v, while the energy equation (3.68) also contains integrals of u and T that all need evaluating. Therefore, in accordance with (3.50), the momentum integrals can be expressed as leading and first order integrals:

$$\int_0^h u^2 \, dy = \int_0^h \left(u^0\right)^2 \, dy + 2\varepsilon \int_0^h \left(u^0 u^1\right) \, dy + O\left(\varepsilon^2\right), \tag{3.96}$$

$$\int_0^h uv \, dy = \int_0^h \left(u^0 v^0\right) \, dy + O\left(\varepsilon\right), \tag{3.97}$$

$$\int_0^h \int_0^h u^2 \, dy \, dy - \int_0^h \int_0^y u^2 \, dy \, dy = \int_0^h y \left(u^0\right)^2 \, dy + O\left(\varepsilon\right), \tag{3.98}$$

and, by using the velocity coefficients previously calculated for u and v, these integrals are written as a number of functions, named as L^0, J^0, J^1, H^1, H^2, H^3 and P^0

$$\int_0^h \left(yu^0\right) \, dy = L^0, \tag{3.99}$$

$$\int_0^h \left(u^0\right)^2 \, dy + 2\varepsilon \int_0^h \left(u^0 u^1\right)^2 \, dy = J^0 + \varepsilon J^1, \tag{3.100}$$

$$-\varepsilon \int_0^h u^0 v^0 \, dy = \frac{\partial a_0^0}{\partial s} H^1 + \frac{\partial a_1^0}{\partial s} H^2 + \frac{\partial a_2^0}{\partial s} H^3, \tag{3.101}$$

$$\int_0^h y \left(u^0\right)^2 \, dy = P^0, \tag{3.102}$$

with the derivative terms being given as functions D^0 and D^1 and evaluated as

$$\left[\frac{\partial u^0}{\partial y} + \varepsilon \frac{\partial u^1}{\partial y} - \varepsilon y \frac{\partial u^0}{\partial y}\right]_0^h = D^0 + \varepsilon D^1. \tag{3.103}$$

These coefficients from (3.99) - (3.103) are functions which are dependent on the unknowns h and q

$$L^0 = a_0^0\frac{h^2}{2} + a_0^0\frac{h^3}{3} + a_0^0\frac{h^4}{4}, \tag{3.104}$$

$$J^0 = \left(a_0^0\right)^2 h + \left(a_1^0\right)^2 \frac{h^3}{3} + \left(a_2^0\right)^2 \frac{h^5}{5} + \left(a_0^0 a_1^0\right) h^2 + 2\left(a_0^0 a_2^0\right) \frac{h^3}{3} + \left(a_1^0 a_2^0\right) \frac{h^4}{2}, \tag{3.105}$$

$$J^1 = \left(a_0^0 a_0^1\right) h + \left(a_1^0 a_0^1\right) \frac{h^2}{2} + \left(a_2^0 a_0^1\right) \frac{h^3}{3} + \left(a_0^0 a_1^1\right) \frac{h^2}{2} + \left(a_1^0 a_1^1\right) \frac{h^3}{3} + \left(a_2^0 a_1^1\right) \frac{h^4}{4} + \left(a_0^0 a_2^1\right) \frac{h^3}{3} + \left(a_1^0 a_2^1\right) \frac{h^4}{4} + \left(a_2^0 a_2^1\right) \frac{h^5}{5} \tag{3.106}$$

$$H^1 = a_0^0\frac{h^2}{2} + a_1^0\frac{h^3}{3} + a_2^0\frac{h^4}{4}, \tag{3.107}$$

$$H^2 = a_0^0\frac{h^3}{6} + a_1^0\frac{h^4}{8} + a_2^0\frac{h^5}{10}, \tag{3.108}$$

$$H^3 = a_0^0\frac{h^4}{12} + a_0^0\frac{h^5}{15} + a_0^0\frac{h^6}{18}, \tag{3.109}$$

$$P^0 = \left(a_0^0\right)^2 \frac{h^2}{2} + \left(a_1^0\right)^2 \frac{h^4}{4} + \left(a_2^0\right)^2 \frac{h^6}{6} + 2\left(a_0^0 a_1^0\right) \frac{h^3}{3} + \left(a_0^0 a_2^0\right) \frac{h^4}{2} + 2\left(a_1^0 a_2^0\right) \frac{h^5}{5}, \tag{3.110}$$

$$D^0 = 2a_2^0 h, \tag{3.111}$$

$$D^1 = 2a_2^1 h - a_1^0 h - 2a_2^0 h^2. \tag{3.112}$$

The momentum equation of (3.65) may therefore be written

$$\varepsilon Re\left[\frac{\partial q}{\partial t} - \varepsilon\frac{\partial L^0}{\partial t} + \frac{\partial J^0}{\partial s} + \varepsilon\frac{\partial J^1}{\partial s} + \frac{\partial a_0^0}{\partial s}H^1 + \frac{\partial a_1^0}{\partial s}H^2 + \frac{\partial a_2^0}{\partial s}H^3 + \varepsilon\frac{\partial P^0}{\partial s}\right] = \frac{\varepsilon^3}{Ca}\left[h\frac{\partial^3 h}{\partial s^3} + h\frac{\partial h}{\partial s}\right] - \varepsilon\lambda\cos s h\frac{\partial h}{\partial s} + D^0 + \varepsilon D^1 - \left[h - \varepsilon h^2\right]\lambda\sin s. \tag{3.113}$$

The integrals found within the energy equation (3.68) may also be expressed to leading and first order

$$\int_0^h uT\ dy = \int_0^h \left(u^0T^0\right)\ dy + \varepsilon \int_0^h \left(u^1T^0\right)\ dy + O\left(\varepsilon^2\right),$$
$$\left[(1-\varepsilon y)\frac{\partial T}{\partial y}\right]_0^h = \left[\frac{\partial T^0}{\partial y} + \varepsilon\frac{\partial T^1}{\partial y} - \varepsilon y\frac{\partial T^0}{\partial y}\right]_0^h + O\left(\varepsilon^2\right),$$
$$\varepsilon^2 T\frac{\partial^2 h}{\partial s^2} + 2\varepsilon^2\frac{\partial T}{\partial s}\frac{\partial h}{\partial s} = \varepsilon^2 T^0\frac{\partial^2 h}{\partial s^2} + 2\varepsilon^2\frac{\partial T^0}{\partial s}\frac{\partial h}{\partial s} + O\left(\varepsilon^3\right). \tag{3.114}$$

These integral expressions can be expressed as functions of the temperature and velocity coefficients a_i^j and b_i^j, and are given as Q^0, F^0, F^1, M^0 and M^1,

$$\int_0^h \left(yT^0\right)\ dy = Q^0,$$
$$\int_0^h \left(u^0T^0\right)\ dy + \varepsilon\int_0^h \left(u^1T^0\right) dy = F^0 + \varepsilon F^1,$$
$$\left[\frac{\partial T^0}{\partial y} + \varepsilon\frac{\partial T^1}{\partial y} - \varepsilon y\frac{\partial T^0}{\partial y}\right]_0^h = M^0 + \varepsilon M^1. \tag{3.115}$$

These functions will be dependent on the unknown variables h, q and $\bar{T}$ as

$$Q^0 = b_0^0\frac{h^2}{2} + b_1^0\frac{h^3}{3} + b_2^0\frac{h^4}{4}, \tag{3.116}$$
$$\begin{aligned} F^0 = {} & \left(a_0^0b_0^0\right)h + \left(a_1^0b_0^0\right)\frac{h^2}{2} + \left(a_2^0b_0^0\right)\frac{h^3}{3} + \left(a_0^0b_1^0\right)\frac{h^2}{2} + \left(a_1^0b_1^0\right)\frac{h^3}{3} \\ & + \left(a_2^0b_1^0\right)\frac{h^4}{4} + \left(a_0^0b_2^0\right)\frac{h^3}{3} + \left(a_1^0b_2^0\right)\frac{h^4}{4} + \left(a_2^0b_2^0\right)\frac{h^5}{5}, \end{aligned} \tag{3.117}$$
$$\begin{aligned} F^1 = {} & \left(a_0^1b_0^0\right)h + \left(a_1^1b_0^0\right)\frac{h^2}{2} + \left(a_2^1b_0^0\right)\frac{h^3}{3} + \left(a_0^1b_1^0\right)\frac{h^2}{2} + \left(a_1^1b_1^0\right)\frac{h^3}{3} \\ & + \left(a_2^1b_1^0\right)\frac{h^4}{4} + \left(a_0^1b_2^0\right)\frac{h^3}{3} + \left(a_1^1b_2^0\right)\frac{h^4}{4} + \left(a_2^1b_2^0\right)\frac{h^5}{5}, \end{aligned} \tag{3.118}$$
$$M^0 = 2b_2^0h, \tag{3.119}$$
$$M^1 = 2b_2^1h - b_1^0h - 2b_2^0h^2. \tag{3.120}$$

The energy equation (3.68) is then written as

$$\varepsilon Pe\left[\frac{\partial}{\partial t}\left(h\bar{T}\right)-\varepsilon\frac{\partial Q^0}{\partial t}+\frac{\partial F^0}{\partial s}+\varepsilon\frac{\partial F^1}{\partial s}\right]= M^0+\varepsilon M^1+\varepsilon^2\frac{\partial^2}{\partial s^2}\left(h\bar{T}\right)-\varepsilon^2 T^0|_h\frac{\partial^2 h}{\partial s^2}-2\varepsilon^2\frac{\partial T^0|_h}{\partial s}\frac{\partial h}{\partial s}. \quad (3.121)$$

The mathematical derivation of the depth-averaged governing equations have now been completed. The model includes many physical effects found in a bearing chamber, such as inertia and includes the important partial slip boundary condition on the cylinder wall.

3.7 Numerical Methods

This section details procedures which have been used to solve the mathematical model developed in this Chapter, represented by the continuity(3.61), energy (3.121) and momentum (3.113) equations. This system of equations contains spatial and temporal derivatives, therefore methods to discretise these derivatives are necessary to obtain solutions to the unknown variables, $h\left(s,t\right)$, $q\left(s,t\right)$ and $\bar{T}\left(s,t\right)$. The techniques used to discretise the domain and time into small portions are given in this section.

3.7.1 Spatial Discretisation

There are numerous methods to approximate spatial derivatives, one of the most familiar will be the finite difference method. The main aspect of spatial discretisation is to disperse nodes throughout the domain. These nodes contain solution information and can be homogenously distributed. However, for this thesis a pseudo-spectral method has been used due to its high level of accuracy. The key difference between these two methods is finite difference acts on a narrow spatial region of these nodes while spectral methods are a global scheme and use every node. The pseudo-spectral method used in this thesis is based on Fourier transforms, creating differentiation matrices which can be directly applied to the derivative functions. The book *Spectral Methods in MATLAB* by Trefethen [176] goes into detail about spectral methods, offering valuable specifics about practical implementation in the MathWorks MATLAB software package.

The advantage of using the Fourier spectral method is that while the cost of solving with a dense matrix is greater than with a sparse matrix, the rate of convergence is significantly faster. This is shown in figure 3.3, where a fourth-order finite difference approximation is compared to the Fourier spectral method in

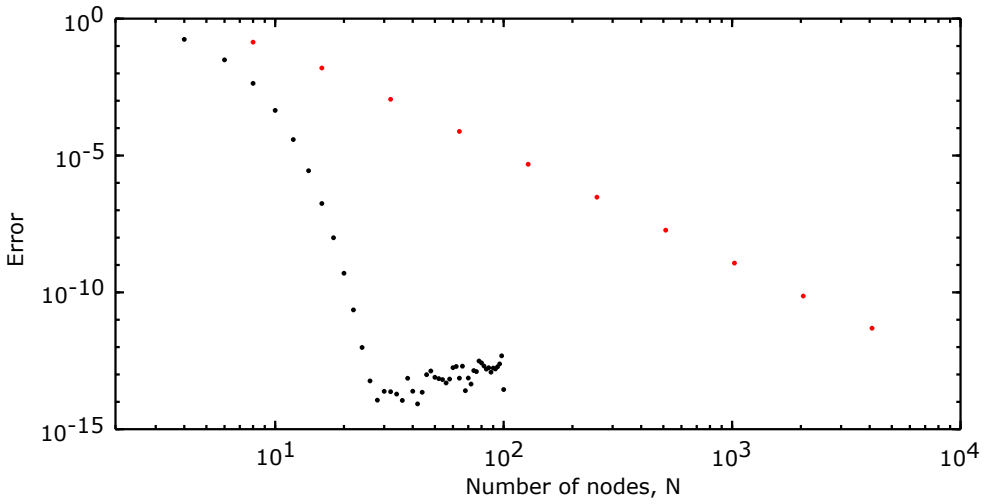


Figure 3.3: The numerical convergence of a fourth order finite difference scheme in *red* and the numerical scheme of this thesis in *black* in approximating the derivative of $e^{cos(x)}$.

approximating the derivative of $e^{cos(x)}$. It is clear that the fourth-order finite difference approximation has a convergence rate of only $O(N^{-4})$, necessitating a high N count to achieve a good level of accuracy. However, the convergence of the spectral method is much greater, typically to $O(N^{-m})$, with the value of m being dependent upon the function smoothness and order of approximation. Therefore, fewer nodes are necessary to achieve equal or greater accuracy in approximating derivative functions.

As depth-averaging has made the problem one-dimensional, only the azimuthal direction needs to be discretised, so nodes only need to be distributed in $s \in [-\pi, \pi]$. The initial Fourier differentiation matrices place a defined number of nodes, N in the temporary domain of $\eta \in [-1, 1]$. This mesh can be transformed with stretching functions, for this thesis a hyperbolic sine function has been used, however other functions which are relevant to the problem being solved may be used. The hyperbolic sine function was chosen for its characteristic of clustering nodes in the domain centre to help capture the film profiles accurately and is given as

$$f(\eta) = \frac{\pi \sinh(c\eta/\pi)}{\sinh(c)}. \tag{3.122}$$

The meshing parameter, c is introduced to control the distribution of nodes within $s \in [-\pi, \pi]$. As the meshing parameter gets larger, $c > 1$, the nodes are increasingly clustered symmetrically towards the domain centre. To create a uniformly distributed mesh, the meshing parameter must be set to $c = 1$. In most cases, the meshing parameter has been set to 1.3 to improve the node

clustering where capillary ripples form. With the mesh transformed onto $s \in [-\pi, \pi]$, the differentiation matrices need to be transformed onto the domain. The transformation method is outlined by Boyd [177], with the general transformation functions given as

$$\frac{d}{ds} = \frac{1}{f}\left[\frac{d}{d\eta}\right], \tag{3.123}$$

$$\frac{d^2}{ds^2} = \frac{1}{f^3}\left[\dot{f}\frac{d^2}{d\eta^2} - \ddot{f}\frac{d}{d\eta}\right], \tag{3.124}$$

$$\frac{d^3}{ds^3} = \frac{1}{f^5}\left[\left(\dot{f}\right)^2\frac{d^3}{d\eta^3} - \left(3\dot{f}\ddot{f}\right)^2\frac{d^2}{d\eta^2} + \left(3\left(\ddot{f}\right)^2 - \left(\dot{f}\dddot{f}\right)\right)\frac{d}{d\eta}\right]. \tag{3.125}$$

The functions $\dot{f}$, $\ddot{f}$ and $\dddot{f}$ being defined as the derivatives of $f(\eta)$ with respect to η. The Fourier spectral method works on periodic domains, so with the ends of the cylindrical domain defined as

$$h(-\pi) = h(\pi), \qquad q(-\pi) = q(\pi), \qquad \bar{T}(-\pi) = \bar{T}(\pi), \tag{3.126}$$

the periodicity requirement is satisfied neatly.

A second transformation has been applied to the domain, using a shifting parameter, β, therefore the domain centre can be moved to be higher up either side of the cylinder wall. This transformation is only utilised in Chapter 6, to improve the mesh resolution around waves with particularly small wavelengths. The transformation function is given as

$$f(s+\beta) = f(s) + \beta. \tag{3.127}$$

The spacing between each node remains the same, as the shift is a linear transition, therefore it is not necessary to transform the differential matrices with respect to β as $\dot{f}(s+\beta) = 1$ and $\ddot{f}(s+\beta) \equiv \dddot{f}(s+\beta) \equiv 0$.

With the domain now split into small sections, the integral of the filling fraction equation (3.60) needs to be approximated. For this thesis, the trapezium rule has been used and is defined as

$$A = \frac{\varepsilon}{\pi}\int_{-\pi}^{\pi} h\, ds = \frac{\varepsilon}{2\pi}\sum_{i=1}^{N}\left(h_i + h_{i+1}\right)\Delta s_i. \tag{3.128}$$

This equation can be used to ensure a steady-state film, the rate of convergence is $O(N^{-2})$ and necessitates a high number of nodes to achieve a good level of accuracy.

3.7.2 Temporal Discretisation

The temporal derivatives may be approximated by dividing the time into discrete steps, Δt and approximating the next step in the solution. This can be used to march the solution forward in time to simulate transient solutions. There are explicit and implicit methods to express the time derivative, for this thesis a first order implicit method has been used, where

$$\frac{\phi^{n+1} - \phi^n}{\Delta t} = F(\phi). \tag{3.129}$$

The implicit method is always stable for any value of Δt. However, small values of Δt are required to capture the fluid motion accurately and is typically monitored by the Courant number, which is defined as

$$C = \frac{u\Delta t}{\Delta s} \leq C_{max}. \tag{3.130}$$

The implicit method means larger values of C_{max} can be tolerated, but for the work in this thesis the time step size is typically $\Delta t \leq 0.01$.

3.7.3 Programming the Algorithms

The numerical algorithms to approximate the governing equations may be implemented in any programming language. For this thesis, this has been the MathWorks software package MATLAB. These programs are typically referred to as solvers and are split into two types, the steady-state and transient solvers. The first assumes the flow has reached a steady situation while the second marches the solution in time and is not necessarily steady.

These solvers require several equations to determine several unknown variables (h, q and $\bar{T}$), the number needed is dependent on if either the steady or transient solver is being used. Both steady and transient solvers solve the momentum equation (3.113) at each node. Therefore, there are N number of equations to be solved. For the steady solver, the filling fraction equation (3.128) presents only 1 equation which needs to be solved for the domain, whilst the continuity equation (3.61) needs to be solved at every node and is an additional N equations. The energy equation (3.121) also needs to be solved at every node for the film's thermodynamics, so is N equations to be solved.

The steady state solver gives solutions to h and $\bar{T}$ at each node and a single value of q for the domain, which is $N + 1$ unknowns for the isothermal model and $2N + 1$ for the non-isothermal model. The transient solver gives solutions for h, q and $\bar{T}$ at each node, which is $2N$ unknowns for the isothermal model and $3N$ for the non-isothermal model.

These solvers have been developed in purposefully built MATLAB scripts, where solutions to the non-linear equations are approximated with the inbuilt non-linear function solver *fsolve*. There are many criteria and options available to calculate the solutions, where the aim is to minimise the equation residuals so that

$$F\left(\phi^i\right) \leftarrow 0. \tag{3.131}$$

This is done by starting with an initial solution value, ϕ^0 which is used to calculate a better approximation within *fsolve*, giving the solution ϕ^1. This is repeated until the ϕ^i solution satisfies (3.131).

3.7.4 Computational Resources

The algorithms of this thesis were performed on a Windows 7 64-bit operating system using the MathWorks software package MATLAB versions R2017b and R2019a. The processor was an Intel Xeon E5-1620 v3 (8 Cores) CPU running at 3.50GHz with 32Gb of RAM. The time for each simulation was dependent upon the number of nodes, N being used in the simulation, but each simulation typically took several minutes. However, for the work in Chapter 6 the very large mesh of $N = 5,000$ took several hours to run until a steady solution was obtained.

A standard floating-point number incurs some rounding when being processed by a computer, normally these are described as a single precision or double precision number. A single precision number is broken into 3 parts, the sign (1 bit), the exponent (8 bits) and the remaining 23 bits are used for the fraction. For a double precision number, the first 12 bits store the sign and exponent information, while the remaining 52 bits store a greater amount of information on the fractional part. This means that a single floating-point number has an accuracy of only 6 to 9 significant figures, while the double floating-point precision has an accuracy of 15 to 17 significant figures. The default setting of MATLAB is to use double precision for storing floating-point values using 8 bytes of data per number.

3.7.5 Solver Convergence

The computer model has two types of criteria that must be adhered to in order to determine solutions. The two criteria are as follows, monitoring the transient solver to determine when it is steady. Secondly, when the iterative procedures can be stopped. The first criteria determines if the solution of the transient solver may be assumed to be steady, this is done by checking the absolute error between

the solution values at time step i and $i-1$. If this error is lower than the specified threshold of $1e^{-10}$, the solution is determined to be steady.

The criteria to stop the iterations of *fsolve* encompasses two main parts, these are the maximum number of iterations that may be performed and the difference between iteration steps. The maximum number of iterations that can be performed for the steady solver is $N * 20$. For example, if $N = 1,000$, there may be up to $20,000$ iterations until the solver stops iterating and the solution has failed to converge. The second part measures the change in the solution between iteration steps, where the absolute difference between solutions at each node must be lower than the limit of $1e^{-20}$. There are additional settings which have been changed from the default values of *fsolve* to ensure these criteria will be met. All the results presented in this thesis have either met the convergence criteria outlined in this sub-section or is explicitly stated.

3.8 Chapter Summary

In this Chapter, a set of integral equations which represents the conservation of mass, momentum and energy has been derived from the Navier-Stokes equations for a rimming flow. The review of literature concluded that hydrostatic pressure and surface tension are both important physical effects for rimming flows, while the inclusion of inertia and thermal convection are considered important for the high-speed flows found within the bearing chamber. By applying a thin film approximation to the governing equations, these effects may all be retained within the model, especially those of inertia and convection as moderate Reynolds and Péclet numbers are permitted. Notably, the derivation in this thesis includes the partial slip boundary condition to assess how slip changes the film profiles.

This method of depth-averaging means that the surface boundary conditions may be directly applied to the governing equations, while also introducing a set of mean flow values which replace the full temperature and velocity fields. This technique also reduces the spatially two-dimensional problem into only one-dimension, greatly simplifying the non-linear equations which need to be solved. The full velocity and temperature profiles will be reconstructed from the mean values by an *a priori* selection of polynomials which represent the complete profile.

The model of this Chapter is approximated by a pseudo-spectral method using a clustered domain discretisation which can be used to increase the node density in areas of interest. While there are relevant validation studies which are presented at the beginning of each Chapter, the criteria in determining solver convergence and mesh independence of the steady-state and transient solvers are outlined. These are determined to be appropriate in minimising numerical error.

Chapter 4

Isothermal Thin Film Rimming Flow Driven by Surface Shear

The work in this Chapter has been published in the peer reviewed journal paper of Nicholson et al. [178], though Section 4.7 has not yet been published. The content of this Chapter primarily focuses on the fluid dynamics of the proposed model, using the dimensionless parameters to thoroughly analyse the role that fluid slip has on the developing film profiles. The initial focus is on the change to the classical lubrication theory and fundamental changes due to slip occurring within the cylinder and how including higher order effects can develop solutions that do not exist in lubrication theory.

The flow is assumed to be isothermal in this Chapter, so the governing equations of the flow are (3.113), (3.61) and (3.128). Each section investigates flows where one parameter is typically dominant, such as gravitational or inertial effects, in addition detailing how slip lengths of different sizes effect the flow. With inclusion of inertia equal to leading order effects, the investigation into moderate Reynolds numbers has been performed using both a proportional filling fraction, A and a constant filling fraction to investigate how the flow changes when inertia and fluid slip interact.

4.1 Film Profiles within Classical Lubrication Theory Framework

This Section focuses on the classical lubrication theory limit, which within $\varepsilon \ll 1$ leads to a gravity - viscosity balance in the film with all other forces (inertia, surface tension, pressure gradients) neglected. In this case the governing equation of (3.53) with the partial slip boundary condition reduces to:

$$h^3\frac{\lambda\sin s}{3} - h^2\left(\frac{\tau}{2} - l_s\lambda\sin s\right) - hl_s\tau + q = 0. \tag{4.1}$$

This equation is important as the additional forces which are neglected can be considered as perturbations, so that a lot about the film behaviour can be determined from it. It is also algebraic rather than differential so can be analysed simply. Analysis of (4.1) was first carried out by Moffatt [31] and later by Johnson [23] for the case of a rotating cylinder with no-slip conditions. By exploiting the boundedness of the sine function they determined that the film flow was separated into three regimes corresponding to flows below, at and above a critical value of height and flow rate (flux) which correspond to the values of h and q at $s = \pi/2$. Upon treating λ and τ as constant values, the depressed cubic equation (4.1) is readily solvable with the slip condition included, and the critical values are:

$$h_c = \frac{\tau - 2l_s\lambda}{2\lambda} + \frac{\sqrt{\tau^2 + 4l_s^2\lambda^2}}{2\lambda}, \tag{4.2}$$

$$q_c = -h_c^3\frac{\lambda}{3} + h_c^2\left(\frac{\tau}{t} - l_s\lambda\right) + h_c l_s\tau. \tag{4.3}$$

Typically, the critical flux q_c is used as the parameter to distinguish between the regimes, though h_c can also be appropriate. With a no-slip boundary condition ($l_s = 0$), (4.3) yields the well-known critical film flux for a shear driven flow of $q_c = \tau^3/(6\lambda)^2$ and the critical film height $h_c = \tau/\lambda$ which was reported by Kay et al. [14], Williams et al. [175], Williams [179] and Villegas-Díaz et al. [36]. An asymptotic analysis for an increasing slip length demonstrates that the critical film height tends towards $h_c = \tau/2\lambda$ and the critical flux approaches $q_c = \infty$ in an idealized model where there is no surface shear due to infinite slip. The three distinct classifications of film profiles for a specified film flux are termed as sub-critical, critical and super-critical, defined as:

1. Sub-Critical Case, $q < q_c$. Two branches of real and positive solutions exist. One branch represents a completely wetting solution across the entire domain, in which the cylinder is completely coated in fluid. The second branch represents a non-physical solution in the region $0 \leq s \leq \pi$, with an unbounded film height at the limits of this region.

2. Critical Case, $q = q_c$. The previously mentioned two branches converge at the point $s = \pi/2$, forming a completely wetting solution branch connected to an unbounded solution that exists within $0 \leq s \leq \pi$. At this value of the film flux, the film height forms a peak known as the critical film height, h_c and provides the maximum fluid loading for a continuous profile under the

Slip length, l_s	Film height, h_c	Film flux, q_c	Filling fraction, A_c
0	1	0.1667	0.1258
0.001	0.999	0.1667	0.1256
0.01	0.9901	0.1667	0.1238
0.1	0.9099	0.171	0.1088
1	0.6180	0.3484	0.0682
$\vdots$	$\vdots$	$\vdots$	$\vdots$
∞	0.5	∞	0.0561

Table 4.1: The effects of increasing slip length, l_s on the critical film values, h_c, q_c and A_c.

lubrication approximation, defined as the critical filling fraction, A_c.

3. Super-Critical Case, $q > q_c$. No solutions exist in this regime where fluid completely coats the cylinder's internal surface for classical lubrication theory. Two solution branches exist with a disconnected region located around $s = \pi/2$ in which no real and positive film solution can exist. Inclusion of higher order effects has been shown to bridge this discontinuous region outside of the typical lubrication theory assumptions.

Within these classifications, a single physical solution exists in the region $s \in [-\pi, 0]$, while for $s \in [0, \pi]$, the solution is dependent upon the ratio of q/q_c with physical, unbounded or discontinuous solutions existing. These classical lubrication theory solutions are shown in figure 4.2 along with film profiles where inertial effects are assumed to be equal to leading order terms and is shown to form a fully coated rimming flow.

The variation in critical values with increasing slip lengths are given in table 4.1. As the slip length increases, the effects on the critical film values asymptotically approach their limiting values. The inclusion of a wall slip is found to limit the maximum sustainable filling fraction to half of the value in a no-slip case. It should be noted that for a fixed filling fraction A or film flux q, an increasing slip length l_s alters the transition from sub-critical to super-critical cases, as discussed in the next Section. It is shown that the diminishing critical film height h_c becomes is significant when $l_s \sim O(\varepsilon)$, as shown in figure 4.1 (a), closely matching the trend for the critical fill fraction A_c, as shown in figure 4.1 (c). In contrast, the film flux is shown to exponentially increase with l_s in figure 4.1 (b).

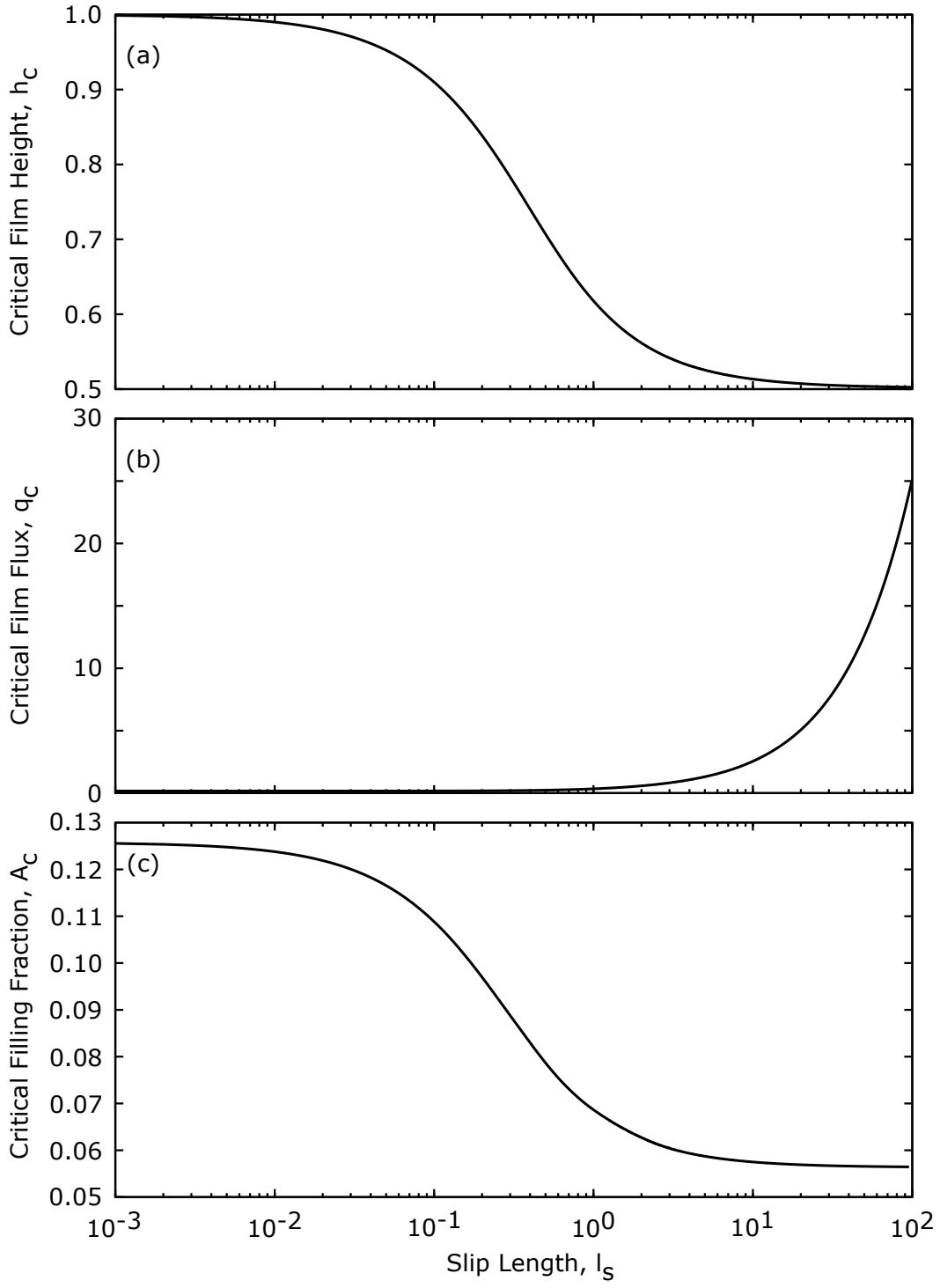


Figure 4.1: The effect of slip length, l_s on the critical film values under classical lubrication theory, as calculated from (4.1) with h_c in (a), q_c in (b) and A_c in (c).

4.2 Film Profiles in Comparison to Classical Lubrication Theory

In accordance with classical lubrication theory, the existence of fully coating flows beyond $q > q_c$ are introduced by higher order effects when taking surface tension to be of first order, such that $\varepsilon^3/Ca \sim O(\varepsilon)$. This provides a smoothing effect, bridging across the non-physical solution region in the super-critical profile as detailed by Benilov et al. [44] and Kay et al. [14]. This smoothing means physical solutions for a completely wetting film can be found even when the film is within the defined super-critical realm, as shown in figure 4.2 (c), whereas classical lubrication theory predicts a non-physical region. The presence of solutions within the super-critical class allows for the presence of shock-type solutions to be explored. This is categorised by a film profile that occurs on the smooth solution with a peak, typically located on the cylinders rising side that connects to the unbounded solution found in sub-critical cases as in figure 4.2 (a). The addition of inertial effects has smoothed the peak film height, shown at the critical film profile of figure 4.2 (b), with the solution branches intersecting.

4.3 Stronger Gravitational Effects with Negligible Inertia

In treating the inertial effects as negligible, films with filling fractions equating to $A > A_c$ are explored. For flow driven by the cylinder rotation, Ashmore et al. [49] studied the effect of gravity-dominated solutions in the formation of pooling films. They varied the equivalent parameter of λ for the ratio of gravitational to viscous forces. Next, the effect of gravity on film profiles with slip are studied. At the first instance, the slip values are chosen to be small to obtain film heights which are comparable to those by Ashmore et al. [49]. As noted previously, increasing λ transitions the film profile from a smooth rimming flow towards a deepening pool solution at the cylinder base. In accounting for the differences of rotational and shear driven flow, the film profiles in figure 4.3 were found to be comparable to Ashmore et al. [49] for both high and low gravitational effects.

When the gravitational effects are weak ($\lambda = 1 - 2$), the film is shown to spread relatively uniformly across the cylinder, as in figure 4.3. When $\lambda > 5$ however, we observe a solution pooling deeply at the bottom, where much of the film coating the cylinder becomes very thin. Therefore, the effect of slip is expected to be substantial in the latter case. In the next Section we will investigate how an increasing slip length influences the transition from a smooth profile to a

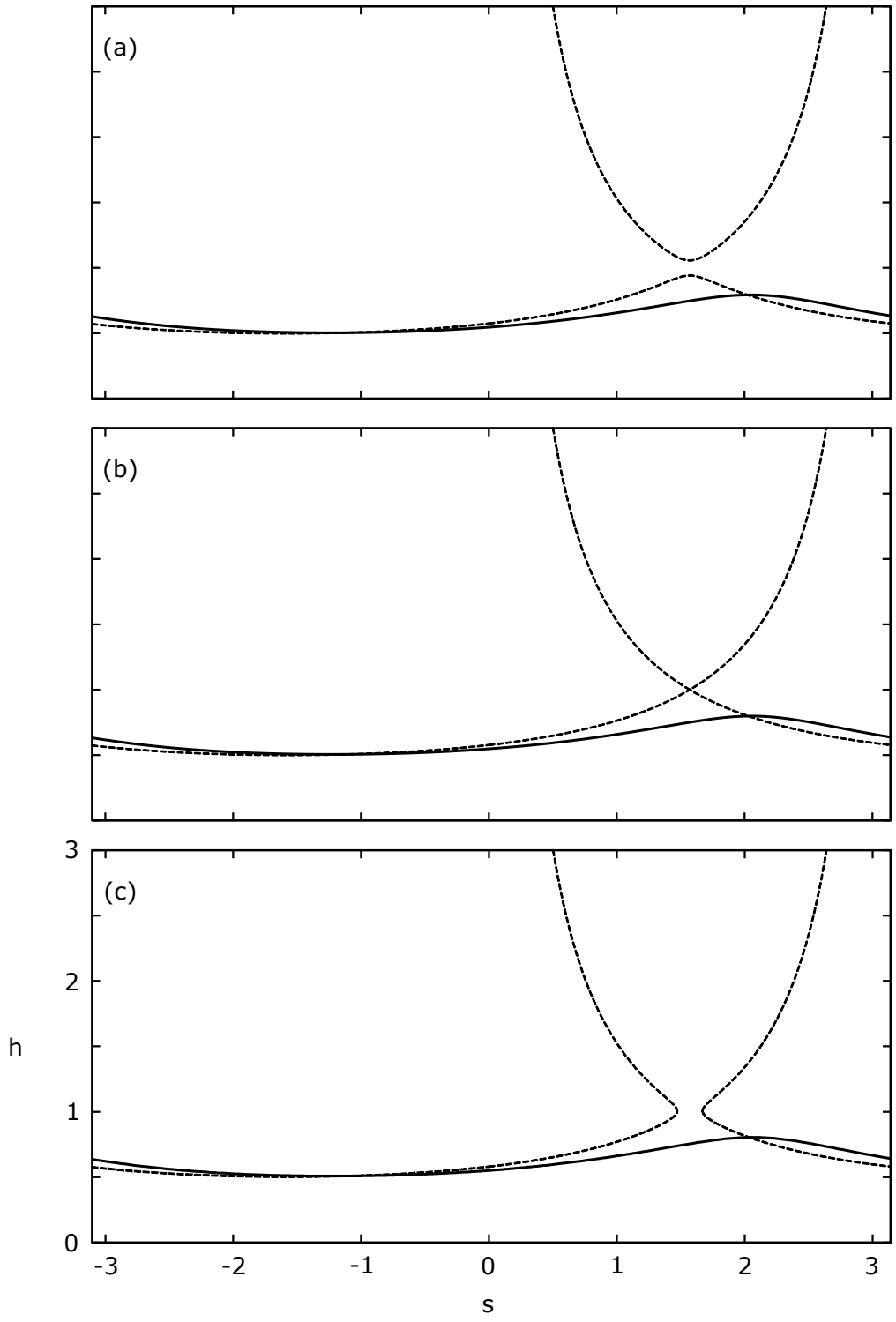


Figure 4.2: The three possible regimes of sub-critical (a), critical (b) and super-critical (c) film profiles for; $\lambda = 1$, $\tau = 1$, $l_s = 0$, $Re^* = 30$, $\varepsilon = 10^{-2}$, $Ca = 10^{-3}$. The unbounded solutions are shown in parts (a) and (b), while the non-physical region is shown in part (c). With *dotted* lines indicating solutions to (4.1) and *solid* lines as solutions to the coupled equations of (3.113), (3.61) and (3.60).

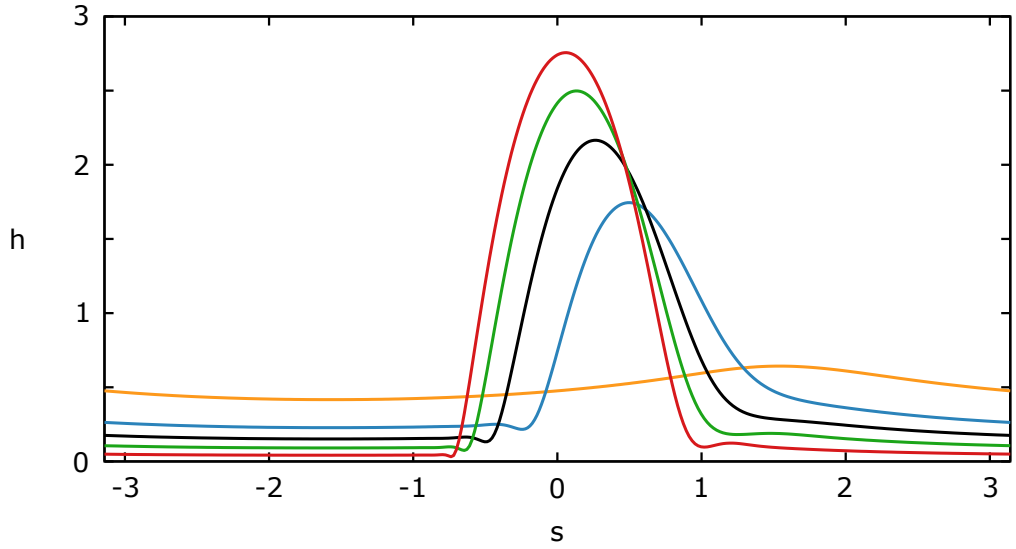


Figure 4.3: Profiles for increasing gravitational forces for; $\tau = 1$, $\varepsilon = 0.1$, $Re^* = 10^{-3}$, $Ca = 0.1$, $A = 0.1$ and $l_s = 0.01$. With the coloured lines given as *orange* for $\lambda = 1$, *blue* for $\lambda = 2$, *black* for $\lambda = 3$, *green* for $\lambda = 5$ and *red* for $\lambda = 10$.

pooling solution.

Typically, when there are higher film heights around the cylinder base; the solutions are known as pooling films. These films will have a recirculation region, which is shown in figure 4.4 and matches the film profile of figure 4.3 (b) with $\lambda = 3$. The bulk of moving fluid from the thin region is driven over the recirculation region by the applied air shear at the surface.

4.4 The Balancing of Slip and Gravity

We will now look at how the transition between smooth and deeply pooled solutions (presented in figure 4.3) are affected by the slip length. The film profiles for slip lengths up to $O(1)$ are summarised within figure 4.5. With an equal balance of gravitational to viscous forces ($\lambda = 1$), shown in figure 4.5 (a), the film profile shows minor changes between $l_s = 0.01$ and $l_s = 0.1$. We observe a slight thinning of the film outside of $0 < s < \pi$, with the fluid mass accumulating into a raised peak observed at $s = \pi/2$. When the slip length increases towards a near drag free setting of $l_s = 1$, a substantial thinning of the film is observed, with a reduction of the thickness up to half of that reported with $l_s = 0.01$, and a significant deepening of the film for $0 < s < \pi/2$, highlighting the importance of surface effects at $l_s \sim O(1)$.

Figure 4.5 (b) shows the same collection of film profiles with different l_s, but with a relatively stronger gravitational force ($\lambda = 2$). Here, we obtain a pooled

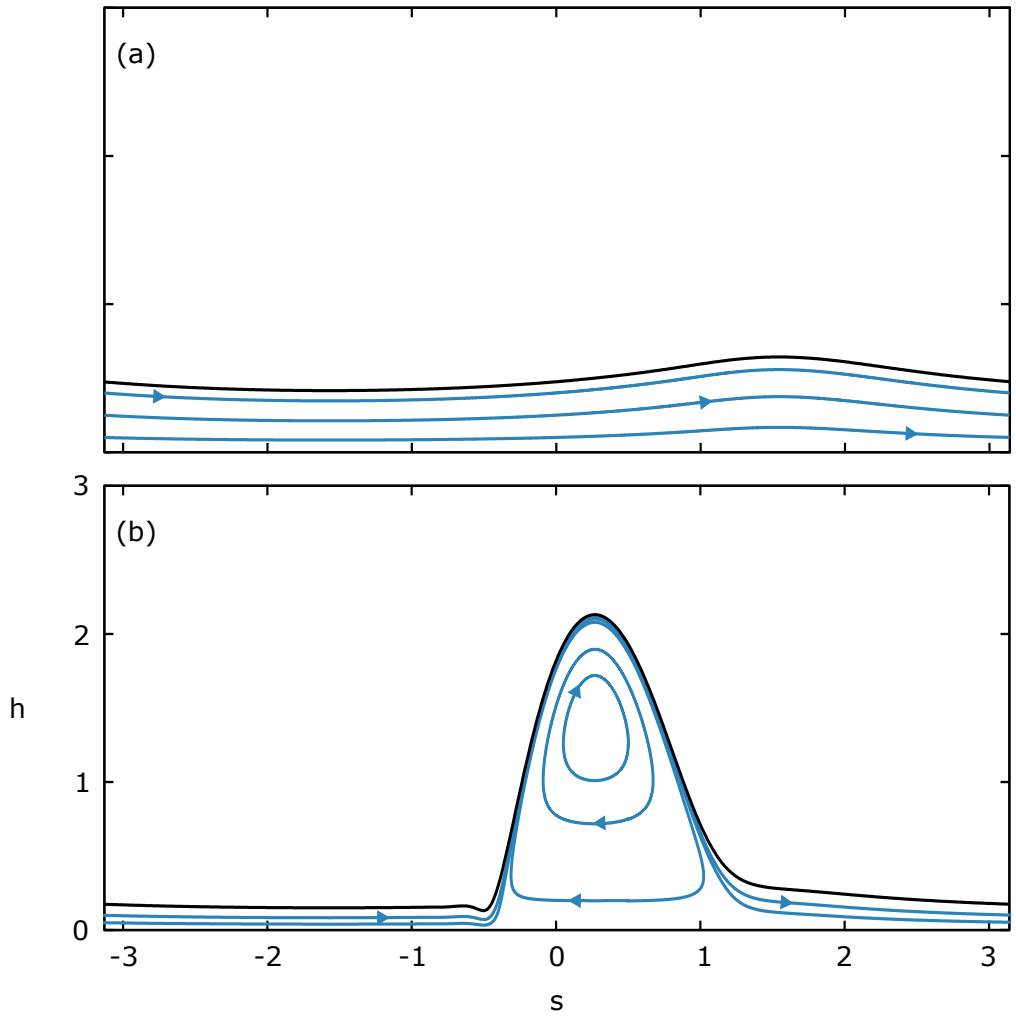


Figure 4.4: Streamlines of pooled and smooth solutions, for $\lambda = 1$ in (a) and $\lambda = 3$ in (b), showing the fluid recirculation of the solutions presented in figure 4.3.

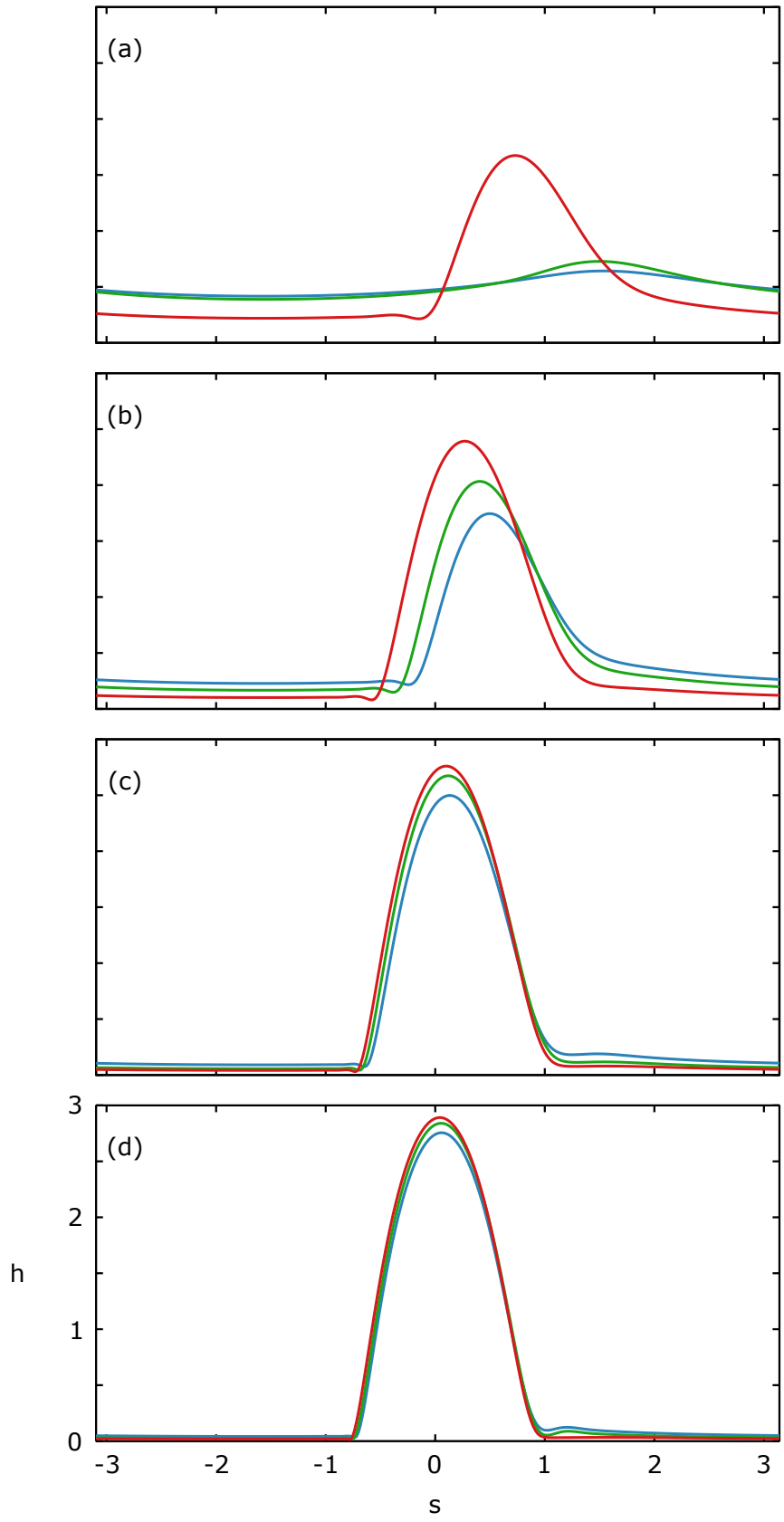


Figure 4.5: Changes to gravity dominate flows due to slip, for $\varepsilon = 0.01$, $Re^* = 0$, $Ca = 10^{-3}$, $A = 0.1$. Where λ is 1 in (a), 2 in (b), 5 in (c) and 10 in (d). Coloured lines represent $l_s = 0.01$ in *blue*, $l_s = 0.1$ in *green* and $l_s = 1$ in *red*.

solution for all slip lengths, however increasing l_s results in a significant thinning of the film in areas of uniform film height (for $-\pi/4 > s$ and $s > \pi/2$). The pooling of fluid within the domain is attributed to the fixed filling fraction, thereby resembling a pooling solution even at low gravitational forces. In Section 4.1, the largest changes to critical film values are found around $O(\varepsilon)$, with figure 4.5 $(a) - (b)$ demonstrating a significant divergence from the previous profiles as l_s transitions beyond $O(\varepsilon)$. Larger slip lengths furthers the thinning of the flow profile and leads to a large pool within the weak gravity regime. It is within the limit of $Re^* \ll 1$ and $\lambda \leq 5$ that the most significant effects of wall slip are found, where even small slip lengths of $l_s \sim O(h^*)$ result in significant pooling and thinning of the flow.

For very large λ, the subsequents effect of l_s are shown to diminish. At $\lambda = 10$, even the longer slip lengths of $l_s \sim O(1)$ create negligible changes in the film profile. This is due to the overwhelmingly strong gravitational forces affecting the flow, which results in exceedingly low film heights across the domain outside of the pool found at $-1 < s < 1$.

The filling fraction is fixed so that $A > A_c$ means all cases were a super-critical film, which were possible due to surface tension, allowing for deeply pooled and shock formations to exist.

4.5 Transitioning to Smooth Solutions with Inertia

It is within the realm of $A > A_c$ that the most interesting features can be explored for solutions subject to inertia undefined by lubrication theory. Previous studies have highlighted the effects of increased inertia with the no-slip condition, rich features on film solutions are presented by Kay et al.[14] and Benilov and O'Brien [52]. In exploring the parameter space of the reduced Reynolds number, Re^* and corresponding film flux, q, differences due to the addition of slip at varying lengths can be evaluated against the no-slip condition, as encapsulated in figure 4.6. The influence of slip length on the critical filling fraction A_c means that when maintaining the necessary ratio of A/A_c for comparable results on the flux ratio q/q_c, the volume of fluid A reduces between the no-slip and partial slip profiles.

It is possible to summarise the typical behaviour of a rimming flow with a no-slip condition on the wall when maintaining a filling fraction of $A > A_c$ for several distinct levels of inertia as depicted in figure 4.7 (which are comparable in shape to the films with a slip length of $l_s = 0.01$, shown in figure 4.9). If the inertial effects are relatively weak, e.g. $Re^* = 0.01$, what is typically referred to as

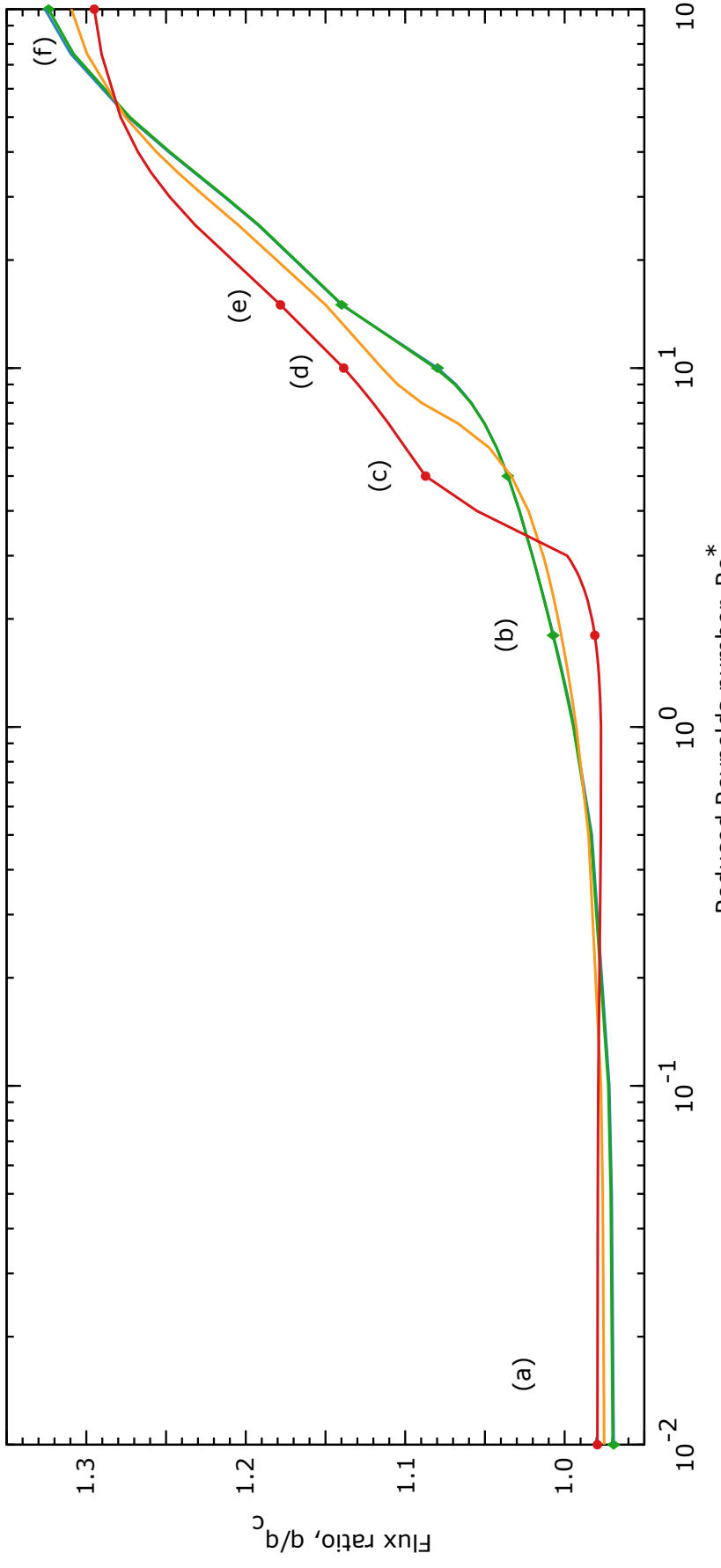


Figure 4.6: Effect of increasing Re^* with and without slip: $l_s = 0$ *blue* and $l_s = 0.01$ *green*, $l_s = 0.1$ in *orange* and *red* for $l_s = 0.2$, with $\tau = 1$, $\lambda = 1$, $Ca = 10^{-3}$, $\varepsilon = 10^{-2}$ and $A/A_c = 1.073$. The points correspond to: $Re^* = 0.01$, $Re^* = 1.8$, $Re^* = 5$, $Re^* = 10$, $Re^* = 15$, $Re^* = 20$ and $Re^* = 100$, with solutions found in figures 4.7 and 4.8.

a pooling film develops, shown in figure 4.7 (a). In this pooling film a recirculation region can be found with an adjacent hump that arises as a consequence of surface tension which stabilises the film. Moreover, the solutions that exist within the limit $q/q_c < 1$ of figure 4.6 will all contain a pool of fluid on the rising cylinder wall, shown in either figure 4.7 (a) or figure 4.8 (b). Stronger inertial effects will lead to the eventual smoothing of the flow into a uniform profile, see the profile of figure 4.7 (f) with $Re^* = 100$.

However, as Re^* increases through low to moderate values, the solitary hump grows in the region ahead of the sharp front until the area is dominated by small wavelength disturbances as a consequence of surface tension. These surface waves grow rapidly in amplitude with Re^* until they are eventually suppressed due to the dominating effects of inertia. These small wavelength disturbances, identified as capillary waves, are most prominent for $Re^* = 5$ and 10, see figure 4.7 (c) and (d). There is a limitation in (3.50) that may be breached with high Re^*, unless the film remains smooth so that $h' \ll 1$. This means inertia has a limited effect on the film as the inertial terms are dependent on h'. The capillary waves are known to be an effect of the additional surface tension terms that ensure solution stability. However, these capillary ripples can pose a challenging problem to resolve numerically, for example their high frequency may lead to issues with under-sampling.

The possibility of smoothed solutions for super-critical filling fractions arises from the levelling of the supplementary inertial terms, therefore satisfying (3.50) as the film mass is almost uniformly distributed across the domain. By imposing slip on the cylinder wall, $l_s = 0.01$, the parameter space changes. For small lengths of l_s, the solutions at each stage of the parameter space have very small differences which are shown in figure 4.9 for $l_s = 0.01$.

The profile for a large slip flow with $l_s = 0.2$ and $Re^* = 0.01$ is proportional to the no-slip case, with a deep pool being found on the rising cylinder side and is within the regime of $q/q_c < 1$, as depicted in figure 4.8 (a). While containing a steep front, akin to a shock solution, areas of recirculation form on the rising cylinder side within a pool, similar to those of figure 4.4. By increasing Re^*, the depth of the pool diminishes as fluid is spread across a larger portion of the rising cylinder wall and the capillary waves are more apparent in front of the pool. As $Re^* \to 5$, a number of small capillary ripples are found but are much smaller than those previously found to stabilise the film as Re^* increases above 1.80, see figure 4.8 (c).

At $Re^* = 10$, the film has become smooth due to the large slip reducing the strength of inertia needed to smooth the film, as shown in figure 4.8 (d). Previously, this was a shock solution with significant rippling of the surface for

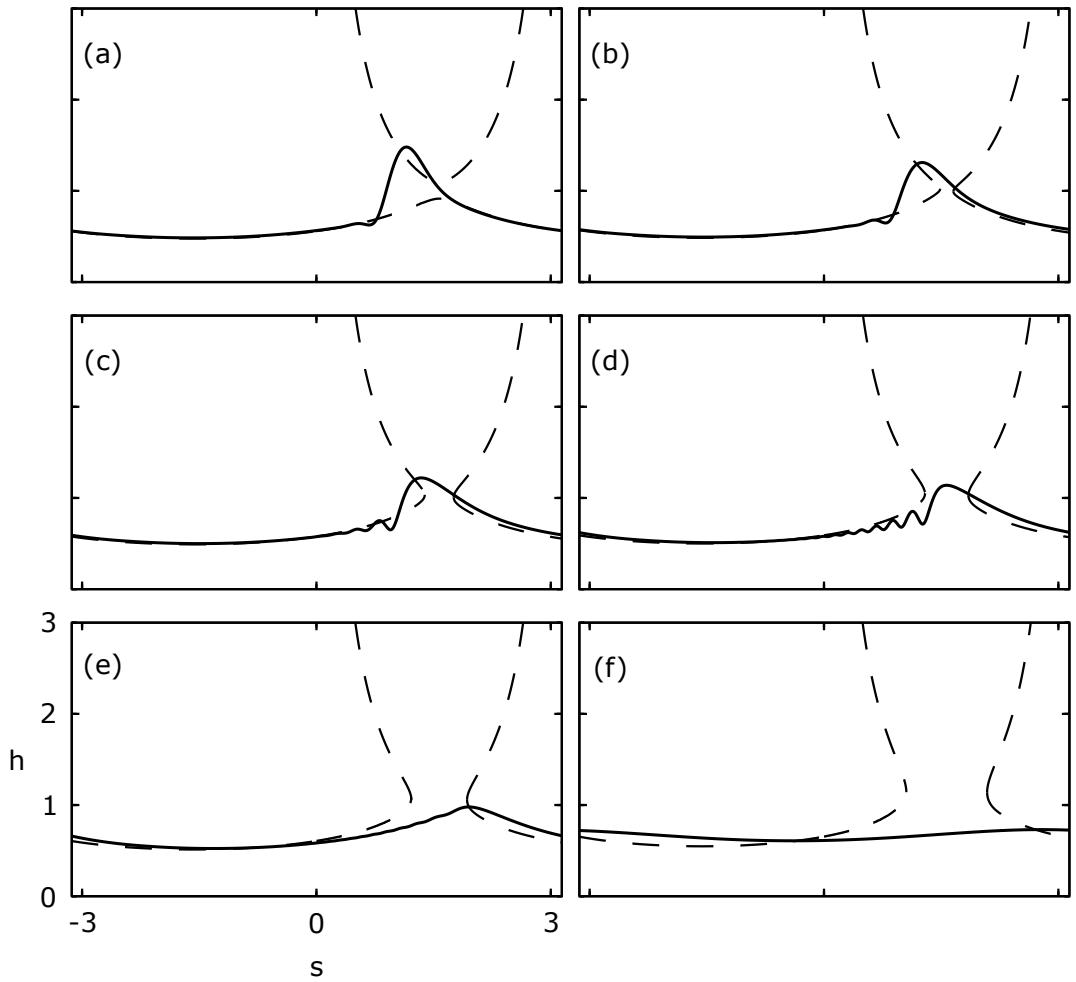


Figure 4.7: The effect of inertia on the slip boundary condition from figure 4.6, for $\tau = 1$, $\lambda = 1$, $Ca = 10^{-3}$, $\varepsilon = 10^{-2}$ and $A/A_c = 1.073$. With $Re^* = 0.01$ in (a), $Re^* = 1.8$ in (b), (c) with $Re^* = 5$, (d) with $Re^* = 10$, $Re^* = 15$ in (e) and (f) with $Re^* = 100$ for $l_s = 0$.

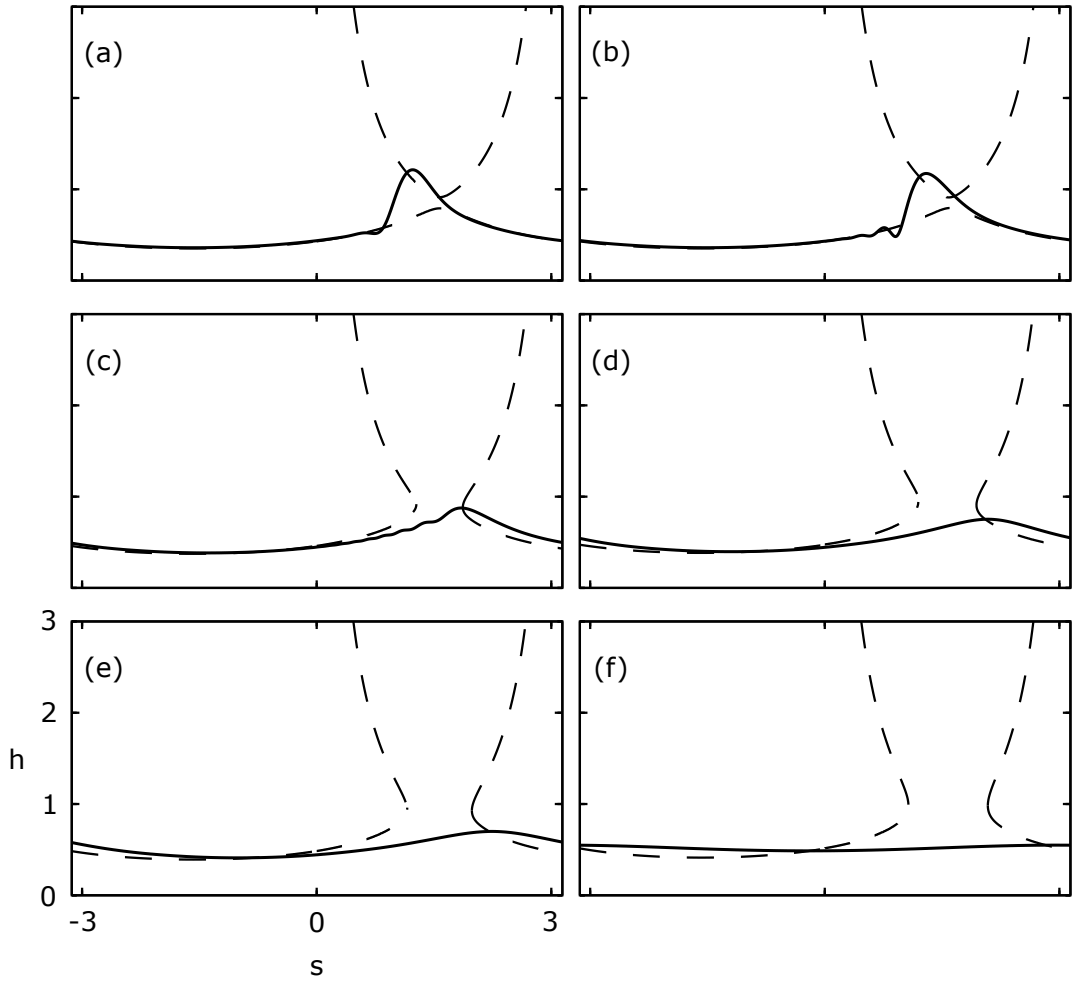


Figure 4.8: Effect of the slip boundary condition and inertia with $l_s = 0.2$ from figure 4.6. Where the reduced Reynolds number of (a) is $Re^* = 0.01$, (b) with $Re^* = 1.8$, (c) with $Re^* = 5$, (d) with $Re^* = 10$ and $Re^* = 20$ and $Re^* = 100$ in (e) and (f). With $\tau = 1$, $\lambda = 1$, $Ca = 10^{-3}$, $\varepsilon = 10^{-2}$ and $A/A_c = 1.073$.

smaller slip lengths. The almost uniform rimming flow of figure 4.8 (f), ensures that $h' \ll 1$, therefore (3.50) is satisfied and subsequent increases to inertia have minimal effect. For $Re^* > 20$, by including inertia, smooth solutions to exist for $q/q_c > 1$ which is contrary to classical lubrication theory's detached solution branches. Equally, film profiles have been found where the flux ratio is in the sub-critical regime, $q/q_c < 1$ even though the volume is larger than the the critical filling fraction, $A > A_c$, this is due to the inertial terms.

With large slip, the point where the film surpasses the critical flux limit of $q = q_c$ is found to be almost double the Re^* of the equivalent point for the no-slip case. However, this comes with an increase in the transition across the intermediate range between the pooled and smoothed film. This means the films become smoother much earlier in the parameter regime if slip is present. It also means that with the faster transition the formation of significant capillary ripples

are found at much lower values of Re^*, as shown by figure 4.6. This presents an interesting case where the increased inertial effects are restricted in their ability to smooth the pool solution initially. Therefore, larger inertial effects are required to raise the fluid along the cylinder wall and begin the eventual removal of the capillary ripples. While the transition to super-critical flow occurs at a much lower Re^* due to the increase in flux being faster with slip for increasing Re^*, this is only accurate for $Re^* \leq 10$. At higher Re^* the rate of increase to q/q_c slows above $Re^* > 50$ as the smoothing from stronger inertia is drastically diminished as the film is already smooth. The overall trends on the pooled, shock and smooth solutions are typically unchanged in appearance, notably as inertial smoothing becomes the dominant mechanism for $Re^* > 20$. There are only minor ripples in all cases, which dissipate shortly thereafter. With larger slip lengths, capillary ripple formations are significantly harder to resolve numerically.

This flow behaviour indicates that up to moderate inertia the no-slip flows have a larger fluid flux around the cylinder and there is a small region in the parameter space where flows subject to slip have a larger flux. The over-arching characteristic is that as inertia increases for each value of Re^* which is shown in figure 4.9, the pool becoming smoothed into a uniform film has been consistently observed for all slip lengths. However, there is an ability to control the flow rate presented by incorporating a surface that may slip and is shown by the different profiles in figure 4.6. This highlights a benefit of the slip boundary condition in forming a levelled profile, which is not subjected to recirculation regions if inertia is weak. Slip could therefore be used to avoid problems where prolonged exposure due to flow recirculation in the chamber will leads to a deterioration of the oil properties.

With the fixed ratio of fluid volume to the critical volume of $A/A_c = 1.073$ and relatively large slip length of $l_s = 0.2$, the initial film where $Re^* = 0.01$ is substantially shallower than that for the no-slip case, as in figure 4.9 (a). The features are predominantly similar, where surface tension is the cause of a single shallow trough appearing in front of the sharp increase in the film profile which still corresponds to a recirculating pool. As the strength of inertia increases, the capillary ripples are distinct at $Re^* = 1$ in front of the deeper pool in figure 4.9 (b). Unlike in the no-slip case, the solutions to the cubic equation of (4.1) show the film is still in a sub-critical regime. The flow still has a small recirculation region within the pool towards the cylinder wall. However, at $Re^* = 5$ this region of fluid pooling no longer exists, as shown in figure 4.9 (c). Instead, the fluid has a largely equal depth around the cylinder, with a slight thickening on the rising cylinder wall. The film is not smooth though, as the capillary waves from surface tension effects are still distinct around the thicker portion of the film but

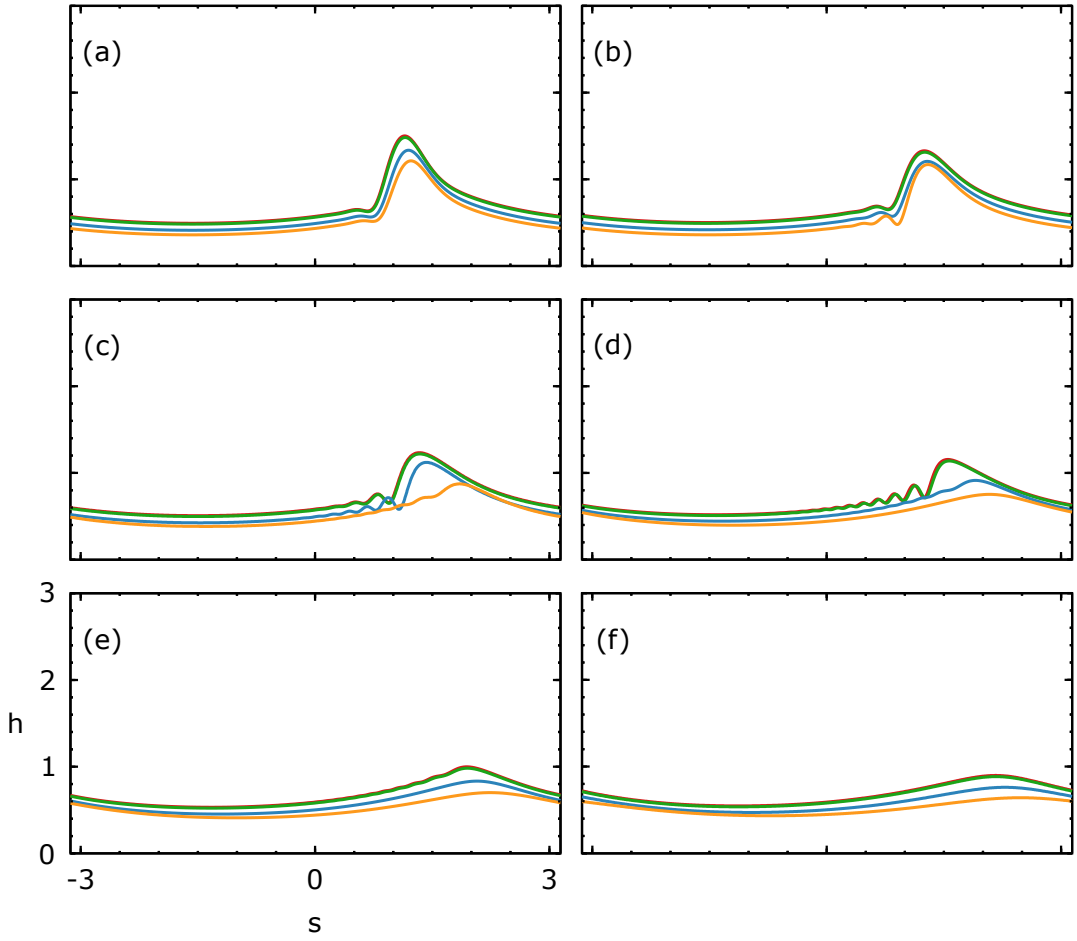


Figure 4.9: The changing film profiles due to fluid slip at different levels of inertia as detailed in figure 4.6, where the parameters are given as $\tau = 1$, $\lambda = 1$, $Ca = 10^{-3}$, $\varepsilon = 10^{-2}$ and $A/A_c = 1.073$. The values of Re^* are; 0.01 in (a), 1.8 in (b), 5 in (c), 10 in (d), 15 in (e) and 100 in (f). The slip lengths are given by the coloured lines; *red* for $l_s = 0$, *green* for $l_s = 0.01$, *blue* for $l_s = 0.1$ and *orange* for $l_s = 0.2$.

are at a significantly smaller amplitude. These ripples are gone from the surface by $Re^* = 10$ when $l_s \geq 0.1$ and the films can be treated as smooth, see figure 4.9 (d). The disappearance of these small wavelength ripples notably occurs at a much lower Re^* than if the cylinder wall has an assumed no slip condition. If the inertial forces are significant, the forces within the film are predominantly those of inertia and those from gravity and viscosity can be assumed as negligible and the film has a constant fluid depth, figure 4.9 (e).

From figure 4.9 (a), as the length of slip is increased it is clear that while the volume of fluid contained within the film is comparable when $l_s = 0$ and $l_s = 0.01$, as the slip length increases by an order of magnitude the change in fluid volume is more apparent, see figure 4.9 (f). As expected of a film that contains a super-critical volume of fluid which is balanced between gravitational and viscous effects, a pool of fluid forms for each case of l_s, shown in figure 4.9 (a). The larger capillary ripples and the number of visible ripples are becoming distinct at $Re^* = 1$, but the film profiles are still comparable in shape across the majority of the domain. However, when $Re^* = 5$, up to moderate slip lengths of $l_s = 0.1$ the films are still qualitatively comparable in shape, with a sharp ridge on the rising wall that is preceded by a number of capillary ripples. With $l_s = 0.2$, the profile no longer has the ridge of the pool and has been mostly smoothed by inertial forces with traces of the capillarity on the lower side of the rising wall.

The smoothing of the film for lower l_s values is shown at higher Re^* values in figure 4.9 (d), with the film that corresponds to $l_s = 0.1$ now having a profile similar to that where $l_s = 0.2$ with a slightly thicker region on the rising cylinder wall. The films for $l_s = 0.01$ and 0 have a much thicker region near the middle of the rising wall and large amplitude short wavelength ripples ahead of this region. At $Re^* = 20$, there are some trace elements of the surface tension effects with small capillary ripples for the lower values of l_s but the films are essentially smooth and the main difference is in the volume of fluid contained within the cylinder for each l_s.

4.6 Determining the Presence of Non-Unique Solution Branches

By the inclusion of high order surface terms into (3.113), a region within a parameter space has been shown to contain non-unique solutions by Kay et al. [14]. Their added wall friction factor highlighted novel characteristics of the flow dynamics, having employed a cubic polynomial for improvements in the depth-averaging method. In a similar fashion, the implementation of a slip boundary

condition was explored across a parameter space, shown in figure 4.10.

Next, solutions for varying filling fraction A/A_c are investigated with a fixed Reynolds number, where non-unique solutions exist for a flow with wall slip, while the no-slip flow solution remains unique for the same parameters. An initial profile of a fixed low filling fraction, passed through the steady-state solver achieves a smooth rimming flow profile shown in figure 4.11 (a). When the filling fraction is increased from zero, the smooth solution develops toward the critical flux ratio $q = q_c$ at point (b) which is shown in figure 4.11 with fluid pooling on the lower rising side of the cylinder. By raising the filling fraction, transitioning above $q > q_c$ and $A > A_c$, as shown in figure 4.10 shows further fluid accumulating on the rising cylinder wall in figure 4.11 (c). This development can be understood by the smooth solution profile connecting the bounded and unbounded solutions from lubrication theory of (4.1) for the sub-critical classification of, $q < q_c$. Subsequent increments of the filling fraction lead to a minor reduction in the fluid flux for film profiles which remain consistently within the sub-critical classification. The increased fluid within the domain accumulates within a deepening pool at the lower half of the rising cylinder wall, captured in figure 4.11 (d), and further addition to the filling fraction leads to capillary ripples becoming more prevalent. This parameter space for no-slip contains only one unique solution for any A/A_c.

The hump for the no-slip parameter space is enlarged with the inclusion of low reduced Reynolds numbers. Next, we will retrace the filling fraction-space with a high slip length, $l_s = 0.5$. The profile at low filling fraction is shown in figure 4.12 (e), and is very similar to the no-slip profile for the same A/A_c of figure 4.11. The profiles approaching $A = A_c$ bear similarities, beyond which the parameter space of figure 4.10 and subsequent profiles differ considerably. When increasing the filling fraction above the critical ($A/A_c > 1$), the flux ratio q/q_c increases towards a maximum attainable value, for which the profile is shown in figure 4.12 (g). Careful adjustment of the filling fraction then leads to a reduction in the fluid flux to figure 4.12 (h), beyond which solutions have failed to converge with increases in the filling fraction.

Enforced reduction to the flux allows for a parameter space to be explored between figure 4.12 (h) and figure 4.12 (j) with the steady state solver for a defined flux rather than filling fraction, this allows the filling fraction to be recalculated. Beyond figure 4.12 (j), increases to the filling fraction lead to accumulation of the extra fluid pooling on the rising cylinder wall exhibited in figure 4.12 (k) comparable to the no-slip scenario with larger filling fractions (Fig 4.11 (d)), the observed shock structure experiences substantial short wavelength formations in advance of the shock front located on the rising side of the cylinder. This parameter space shows a region of defined filling fractions which lead to multiple solution

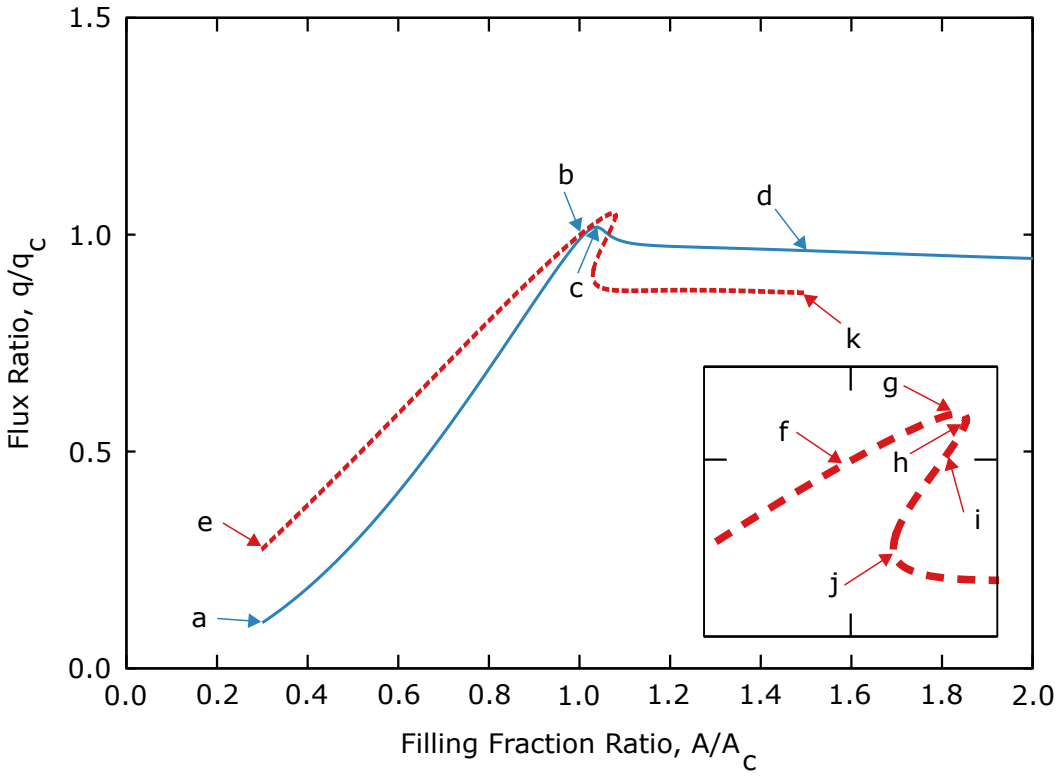


Figure 4.10: Parameter space q/q_c against A/A_c for smooth solutions transitioning to deep pooling solutions with wall slip. For; $Re^* = 1$, $\tau = 1$, $\lambda = 1$, $Ca = 10^{-3}$, $\varepsilon = 10^{-2}$. With $l_s = 0$ coloured in *blue* and dashed *red* representing $l_s = 0.5$. The films at each point can be found in figure 4.11 and figure 4.12 for the no-slip and slip cases respectively. The insert is the magnification of the slip line for $s \in [0.9, 1.1]$.

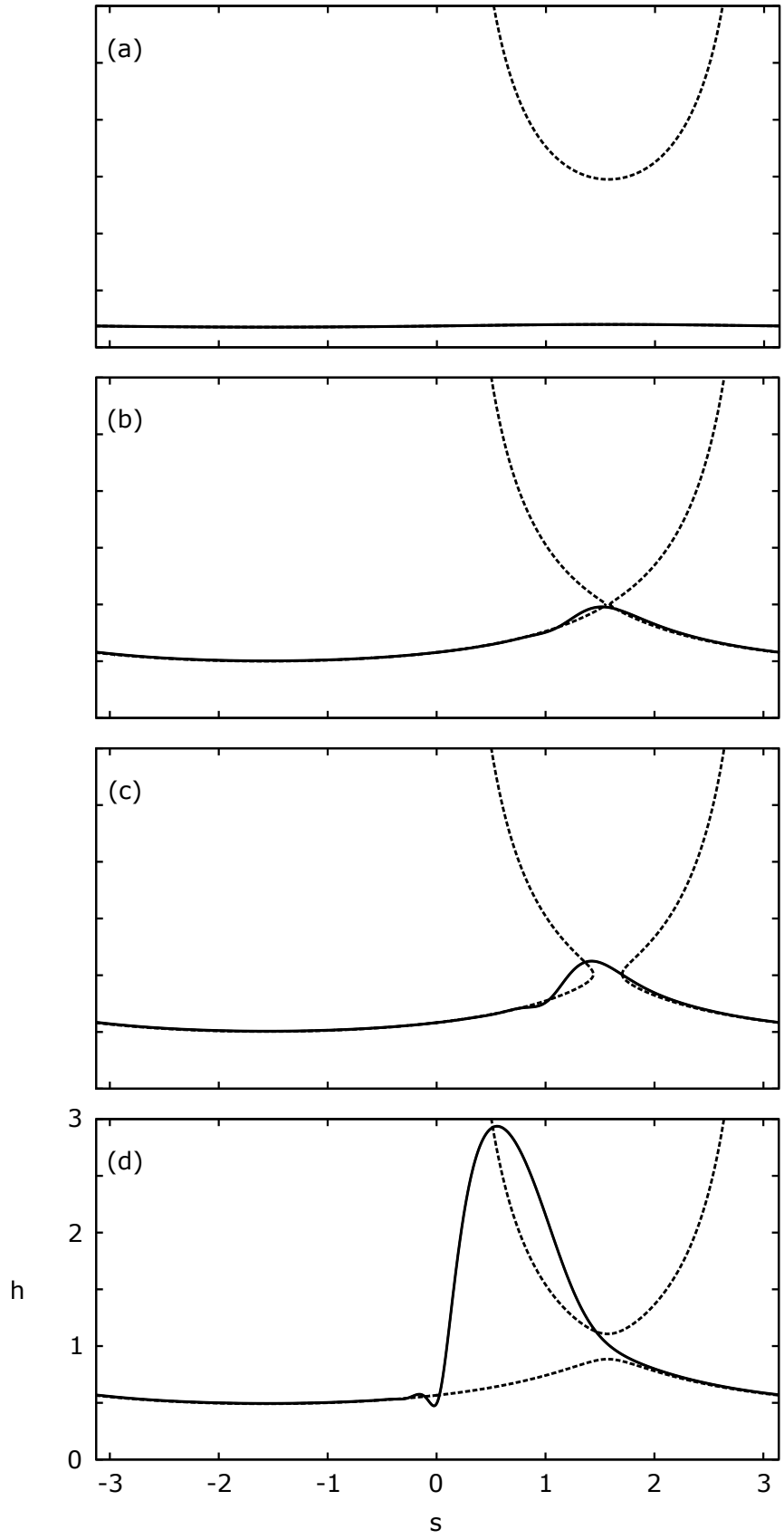


Figure 4.11: Film profiles of results represented in figure 4.10 for no-slip, detailing the transition films of points (a), (b), (c) and (d).

profiles attainable, defined by the non-unique region between $1 < A/A_c < 1.2$ shown in figure 4.10. The rimming flow profile presented in figure 4.12 (i) was found to be stable, indeed between solutions figure 4.12 (h), and figure 4.12 (j), and all solutions in the parameter space appeared to be stable following analysis by the transient solver. This is in agreement with the theory on the location of shock solution stability, shown in Villegas-Díaz et al. [36], where fluid on the rising cylinder side is stable when on the lower cylinder section.

The use of slip means the maximum attainable flux ratio is increased and a larger fluid filling fraction ratio is required before reaching the same transition region between the smooth and shock solutions as the no-slip case. The onset of capillary ripples is more profound across the entire parameter range for slip, exhibited between figure 4.12 (g) and figure 4.12 (k) unlike the no-slip results. Both slip and no-slip cases experience a flux reduction, located at the transitional region where the smooth film transforms into a shock film. The accumulation of fluid in the lower cylinder as a deepening shock solution provides the reduction in fluid flux required for maintaining a smooth rimming flow. The non-unique region reported by Kay et al. [14] when implementing a wall friction factor also shows that surface effects may develop this non-unique solution region. Therefore, this non-unique solution region is not surprising.

4.7 The Effect of Larger Slip Lengths on a Controlled Fluid Volume with Increasing Reynolds Numbers

In the previous Sections 4.5 and 4.6, the filling fraction A was defined in relation to the critical filling fraction A_c which is dependent on the slip length for the chamber walls. This Section retains a constant filling fraction, A to quantify how the flow can be changed with longer slip lengths.

For a filling fraction A fixed at 0.0135, there may be enough fluid contained within the cylinder for a recirculating pool to develop. The formation of a pool assumes that neither the inertial forces or viscous forces can prevent the fluid from pooling, this is shown in figure 4.13 (a) for $Re^* = 0.01$ and $l_s = 0$. The damping of surface tension against the increase in film depth is shown as a small dimple in front of the pool, but in figure 4.13 (b) this dimple is larger as surface tension acts against the increased inertia of $Re^* = 1.8$. The pool is also shallower, though there is no significant change to the film outside of the pool, therefore the displaced fluid is spread around the cylinder as a wider pool ending higher up on the rising wall. There is a development of strong capillary ripples, shown with the

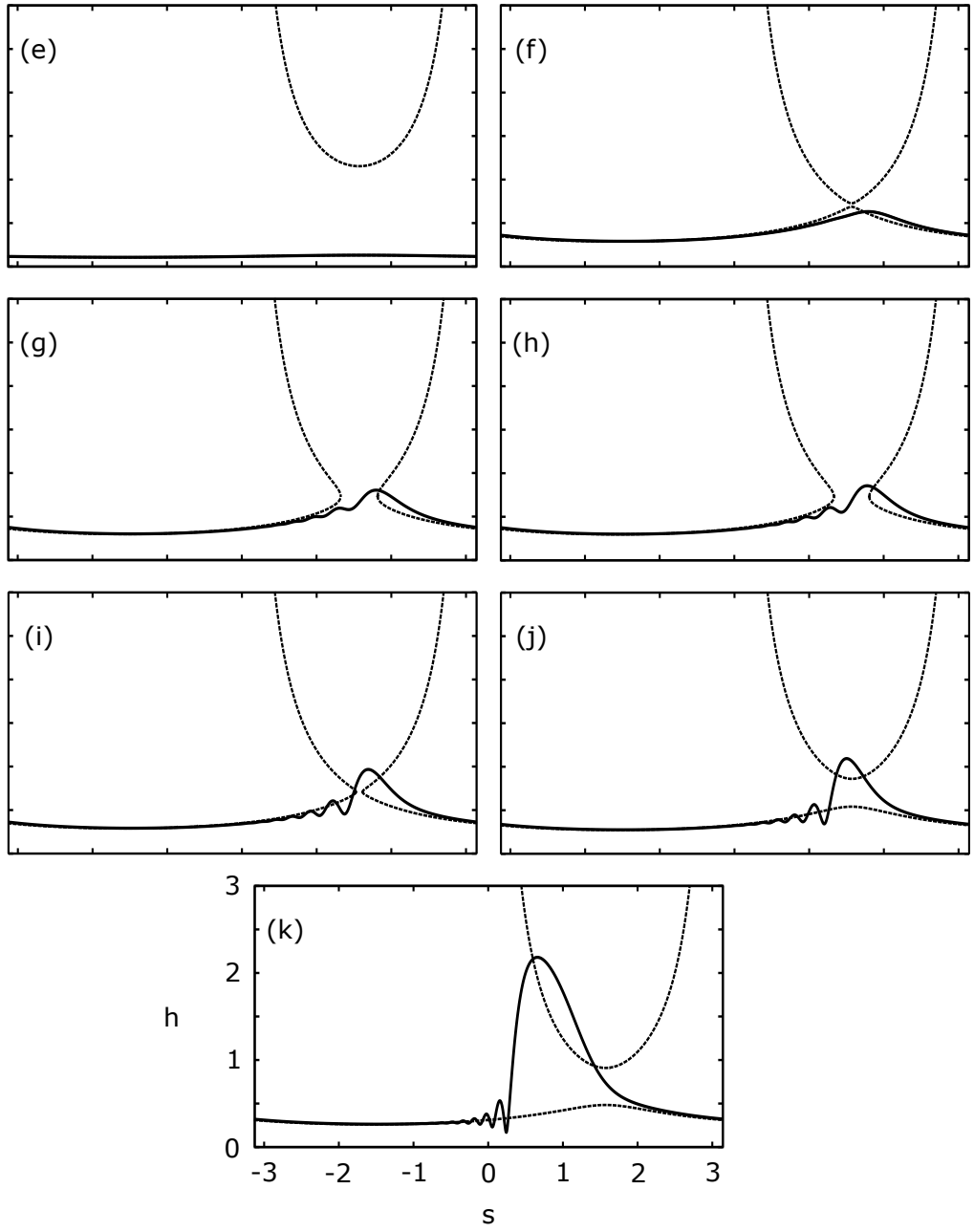


Figure 4.12: Profiles from figure 4.10 with $l_s = 0.5$, for the films at points (e), (f), (g), (h), (i), (j) and (k).

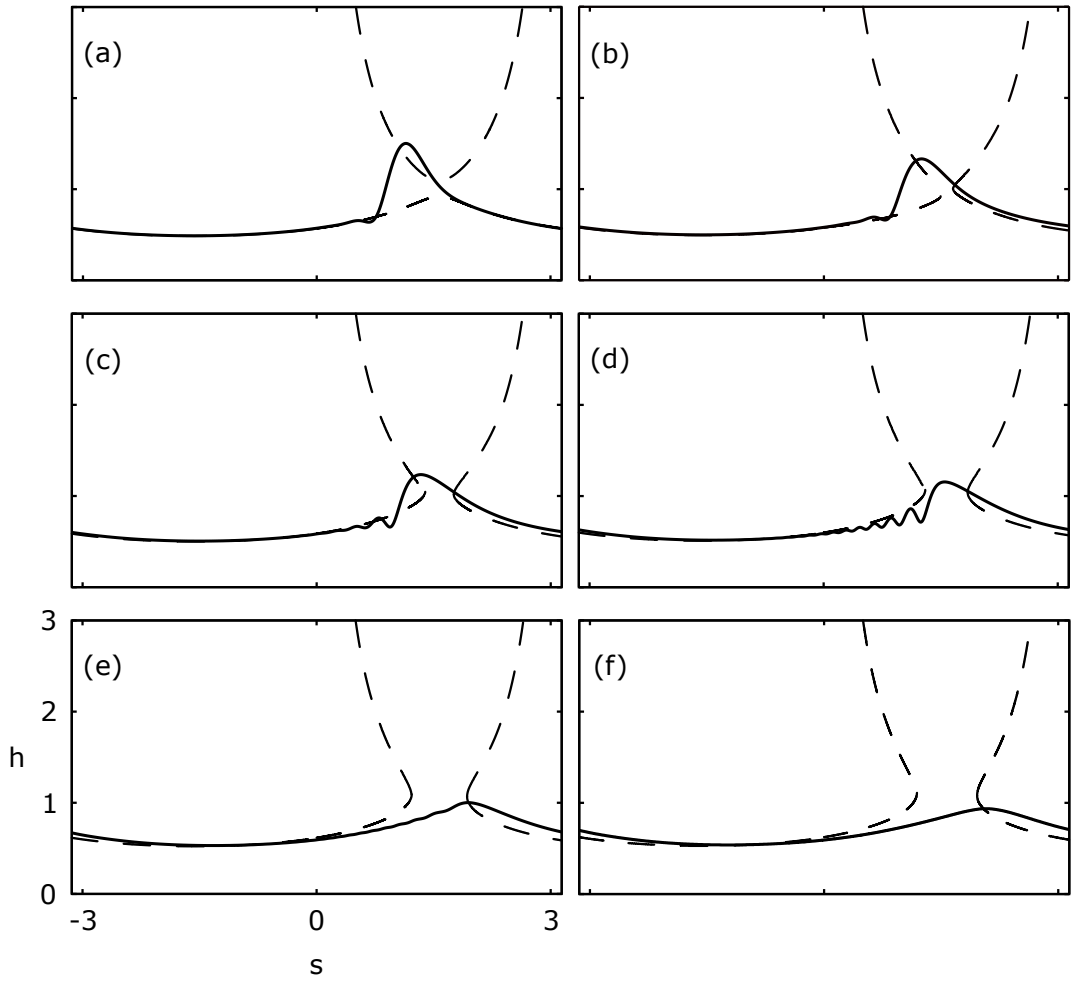


Figure 4.13: The effect of increasing Re^* on a fixed filling fraction $A = 0.013494$ with the no-slip condition. With $\tau = 1$, $\lambda = 1$, $Ca = 10^{-3}$ and $\varepsilon = 10^{-2}$. The reduced Reynolds number of each panel is given as; 0.01 in (a), 1.8 in (b), 5 in (c), 10 in (d), 15 in (e) and 20 in (f).

beginning of small wavelength surface ripples in figure 4.13 to stabilise the flow against the larger inertial effects of $Re^* = 5$. The pool has been elongated further up the rising wall as fluid is moved from the pool and the height has reduced accordingly. At $Re^* = 10$, the size of the recirculating pool has diminished, with the film now approaching a more uniform height in figure 4.13 (d). The strong capillary ripples have propagated across even more of the chamber preceding the pool, which allows for these stable films when transitioning between those of weak and moderate inertia.

The larger reduced Reynolds number, $Re^* = 15$ in figure 4.13 (e) shows that the pool has been completely removed from the cylinder as a result of the heightened inertial force. However the film is not completely smooth, as small amplitude waves are apparent on the film surface in the region of $s \in [0, 1.5]$. These waves are a consequence of the capillary waves dissipating as the need for

strong stabilising effects in the film are no longer required. Finally in (f) of figure 4.13, the film profile appears to be equivalent to the viscous dominant flow with $Re^* = 20$, due to the higher inertial effects eliminating both the capillary ripples and pool. The film cannot be considered as uniform due to the thickening of the film on the rising wall which is due to the gravitational pull on the film, which also creates the thinner region as fluid is accelerated down the falling wall.

The features of the flow for the range of Reynolds numbers implemented are largely similar when there is a modest slip length defined, such as $l_s = 0.01$ in figure 4.14, moving from the pooled film to the eventual smooth film at $Re^* = 20$. There is a deeper pool of the film initially in figure 4.14 as the introduction of fluid slip has caused a shedding of fluid around the chamber, which accumulates into this deeper pool with a stronger recirculation zone. As the Reynolds number is increased to 1.8 and 5, the pool of figure 4.14 is consistently deeper than those of figure 4.13, with the small dimples related to surface tension being predominantly similar in shape and wavelength. At $Re^* = 10$, the surface waves are comparable in wavelength to those of figure 4.13, however the amplitude of these waves is larger due to the deeper pool and associated film thinning due to slip.

At a moderate level of inertia corresponding to $Re^* = 20$ in (f), the film is indistinct from the previous profiles of figure 4.13, as the inertial forces have smoothed the pool into a more uniform film. The slight thinning and thickening of the film is once more due to gravity. In the profile in figure 4.14 (e) which corresponds to $Re^* = 15$, the surface waves that are linked to the capillary waves are larger in amplitude with $l_s = 0.01$ acting on the cylinder wall. However, the main differences between the no-slip and slip of $l_s = 0.01$ is the deeper pool and the amplitude of the capillary ripples, but they are mainly comparable for the change to the Reynolds number.

If the cylinder has been made so that it may support a large slip length of $l_s = 0.1$ to act on the fluid, the results for the film profiles in figure 4.15 are vastly different to those of either figure 4.13 or figure 4.14. This larger slip length has had a dramatic impact on the depth of the fluid pool, shown in figure 4.15 (a) where the pool is almost 40 % larger than a pool with no-slip. The cause of this deeper pool is that a large volume of fluid which is lost from the cylinder walls drains into the pool and therefore has a more substantial size than that of figure 4.14 (a) where $l_s = 0.01$, with a minimum film which is almost 20 % shallower. Once more as the Reynolds number increases, the initially deep pool of $Re^* = 0.01$ is smoothed in the direction of the core rotation, this is shown as a wider pool which spreads higher up the rising wall in figure 4.14 (b). The amplitude of the capillary ripples in front of the pool is increased with the presence of slip, and shown to be considerably larger in figure 4.15 (c) for $Re^* = 5$. These surface waves

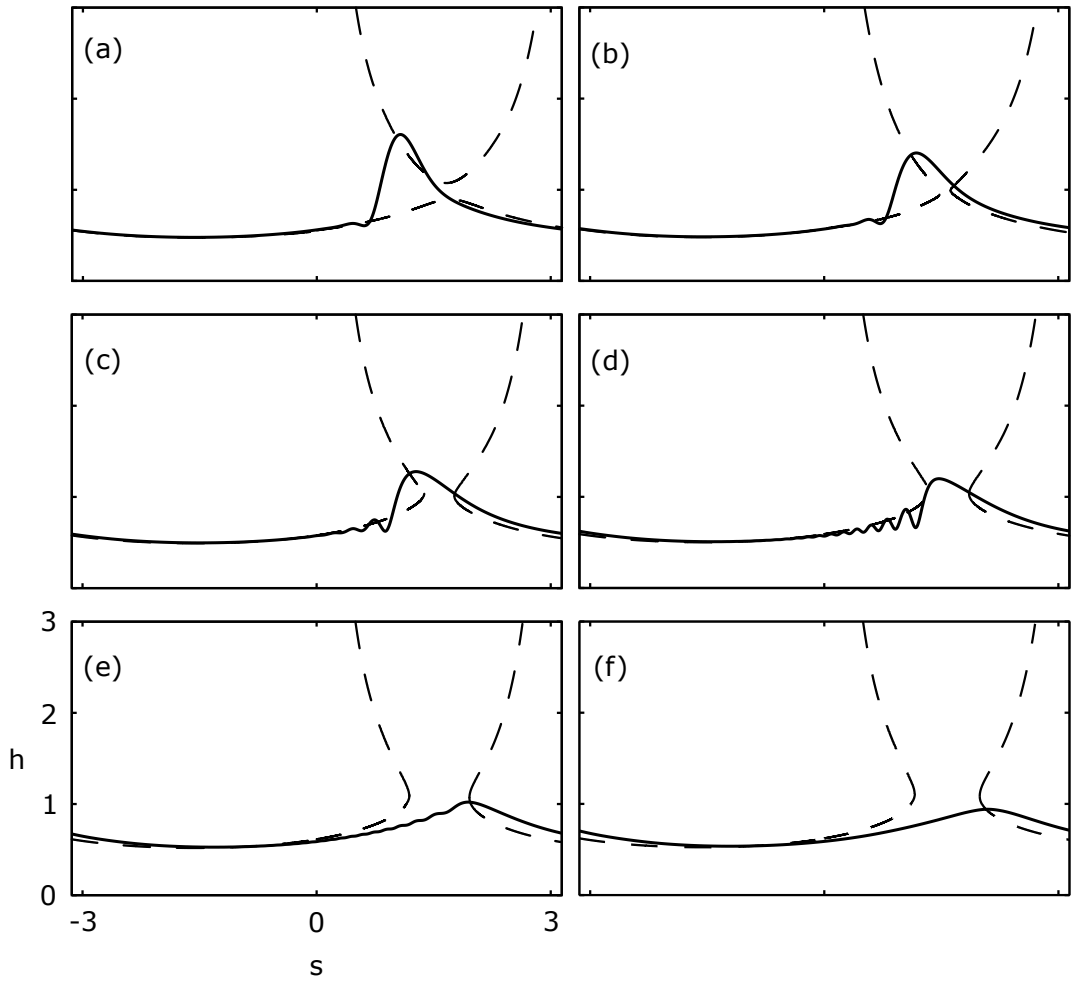


Figure 4.14: The effect of moderate slip length, $l_s = 0.01$ for a fixed filling fraction $A = 0.013494$ for increasing Re^*. In each panel, the reduced Reynolds number is given as 0.01, 1.8, 5, 10, 15 and 20 in (a), (b), (c), (d), (e) and (f) respectively. The remaining flow parameters are; $\tau = 1$, $\lambda = 1$, $Ca = 10^{-3}$ and $\varepsilon = 10^{-2}$.

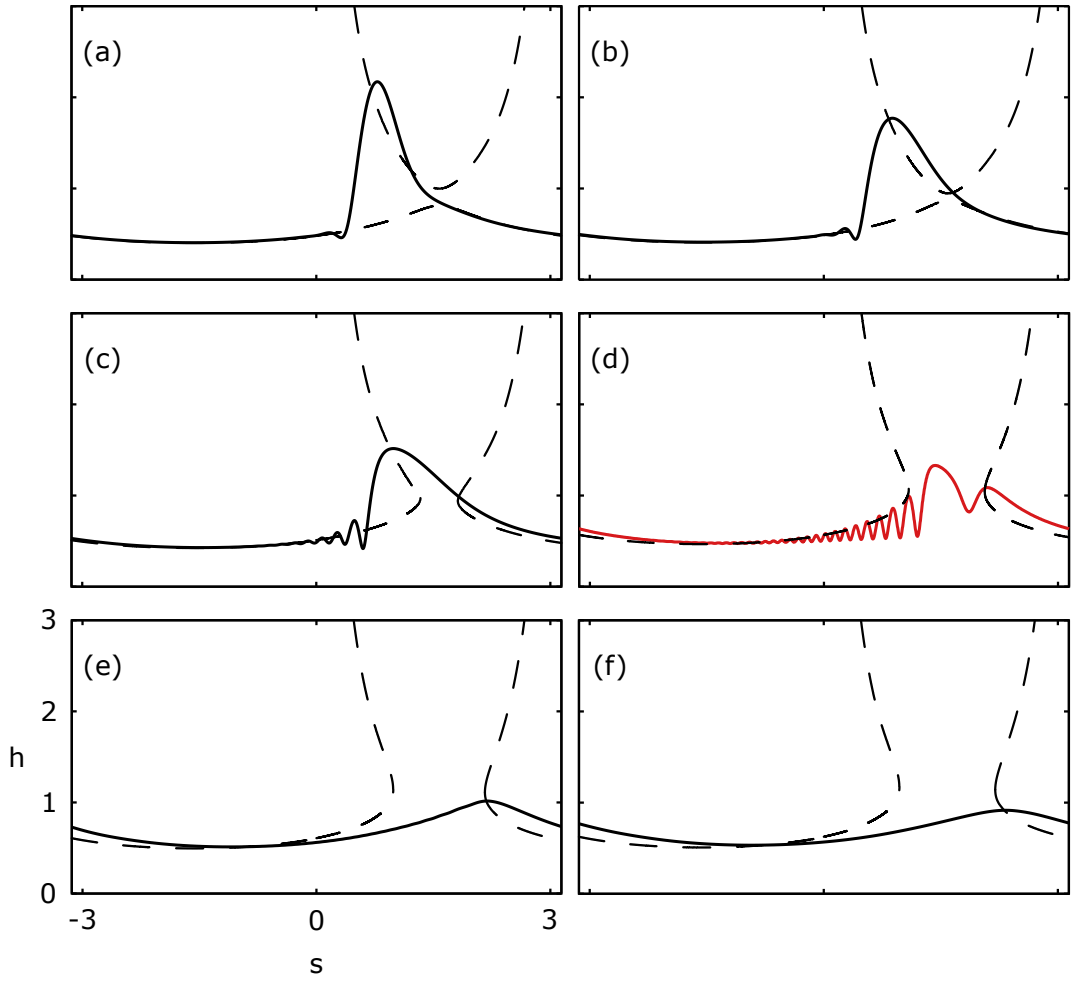


Figure 4.15: Effect of inertia for a constant filling fraction $A = 0.013494$ with large slip, $l_s = 0.1$ condition. Where the parameters are given as $\lambda = 1$, $\tau = 1$, $\varepsilon = 10^{-2}$ and $Ca = 10^{-3}$. With $Re^* = 0.01$ in (a), (b) $Re^* = 1.8$, $Re^* = 5$ in (c), $Re^* = 10$ in (d), $Re^* = 15$ in (e) and $Re^* = 20$ in (f). The *red* line in (d) indicating an unstable solution.

are the result of stabilising the now much larger gradient in the film surface due to the deeper pool. With all cases for $Re^* \leq 5$ in figure 4.15, the recirculation region is much larger and stronger as a result of the greater volume of fluid within the pool.

As the inertial effects increase, the role of surface tension in creating a stable film is shown by the significant surface waves being present across a larger area of the cylinder. The film with $Re^* = 10$ in figure 4.15 (d) can be considered an unstable solution. This is an issue due to the numerical solver failing to converge to a steady-state solution within a reasonable iteration limit from the previous solution of (c). This is likely due to the surface tension creating large ripples. While the larger ripples are expected, an even higher mesh resolution and increased iteration count than previously used in this thesis were found to be insufficient. This does not infer a stable solution does not exist in this parameter range, but the ability to find a solution using the current methodology would require a significant venture which is largely unreasonable as the solution is a transition between the pooling and smoother solutions of (c) and (e).

With the stronger presence of inertia for $Re^* \geq 15$ in figure 4.15 (e), the film can be treated as a smooth solution, similar to those previous for $l_s = 0.01$ and $l_s = 0$ once $Re^* = 20$ in figures 4.13 and 4.14. However the distinction is that these smooth films occur far earlier when increasing the inertial strength which is attributed solely to the slip condition, which also moves the position of the film maxima around the cylinder, occurring at a higher point in the cylinder due to the faster fluid velocity as a result of slip.

4.8 Chapter Summary

The thin film model developed in Chapter 3 is thoroughly explored in this Chapter in the context of isothermal flows. There is a key interest in determining the role that partial slip has on the rimming flow problem, which is established to be a gap within the current literature.

In the classical lubrication theory model of gravity and viscosity, the slip boundary condition is found to change the cubic flux equation limits. The critical film height, which is the maximum sustainable height for a given shear rate, reduces with longer slip. An asymptotic analysis shows this critical height approaches $\tau/2\lambda$, which is half the height when excluding slip. At a fundamental level slip will reduce the volume of fluid that can be sustained on the cylinder walls.

The validity of the numerical model has been compared to previous works, most notably those of Ashmore et al. [49] and Kay et al. [14]. The model significantly agrees with the literature, accurately capturing the different profiles

when there is either strong gravitational or inertial effects.

Under the stronger force of gravity, the fluid develops an increasingly deeper pool with a growing recirculation region. With the addition of slip, a thinning of the outer bounds of the domain occurs and causes these pools to be even deeper. When slip has a comparable length to the film depth, there is an extreme case of fluid draining from the cylinder walls, this causes what was a smooth film to collapse into a pool. However, when gravity is sufficiently large, the impact that moderate slip has on the film is reduced substantially.

When modelling strong inertial effects, the pooling solution can be dampened into a smooth solution at very high Reynolds numbers. At this level of inertia, there is little difference between films with no-slip and slip, while at low to moderate Reynolds numbers this is not the case. Notably, by including surface slip the capillary waves on the film surface at a given Reynolds number may be amplified. This amplification is also combined with the earlier onset of these capillary ripples at weaker inertial states, which is related to the length of slip on the cylinder walls. However, by including slip, the level of inertia necessary to cause smooth films and avoid capillary waves altogether is substantially lower.

When there is no slip, the parameter space of fluid volume to fluid flux encompasses purely unique solutions for any given volume of fluid. By modelling fluid slip, this is no longer the case and a non-unique solution region is found. This non-unique solution region is found to contain three simultaneously feasible and steady solutions which are wholly stable according to both the steady-state and transient solvers.

It is apparent that when including fluid slip, the thinning of the film profile towards the domain boundaries is significant. This may be detrimental to the bearing chamber as this causes larger volumes of fluid to accumulate into bigger recirculation regions. However, this development can be countered by lowering the volume of fluid within the chamber.

Chapter 5

Surface Driven Non-Isothermal Thin Film Rimming Flow

This Chapter investigates how fluid slip at the cylinder wall effects the thermal profiles of rimming flows. As reducing the film temperatures is an important way to avoid oil degradation which may occur within the bearing chamber. The oil properties will be dependent on the engine specification, the manufacturer of the oil and how long the oil has been in use. The walls of the bearing chamber and the air flow will also change temperature over time, due to the operating conditions. However, for this thesis the assumption is that the net heat transfer into the air and cylinder is zero. This means the cylinder walls and air remain at a constant temperature and allows for steady results to be modelled. In the bearing chamber, the air will be continuously cycled through the oil system. Therefore, the air flow in this model has been assumed to be colder than the metal chamber. With this assumption, the thermodynamics are thoroughly studied using the dimensionless parameters of the depth-averaged model from Chapter 3, where the primary focus has been to determine the thermodynamic changes caused by fluid slip. A significant portion of the work contained in this Chapter has been compiled and submitted to the Journal of Fluid Mechanics, see Nicholson et al. [180].

As the flow through the bearing chamber Is thought to have high Péclet numbers, the model allows for strong thermal convection effects to be included when solving (3.121). The model has been derived so that the convective terms may be equivalent to a leading order term for moderate Péclet numbers.

This investigation focuses on the three distinct flow cases of the smooth, shock and pooling films. However, results have found that the film temperatures are sensitive to the Biot number, which defines the heat transfer coefficient of the surface to the thermal conductivity of the fluid. Therefore, a Biot number which creates significant thermal gradients across the film has been assumed so that the

temperature scalings are suitable for analysis. The effect of longer slip lengths has been explored with several Péclet numbers which range from low to moderate for films which are smooth and pooling. The effect of slip has also been studied across the combined parameter space of inertia and thermal convection. The inertial effects lead to the formation of several transitional films which exist between a smooth and pooling film which were previously shown in Chapter 4. These transitional films have unique film profiles which affect the thermal structures within the film. The aim is to show the role that surface slip may have on film temperatures and how it may improve the thermal performance of the bearing chamber.

5.1 Outlining the Non-Isothermal Model without Slip

In order to study the thermodynamics of the rimming flows when fluid slip occurs on the cylinder walls, it is beneficial to characterise the three most common flow configurations which will be studied. These are known as a smooth film (a), a shock film (d) and a pooling film (g) of figure 5.1. These films have a very low Biot number, $B = 10^{-10}$, meaning the cold airflow in the cylinder is insulated from the heated oil. This insulation effect is shown in figure 5.1 panels (c), (f) and (i), where the film temperature is approximately equal to the applied wall temperature of $T_w = 1$.

The smooth film, also known as a uniform film due to its consistent depth, is where a film coats the cylinder surface and the flow travels in either a clockwise or counterclockwise direction. There is no stationary or reverse flow and there may be a slightly thicker region, which is found on the rising cylinder wall due to gravity. A shock profile is when there is a larger volume of fluid within the chamber and is when the driving force is too weak to maintain a uniform film. The fluid still flows in one direction around the cylinder, however there is now a stagnation point within the film. The main feature which characterises a shock film is the steep front where $h' \gg 1$, as shown in figure 5.1 (e). The main feature of the pooling film is the fluid back-flow, also known as a recirculation region, that forms because of the gravitational effects on the large fluid volume. The fluid volume is larger than the previous two cases and the driving force cannot support the fluid flowing in one direction around the cylinder. This recirculation and large fluid volume which accumulates around the cylinder base is shown in figure 5.1 (h). There is a narrow film which is pulled from the pool due to the driving shear force. This narrow film is largely uniform in depth with the flow moving in one

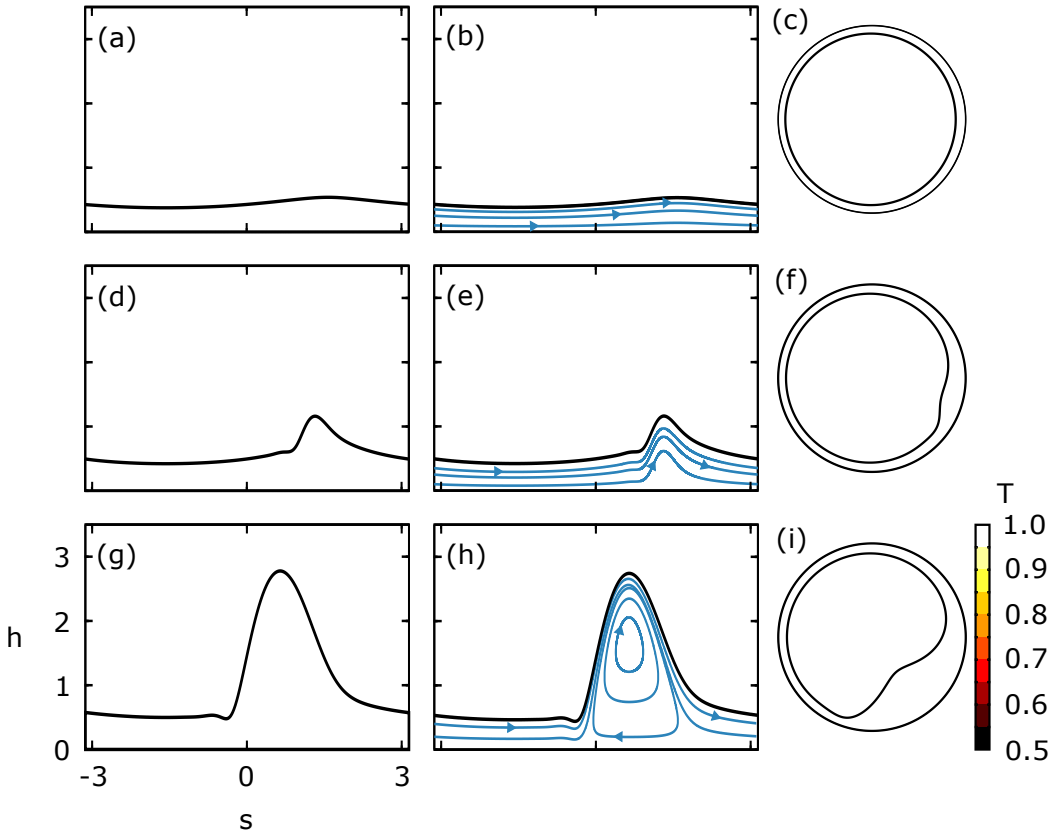


Figure 5.1: The typical film profiles for smooth (a), shock (d) and pooling (g) solutions using parameters from table 5.1. The temperature bar shows the uniform temperatures across all of these films. The velocity streamlines of each film show when recirculation occurs in panels (b), (e) and (h). The film profiles and the film temperatures have been plotted into a cylindrical representation in (c), (f) and (i) for each flow respectively.

direction around the cylinder. The remaining results of this Chapter focus on these flows which are characterized by the parameters detailed in table 5.1.

The presence of fluid slip and the inclusion of inertia are important features of this work as film profiles are different than those found with classical lubrication theory of rimming flows. The classical approach leads to a set of limiting critical values, known as the critical filling fraction, A_c and critical film flux q_c which were detailed in Chapter 4. The retention of inertial terms that may be equivalent to leading order terms with large Reynolds numbers in the model mean a variety of solutions can be found. However, when inertial effects are significant there is a limit as part of (3.50) for h' where $h' \ll 1$. The films with strong inertia have been detailed in the previous Chapter 4, along with the effects of partial slip for isothermal films. The critical values are shown to be modified with the addition of surface slip and a method of maintaining consistency for film comparisons is required to investigate the thermal effects.

Profile	ε	Re^*	Ca	τ	λ	l_s	A
Smooth	10^{-2}	1	10^{-1}	1	1	0 - 0.5	0.88ε or $0.75A_c$
Shock	10^{-2}	10^{-2}	10^{-3}	1	1	0.1	1.1492ε
Pool	10^{-1}	0.1 - 10	10^{-1}	1	1	0 - 0.5	1.987ε or $1.576A_c$

Table 5.1: Parameters for establishing a smooth or pooled solution.

There are two variations to determine the volume of fluid in the cylinder using the filling fraction. The first defines a specific ratio of A/A_c for a given set of parameters and is used to determine if the fluid volume will lead to either smooth or pool profiles to form. The second uses a constant value for the filling fraction, A to define the three film types. This second method means the films with longer slip lengths can be compared to show changes in both the film and temperature profiles.

This Section outlines the requirements in defining one of the three rimming flow profiles so that a comparison of the film profiles and mean temperatures can be completed. The rest of this Chapter examines the thermodynamic changes that different parameter regimes have, with a specific focus on slip.

5.2 Impact of the Surface Heat Transfer Coefficient and Slip Length on Film Temperatures

The role of the free surface heat transfer rate, or the Biot number has been explored for both the smooth and pooled films. The flows have been simulated using the parameters in table 5.1 and with the second filling fraction constraint. The flow has been modelled as conduction dominant, with $Pe^* = 0.01$. The films are subjected to higher heat transfer rates at the free surface with films where there is no-slip and a moderate slip length at the wall.

With a low Biot number of $B = 0.01$, the temperature of the film is approximately equal, shown in figure 5.2 (a) where there is no variation across the film depth. By increasing the heat transfer coefficient of the film surface, temperature gradients develop across the film as heat is more easily transferred to the air, this is shown in figure 5.2 (c). For larger Biot numbers, the film temperature reduces as the film transfers more heat to the surrounding air. This is shown in figure 5.2 (e) with the mean temperature profiles for several Biot numbers.

With the addition of partial slip, the thermal profile is largely equivalent to the profiles with no-slip. This is due to the temperature profile being conduction

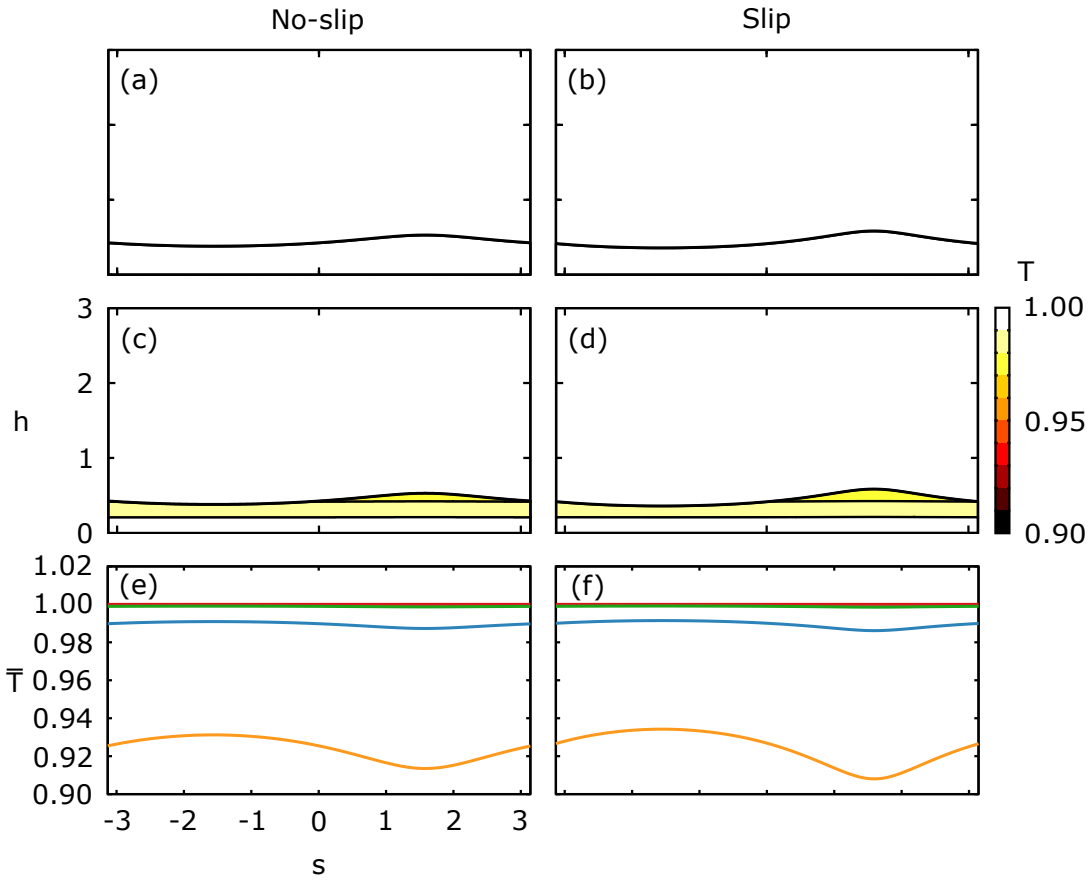


Figure 5.2: The effect of different surface heat transfer rates and slip lengths on smooth and pooling films with weak thermal convection has been explored in this Section. In the first column $l_s = 0$ and $l_s = 0.1$ for the second. Panels (a) and (b) are with $B = 0.01$ while panels (c) and (d) have $B = 0.1$ respectively. The mean temperature lines in (e) and (f) are coloured for each Biot number and represented as; $B = 10^0$ with *red*, $B = 10^{-1}$ in *green*, $B = 10^{-2}$ with *blue* and $B = 10^{-6}$ with *orange*.

dominant, though the minimum temperature is lower (1 %) with slip as the film is slightly thicker by around 10 %. This increase in depth inhibits the heat transfer by conduction, the larger film depth is shown in figure 5.2 (d).

When the film is pooling and the Biot number is low, the temperature is nearly constant across the film. This is shown in figure 5.3 (a) and (b) where there is no-slip and a moderate length of slip. However, there is a slight colder region at the pool surface as the distance between the free surface and wall is large. When the heat transfer rate of the free surface is higher, there is a greater amount of cooling that occurs at the surface of the pool. There is still a thin layer of fluid around the cylinder which is roughly equal in temperature. With slip, the film is found to be much thinner across the majority of the cylinder compared to the no-slip case, this can be as much as 20 % which is shown in part (b) of figure 5.3. The pool is also much deeper as the fluid accumulates at the base due to the

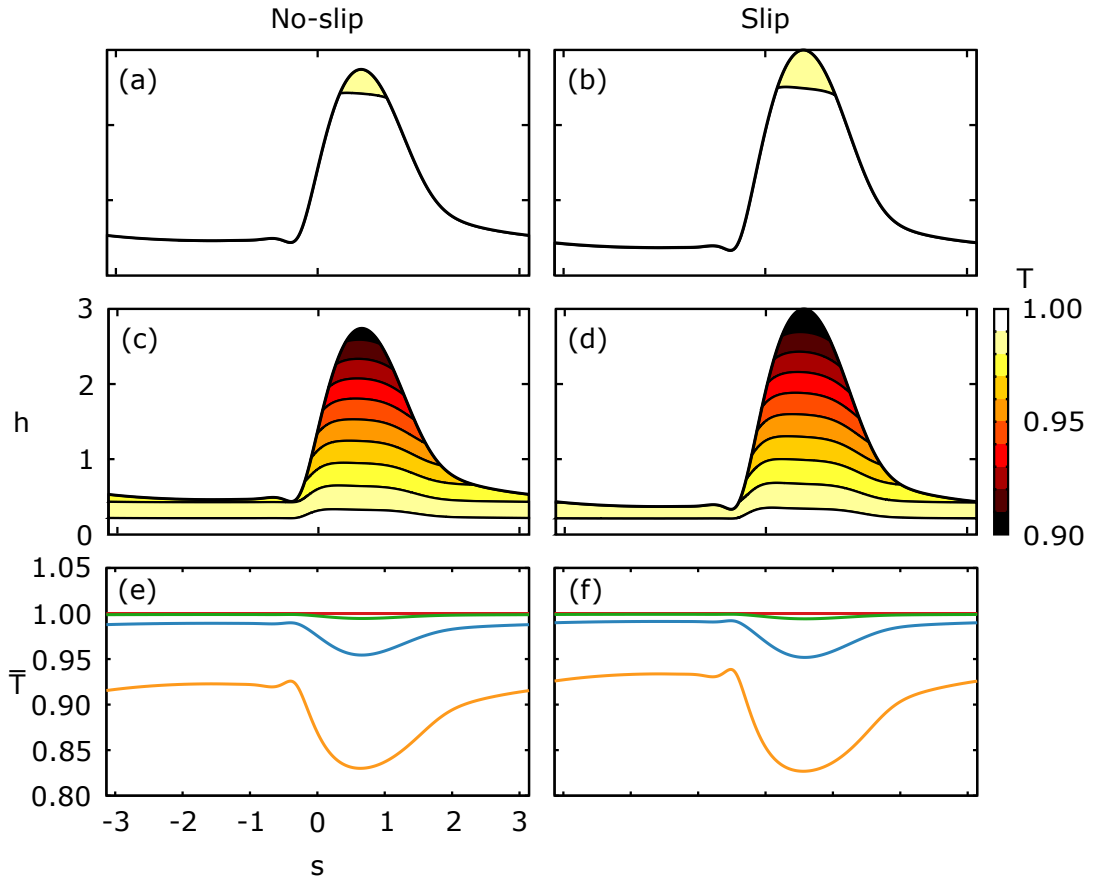


Figure 5.3: Panels (a) and (b) are with no-slip and for $B = 0.01$ and $B = 0.1$ respectively, while the second row is with $l_s = 0.1$ with the same Biot numbers. The Biot numbers of the last row of panels are; *red* is $B = 10^0$, *green* represents $B = 10^{-1}$, *blue* shows $B = 10^{-2}$ and $B = 10^{-6}$ is given by *orange* for the mean temperature $\bar{T}$.

reduced volume entrained around the cylinder, this depth increase is almost 10 %. The thermal changes with the different Biot numbers match closely between the slip and no-slip cases. However, the minimum temperature of the pool is lower due to this change in fluid depth when slip is present.

The effect of slip length on the mean temperatures for two Biot numbers of $B = 0.01$ and $B = 0.1$ for smooth and pooling films is shown in figure 5.4. For these profiles the first fluid volume constraint has been used, so the ratio of A/A_c has been kept constant for the smooth (a, b), and pooled films (c, d). The volume of fluid reduces for each film as the slip length increases, as A_c decreases with slip.

For smooth solutions, small slip lengths give only minor variations on the mean temperatures, $\bar{T}$, while large slip lengths show the mean temperature features are enhanced, with the dip in smooth solutions being noticeably amplified in figure 5.4 (b). The longer slip lengths have higher mean temperatures across the film in comparison to flows with no-slip.

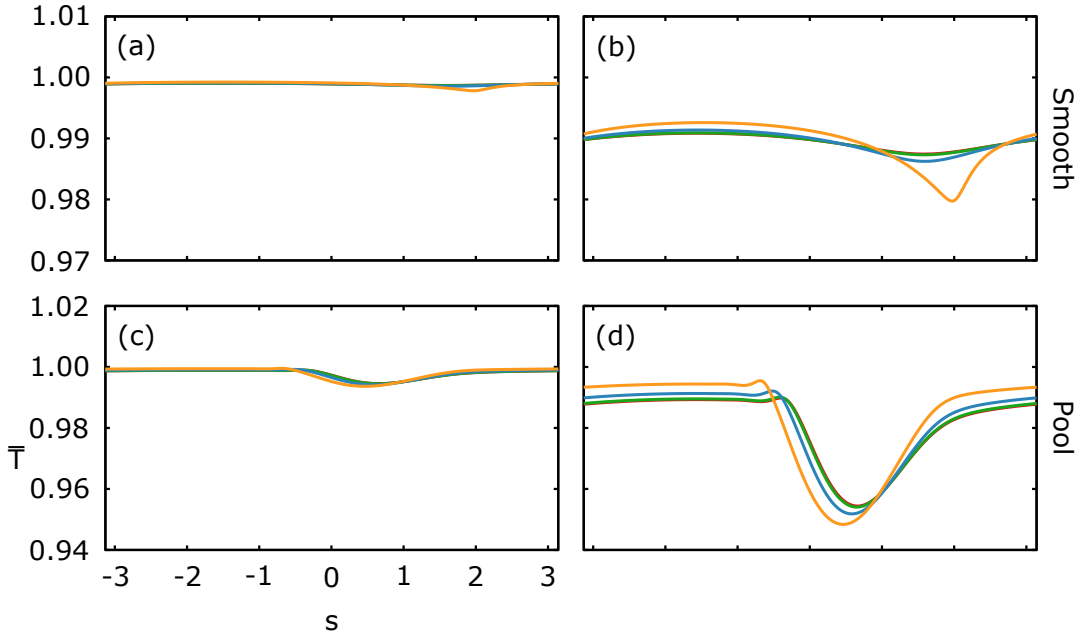


Figure 5.4: The influence of slip length, l_s on the fixed volume smooth films of (a) and (b), and on the pooled films (c) and (d) for Biot numbers $B = 0.01$ and $B = 0.1$ in (a), (c) and (b), (d) respectively. The slip lengths are indicated by the coloured lines; $l_s = 0$ in *red*, $l_s = 10^{-2}$ in *green*, $l_s = 10^{-1}$ by *blue* and $l_s = 5 \times 10^{-1}$ with *orange*.

This behaviour has also been found for the pooled films with the peak and troughs in the mean temperature profiles being amplified. There is also a widening of the thermal features, which means they occur over a larger width of the domain. For the remainder of this thesis, a Biot number of $B = 0.1$ has been used to provide a large thermal gradient so that the changes in temperatures of the film can be observed.

5.3 Influence of Convection on the Thermal Profiles

The strength of thermal convection through the film has been small in Sections 5.1 and 5.2, with $Pe^* \ll 1$. However, convection was shown to be important by Kay et al. [15], so the Péclet number is increased so that thermal convection within the film becomes significant. A constant filling fraction is used in this Section for the smooth and pooling films, so the changes to the temperature profiles can be studied with different Péclet numbers and lengths of slip.

The smooth films, where $q < q_c$ are found to be largely independent of the effects of thermal convection. This is because the azimuthal gradient is small and thermal convection is dependent on $h' \gg 1$, which is shown in (3.68). This

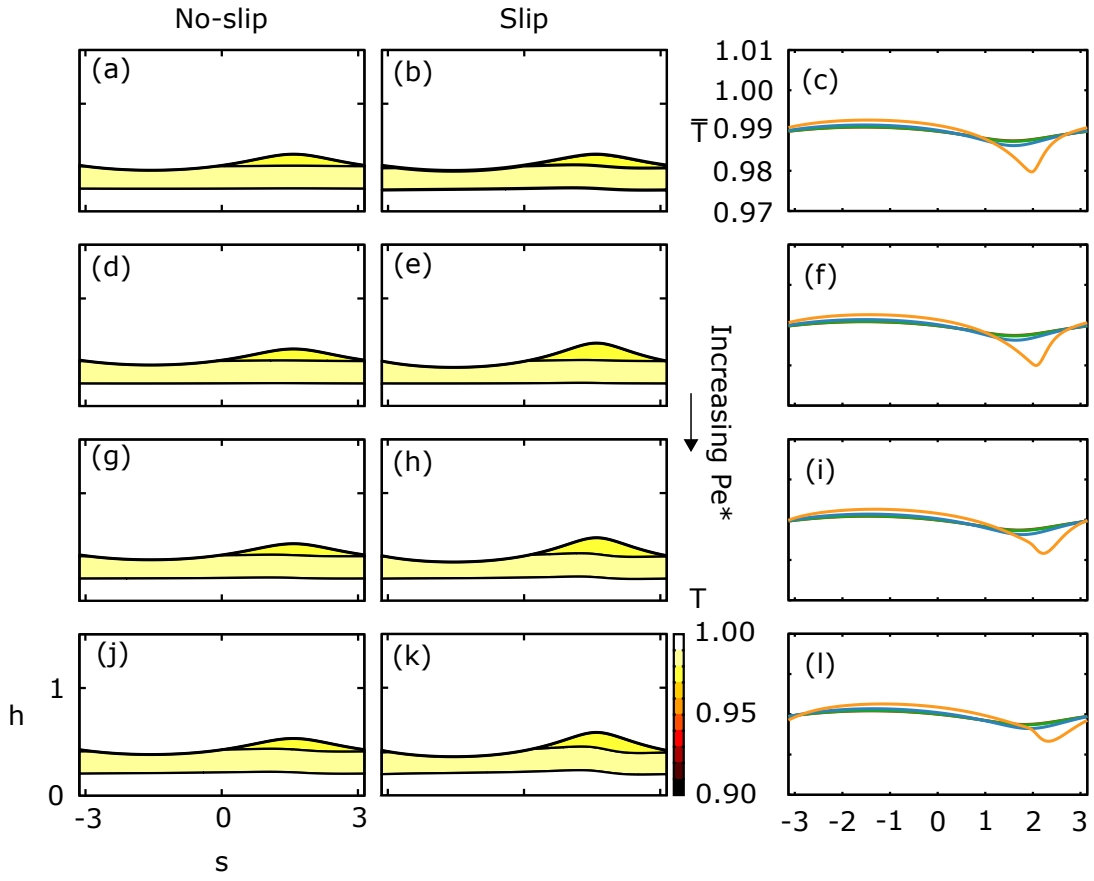


Figure 5.5: The role of convection on smooth films, the first column is for $l_s = 0$ and $l_s = 0.1$ in the second column. Panels (a) - (c) are with $Pe^* = 0.01$, row two for $Pe^* = 1$, row three for $Pe^* = 5$ and the last row by $Pe^* = 10$. The third column is the mean temperatures for various slip lengths, with $l_s = 0$ given in *red*, $l_s = 10^{-2}$ in *green*, $l_s = 10^{-1}$ in *blue* and $l_s = 5 \times 10^{-1}$ coloured *orange*.

is confirmed by the temperature profiles in figure 5.5, where the temperature is shown to change with strong thermal convection at $Pe^* \geq 5$. With partial slip on the chamber wall, the smooth solutions show several changes in temperature with convection. This is shown in figure 5.5 for a moderate slip length of $l_s = 0.1$. These changes are a reduction in mean temperature at the thickest film and an increase in the thinnest part, shown in the mean temperature profiles of figure 5.5.

Contrary to the independence of smooth films to convection, the temperatures in the pooling films are found to be strongly affected by thermal convection. With a constant filling fraction of $A = 1.982\varepsilon$, a comparison of the film profiles and temperature fields is presented with partial slip acting on the wall and when there is no-slip.

When the flow has a low Péclet number, the conduction is dominant, meaning the temperature is found to reduce as the radial distance from the wall increases. This creates a cold region at the surface of the pool, shown in figure 5.6. When

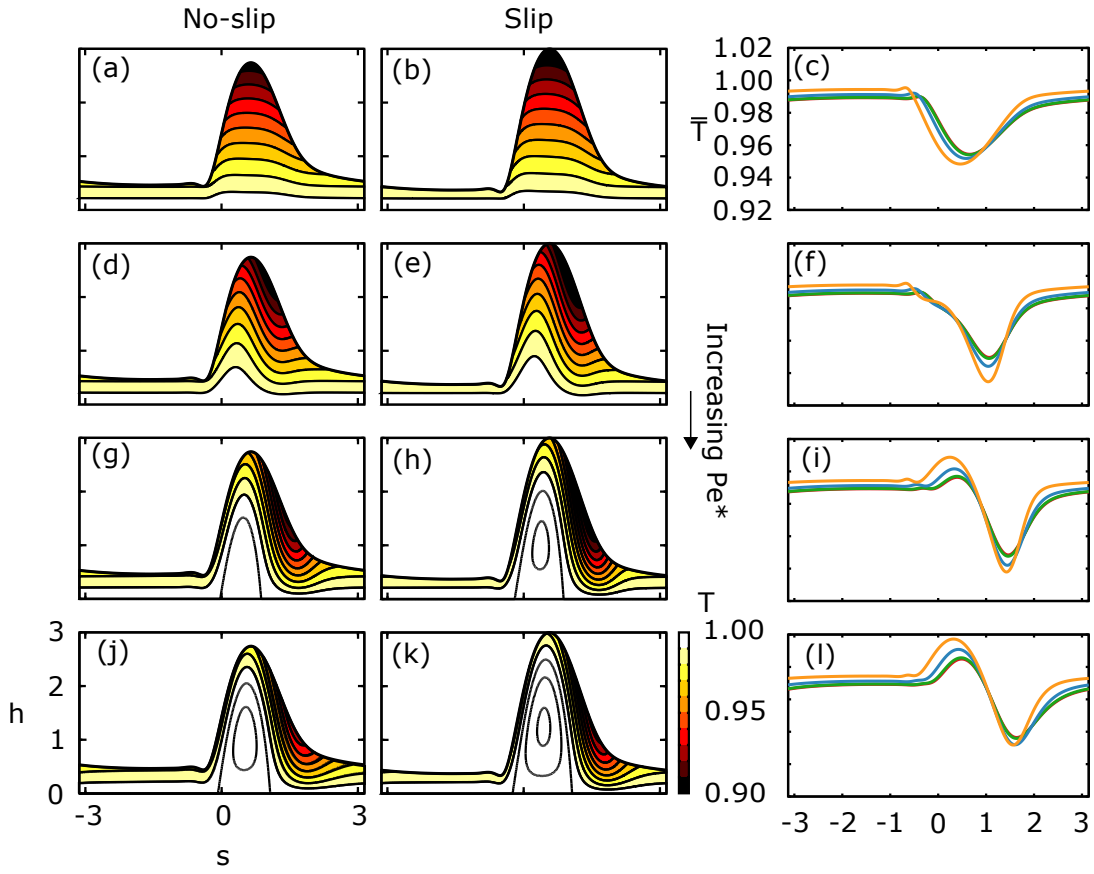


Figure 5.6: The role of convection on pooled films, the first column of panels are with $l_s = 0$ while $l_s = 0.1$ is for the second column of panels. The first row are for $Pe^* = 0.01$, the second row with $Pe^* = 1$, the third row is with $Pe^* = 5$ and $Pe^* = 10$ in panels (j), (k) and (l). The mean temperatures for various slip lengths in the third column are given by; *red* for $l_s = 0$, *green* for $l_s = 10^{-2}$, $l_s = 10^{-1}$ by *blue* and *orange* for $l_s = 5 \times 10^{-1}$.

the strength of convection increases, the cooled region at the pool surface is moved up higher on the rising wall. There is also significant heating at the front of the pool, which rapidly propagates throughout most of the pool. This is shown for $Pe^* \geq 1$ in figure 5.6.

The transition to hotter pools as Pe^* increases also causes a second peak in the mean temperature profile to develop as heat enters the pool. This is shown in the mean temperature profiles in figure 5.6 (i), where this second peak is significant. The initial hump in the mean temperatures arises due to the capillary forces creating a small dimple ahead of the pool entrance, which is located near $s = 0$, this is shown in panel (c) of figure 5.6 (c). There is a conduction dominant region outside of the pool irrespective of the Péclet number. Which is in the narrow thin film coating the cylinder, like the smooth profiles. The narrow film has small azimuthal gradients and is therefore independent of convection.

The film temperatures are very similar with a moderate slip length, though

the pool is deeper by as much as 9.4 %. This is because fluid has been drained from the thin coating region around the cylinder. This deeper pool has reduced the minimum film temperature by approximately 1 %, with the deeper and colder pool shown in figure 5.6 (c).

The cooler region at the pool surface is an important feature of the thermal profiles, this is shown in figure 5.6 (a). This region is found to be moved by the effects of including moderate fluid slip effects at the cylinder wall, which is shown in figure 5.6 (b). However this is clear when the effects of moderate thermal convection are included, noticeably when $Pe^* = 1$ and $Pe^* = 5$ the colder fluid is higher up the cylinder wall. This is shown in panels (e) and (h) of figure 5.6. As convection increases, the temperature of the fluid at the entrance to the pool has been found to increase if there is no-slip. This temperature increase is found to be greater as the thermal convection effects combine with effects from slip to make the pool entrance hotter, which is shown in figure 5.6 (h) and (k). This increase in temperature of the pool also causes the colder region to reduce in size and is clearly shown between the panels of (j) and (k) with $Pe^* = 10$ in figure 5.6.

The convection independent flow outside of the pool combines with the changes to the cooled region, to create greater thermal gradients, this is shown in the mean temperature profiles of figure 5.6 (i). Along with the heating effects from slip, the minimum film temperatures are also much lower in comparison to the temperatures with no-slip. When the convective effects are equal or stronger than conduction with $Pe^* > 1$, the film temperatures at the surface of the deepest part of the pool are much higher as the cooled region has moved around further due to slip, shown in figure 5.6 (f, i, l).

5.4 Combined Effect of Inertia and Convection on Temperatures both with and without Slip

With the influence of thermal convection established, the effects of inertia on pooling films are investigated. The pooling films are studied as smooth films, which are typically thin conduction dominant flows with little variation from fluid slip. The reduced Reynolds number is gradually increased from an initially low value of $Re^* = 0.01$ until the inertial terms may be equivalent to leading order terms. Initially the films are equal to those that were previously detailed in Section 5.3 where a deep pool forms. Most of the thermal effects will be concentrated within the pool and the immediately adjacent region leading out of the pool.

Irrespective of the thermal properties of the film, the profiles of the film

follow a clear pattern regarding inertial effects for the constant filling fraction of $A = 1.987\varepsilon$. The film profile starts as a deep pool when there is low inertia, shown for $Re^* = 0.01$ in figure 5.7 (a). A large scale smoothing effect of the film surface happens with moderate inertia, this is shown for $Re^* = 1$, in figure 5.7 (b). This smoothing leads to a reduction in the pool depth that can be measured and causes an increase in the thickness of the film trailing from the pool. These films have capillary ripples at the surface as surface tension stabilises the films, these ripples are clearly shown for $Re^* = 5$ in panel (c) of figure 5.7 and form in front of the bulk fluid contained within the pool. These surface ripples are amplified considerably as inertia gets stronger, shown in figure 5.7 (d) with $Re^* = 10$. The pool depth also reduces with inertia and the trailing region becomes thickened by the smoothing effect of stronger inertia. If the inertial effects are very strong when $Re^* = 100$, the films are nearly uniform in height. These are equivalent to a thicker variation of the smooth solutions where there are only small azimuthal gradients, these are shown in figure 5.7 (e). These strong inertial effects assumes $h' \ll 1$ from (3.50) and the smooth solutions satisfies this condition. These trends are shown for each row of figures 5.7 and 5.8, while only the Péclet number is varied for each column.

In flows where the thermal conduction is the dominant force, the temperatures within the films are dependent on the radial distance from the cylinder wall. This is characterised by the flows with $Pe^* = 0.01$ in panels (a, b, c, d, e) of figure 5.7. The radial temperature gradients of each of these films are found to be independent from inertial effects, which is best shown in panel (d) of figure 5.7. There are small temperature variations in the azimuthal direction, which are proportional to the variations in the free surface. The effect of inertia has been to reduce the maximum film depth and cause the capillary ripples to form from surface tension effects. While the film surface has changed, the radial temperature gradients have remained the same between panels (a) and (e) of figure 5.7.

When the fluid is pooling around the cylinder base, the temperature within the pool will increase with increasing Pe^* while the cooled region will advance up the rising cylinder wall. This was shown in Section 5.3 and is shown for $Re^* = 0.1$ in panels (a, f, k, p). If the inertial effects are comparable to the viscous effects with $Re^* = 1$, the film profile is similar to the flow with $Re^* = 0.1$. The film profile still resembles a pooling solution and the changes to film temperatures with thermal convection are similar. The pool becomes heated with stronger convection and the location and volume of the cooled fluid are changed.

With inertia at a moderate level and convection equal to conduction, corresponding to $Re^* = 5$ and $Pe^* = 1$, a small ripple in the temperature of the film is found. This ripple matches the waves on the surface, which are shown in figure 5.7

(h). This is also found with stronger convection as the temperature more closely resembles the film surface, shown in parts (m) and (r) of figure 5.7. The cooled region is convected up the cylinder wall where the bulk of the fluid has pooled. This pool of fluid would be lower in the cylinder if inertia were negligible.

There are big differences between the films in parts (c) and (m) of figure 5.7. The film shows a significant heating effect from convection which occurs in the bulk of the fluid. The temperature profile also matches the surface waves as the fluid temperature close to the wall varies significantly in the region with capillary ripples. While this is found when $Re^* = 10$ and $Pe^* \geq 1$, this is not found if $Pe^* < 1$.

The film has a uniform depth across the domain with very strong inertia, shown in figure 5.7 (e, j, o, t) where $Re^* = 100$. These uniform films have lost the temperature changes that come with thermal convection. These films are thicker variation of the smooth films where the azimuthal gradients are zero, so they are independent from convection.

The effects of moderate slip in combination with inertia and convection have been explored with the same filling fraction used for the films with no-slip of figure 5.7. These films are presented in figure 5.8. The main difference between the films with weak inertia is that the pool is significantly deeper by 9.6 %. This deeper pool is a result of the depth of fluid around most of the cylinder being much thinner. The minimum film thickness has reduced by 20 % due to the slip at the cylinder surface. These differences are shown in figure 5.8 (a) when compared to figure 5.7 (a). With weak thermal convection the films with and without slip are similar. However, the deeper pool means the temperatures at the surface are lower by 1 % as the cooling effects of the air flow increase.

With fluid slip on the cylinder, the film profiles at each Reynolds number are like those with no-slip. As inertia increases, the pool also becomes smoothed, this is shown in figure 5.8 (b) with $Re^* = 1$. The maximum film height with $Re^* = 1$ with slip is approximately the same as the height when there is no-slip and $Re^* = 0.1$, shown in figure 5.7 (a). At moderate inertia, the film surface has features which are very similar to those described for no slip, when the reduced Reynolds numbers is between 5 and 10. However, the amplitude and frequency of the capillary ripples at the surface are now higher due to the slip condition. This change is clearly shown in figure 5.8 (d) where the number of observable ripples has doubled. With a Reynolds number of 100, the film becomes dominated by inertial effects which causes significant smoothing. The large fluid slip of $l_s = 0.1$ has no change on the film temperatures of the films with strong inertia as the films have a uniform depth around the cylinder. These inertia dominant films have a temperature profile which solely depends on the radial distance from the

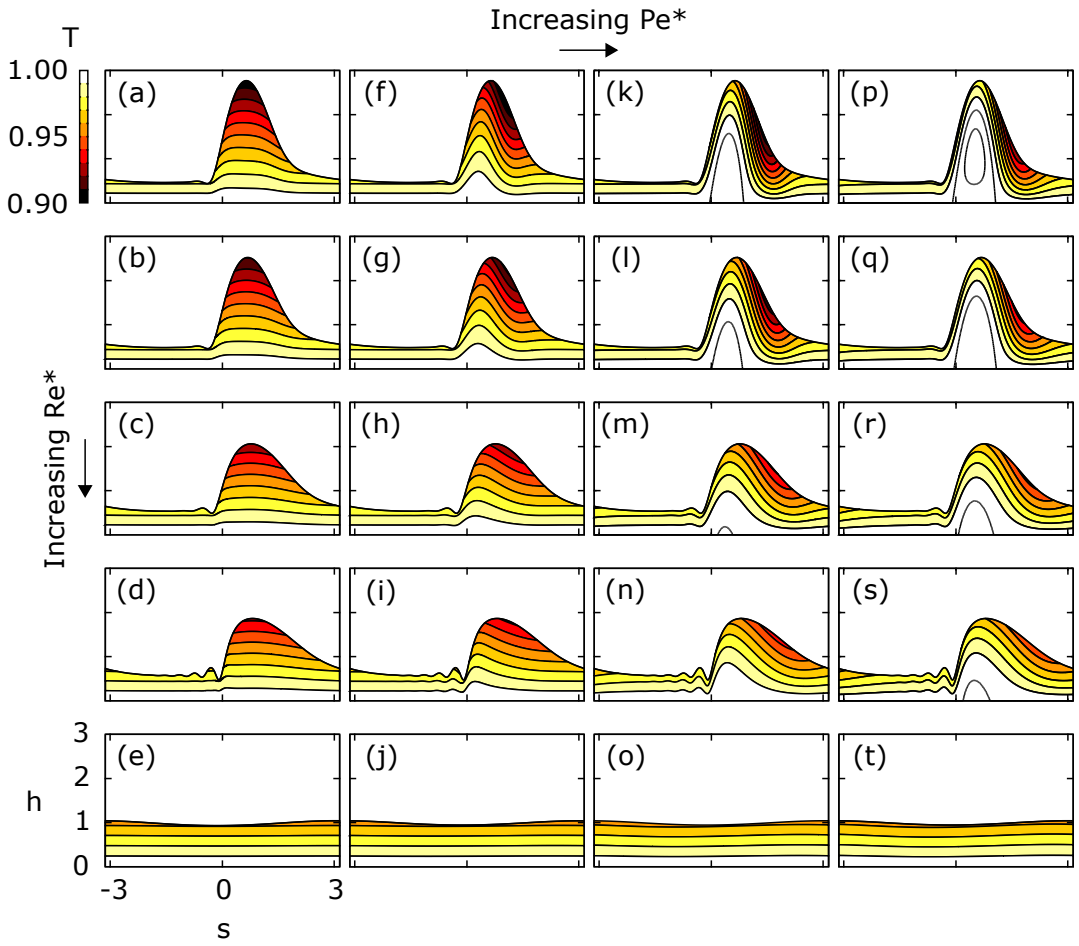


Figure 5.7: Inertial and thermal convection on pooling films, for the no-slip case. The Péclet number, Pe^* is given as 0.01, 1, 5 and 10 for columns one, two three and four respectively. The magnitude of inertia by the Reynolds number, $Re^* = 0.1$ in row one, $Re^* = 1$ for row two, $Re^* = 5$ for row three and $Re^* = 10$ in row four. The last row of panels are for $Re^* = 100$.

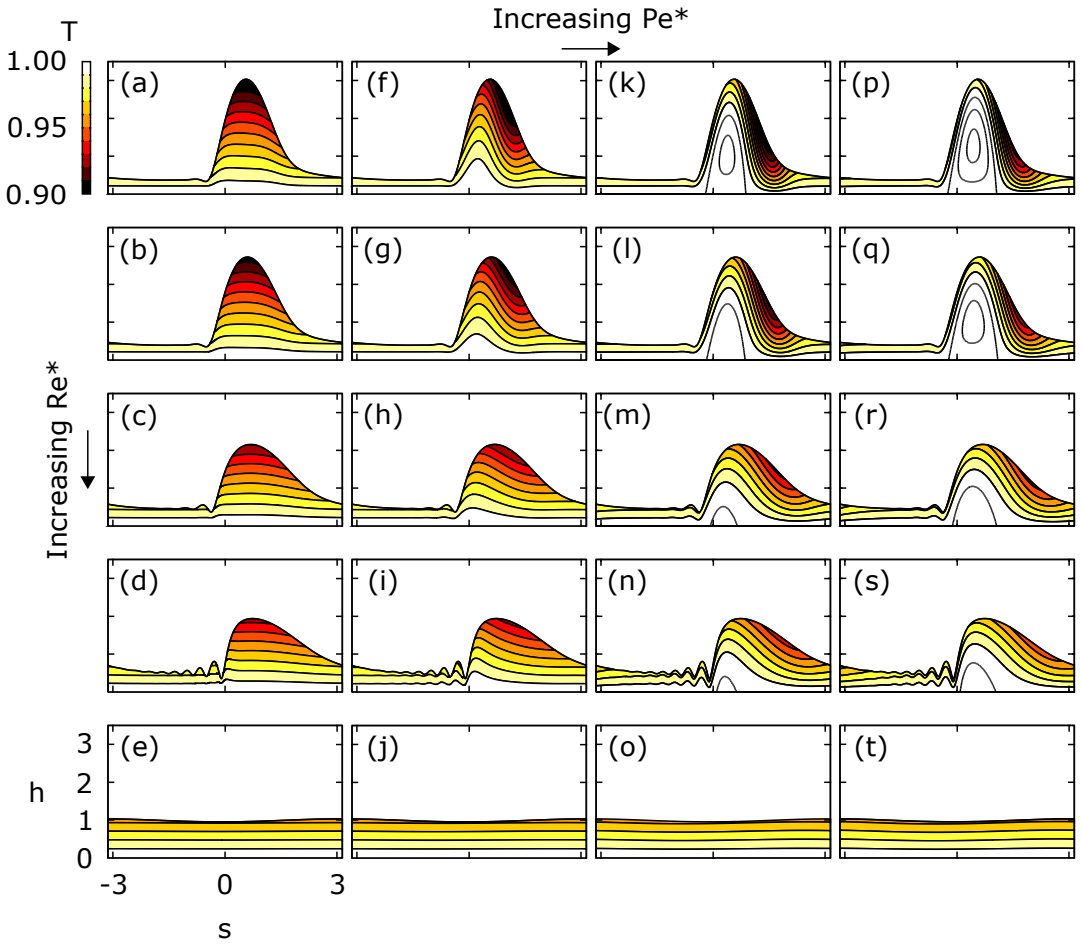


Figure 5.8: Inertial and thermal convection on pooling films, for $l_s = 0.1$ and $A = 1.987\varepsilon$. The Reynolds number of row one is $Re^* = 0.1$, increasing to $Re^* = 100$ in the last row, row two has $Re^* = 1$, row three is with $Re^* = 5$ and row four has $Re^* = 10$. The Péclet number, Pe^* increases between each column, from 0.01, to 10, with columns two and three having $Pe^* = 1$ and $Pe^* = 5$ respectively.

wall, which are shown in figure 5.8 (e, j, o, t).

The temperature gradients across the film when conduction is dominant are similar for every Reynolds number, shown in the first column of figure 5.8. The effect of slip in creating a deeper pool which has a colder region is an important feature to observe when convective effects increase. When the convective effects are equal to conduction at $Pe^* = 1$, this colder cool region near the peak of the film is moved higher up the rising wall. This effect was also found when there is no-slip, though the minimum temperature of the films with slip is lower. The film is shallower around much of the cylinder with slip on the walls, which causes the surface temperatures for most of the film to be higher. This is clear in panels (g) of figure 5.8 in comparison to panel (g) of figure 5.7, where the only parameter difference is that slip is acting on the wall. The stronger effect of convection with

$Pe^* = 1$ is found to causes the cold tips at the surface of the capillary ripples to move closer to the pool which is shown in figure 5.8 (i). This effect has been amplified by slip, moving the cold surface further than if there was no-slip.

When the effects of convection are several times stronger than conduction, the cooler region is even higher up the rising wall with slip and the Péclet number is 5. This is shown in figure 5.8 where $Re^* \leq 5$. With a Reynolds number which is higher than 5, the cooler region with slip remains colder though there is a clear difference in the internal temperatures. The temperatures fluctuations beneath the capillary ripples have a greater amplitude with slip, shown in figure 5.8 (n) where the temperature gradients reflect the film surface gradients.

Many of the unique changes that occur with thermal convection have been detailed with no-slip and slip $Pe^* = 5$ in figures 5.7 and 5.8 respectively. The cold region that is found at the surface of the pool has diminished in size and moved location, while the film has increased temperature for most Re^*. The exception to this has been when $Re^* = 100$ as the films with and without slip are identical, shown in figure 5.8 parts (p, q, r, s) and figure 5.7 parts (p, q, r, s).

The changes that come with very strong convection at $Pe^* = 10$ have already been shown with weaker convection, though the effects detailed at each stage are greater, as shown in the last column of figure 5.8. Interestingly, the differences in the film temperatures between the no-slip and slip solutions are smaller. This is because thermal convection has become the dominant effect for the temperatures. The thermal gradients within the film are much larger around the pool and leads to greater variation in the mean temperatures, as shown in figure 5.8 (p). However, these variations lead to simulated mean temperatures, $\bar{T}$ which are higher than expected within the film.

The effect where slip causes the film speed u to be faster means that the thermal convective terms which are connected to the film velocity are amplified. These terms are shown in (3.121) and lead to the larger movement of the cold regions in comparison to those with no-slip.

The mean temperature profiles provide a quantitative comparison between the films where there is slip and no-slip. The effects of thermal convection and inertia on the mean temperatures are presented in figure 5.9. When the viscous effects are stronger than the inertial effects, the greatest difference in the mean temperatures are found when $l_s = 0$ and $l_s = 0.1$ are found. This is shown in the first row of mean temperature profiles of figure 5.9 where $Re^* \leq 1$.

The azimuthal gradients in the mean temperatures, $\bar{T}$ have been increased with slip, this is clear with stronger convection in parts (k) and (p) of figure 5.9 where $Pe^* \geq 5$. However, these bigger gradients have been connected to difficulties in calculating the internal film temperatures accurately. This difficulty is because

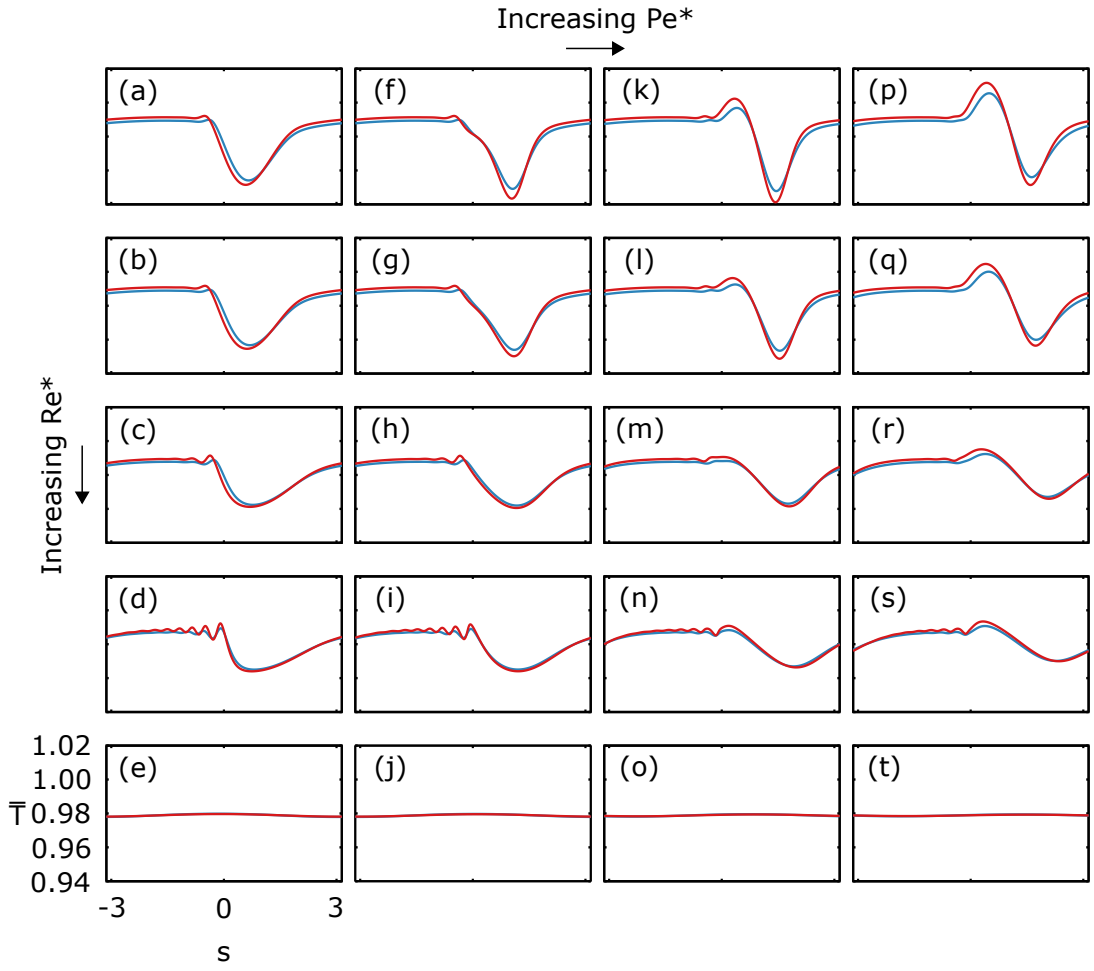


Figure 5.9: Comparing the role of slip on the mean temperature fields from figure 5.7 and figure 5.8, for $l_s = 0$ in *blue* and $l_s = 0.1$ in *red*. The increasing inertia between each row from $Re^* = 0.1$ to $Re^* = 100$ and Péclet number from Pe^* and $Pe^* = 10$ are equal to figures 5.7 and 5.8.

the mean temperature, $\bar{T}$ may be discontinuous across the domain s. This is because there may be local variations in the film temperature in steady-state flows. However, the definition for the mean temperature $\bar{T}$ appears to be best for flows with smaller azimuthal gradients. This is because the flow flux is thought to be an accurate representation of the mean velocity. While the flow flux is also a continuous function throughout the domain s, for a steady-state film the value of q must be constant across the domain. This is because the volume of fluid flowing from one area of the domain must be equal to the volume of fluid in any other area. However, the temperature distribution in one area of the domain does not have to be the same as another area. This is mainly when there are large changes in the depth of the film. Therefore, it may be possible that a higher order polynomial used to approximate the temperature profile may be more accurate. As the additional terms may provide the necessary flexibility with film profile variations that the local temperature effects can be determined accurately.

Overall, the change in temperatures with Re^* and Pe^* can be summarised with the following features; there is a narrowing of the wide trough for $Re^* \leq 1$ as convection increases, the thermal ripples found at $Re^* = 5$ and $Re^* = 10$ are larger with convection and the films $Re^* = 100$ are independent of convection. This behaviour is found for flows where there is slip and no-slip and have been shown in figure 5.9. There is also a clear difference in the film temperatures for flows where there is slip. This is mainly the amplifying effects that slip has on the convective effects, which have been shown in figure 5.8 in comparison to figure 5.7.

5.5 Development of Shock Solutions with Inertial and Thermal Convective Effects

With the influence of thermal convection and inertial forces detailed for a pooled film, a smaller fluid volume of $A = 0.011\varepsilon$ leads to a shock type flow with moderate slip, $l_s = 0.1$. This steady state film is at the precipice of developing into a recirculating pool for the applied surface shear while still maintaining unidirectional flow. The reduced Reynolds numbers, $Re^* = 0.1$ in figure 5.10 (a, b) or $Re^* = 1$ in (d, e) show a typical shock front at $s \in [0, 2]$ in the form of large h'.

The capillary ripples from surface tension that counter rising instabilities from inertia, similar to those of the pooled solution are noticeable in front of the steep pool at $Re^* = 5$ of figure 5.10 (g) and (h). This sharp front is largely smoothed at $Re^* = 10$ in figure 5.10 (j, k). The key thermal difference between those of shock and pooled films is the smooth films occur at a lower Re^*, therefore become independent of convection due to the film being smooth. Otherwise, the increase

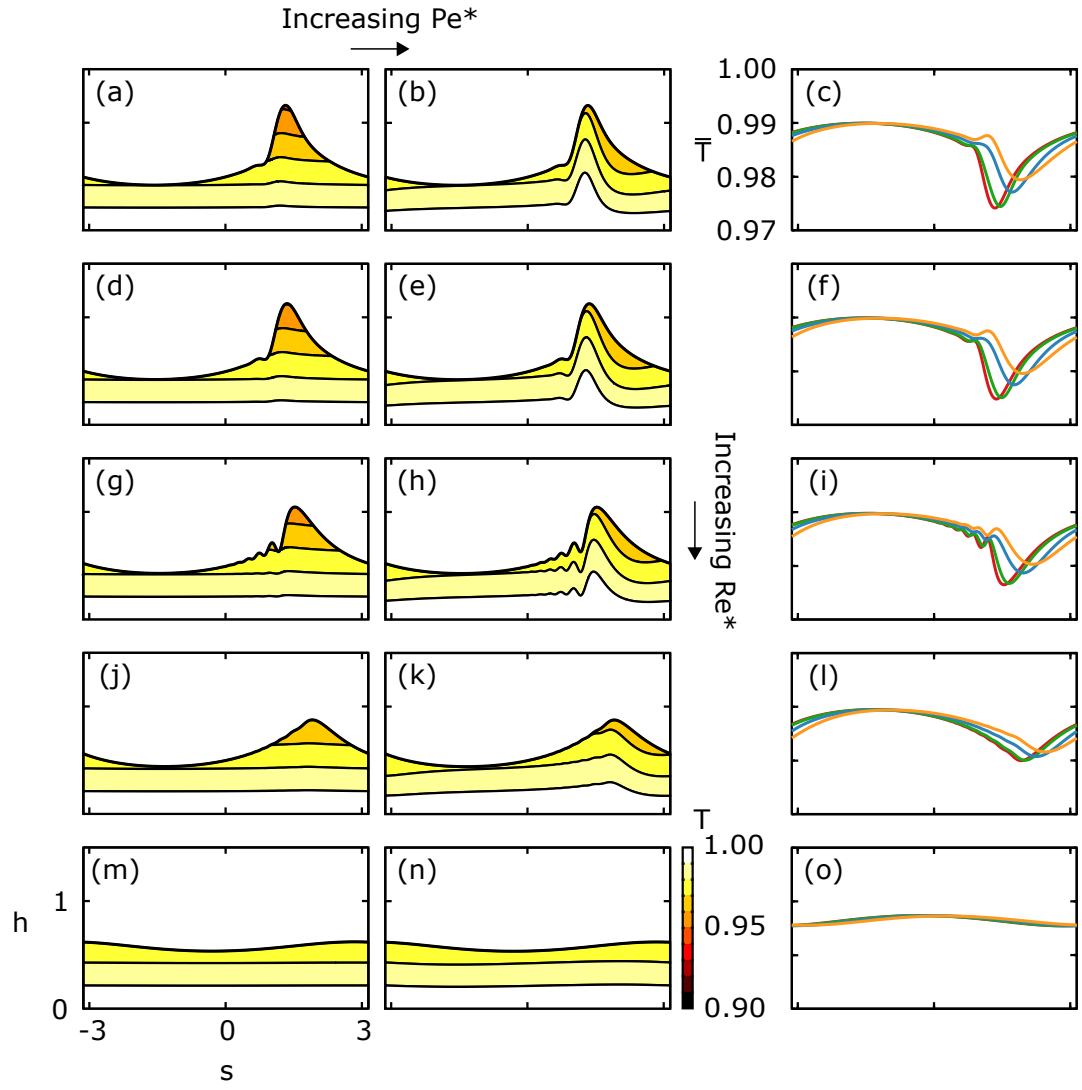


Figure 5.10: The shock solution, with the Péclet number $Pe^* = 0.1$ in column one and $Pe^* = 10$ in column two while the mean temperatures for several Péclet numbers are in panels (c), (f), (i) and (l). The Reynolds number for each row is given as 0.1, 1, 5, 10 and 100 respectively. The varying Péclet numbers in column three are coloured as $Pe^* = 0.1$ in *red*, $Pe^* = 1$ in *green*, $Pe^* = 5$ in *blue* and $Pe^* = 5$ coloured in *orange*.

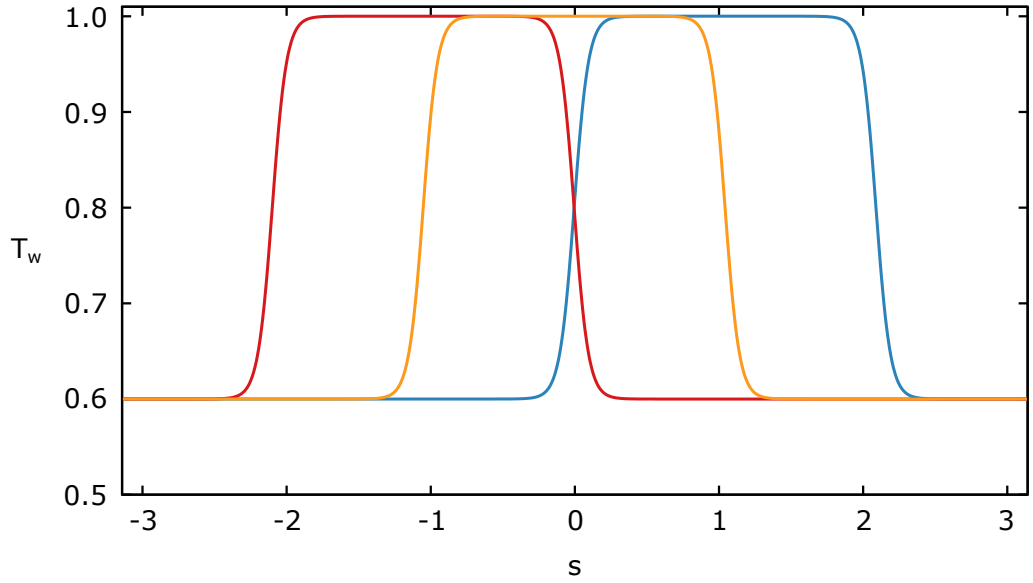


Figure 5.11: The step functions for defining the rising *red*, central *orange* and falling *blue* wall locally heated sections.

to thermal convection reflects the observations outlined previously in Section 5.4.

5.6 Localised Thermal Effects Across a Heated Patch

The prescribed wall temperature on the fluid boundary in (3.47) has been changed to a non-uniform temperature function for this Section. A hyperbolic tangent function has been used to create a smooth step profile where the temperature can be higher in a small area of the cylinder, this is given as

$$T_w = 1/2\,(T_m - T_M)\,[1 - \tanh\,(-k\,[|s+\delta| - L])] + T_M, \tag{5.1}$$

where we define T_m as the minimum cylinder wall temperature and T_M as the maximum wall temperature to create a hotter patch on the wall. The transformation region between T_m and T_M is controlled by the parameter k, where the imposed wall temperature T_w appears as a sharp step function as $k \to \infty$. To allow for an asymmetric wall temperature in the chamber, δ acts to shift the patch around the domain and L defines the half length of the patch, such that the patch is found at $-L + \delta < s < L + \delta$ for $L = \pi/3$. The transition parameter set to $k = 10$ creates a smooth step function, which ensures a smooth introduction of a localized heating on the film. By assuming $T_m > T_a$, a positive temperature gradient between the air and cylinder is maintained which draws heat from the cylinder and across the film.

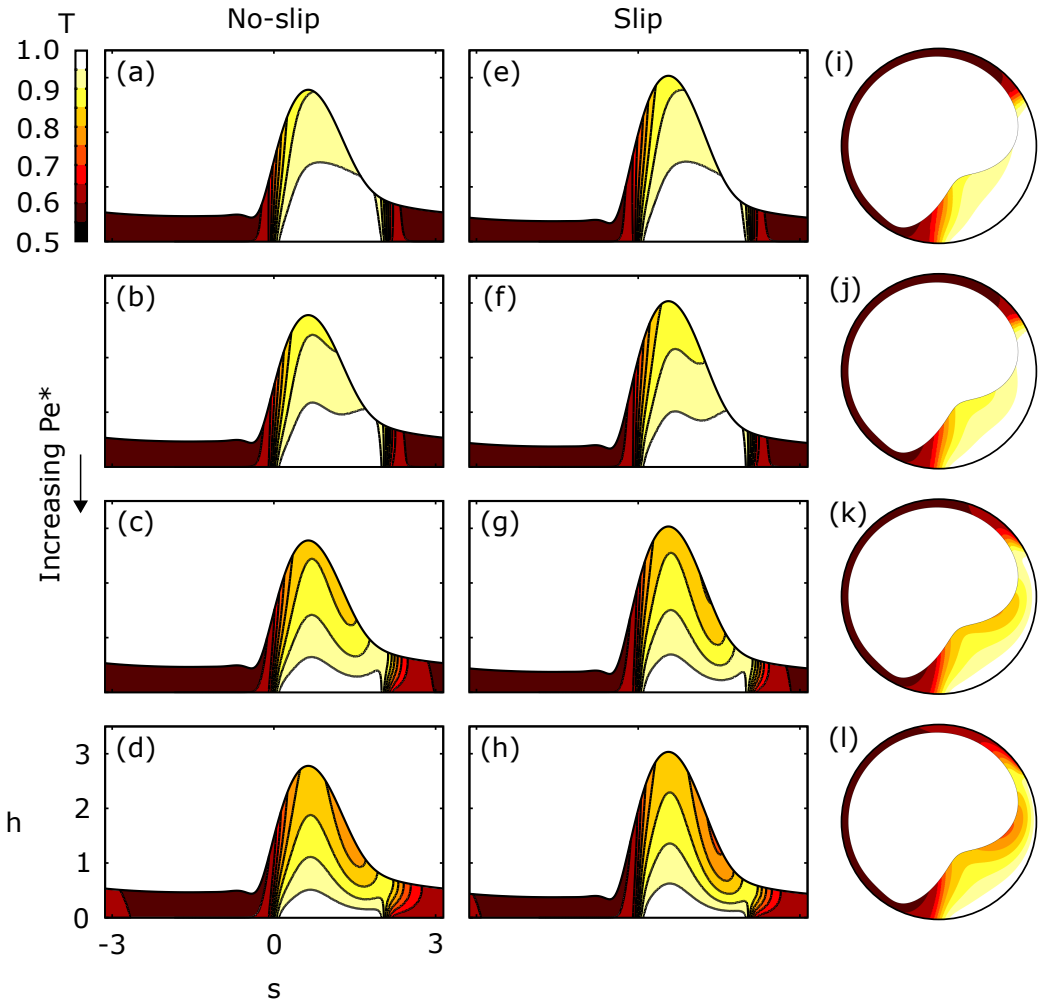


Figure 5.12: Thermal convection and partial slip on the rising wall heated patch, with Pe^* given in increments of 0.1, 1, 5 and 10 for each row from top down respectively. The temperature profiles in column one are for no-slip and column two for $l_s = 0.1$. The third column is the cylindrically mapped temperature profiles with $l_s = 0.1$.

5.6.1 Heating a Section of the Rising Wall

With the heated patch defined by $T_m = 0.6$ and $T_M = 1$, we cause the rising wall to experience a local heating by setting $\delta = -\pi/3$, as shown in figure 5.11, to investigate how convection and partial slip alter the film profiles and thermal solutions. In a conductive flow, solutions for $Pe^* = 0.1$ in figure 5.12 (a) represent a large heated region in proximity to the patch that exhibits sharp temperature gradients, with minor thermal spreading from the heated region due to conduction. As convection is increased (figure 5.12 (b)), there is a spreading of the heat away from the patch. Whilst the colder thin coating film is conveyed across the pool, leading to a reduction in the proportion of heated fluid within the pool.

These effects are further emphasized with stronger convection, shown in parts

(c) and (d). The presence of slip on the surface using the same filling fraction results in the thinning as shown previously, leading to the deeper pool of fluid. The increased velocity of the fluid at the wall is found to intensify the convection of the fluid and enhances the cooling of the pool by the core airflow. This is also coupled with greater spreading of the heat within the pool and away from the patch, which is shown by reductions in both the temperatures within the film in figure 5.12 (g). More evidence of this effect with stronger convection is shown in part (h) of figure 5.12 where slip has caused the heated region to shrink in size.

5.6.2 Films Being Heated at the Falling Wall

Upon relocating the heated patch around the cylinder and away from the pool, setting $\delta = \pi/3$, another view of convection within the film is obtained in figure 5.13. In the conduction dominant solutions of (a), there is minimal permeation of the heat away from the patch with a small spread due to slip in (e). As the convective forces are increased, a spreading of heated fluid into and across the pooled region away from the patch occurs as in figure 5.13 (g). However, with the heated patch being located predominantly under the thinner portion of the film, that is near uniform, the small azimuthal gradients mean thermal convection is not as important as in the pool. The hot regions near to the patch, shown between $Pe^* = 0.1$ in (a) and $Pe^* = 10$ in (d) around the region of $s < 0$ are largely similar, unlike in the rising wall scenario. The increased fluid velocity at the cylinder surface due to partial slip enhances the spreading of heated fluid across the pool, see part (g) and (h) in comparison to (c) and (d) respectively. The main heated region for $T > 0.9$ in the thin section of the film remains unaffected by either slip or thermal convection.

5.6.3 Symmetrical Heating at the Cylinder Base

A symmetrical cylinder with a heated region which is centered about $s = 0$ has the patch located within both the pool and thin coating film, as shown by figure 5.14 where $\delta = 0$. The influence of convection is comparable for the heating of both the rising and falling wall locations of figure 5.12 and figure 5.13. There is a difference in the thin heated region in front of the pool when there is strong thermal convection, where heat is spread further away from the patch, shown in figure 5.14 (c) and (d) with $Pe^* > 1$. The addition of slip causes the heat to permeate further in the film, shown in panels (g) and (h). There is also a noticeable increase in the pool temperature for stronger convection and slip. This leads to a sharp change in the mean temperatures shown in the steep rise about $s = 2$.

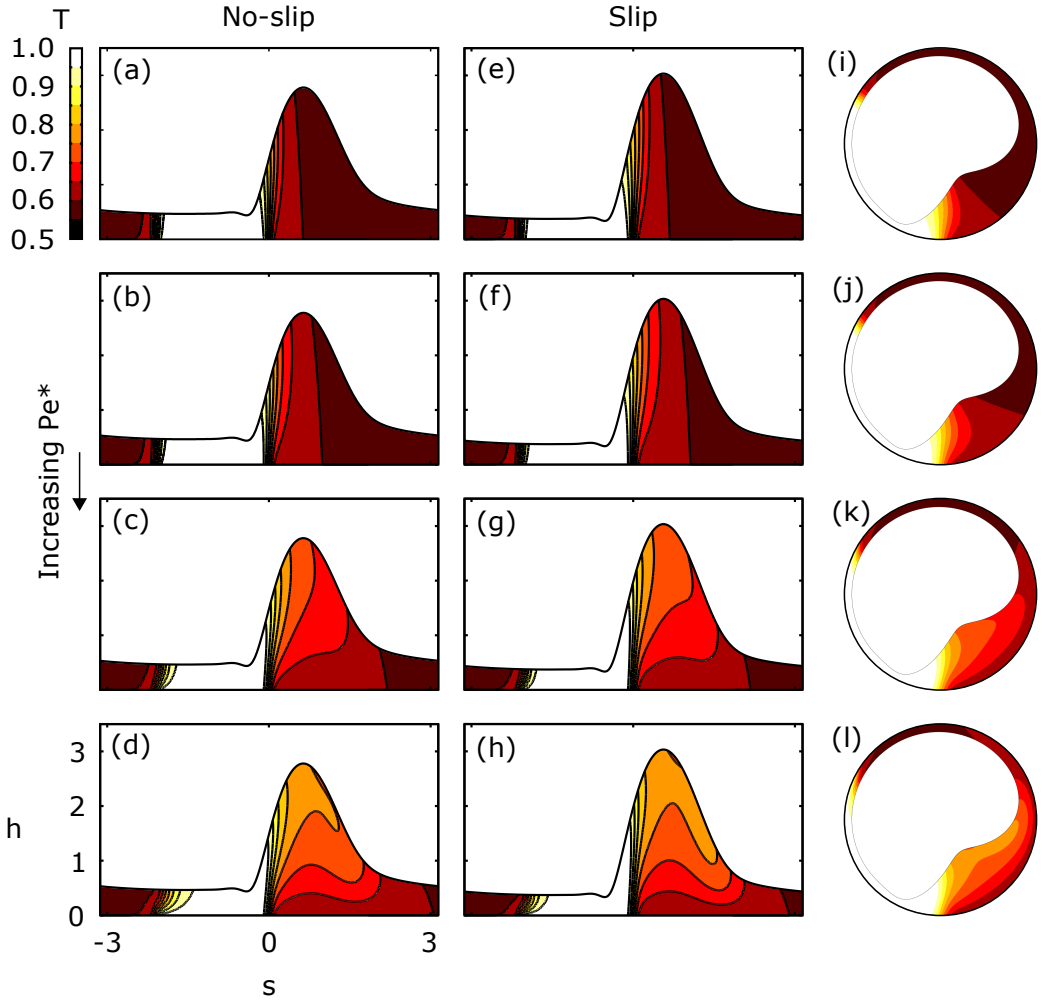


Figure 5.13: The falling wall heated patch with increasing thermal convection and partial slip. The temperature profiles in panels (a) - (d) are for no-slip and panels (e) - (h) for $l_s = 0.1$. The increasing thermal convection down each row is given by $Pe^* = 0.1$, 1, 5 and 10 respectively with the slip solutions reconstructed as cylindrical flow in column three.

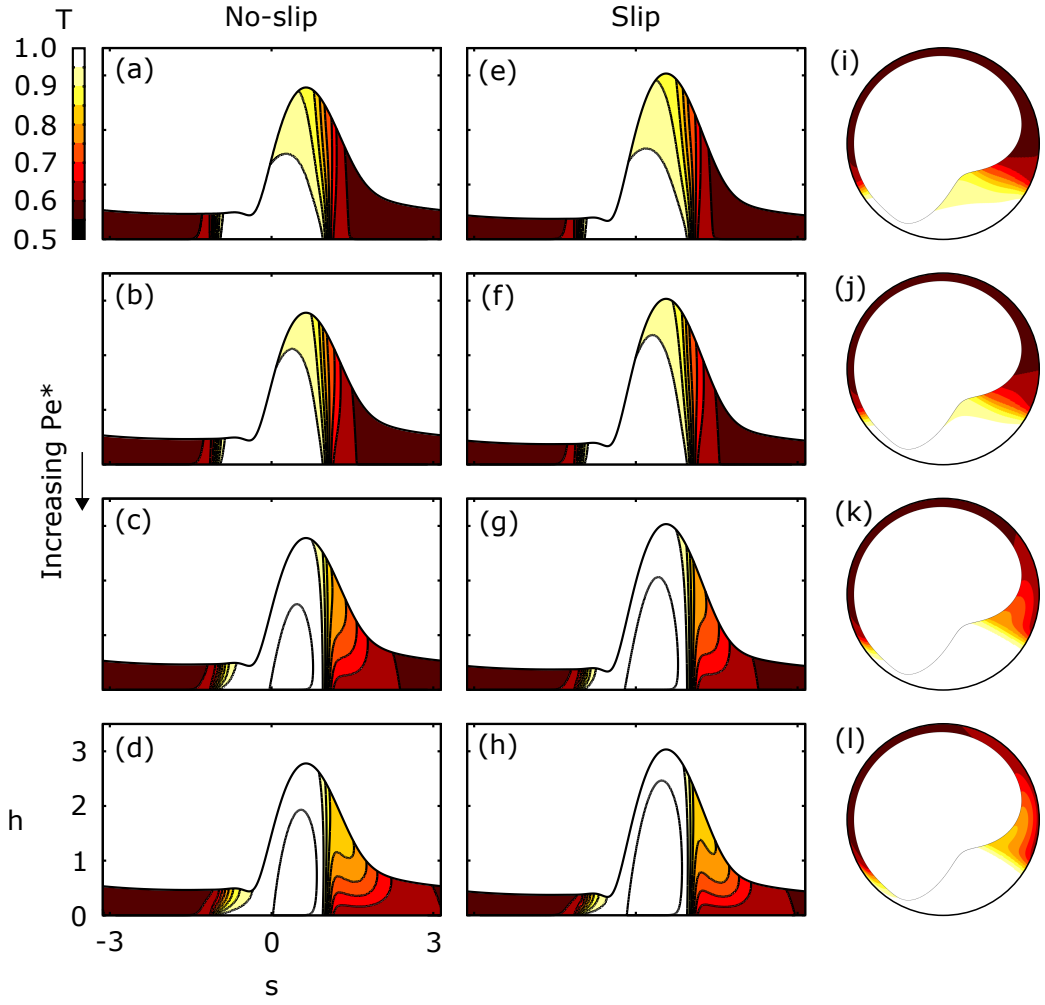


Figure 5.14: The localised heating of the cylinder base, the reconstructed cylinders in panels (m) - (p) are with $l_s = 0.1$. The Péclet number increases across columns one to four at intervals $Pe^* = 0.1$, $Pe^* = 1$, $Pe^* = 5$ and $Pe^* = 10$ respectively. The no-slip condition has been applied for panels (a) - (d) while panels (e) - (h) have a partial slip condition with $l_s = 0.1$.

5.6.4 Localised Heating Effects on the Mean Temperatures

In this Section the location of the heated patch has been quantitatively compared using the mean temperature profiles. The location of the hotter patch has been found to strongly determine how much thermal convection can change the film temperatures.

The difference to the temperature fields in all three locations with $Pe^* = 0.1$ show the differences between the no-slip and slip cases are small, as shown in figure 5.15. However, with stronger convective effects, the effect of slip is clearly shown in figure 5.15. As convection is increased, the cooling of the film is shown with the reduction in the mean temperature with $Pe^* = 1$ in panel (d). This is complemented by the increase to the film thickness which changes the volume of fluid being represented by the mean temperature. Slip also heightens the drop in mean temperature before creating a secondary spike around the pool exit, shown in mean temperature in figure 5.15 (i).

The effect of slip however, can be clearly shown as an amplification of the overall effect that thermal convection has on the film temperature, shown in figure 5.15.

5.7 Chapter Summary

This Chapter details many of the thermal features that are a result of fluid slip on the cylinder walls and how these effects can combine with the effects of thermal convection. Having described the changes in film profiles due to slip previously, the changes to internal temperatures are explored using the depth-averaged model of Chapter 3. A caveat to this study is the assumption that there is a sufficiently high heat transfer rate from the film surface into the air, otherwise the film reaches the wall temperature and there is no discernible variation in the fluid temperatures. The results have shown that when the film has a uniform depth around the cylinder, in most instances there is negligible changes to the temperature profiles with stronger convective or slipping effects.

If the film is not uniform in depth, the changes to temperature with stronger convection is significant. First, the average temperature increases with convection and second, the fluid contained within the pool increases in temperature sharply. With moderate inertial effects within the model, the transitional film profiles outlined in Chapter 4 have also been investigated for different strengths of convection. These findings are in good agreement with the previous studies and have been used to validate the depth-averaged model.

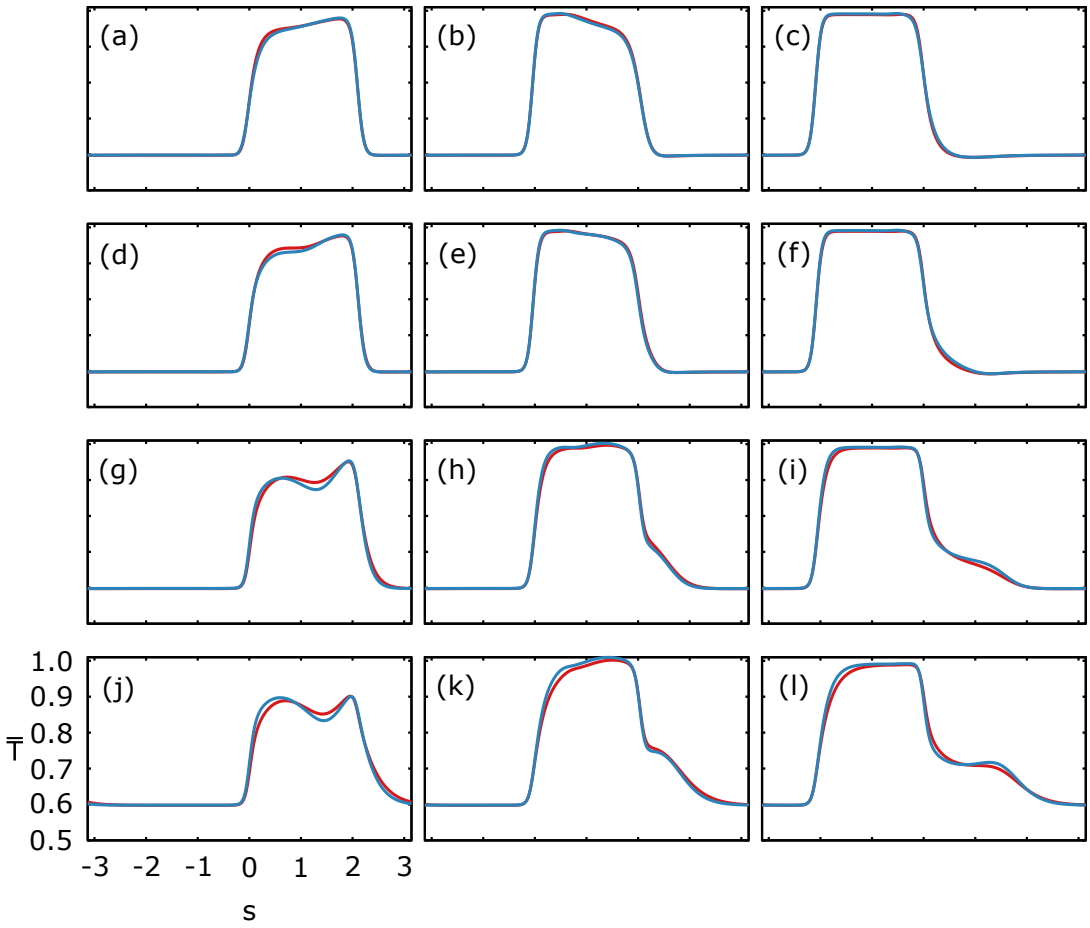


Figure 5.15: The effect of thermal convection and partial slip on the rising wall heated patch, with Pe^* given in increments of 0.1, 1, 5 and 10 for each row. The columns represent the rising, central and falling wall scenarios respectively. The temperature profiles in row one are for no-slip and row two for $l_s = 0.1$. The mean temperature profiles are for no-slip *red* and $l_s = 0.1$ *blue*.

There are no direct changes to the fluid temperature as a result of including slip on the cylinder walls in flows where conduction is the main thermal effect. But the first finding of this Chapter has shown that slip alters the film structures; these are significant enough to elicit changes to the film temperatures. For the pooling film, the addition of slip causes a reduction of fluid volume around most of the cylinder which causes the pool to become deeper. With this increase in depth, the surface of the pool is much colder because it is now located further away from the cylinder walls.

While the first finding is applicable predominantly for a conduction dominant flow, when there is moderate convection the minimum temperature within the pool is lower for all cases when considering slip. With moderate convection, the cooled region at the pooled surface is pushed further up the rising wall as a direct consequence of slip. This is the second finding of this Chapter, where slip is an amplifier to the effects of thermal convection. This finding is further detailed with flow over a localised heating element located in several sections of the cylinder. The effect of slip and convection are shown to move heat from the narrow film around the chamber and into the pool. This presents an interesting characteristic of fluid slip where heat can be moved out of the narrow film when combined with convection.

With moderate inertia, the presence of partial slip causes the capillary waves to be larger and this changes the internal temperatures of the film. These larger surface waves cause a greater variation in the internal temperatures to match the new surface profile.

When the film is not a smooth profile and there is strong thermal convection, the model predicts large fluctuations in the film temperature. There are instances where these fluctuations are not accurately represented by the mean temperature and cause the results to become inaccurate. This inaccuracy is not found with the flow flux, as the variation to the flux must approach zero across the domain for steady solutions. However, the definition for the mean temperature means there can be variation and becomes a problem if the change is large enough.

The effect of convection is shown to be substantial, however the changes to temperature profiles by slip, while relatively minor could be used to ensure heat is adequately displaced throughout the film.

Chapter 6

Physical Applications and Comparative Films

This Chapter focuses on the set of characteristic values which are typical for an aero-engine bearing chamber. The previous Chapters have explored the mathematical model using different parameter regimes; however, this Chapter looks specifically at the characteristic values. Part of this Chapter has investigated a similar model in the literature for rimming flows, where the differences between each model have been thoroughly detailed. The remainder of the Chapter looks at each physical characteristic, such as the fluid density or viscosity to show their importance in determining the flow profiles. This Chapter also presents the most important part of this research, where physical slip lengths have been investigated and shown to have a significant effect on the film profile.

6.1 Modelling the Physical Flow Features and Chamber Conditions

The depth-averaged mathematical model of Chapter 3 has been explored for isothermal films in Chapter 4. However, this study used the six dimensionless parameters which determine the flows separately. This is an ideal case in studying a single physical effect and how it may change the film profile, such as the change with larger reduced Reynolds number Re^*. These dimensionless parameters were detailed in Chapter 3, though they are repeated here for convenience

$$\begin{aligned} \varepsilon &= \frac{h_0}{r_0}, & l_s &= \frac{l_s^*}{h_0}, \\ Re^* &= \frac{\rho U_0 \left(h_0\right)^2}{\mu r_0}, & \frac{\varepsilon^3}{Ca} &= \frac{\sigma \left(h_0\right)^3}{\mu U_0 \left(r_0\right)^3}, \\ \lambda &= \frac{\rho g \left(h_0\right)^2}{\mu U_0}, & \tau &= \frac{\tau_a^* h_0}{\mu U_0}. \end{aligned} \tag{6.1}$$

The characteristic values which define each parameter is important, as it is clear from (6.1) that many of the dimensionless parameters will change a the characteristic value changes. An example of this is the cylinder radius r_0, which does not change each parameter proportionally. It is therefore useful in the modelling of the flow through the bearing chamber, that characteristic values which are representative of the physical system are used and detail how the film will change with each one. An analysis by Kakimpa et al. [1] focused on these characteristic values for the flow inside a bearing chamber in their work on thin film models. Therefore, the first portion of this Chapter is aimed at replicating the flows that were presented by Kakimpa et al. [1]. The oil of the bearing chamber has a density which is similar to water at $930\,kg/m^3$, while the dynamic viscosity is approximately five times higher at 4.83×10^{-3}. The inner shaft speeds of the aero-engines may be in excess of $16,000\,RPM$, meaning if the shaft is $0.1\,m$ in diameter the surface speed will be over $80\,m/s$. There are other studies which provide values for the bearing chamber flow, such as the work by Gorse et al. [7] who gave measurements of the oil film to be up to $1.5\,mm$ at maximum. Chew [5] also provides a set of oil properties and measurements of the bearing chamber which are similar to those of Kakimpa et al. [1].

The remainder of this Chapter aims to demonstrate how important these characteristic values are in determining the type of film profile that will appear within the chamber. The contributions of each physical effect in the model are shown in the azimuthal momentum equation (3.65) in Chapter 3 and for the readers ease is presented here again as

$$\overbrace{\varepsilon Re\left[\frac{\partial}{\partial t}\int_0^h\left[(1-\varepsilon y)\,u\right]dy+\frac{\partial}{\partial s}\int_0^h u^2dy-\varepsilon\int_0^h uvdy\right]}^{\text{Inertia}}=$$
$$\overbrace{-\varepsilon^2 Re\left[\frac{\partial}{\partial s}\int_0^h\int_0^h u^2dydy-\frac{\partial}{\partial s}\int_0^h\int_0^y u^2dydy\right]}^{\text{Inertia}}+\overbrace{\frac{\varepsilon^3}{Ca}\left[h\frac{\partial^3 h}{\partial s^3}+h\frac{\partial h}{\partial s}\right]}^{\text{Surface Tension}}$$
$$\underbrace{-\varepsilon\left[\lambda\cos sh\frac{\partial h}{\partial s}-\lambda\sin s\frac{h^2}{2}\right]}_{\text{Hydrostatic Pressure}}+\underbrace{\left[\frac{\partial u}{\partial y}-\varepsilon y\frac{\partial u}{\partial y}\right]_0^h}_{\text{Viscosity}}-\underbrace{\left[h-\varepsilon\frac{h^2}{2}\right]\lambda\sin}_{\text{Gravity}}. \quad (6.2)$$

The fluid properties, the conditions within the chamber and the size of the cylinder have all been investigated separately. The purpose of this is to determine how the flow profiles change in relation to a specific parameter, an example is how the flow may change if the fluid density was to be either higher or lower than the typical aero-engine oil. The aim is to show how important these time averaged flow parameters can be and to be mindful in selecting them.

It is beneficial to display where the effects of gravity, hydrostatic pressure, inertia, surface tension and viscosity are important. Therefore, a new figure is introduced which shows the total contribution of each force in the momentum equation. The terms of each effect in (3.113) have been summed together for the values of h and q at each node within the domain. As the early works on studying rimming flows in the literature have shown, the film is mainly a balance between those of viscosity and gravity. Nevertheless, the films in these figures emphasise there are flows when these additional effects must be considered.

The investigation of the slip boundary condition is also an important part of this Chapter. This is because a number of slip lengths up to $200\,\mu m$ from the supporting literature of Chapter 2 have been analysed to determine their unique effects on the flow.

6.2 Comparative Study to Existing Rimming Flows

There are many flow configurations that can be found in the current literature of rimming flows, where the flow is driven by either the cylinder rotation or by an imposed air shear. The results of Kakimpa et al. [1] are most suitable due to the shared bearing chamber topic and shear driven flow. The physical values used by Kakimpa et al. [1] to characterise the flow of aero-engine oil have been collated in table 6.1. The previous Chapters used a different approach where the relative strengths of each component were changed using a generalised fluid rather than

Profile	h_0 (m)	r_0 (mm)	U_0 (m/s)	μ (Ns/m^2)	σ (N/m)	τ_a^* (N/m^2)	ρ (kg/m^3)
Smooth	0.55	0.11	0.512	4.83×10^{-3}	0.0245 0.5	9	930
Pool	0.7	0.11	0.109	4.83×10^{-3}	0.0245 0.5	1.5	930

Table 6.1: Key dimensional film parameters as described by Kakimpa et al. [1] to create a smooth or pooling film.

exact physical values.

The Eulerian thin-film model derived by Kakimpa et al. [1] was used to show the damping effect of surface tension has been artificially inflated beyond what is physically suitable for the oil. The surface tension coefficients of the oil found in bearing chambers is expected to be a constant around $\sigma = 0.0245\, N/m$. The surface tension coefficient, σ has been considered a constant in this thesis and in the work by Kakimpa et al. [1]. However, there will be temperature gradients at the surface and this will create thermocapillary effects which means this value is not constant across the oil surface in the bearing chamber. There are models which link the surface tension coefficient to the liquid temperature at the surface, though including the thermocapillary effects are outside the scope for this thesis. There have been endeavours in using linear relationships to modify the surface tension coefficient with temperature, such as the work by Kumawat and Tiwari [84].

The spectral method and steady state solver developed in Section 3.7 solve the governing equations using non-dimensional terms. These non-dimensional parameters are summarised as (6.1). It is therefore possible to use the values found in the parameter table 6.1 to calculate the corresponding dimensionless terms, which can be found in table 6.2. While there are the three distinct rimming flow solutions of a smooth, shock or pooled film, only the solutions of the smooth and pooled films have been studied for this thesis. This is because the narrow spacing between the nodes which is stated by Kakimpa et al. [1] to capture the capillary ripples means that the simulation time is exceedingly long for the pseudo-spectral method. A different clustering function may be used to drastically reduce this computational cost; however, the aim of this Section is to compare the models and validate the work of this Chapter.

The added challenge for finding physical solutions using parameters that are representative of the bearing chamber is the formation of capillary ripples. These ripples are a consequence of the smoothing effects from surface tension. However, Kakimpa et al. [1] stated the surface tension coefficients of previous studies was

Profile	ε	Re^*	Ca	τ	λ	A
Smooth	5×10^{-3}	0.2711	0.1009	2.002	1.116	5.6×10^{-3}
			0.004946			
Pool	6.364×10^{-3}	0.2449	0.02149	1.944	8.491	8.926×10^{-3}
			0.001053			

Table 6.2: Dimensionless parameters table for establishing either a smooth or pooled solution according to table 6.1.

too large, so the wavelength of these ripples were too long. A high node density is therefore required for these smaller wavelengths so that the spacing between each node is less than $0.14\,mm$. The calculated capillary number with the lower surface tension coefficient is almost two orders of magnitude smaller than those of previous Chapters, meaning the smoothing from surface tension is significantly weaker. The ability to cluster nodes using the pseudo-spectral method is shown to significantly reduce the mesh size. However, a uniformly distributed mesh requires approximately $5,000$ nodes to have $\Delta s \leq 0.14\,mm$ and the full differentiation matrix takes longer to simulate. This has been discussed in detail in Section 3.7 and is detailed later in Section 6.2.2.

6.2.1 Obtaining Smooth Rimming Flows

The smooth film is likely to be the most common flow in the bearing chamber due to the very strong driving force of the airflow. The forces within the smooth flow are mainly those from viscosity and gravity. The air shear, τ_a^* is given as a constant $9\,N/m^2$ in table 6.2 and is due to the internal shaft rotating at upwards of $16,000\,RPM$. This strong air shear is able to support a large volume of fluid $A = 1.125\varepsilon$ in a nearly even distribution of the chamber, shown in figure 6.1. While these films are smooth, there is a slight thickening that is found as the gravitational forces are in opposition to the flow direction on the lower portion of the rising wall. This negative force is shown in figure 6.2, along with the positive viscous forces that maintain the flow around the chamber. Directly opposite to the thicker area of the film, the effects from gravity have reversed and the film thins. This is caused by the film on the falling wall accelerating with gravity and being impeded by viscous effects. There are relatively minor effects from inertia around the cylinder base and top, shown in figure 6.2. The effects from inertia are linked to the small changes in the film height, as the inertial terms correlate to h'.

The results of a smooth film with $\sigma = 0.0245\,N/m$ are in good agreement with those of Kakimpa et al. [1], shown in figure 6.1. Though, there is a deeper hump on the rising wall which has caused the film to be shallower film on the

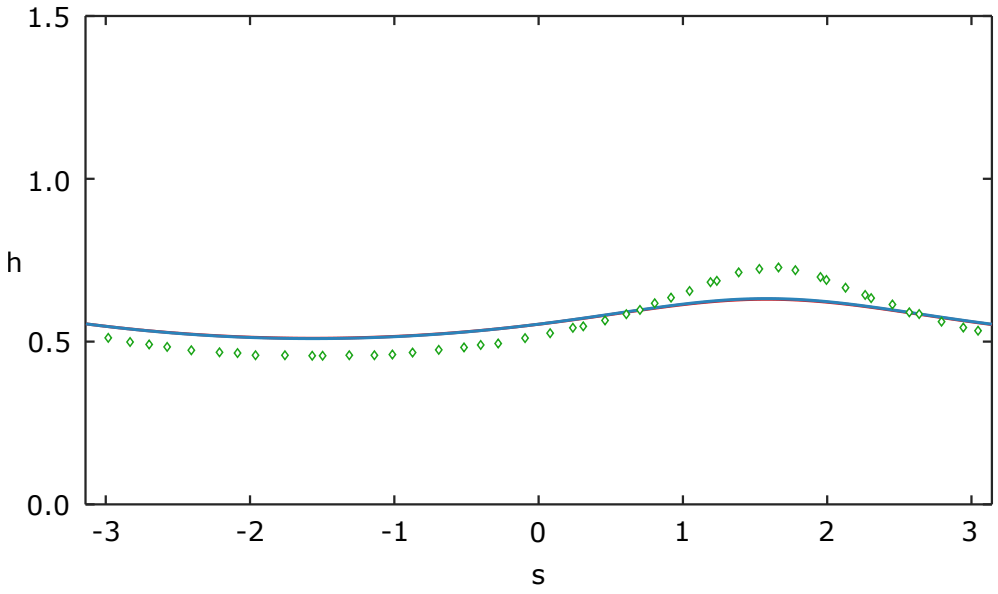


Figure 6.1: The film height profiles of the smooth film found in the work of Kakimpa et al. [1] and those calculated with the current model for a range of surface tension coefficients using the parameters of table 6.2. The *blue* line is with $\sigma = 0.0245\,N/m$ and $\sigma = 0.5\,N/m$ is in *red* (which is perfectly under the *blue* line), while those of Kakimpa et al. are denoted by $\diamond$.

falling walls. These differences are thought to be linked to the representation of inertial terms and a wall shear model used by Kakimpa et al. [1]. However, for a smooth film the changes in inertial terms will not be significant. An imposed wall shear would impede the rotating flow and that may be the cause for fluid to accumulate on the rising wall. The details of the wall shear model were not provided, so the connection of the profile differences and the wall shear model can only be conjectured. It does highlight the importance that surface effects have on the film profile.

The surface tension effects have been added to thin film models as they create stabilising effects in the presence of sharp discontinuous jumps in the film height. However, there is no significant change in the film profile for any of surface tension coefficients that have been simulated, these films are shown in figure 6.1 where σ is between $0.5\,N/m$ and $0.0245\,N/m$. These films are all identical as surface tension has no effect on the smooth films. This is further shown in the forces across the domain being equal. The forces from viscosity and gravity are the strongest of the effects being modelled, shown by figure 6.2.

These smooth films are thoroughly investigated later in this Chapter with a range of characteristic values. Part of this later work is to determine the effect that fluid slip will have on the film profiles using slip length values from $l_s^* = 0\,m$ for the no-slip case up to $l_s^* = 0.0002\,m$, or $200\,\mu m$. These correspond to some of

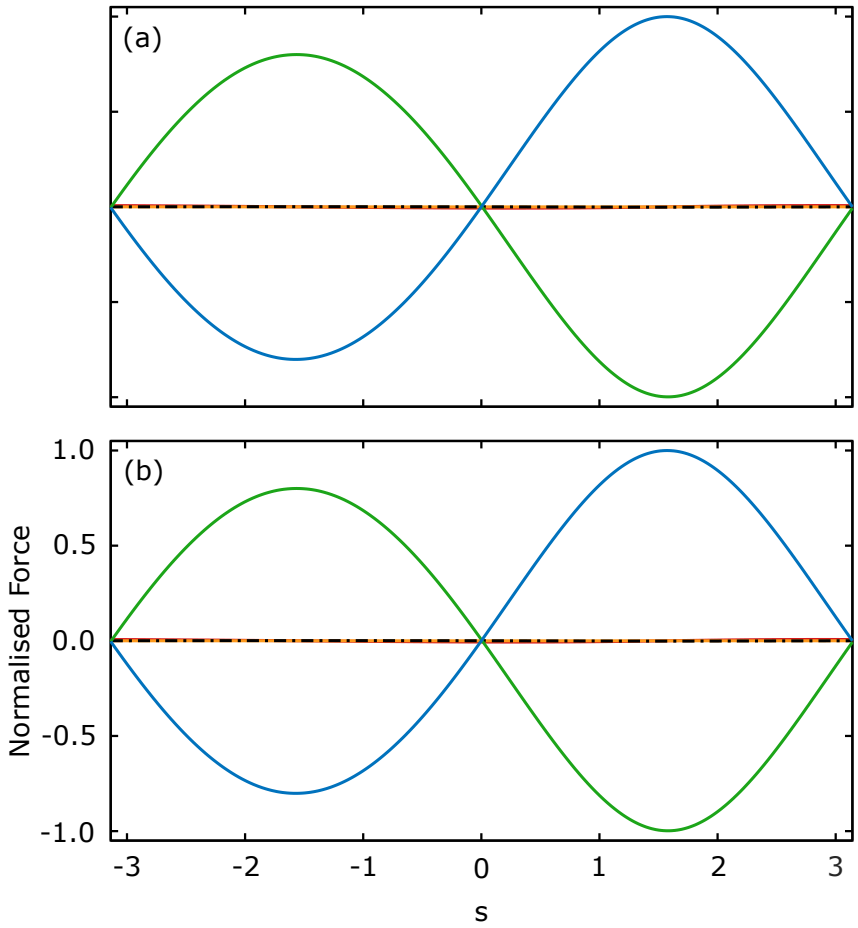


Figure 6.2: The calculated forces within the films when $\sigma = 0.0245\,N/m$ and $\sigma = 0.5\,N/m$ in (a) and (b) respectively. The contributing forces are denoted by *blue* for gravity, *green* for viscosity, *red* for inertia, *orange* for surface tension and *black* for hydrostatic pressure, which is consistently used throughout this Chapter.

the largest slip lengths that have been reported in the literature.

6.2.2 Development of Deep Recirculating Pools

The flow within a horizontal cylinder will typically develop as a pool if a large volume of fluid is contained within the cylinder. With a low surface tension coefficient of $\sigma = 0.0245\,N/m$, Kakimpa et al. [1] determined it was necessary for $\Delta s \leq 0.14mm$ to capture the film surface. Therefore, a uniform node spacing and dense mesh of $N = 5,000$ have been used to capture the surface profile unless otherwise stated. The method for obtaining solutions with the weaker surface tension coefficient has been to use a continuation approach, where solutions with higher value of σ have been used for an initial value of the film. This method greatly reduced the number of iterations required to calculate solutions.

There are two film profiles that have been designated as pooling films by Kakimpa et al. [1], these have been replicated in figure 6.3. When surface tension effects act to smooth the film, there is a small surface ripple that can be found at both the entrance and exit of the pool. If the surface tension coefficient is small, there are no ripples around the pool.

With the dimensional parameters defined in table 6.1, the reduced Reynolds number is calculated as $Re^* = 0.34491$. Kakimpa et al. [1] specified the Reynolds number to be $Re = 54.4$ which is different to the calculated value, therefore the Reynolds number has been artificially modified. The results show that for an initially strong surface coefficient of $\sigma = 0.5\,N/m$, a pooling film will develop and is shown in figure 6.3. The pool is created as liquid accumulates under the strong gravitational pull, as $\lambda = 8.491$ the effects of gravity are over 8 times larger than the viscous effects. This strong gravity significantly impedes the flow around the cylinder, however the viscous forces ensure that de-wetting does not occur. The viscous effects draw a narrow film from the pool that coats the entire chamber, depicted in figure 6.4.

Analysis of the forces around the cylinder show that gravity and viscosity are the most dominant effects, shown by figure 6.4. However, there is also a significant contribution from inertial effects throughout the pool due to the sharp fluctuations in h. The higher surface tension coefficient of $\sigma = 0.5\,N/m$ increases the smoothing effect of the film. This smoothing effect can be found in the transition around the pool becoming more gradual and the sharp rise in hydrostatic pressure effects due to the pool also occurs over a larger region. As the hydrostatic pressure effects are closely linked to the film gradients, the narrower region indicates a sharper surface transition. The development of a dimple at the rear of the pool is also due to surface tension.

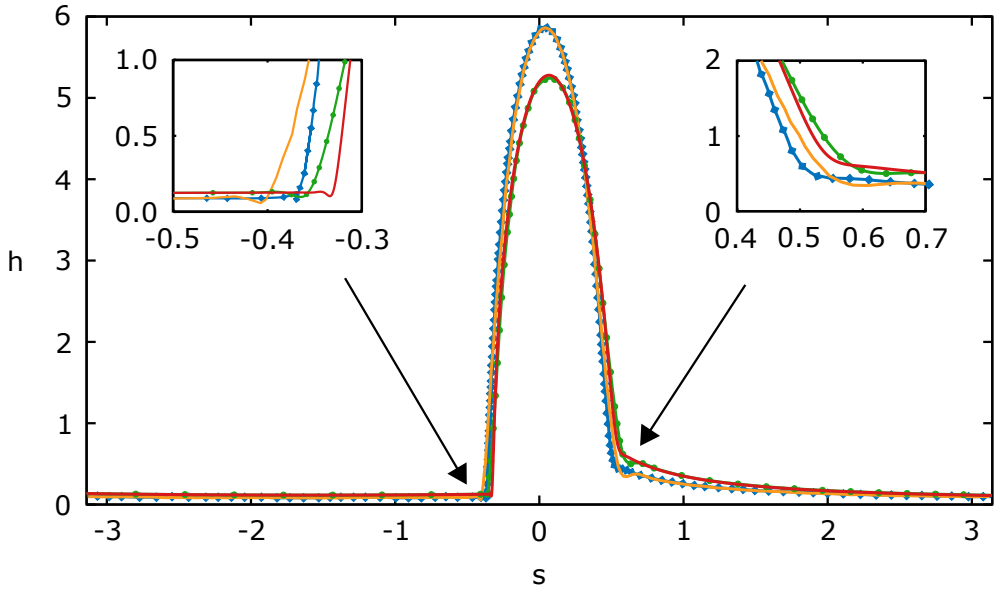


Figure 6.3: A comparison between the films by Kakimpa et al. [1], denoted in *orange* for $\sigma = 0.5\,N/m$ and *blue* for $\sigma = 0.0245\,N/m$ and the film profiles calculated using the parameters of table 6.2. Where the surface tension coefficients for $\sigma = 0.5\,N/m$ in *green* and $\sigma = 0.0245\,N/m$ in *red*. Close up of film height profiles preceding the fluid pool, highlighting the differences between the range of σ values tested.

The solutions of Kakimpa et al. [1] and the solutions of this thesis appear very different in size, shown in figure 6.3. However, the volume of fluid in each solution are equal and the parameters of each flow are also equal. The differences have been explored thoroughly and can be attributed to three likely factors which are now detailed. One of these reasons is the filling fraction ratio, A was interpolated directly from the published figures and is very sensitive to changes. This may result in widely differing film profiles. However, studies using a number of different filling fractions close to the value of $A = 8.926 \times 10^{-3}$ have indicated this is not the case. It is therefore believed that the accuracy of the filling fraction is unlikely to be the main difference. This was not an issue in Section 6.2.1 as the smooth film is easier to interpolate.

As mentioned in Section 6.2.1, the mathematical model for inertial effects is different between the equations in this thesis and those of Kakimpa et al. [1]. This is clear as the centrifugal inertial effects and centrifugal pressure terms have not been retained in the model by Kakimpa et al. [1]. The pooling film contains flow recirculation and therefore modest radial velocities. Therefore, the centrifugal terms will be non-zero and may be significant within the thin-film approximation. By removing these terms from the model of this thesis, the influence that the centrifugal terms have on the film profiles is shown in figure 6.5. The films are largely comparable in shape, though the model with full inertial effects causes

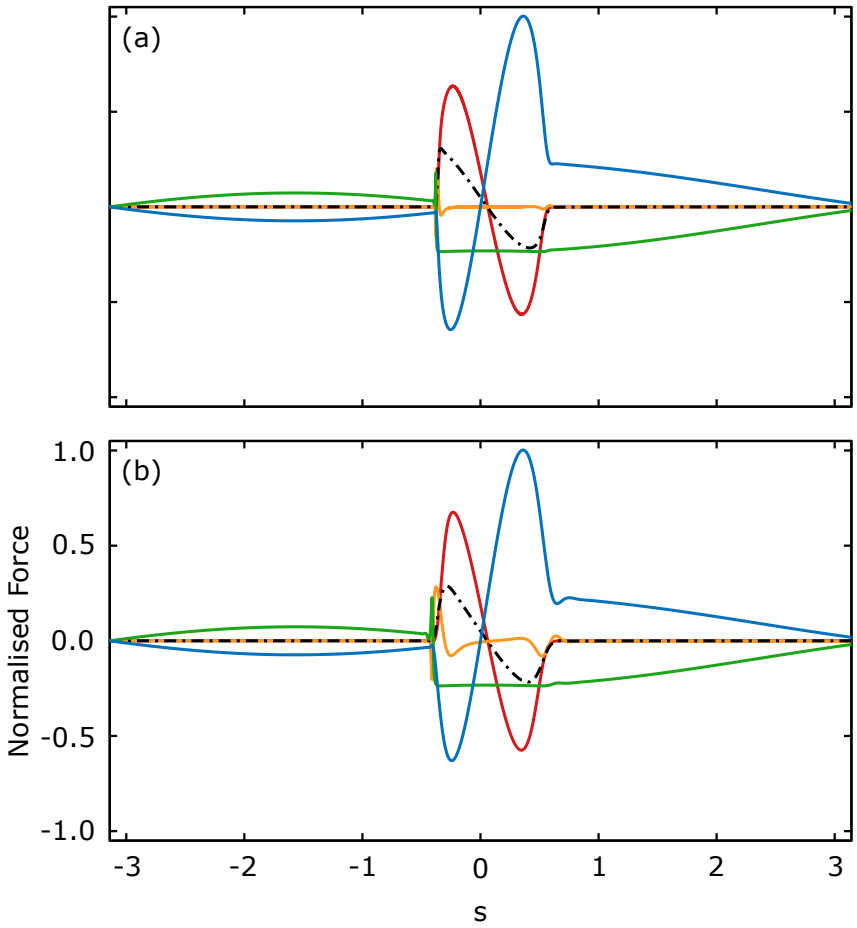


Figure 6.4: The forces found within the films for $\sigma = 0.0245\,N/m$ in (a) and $\sigma = 0.5\,N/m$ in (b), from the films of figure 6.1. The lines are calculated for inertia, viscosity, hydrostatic pressure, surface tension and gravity, given as *red*, *green*, *black*, *orange* and *blue* respectively.

the pool to appear slightly lower on the rising wall. The spike in the absolute percentage error between the films is due to this movement.

The film profiles are similar as the inertial terms from the radial momentum and the azimuthal momentum equations counter-balance each other, shown in figure 6.6. However, these forces are not fully balanced and leads to an increase in the total force that comes from inertia.

From the analysis of the filling fraction and inertial effects, it is surmised that the submodel of the wall shear stress condition which was used by Kakimpa et al. [1] is likely to be the main difference between the models. Unfortunately, this factor cannot be quantified as the model and coefficients are unknown, but the effects of this wall shear on the film profiles may be inferred. If there is a wall surface shear acting in opposition to the flow direction it will inhibit the flow around the cylinder. This will combine with the effects of gravity and should cause the film to drain from the cylinder walls. Therefore, a deeper pool will develop as less fluid is contained on the walls. This seems to be the most probable cause for the differences in the film profiles.

As the continuation method gradually alters the surface tension coefficient from $0.5\,N/m$ to $0.0245\,N/m$, several intermediate films are created for each film. These films are shown in figure 6.7. The overall shape of these films is similar for each value of σ and it is only in the features around the pool where there is any variation. One of these differences is in the width of the pool increasing with smaller σ as the compressive effects of surface tension reduce. The volume of fluid within the pool has been maintained as the maximum depth of the pool decreases.

There is another difference for the four different surface tension coefficients which can be found upon closer inspection of the pool front and rear regions, shown in figure 6.8. In front of the pool, the higher surface tension effects prevent the film from having a steep front. This causes the pool to widen so that it can accommodate a smoother transition and is also found at the pool exit, the pool also returns to the underlying narrow flow at a higher position on the wall. The film profiles with weaker surface tension display more drastic variations in both the steepness of the front and narrowness of the pool. The actual volume of displaced fluid is relatively minor between $\sigma = 0.5\,N/m$ and $\sigma = 0.0245\,N/m$. The requirement for a smaller node spacing if the surface tension coefficient is small means the simulation time increases. However, it is relatively cheap to increase the surface tension coefficient and reduce the time required to approximate the film profiles. The thin-film models are designed to be a faster alternative to full CFD analysis and the differences between surface tension coefficients are largely inconsequential when considering the final film profile.

Next, the benefits of the numerical method in this thesis is investigated for a

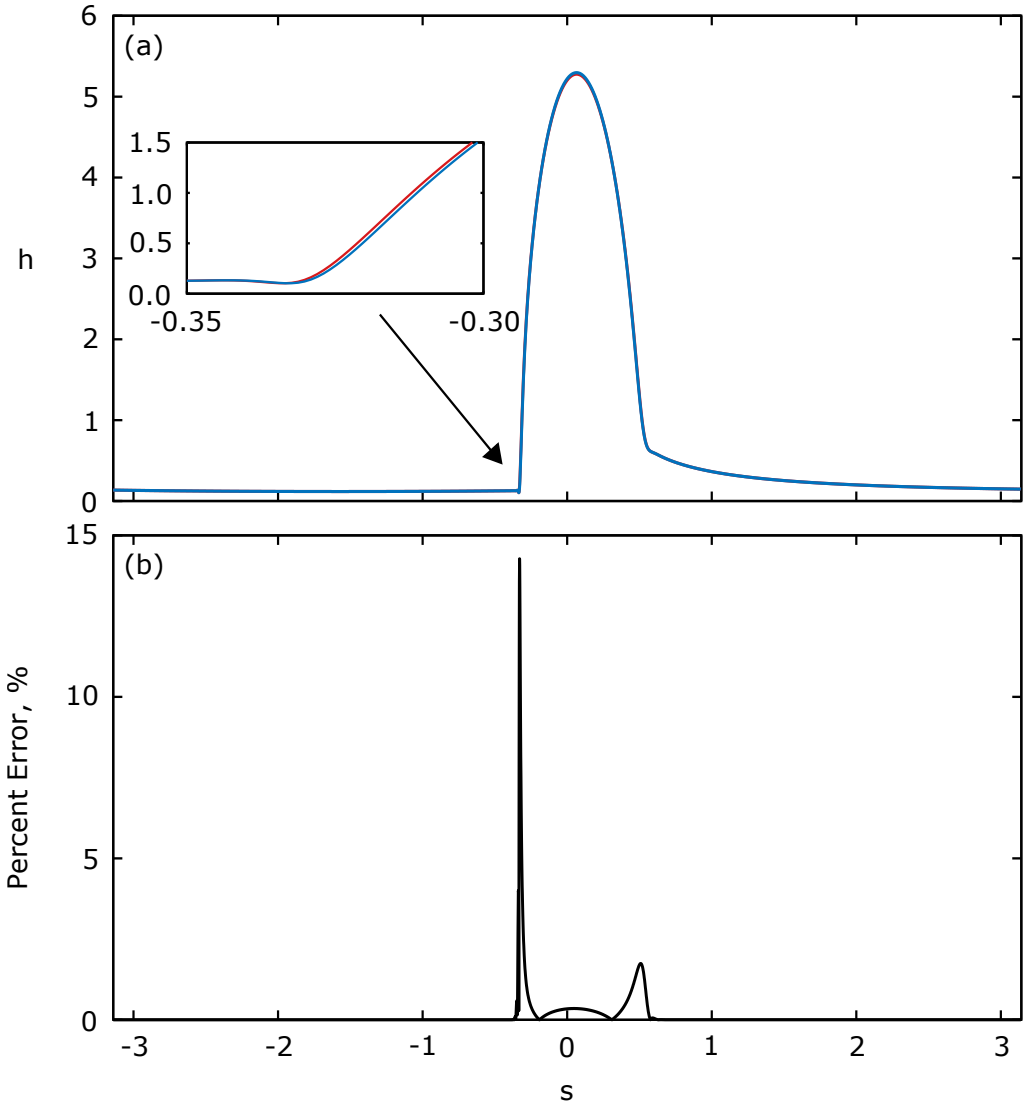


Figure 6.5: The effect of adding centrifugal effects from inertia and pressure on the film profile for $\sigma = 0.0245\, N/m$ in (a), where the full inertial effects are plotted in *red* and the simplified inertial terms are coloured in *blue*. The absolute percentage error between the films with and without centrifugal effects is given in (b).

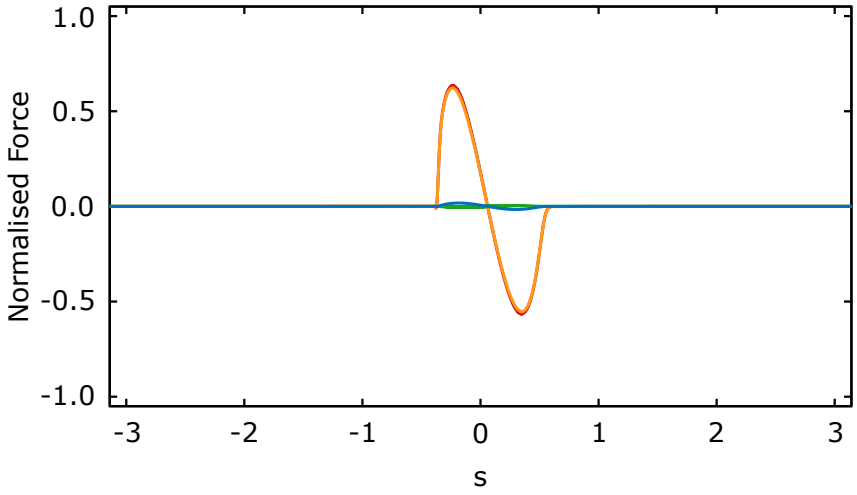


Figure 6.6: The calculated contributions of inertia in the pooling film of figure 6.5, having been normalised to only the inertial effects. The *red* line gives the total inertial contribution, *orange* gives the contribution for the convective terms, *blue* and *green* are for the centrifugal pressure and the centrifugal inertial contributions respectively.

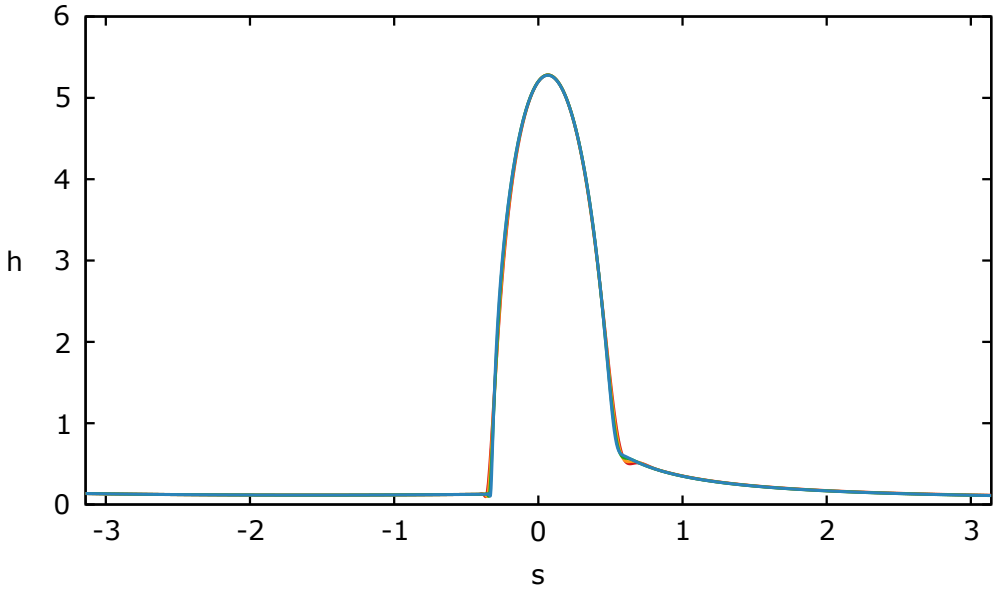


Figure 6.7: How the pooling film changes depending on the surface tension coefficients, where $\sigma = 0.0245\,N/m$ is given by *blue*, $\sigma = 0.1\,N/m$ in *green*, $\sigma = 0.3\,N/m$ with *orange* and $\sigma = 0.5\,N/m$ with *red*. These films are closely investigated in figure 6.8.

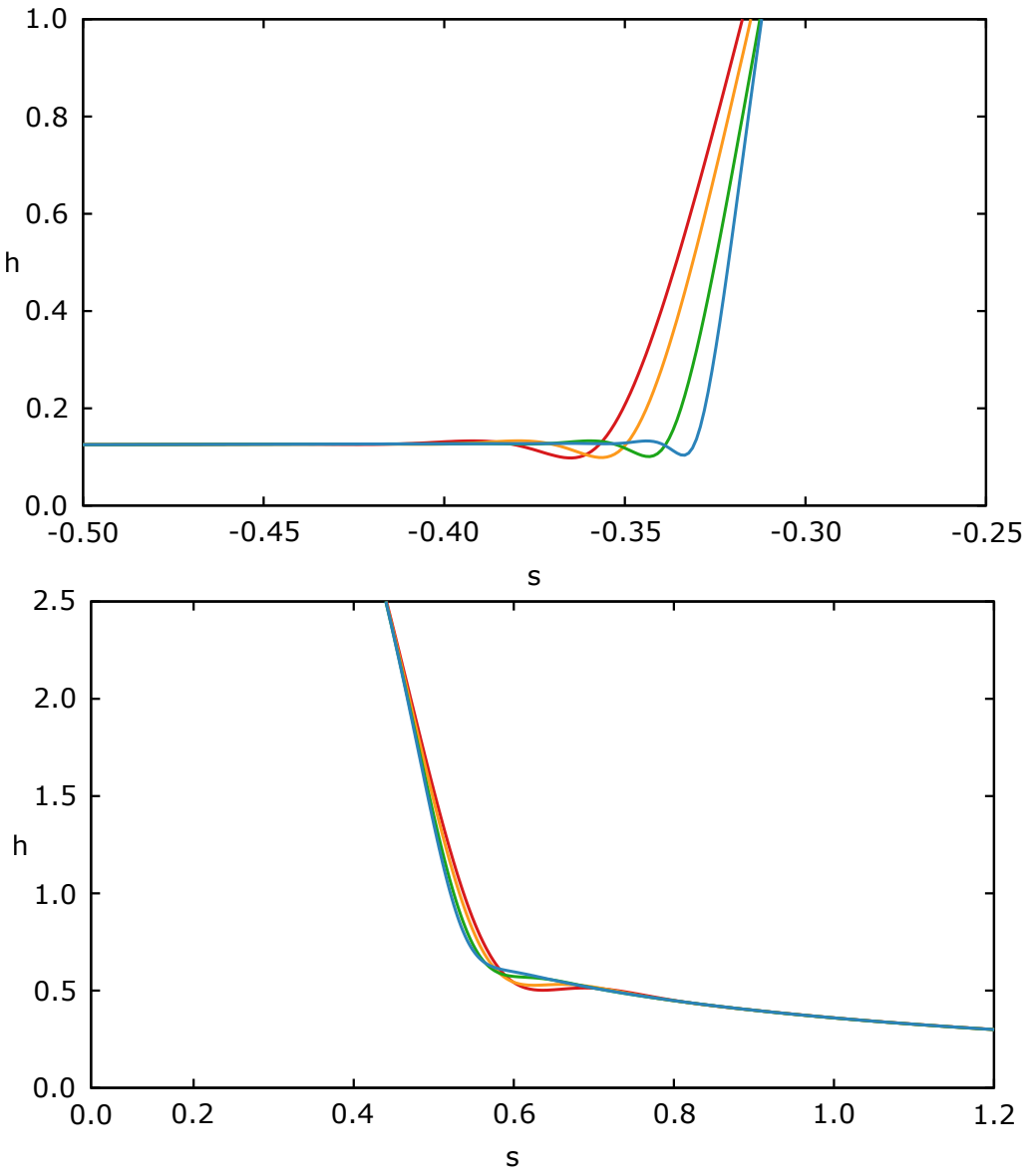


Figure 6.8: Close views at the film in front of and receding from the fluid pool of figure 6.7 in part (a) and (b) respectively to highlight the effect of surface tension, for *blue* with $\sigma = 0.0245\,N/m$, *green* as $\sigma = 0.1\,N/m$, *orange* for $\sigma = 0.3\,N/m$ and $\sigma = 0.5\,N/m$ in *red*.

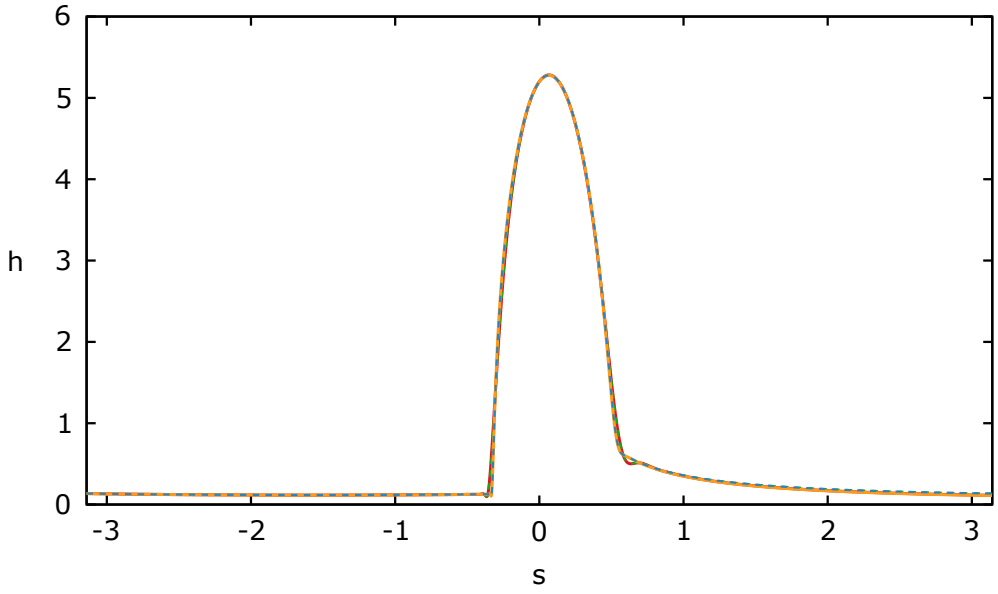


Figure 6.9: A comparison of the obtained solutions between the numerical solver using an *upwind* and a *central* difference method in gradient calculations. Where the upwind solutions to $\sigma = 0.5\,N/m$ and $\sigma = 0.0245\,N/m$ are given by *red* and *orange* lines, and solutions using the central scheme are given as dashed *green* and *blue* lines.

pooling film. The non-linear iterative solver available in the *fsolve* of MathWorks MATLAB has several in-built options that can be adjusted. This includes several methods available in estimating the Jacobian matrix and how the linearization of the equations is implemented. Up to this point, all solutions have used the default option that is recommended by MathWorks to estimate the Jacobian matrix. This is an *upwind* approach to estimate the gradients for each value, which means the variable gradients are only evaluated once. The results obtained throughout this thesis have been consistent with this method. However, it is possible to use a *central* approximation to create the Jacobian matrix, but this doubles the number of evaluations required to create the Jacobian matrix for each iteration. A comparison of the *upwind* and *central* methods has been completed for pooling films with $\sigma = 0.5\,N/m$ and $\sigma = 0.0245\,N/m$. The results from both methods for each film are presented in figure 6.9.

As expected, the films from both methods are computationally identical. This is confirmed by the absolute percentage error between solutions from both method with $\sigma = 0.5\,N/m$ and $0.0245\,N/m$ being negligible and is shown in figure 6.10. Though the *central* method is typically more accurate, the single gradient evaluation of the forward method is suitable. This means that time to obtain solutions can be reduced by using the upwind method and is an important aspect of all computer models to reduce on simulation time.

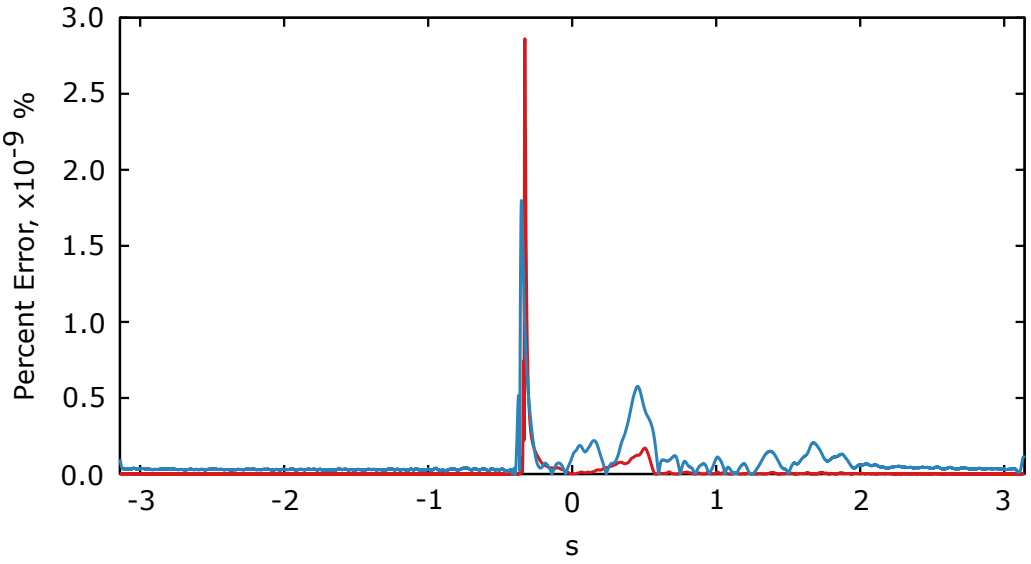


Figure 6.10: The absolute percentage error between the *upwind* and *central* differencing schemes of Matlab's *fsolve* for calculating the pooling film. The *red* line denotes the error in the results for $\sigma = 0.5\,N/m$ and the *blue* line is for $\sigma = 0.0245\,N/m$.

Another advantageous feature of the numerical method is the ability to use non-uniform mesh distributions. This means that a grid refinement can be made for regions of specific interest. The bunching parameter that was defined in Section 3.7 can create a uniform mesh with $c = 1$. To ensure that $\Delta s \leq 0.14\,mm$, the minimum mesh size was $N = 4,938$. The mesh is only approximately uniform, as there is a discrepancy in the mesh which causes a non-uniform spacing connected to numerically approximating trigonometric functions. This discrepancy is shown in figure 6.11.

The area around the base of the cylinder has the greatest changes in the film surface and therefore requires the highest concentration of nodes. This is because both the pool and small wavelength capillary ripples forms here. This area of interest has been highlighted in figure 6.11.

A non-uniform domain can be created by setting the bunching parameter, c to be 2.5. This clustered domain has a centre spacing Δs that is approximately 4 times smaller than the outer edges, this is shown in figure 6.11. However, the pool is not centred exactly around $s = 0$ while the domain is centred around $s = 0$. It is useful to transform the domain so that the pool centre will align with the domain centre. In Section 3.7, a linear transformation of the domain was implemented using β. This transformation does not require the differential matrices to change as the spacings between each node remains constant. By setting $\beta = 0.15$, the domain becomes centred around $s = 0.15$ which is approximately the pool centre and the domain is now $s \in [-\pi + 0.15,\, \pi + 0.15]$.

The mesh now has $3,750$ nodes in comparison to the $4,938$ nodes of the uniform mesh, which is a reduction in the mesh size of approximately $20\,\%$. This means there are 9 million cells fewer in the differentiation matrices that are $N \times N$ in size. Therefore, with the global method using a full matrix there are 9 million fewer calculations at each iteration of the non-linear solver. This has a significant reduction in the simulation time.

A comparison of the film profiles using this concentrated mesh and the uniform mesh have found that the solutions are identical. These films are shown in figure 6.11, with details of the node spacing around the domain. The periodic domain means that the start and end points of each mesh are different, the solution profiles are the same and have been offset with $\beta = 0.15$.

The mathematical and numerical models in this thesis have been able to calculate solutions that are accurate in simulating a pooling film. The changes to the depth and width of the pool with the different surface tension coefficient value of $\sigma = 0.0245\,N/m$ are close to the films of Kakimpa et al. [1]. The differences between this thesis and the film profiles by Kakimpa et al. have been detailed thoroughly. The hyperbolic sine function used to cluster the nodes in the domain has been beneficial with significant computational savings. However, there are alternative functions that may redistribute the nodes more effectively and can be used for other domains. The pseudo-spectral method in this thesis is advantageous as it may use a non-uniform mesh for simulating rimming flows.

6.3 Smooth Solutions with a Strong Driving Shear

This Section focuses on changing the parameters used by Kakimpa et al. [1] for smooth films and details which parameters are important when simulating steady films. The smooth solution has been chosen as it is likely that the flow in the bearing chamber is smooth. There is also the issue of gravitational effects being dominant for pooling films, so changes in the characteristic values will have little effect. While the lower surface tension coefficient of $0.0245\,N/m$ may be more realistic of the aeroengine oil, $\sigma = 0.5\,N/m$ has been used unless clearly stated otherwise to reduce the numerical costs in simulating each film.

6.3.1 Importance of Fluid Density on Attainable Films

The film is driven by a very strong surface shear, $\tau_a^* = 9\,N/m^2$ which creates a smooth film. The density of the oil found in aero-engines is $\rho = 930\,kg/m^3$, however this will change with the oil temperature during the engine operation.

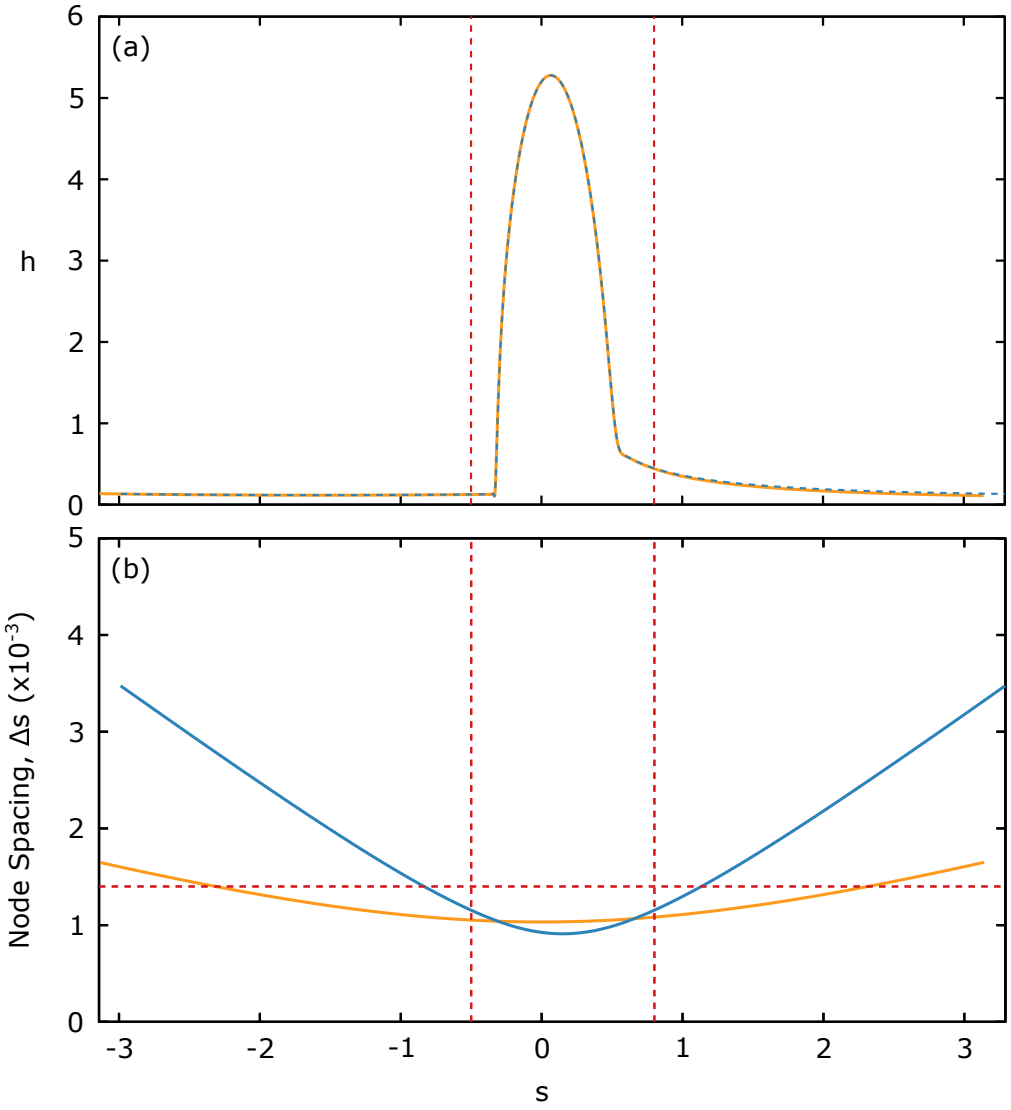


Figure 6.11: The uniform and centrally clustered meshes, showing the obtained solutions for the pooling film in (a), with *orange* for the uniform mesh while *blue* is on the clustered mesh. The spacing between each node across the domain is shown in (b), where *orange* is for $N = 5,000$ and *blue* is for $N = 3,750$.

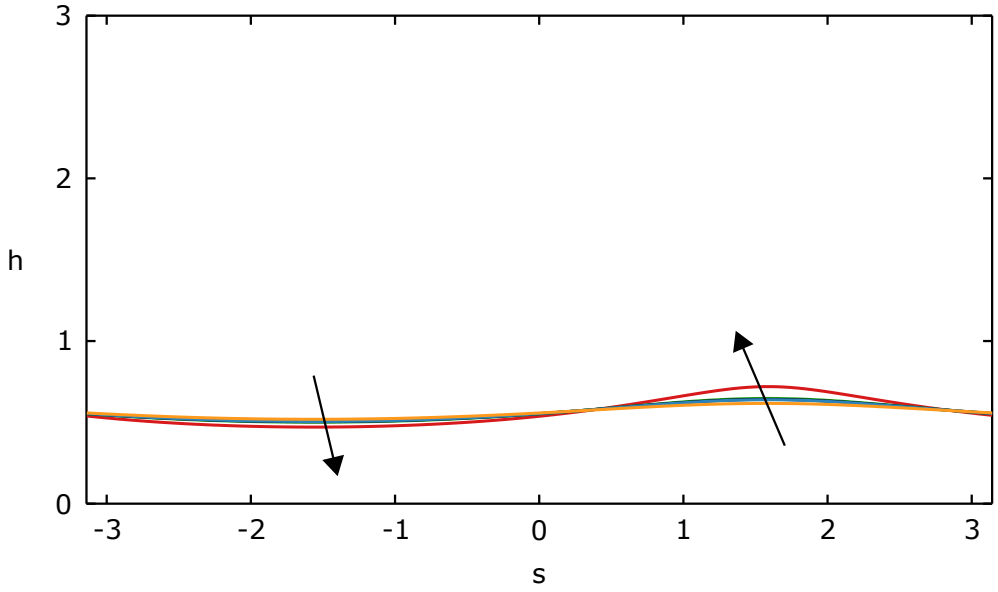


Figure 6.12: The influence of the fluid density, ρ on the smooth solution characterised by table 6.2. The solution profiles for each value of the fluid density is given as *orange* for $730\,kg/m^3$, *blue* for $930\,kg/m^3$, *black* for $950\,kg/m^3$, *green* for $1000\,kg/m^3$ and *red* for $1500\,kg/m^3$.

If the fluid density changes, the effect of gravity can be either strengthened or weakened. In the context of fluid densities; water has a density of $1000\,kg/m^3$, some organic hydrocarbons have a significantly higher density of $1500\,kg/m^3$ and there some that have a much lower density, such as petrol at $700\,kg/m^3$. Flows have been simulated using several fluid densities across this range of $1500\,kg/m^3$ and $700\,kg/m^3$.

The effect of gravity is severely weaker with a density of $700\,kg/m^3$. This causes the film to be thinner around $s = 1.5$, this is shown in figure 6.12. This thinning is due to the gravitational pull that impeded the flow around the cylinder being smaller. There is also a thickening at $s = -1.5$, where the accelerating effects from gravity have reduced. These changes in the gravitational forces are shown in figure 6.13 and means the film has a more uniform depth.

In contrast to the smoother film, if the fluid has a higher density there is a thickening of the film on the rising wall. This is because the force from gravity increases with density. There is an equal reduction in the fluid depth at $s = -1.5$, as the film speed increases due to the positive pull of gravity, as shown in figure 6.13.

The effect of density on the film profile and the change in internal forces are small. This is due to the high shear rate τ_a^*, which drives the fluid to form a smooth film.

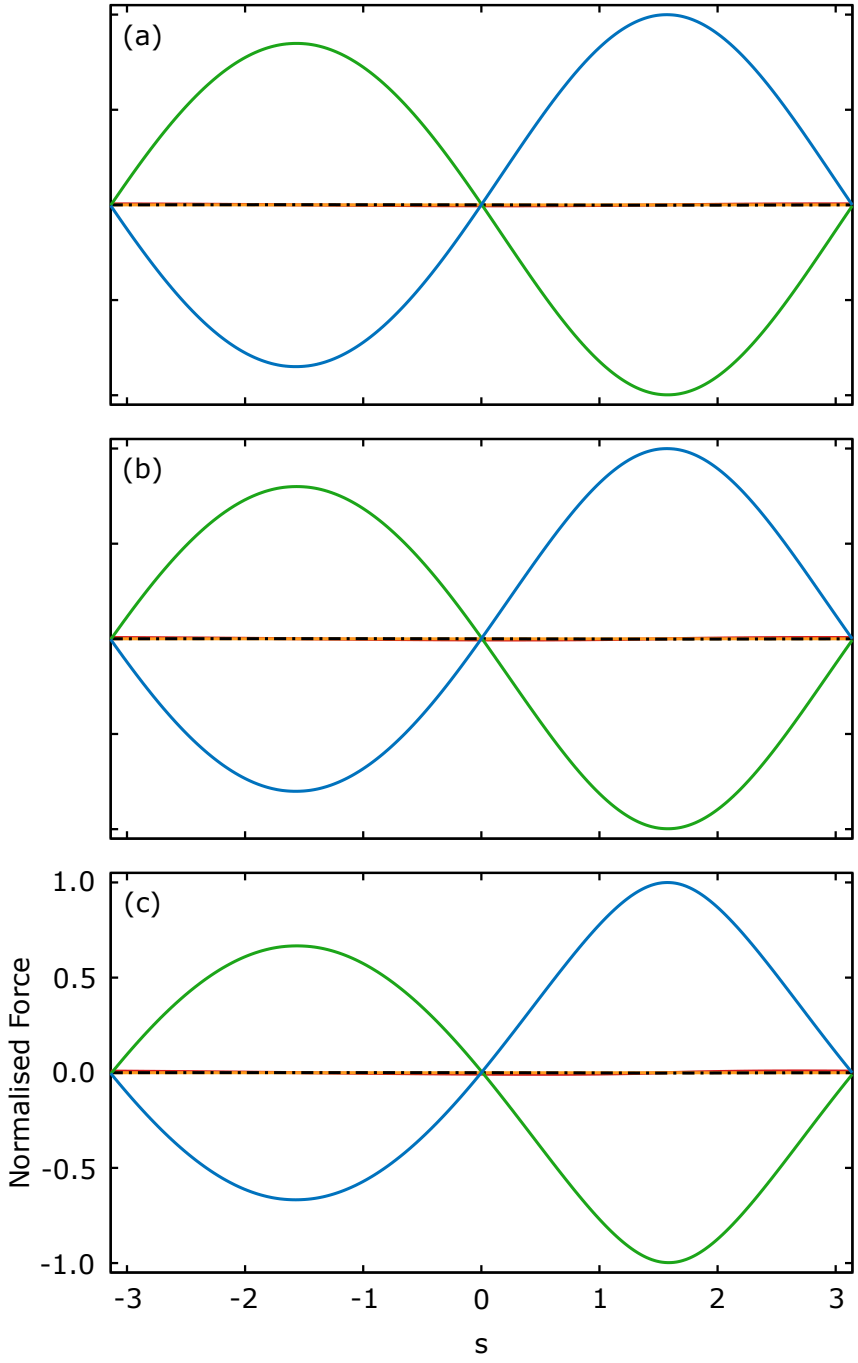


Figure 6.13: With inertia, hydrostatic pressure, surface tension, viscosity and gravity plotted as *red*, *black*, *orange*, *green* and *blue* respectively, the change in forces from figure 6.12 with different values of ρ, with $700\,kg/m^3$ in (a), $930\,kg/m^3$ in (b) and $1500\,kg/m^3$ in (c).

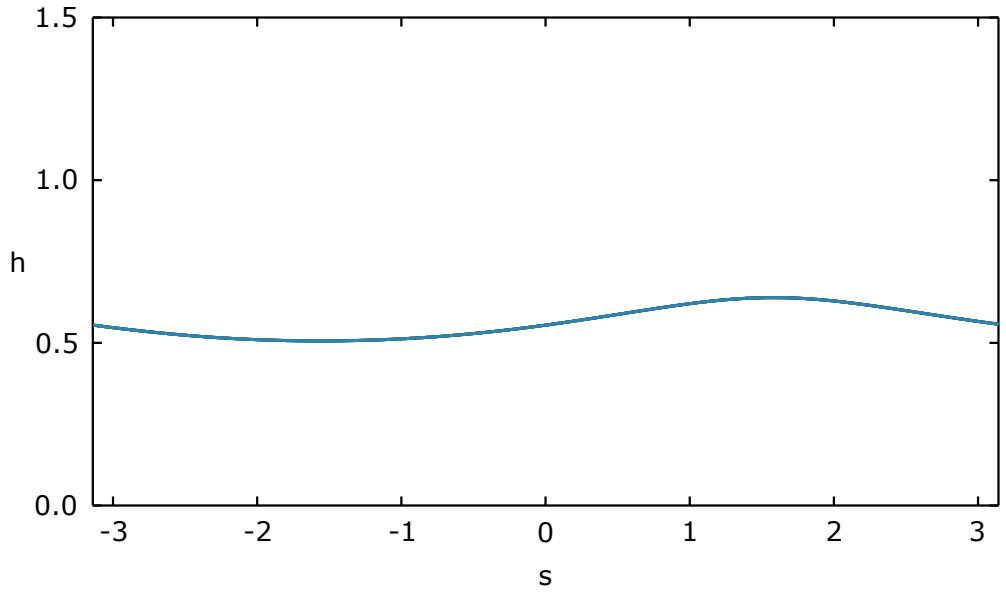


Figure 6.14: The resulting film profiles for various film speeds, denoted by U_0 of the smooth film, with *orange* for $0.1305\,m/s$, *blue* at $0.261\,m/s$, *black* having $U_0 = 0.512\,m/s$, *green* with $U_0 = 1.024\,m/s$ and *red* for $2\,m/s$.

6.3.2 Solutions with Changing Film Speeds

The oil film speed of the bearing chamber is around $0.1305\,m/s$ and is an interesting characteristic parameter to study. This is because it would be expected that as the film speed reduces, a coating flow would no longer be sustainable. This is due to the film travelling so slowly that gravity will cause the film to de-wet the surface. However, the non-dimensional parameters Re^*, λ, τ and Ca that define the four fundamental parameters are all linearly dependent on the film's characteristic velocity, U_0, as shown in (6.1). Therefore, as U_0 changes, all of the non-dimensional parameters change proportionally.

The film profiles for high and low speeds are identical, even with speeds of $U_0 = 2\,m/s$. These films are shown in figure 6.14 which agrees with the mathematical behaviour of the dimensionless parameters. The balance of forces within each film are predominantly those from gravity and viscosity, shown in figure 6.15 for speeds of $0.1305\,m/s$, $0.512\,m/s$ and $2\,m/s$. As there are no changes to the film profiles, changes to U_0 are not investigated further.

6.3.3 How Viscosity Affects the Observable Film Profiles

The oils for aero-engines are specifically chosen to reduce component friction so the viscosity is low. However, if the viscosity is too large the frictional losses would increase to overcome the additional fluid friction. Therefore, the oil has a high viscosity in comparison to water at $\mu = 0.00483\,Ns/m^2$ as it will help reduce

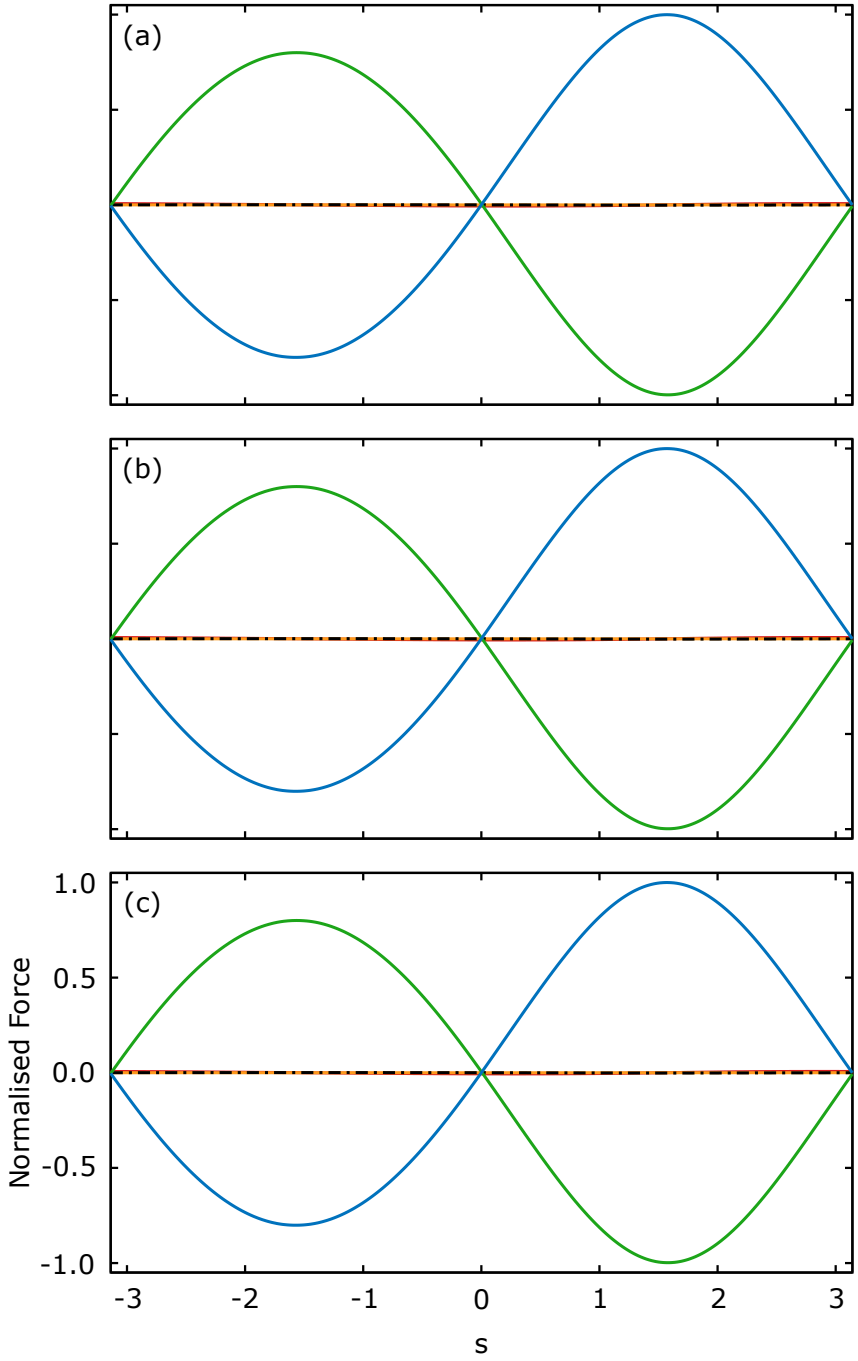


Figure 6.15: The effective forces of figure 6.14, with inertia (*red*), hydrostatic pressure (*black*), viscosity (*green*), gravity (*blue*) and surface tension (*orange*). The characteristic velocities of each panel are $0.1305\,m/s$ in (*a*), $0.512\,m/s$ in (*b*), and $2\,m/s$ for (*c*).

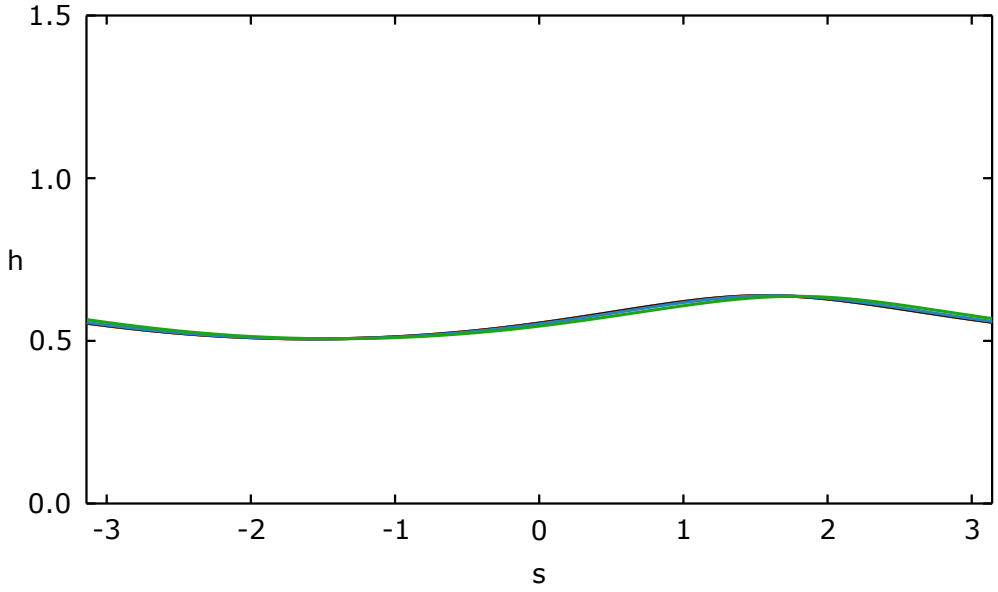


Figure 6.16: The film profiles that develop with changes to the fluid viscosity μ for a smooth solution, with $0.001\,Ns/m^2$ in *orange*, $0.002\,Ns/m^2$ in *blue*, $0.00483\,Ns/m^2$ in *black*, $0.0075Ns/m^2$ in *green* and *red* for $0.01\,Ns/m^2$.

wear in the bearings.

A higher viscosity will reduce the effects of inertia, surface tension and the driving shear of the film. The effects of gravity will also reduce with higher viscosity. However, the relatively weaker driving shear is found to still maintain a smooth profile, shown in figure 6.16 with $\mu = 0.001\,Ns/m^2$. As effects reduce with larger viscosity values, when viscosity is weaker the opposite is found. There is a significant increase to the inertial effects across the entire domain with lower μ, shown in 6.17. However, the difference in film profiles is minor even though the change in forces is significant.

6.3.4 Film Profiles with Varying Characteristic Film Heights

The study of films with the thin film approximation requires the characteristic film height, h_0 to be significantly smaller than the cylinder radius r_0. The non-dimensional parameters that determine the flow behaviour are all dependent on h_0, with the only exception being the capillary number. One of the roles of the characteristic film height is to determine the fill fraction A. If h_0 changes, the calculated filling fraction of each film will no longer be consistent if A is kept constant, therefore the equation is now expressed as

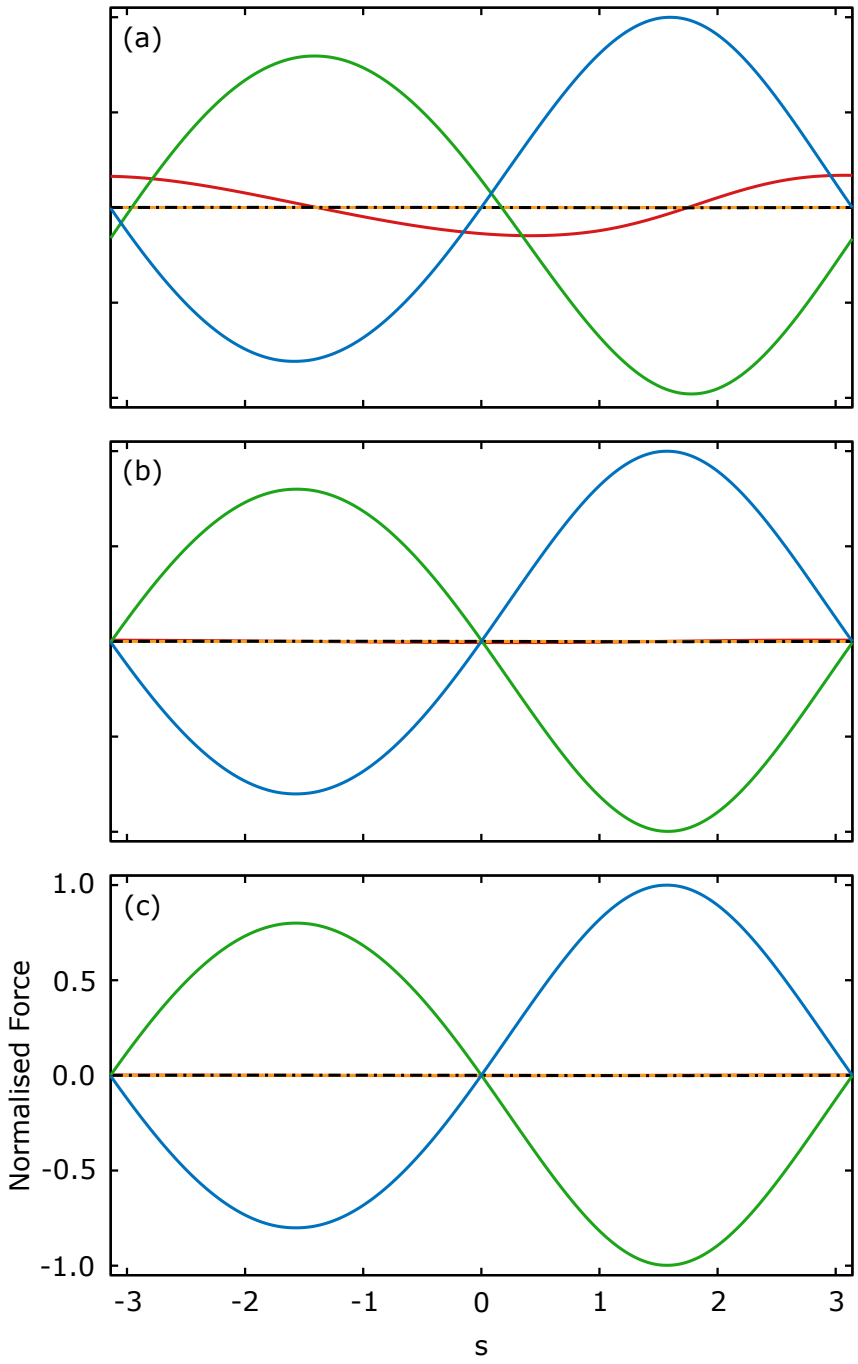


Figure 6.17: The contributing forces found for changes to the fluid viscosity of figure 6.16, specifically those of $0.001\,Ns/m^2$ in (a), $0.00483\,Ns/m^2$ in (b) and $0.01\,Ns/m^2$ for (c). The lines represent the effect of inertia, viscosity, gravity, hydrostatic pressure, and surface tension calculated at each node, given as *red*, *green*, *blue*, *black* and *orange*.

$h_0\ (m)$	A	λ	Re^*	ε	τ
1×10^{-5}	1.02×10^{-4}	3.69×10^{-4}	8.96×10^{-5}	9.09×10^{-5}	3.6×10^{-2}
5×10^{-5}	5.11×10^{-4}	9.22×10^{-3}	2.24×10^{-3}	4.55×10^{-4}	1.8×10^{-2}
5.5×10^{-4}	5.63×10^{-3}	1.12×10^{0}	2.71×10^{-1}	5×10^{-3}	2×10^{0}
7×10^{-4}	7.16×10^{-3}	1.81×10^{0}	4.39×10^{-1}	6.36×10^{-3}	2.6×10^{0}
1×10^{-3}	1.23×10^{-2}	3.69×10^{0}	8.96×10^{-1}	9.09×10^{-3}	3.6×10^{0}
1×10^{-2}	1.02×10^{-1}	3.69×10^{2}	8.96×10^{1}	9.09×10^{-2}	3.6×10^{1}

Table 6.3: The dimensionless parameters and calculated filling fractions for changing h_0 to establish a smooth solution which is consistent in volume to those presented in table 6.2.

$$A = \frac{\varepsilon}{\pi} \int_{-\pi}^{\pi} h \, ds, \tag{6.3}$$

$$\therefore \frac{A\pi}{\varepsilon} = \int_{-\pi}^{\pi} h \, ds = \ constant, \tag{6.4}$$

This new equation ensures a consistent volume between each film and is used if h_0 or r_0 change. The new values of the filling fraction are presented in table 6.3, along with the other dimensionless parameters for the different values of h_0.

A smooth film has been found for all film values of h_0 which were tested, with h_0 as small as $10\,\mu m$ as shown in figure 6.18. As the characteristic film height reduces, the film profiles became more uniform in depth across the domain. This is because the value of λ is proportional to the square of the film height $(h_0)^2$, so the effect of gravity within the cylinder is reduced significantly with smaller values of h_0. The changes in gravity and viscosity mean the forces are equal on the rising and falling walls and is why the film is smooth, shown by figure 6.19.

In all the cases, where $h_0 \leq 1\,mm$, the film can be considered smooth. However, there is a region of the film which has become much deeper with larger film heights. This increase in depth is more apparent with $h_0 = 1\,mm$, where the surface has a much larger gradient across the domain. This is because the effect of gravity has a quadratic growth with larger h_0, which acts to impede the flow up the rising wall. There is also an increase in the inertial effects, which is due to inertia being a gradient determined force, shown in figure 6.19.

There was a limit to the size of h_0 that was able to be simulated. This is because as λ increases at second order, the effect of gravity becomes much stronger than viscosity. This creates a pooling film. The small parameter term ε also changes significantly and has a large impact on the surface tension effects. The smoothing that occurs as a result from surface tension is a third order term in ε, so the changes to h_0 can lead to very strong surface tension effects around

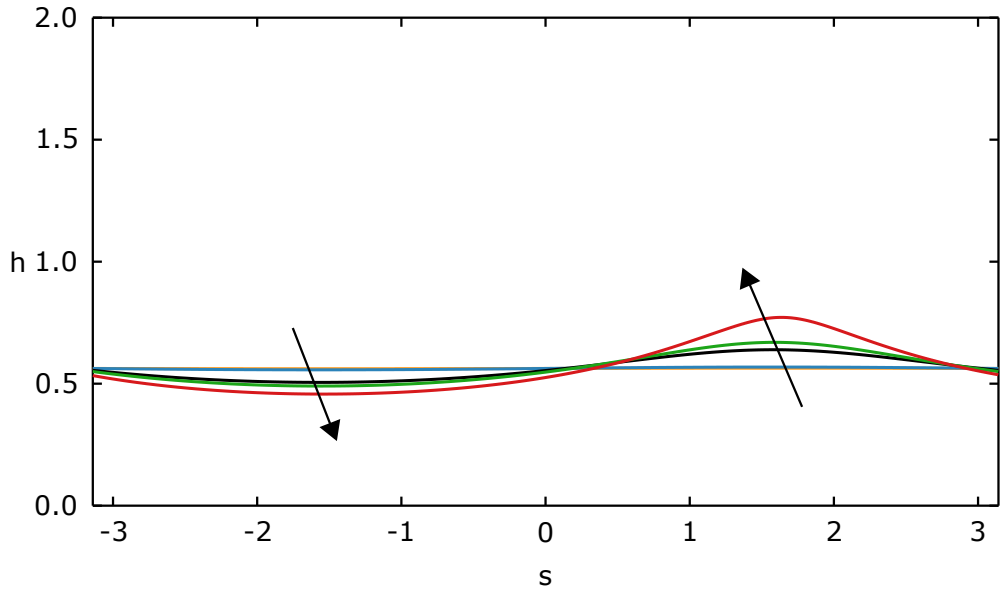


Figure 6.18: With changes to the characteristic film height h_0, the resulting film profiles and shown for $1\,mm$ in *red*, $0.7\,mm$ in *green*, $0.55\,mm$ in *black*, *blue* for $0.05\,mm$ and $0.01\,mm$ as *orange*.

the pool. This increase in surface capillarity and gravitational effects has caused difficulty in calculating stable films with large values of h_0.

6.3.5 Effects of Cylinder Size on Film Profiles

The cylinder radius is an important value in the thin film approximation, only appearing in the dimensionless parameter ε. The thin film approximation assumes that $\varepsilon \ll 1$, so the smallest cylinder size is limited by the film depth of $h_0 = 0.55\,mm$. Therefore, cylinders as small as $10\,mm$ and as large as $1\,m$ have been simulated. The consistency between films must be maintained for each film with different cylinder radii. Therefore, the method for adjusting the filling fraction in the previous Section has been used to calculate the filling fraction of several cylinders. These are presented in table 6.4 along with the reduced Reynolds numbers and values of ε.

A broad range of cylinder sizes have been studied, but because r_0 only appears in first order terms or higher the effect on the film profiles is small. This is shown in figure 6.20 where the films are all smooth. The viscous and gravitational forces are the strongest effects within all of the films, see figure 6.21.

When the cylinder is smaller, the first order effects become stronger as r_0 reduces. Specifically, the inertial and surface tension effects are found to be significantly stronger though they are normally large only when the film is not smooth. The very small surface gradients where the fluid is slightly deeper have

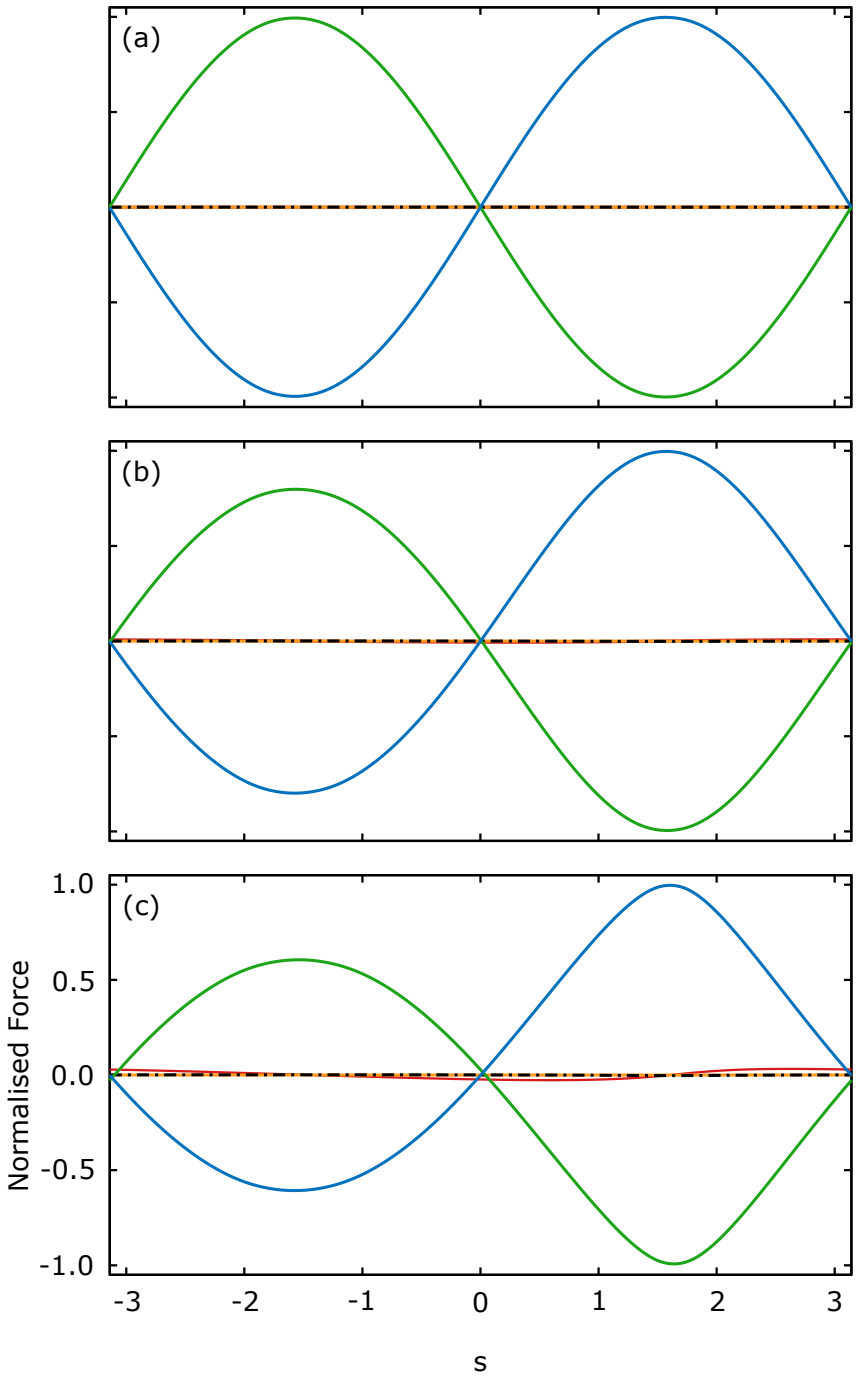


Figure 6.19: The effective force of inertia (in *red*), gravity (in *blue*), viscosity (in *green*), hydrostatic pressure (in *black*) and surface tension (in *orange*) for the films where $h_0 = 0.01\,mm$ in (a), $h_0 = 0.55\,mm$ in panel (b) and $h_0 = 1\,mm$ in (c).

$r_0\ (m)$	A	Re^*	ε
1×10^{-4}	6.1875×10^{0}	2.982×10^{3}	5.5×10^{1}
1×10^{-3}	6.187×10^{-1}	2.982×10^{2}	5.5×10^{0}
1×10^{-2}	6.188×10^{-2}	2.982×10^{1}	5.5×10^{-1}
5×10^{-2}	1.238×10^{-2}	2.982×10^{0}	5.5×10^{-2}
1.1×10^{-1}	5.625×10^{-3}	2.711×10^{-1}	5×10^{-3}
5×10^{-1}	1.238×10^{-3}	2.982×10^{-2}	5.5×10^{-4}
1×10^{0}	6.188×10^{-4}	2.982×10^{-3}	5.5×10^{-5}

Table 6.4: The changed non-dimensional parameters for establishing a smooth solution which are dependent upon r_0, with the remaining parameters given in table 6.2.

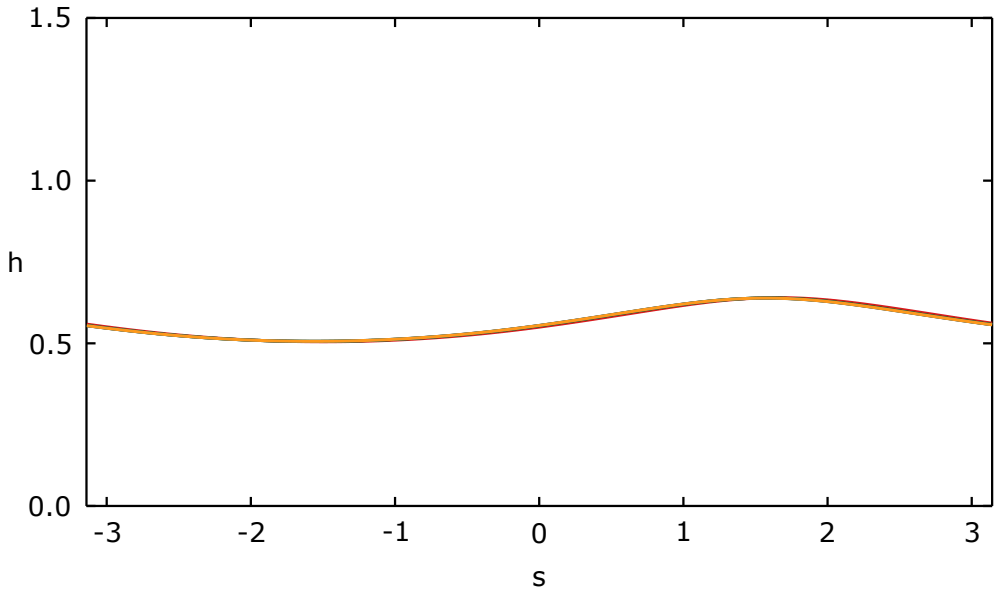


Figure 6.20: The influence that the cylinder radius, r_0 has on the smooth solutions, for $r_0 = 1\,m$ represented by the *orange*, $0.5\,m$ in *blue*, $0.11\,m$ in *black*, $r_0 = 0.05\,m$ with the *green* line and $0.01\,m$ with *red*.

been amplified by the larger dimensionless parameters and these terms are now significant, even though the film is relatively smooth, shown in figure 6.21.

6.3.6 How the Driving Surface Shear Affects Flow Rotation

The constant air shear τ_a^* is large in comparison to the other parameters, where λ is normally equal to τ. A stronger τ leads to films that have a more uniform profile around the cylinder, as the stronger driving force will accelerate the flow and remove any surface variation. If the surface shear is stronger at the film surface the film has a more uniform depth around the chamber which is shown in figure 6.22.

It is therefore beneficial to observe the film behaviour with weaker shear rates. This may happen in the bearing chamber if the shaft speed slows and the gravitational effects become significant. If the driving shear is halved to $\tau_a^* = 4.5\,N/m^2$, the film remains smooth. However, the peak is sharper and the change in forces are almost linear in figure 6.23. This shows the film is close to pooling as the force reversal is more sudden, indicating reverse-flow will occur if τ_a^* is reduced further.

With $\tau_a^* \leq 3\,N/m^2$, the driving shear can no longer overcome gravity to create a smooth film and a pool will develop with a sharp jump on the film surface. As the driving shear reduces, the pool deepens as fluid is pulled from the walls and into the pool by gravity. However, unlike the pool type solutions of Section 6.2 where gravitational effects are strong, the driving shear still smooths the receding film from the pool.

There is an increase in inertial effects with large τ_a^*, as the fluid velocity u will be faster due to the higher shear rate. This accelerates the film and increases the calculated inertial force. When the film is a pool with weak surface shear, the forces within the film fluctuate more. The hydrostatic pressure effects have become significant due to the sudden change in film depth and there are significant surface tension effects which smooth the film surface. The peak in gravitational effects is counterbalanced by a rise in the viscous forces. There is also a negative contribution from the hydrostatic pressure terms at both the pool peak and receding regions towards the pool exit.

The value of the driving shear force is important as it determines if a smooth film or a pool will form. The driving shear is a strong force which keeps the film smooth in most cases. Therefore, the shear force τ_a^* is reduced to $4.5\,N/m^2$ in Section 6.4. The film will be smooth, but it will be much easier to change the film profile with different parameters.

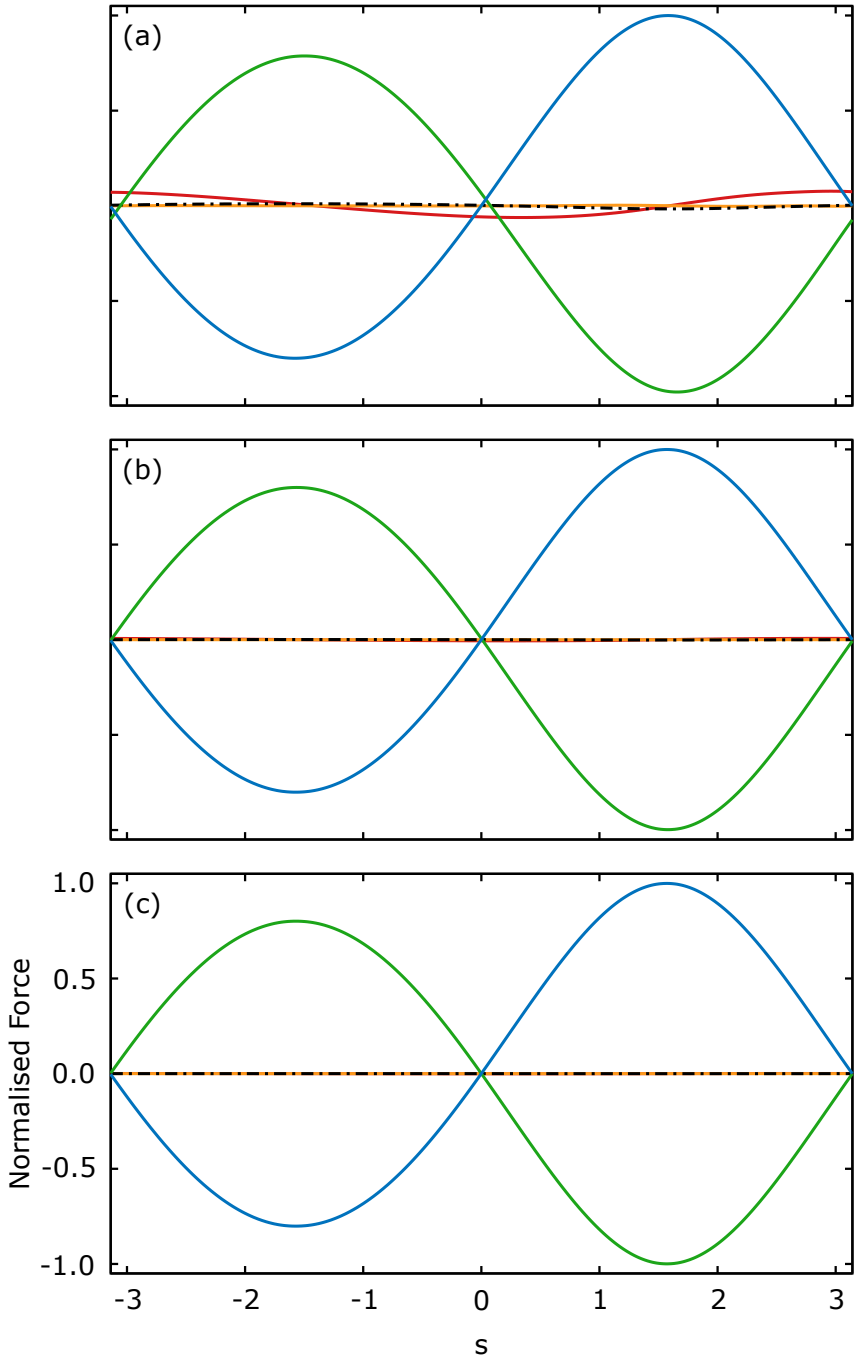


Figure 6.21: A graph detailing the forces found within the fluid film for the cylinder radius, r_0, where (a) is for $0.01\,m$, (b) for $0.11\,m$ and in (c), $r_0 = 1\,m$. The relevant forces are given as hydrostatic pressure in *black*, surface tension in *orange*, gravity and viscosity in *blue* and *green* respectively and inertia in *red*.

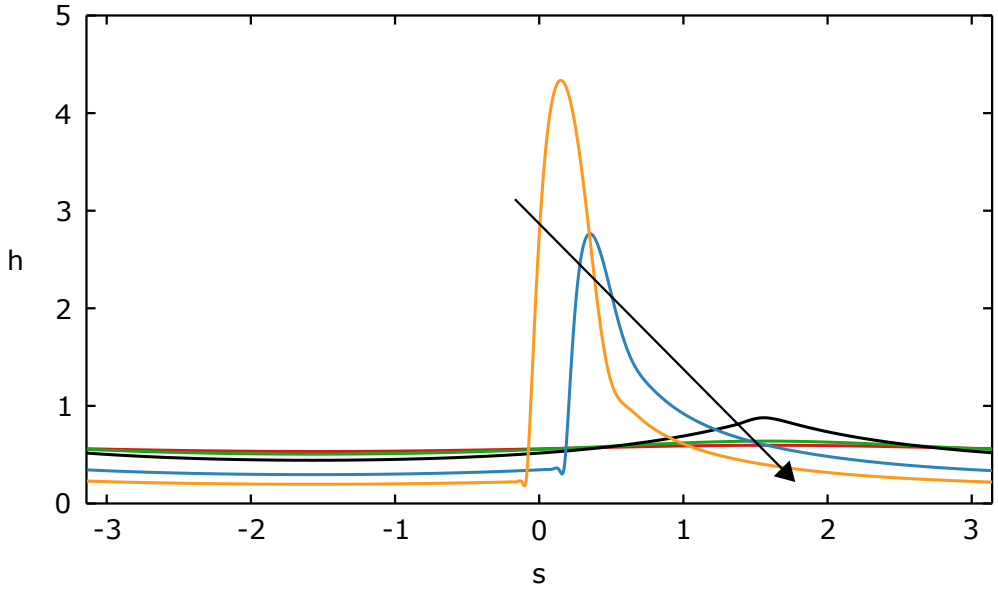


Figure 6.22: Effect of the applied driving shear force τ_a^* at the surface, and the sensitivity the film profiles to the strength of the driving surface shear with a fixed fluid volume. Where $\tau_a^* = 2\,N/m^2$ in *orange*, $3\,N/m^2$ in *blue*, *black* for $4.5\,N/m^2$, *green* for $9\,N/m^2$ and $18\,N/m^2$ is in *red*.

6.3.7 How Slip Effects a Strongly Driven Film

This thesis has focused on determining the effect that fluid slip on the cylinder wall will have on the film profiles of rimming flows. The current literature on fluid slip has reported slip lengths from $0\,\mu m$ up to $200\,\mu m$. However, the films in this Chapter so far have assumed there is no-slip on the cylinder wall. Therefore, several flows have been simulated with slip lengths founding in the literature to determine the size of slip necessary to have a significant effect on the film.

For a small slip length of $10\,\mu m$, the maximum depth of the film is increased. This increase in depth of the film is caused by the flow accelerating as the velocity is no longer zero at the cylinder wall. This causes the falling wall to be drained of fluid which accrues on the rising wall. The volume of fluid required for the given shear rate and viscous effects are lower because of slip. This increase in depth is small but this size of slip is thought to be readily attainable with the current knowledge contained in the literature.

This increased depth with slip is also found with $l_s^* = 50\,\mu m$. The depth is further increased on the rising wall while the falling wall has shown a bigger decrease in film thickness. As slip increases up to the largest length of $200\,\mu m$, the thickening and thinning of the film which occurs on diametrically opposite sides are magnified. Though the changes to the film profiles appear to be minor, this has also been the case for most of the results in this Section. However, the analysis of the internal forces within the film show that with larger slip lengths,

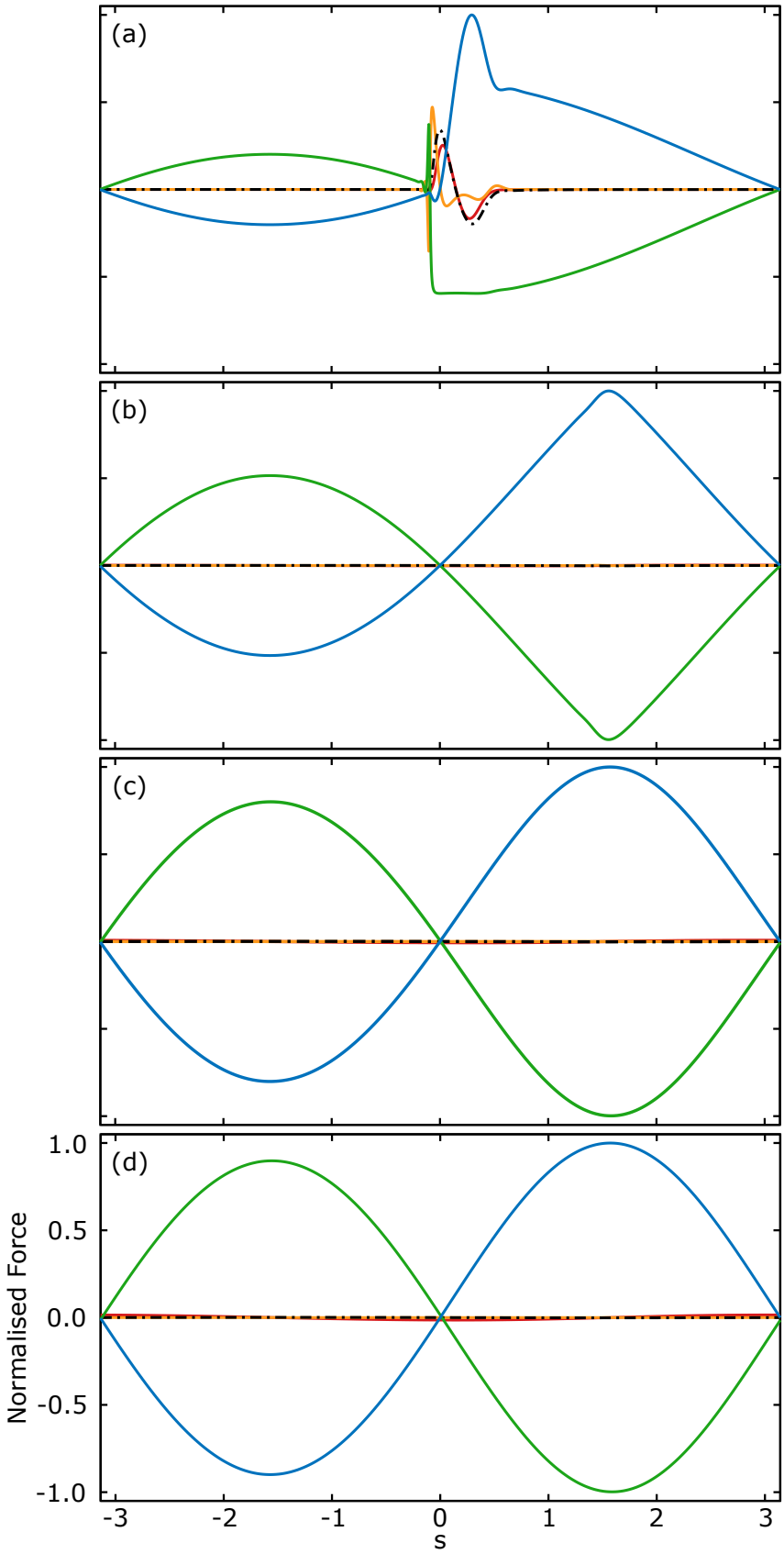


Figure 6.23: Forces for changing τ_a^*. With inertia in *red*, gravity in *blue*, viscosity in *green*, hydrostatic pressure in *black* and surface tension in *orange*. Where (a), (b), (c) and (d) are for solutions to $\tau_a^* = 2\,N/m^2$, $4.5\,N/m^2$, $9\,N/m^2$ and $18\,N/m^2$.

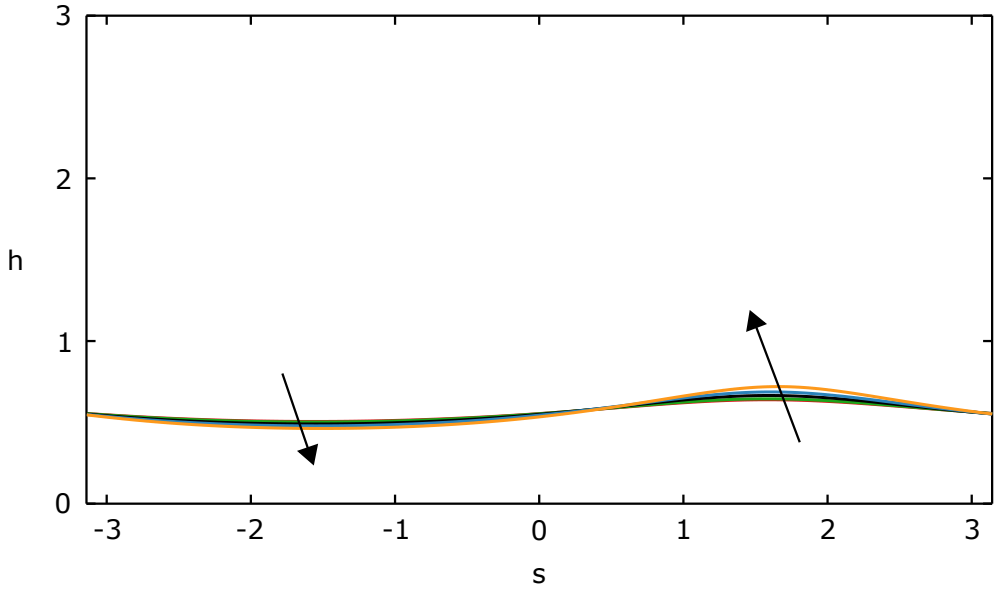


Figure 6.24: The importance of the slip length, measured in m on the film profile of the strongly driven flow. The lines correspond to no-slip *red*, $l_s^* = 0.00001\,m = 10\,\mu m$ in *green*, $l_s^* = 0.00005\,m = 50\,\mu m$ in *black*, $l_s^* = 0.0001\,m = 100\,\mu m$ in *blue* and $l_s^* = 0.0002\,m = 200\,\mu m$ is depicted in *orange*.

the faster film velocities u have made the effects of inertia stronger.

The change in flow velocity with slip also changes the location where the maximum fluid depth is found. This movement is because the faster film will require a greater amount of deceleration from gravity for the film to slow down and develop into this hump on the rising wall.

This Section has observed minimal changes for any of the parameters due to the strong surface shear rate applied at the surface and was also found for the increase in slip length. However, the changes in the film profiles and the internal forces with slip suggest that if the surface shear rate was to be weaker, slip would cause a significant change in the film. This is shown in Section 6.4.

6.4 A Weakly Driven Film without Fluid Pooling

The high surface shear in Section 6.3 meant that the changes in film profiles with different characteristic values was small. The solutions were mostly smooth films. But it was shown in Section 6.3.6 that with a smaller driving shear force, the smooth film is close to developing into a pool and there are significant variations to the internal forces within the domain. This Section investigates the role of each characteristic value to determine how the flow will change when the air shear is

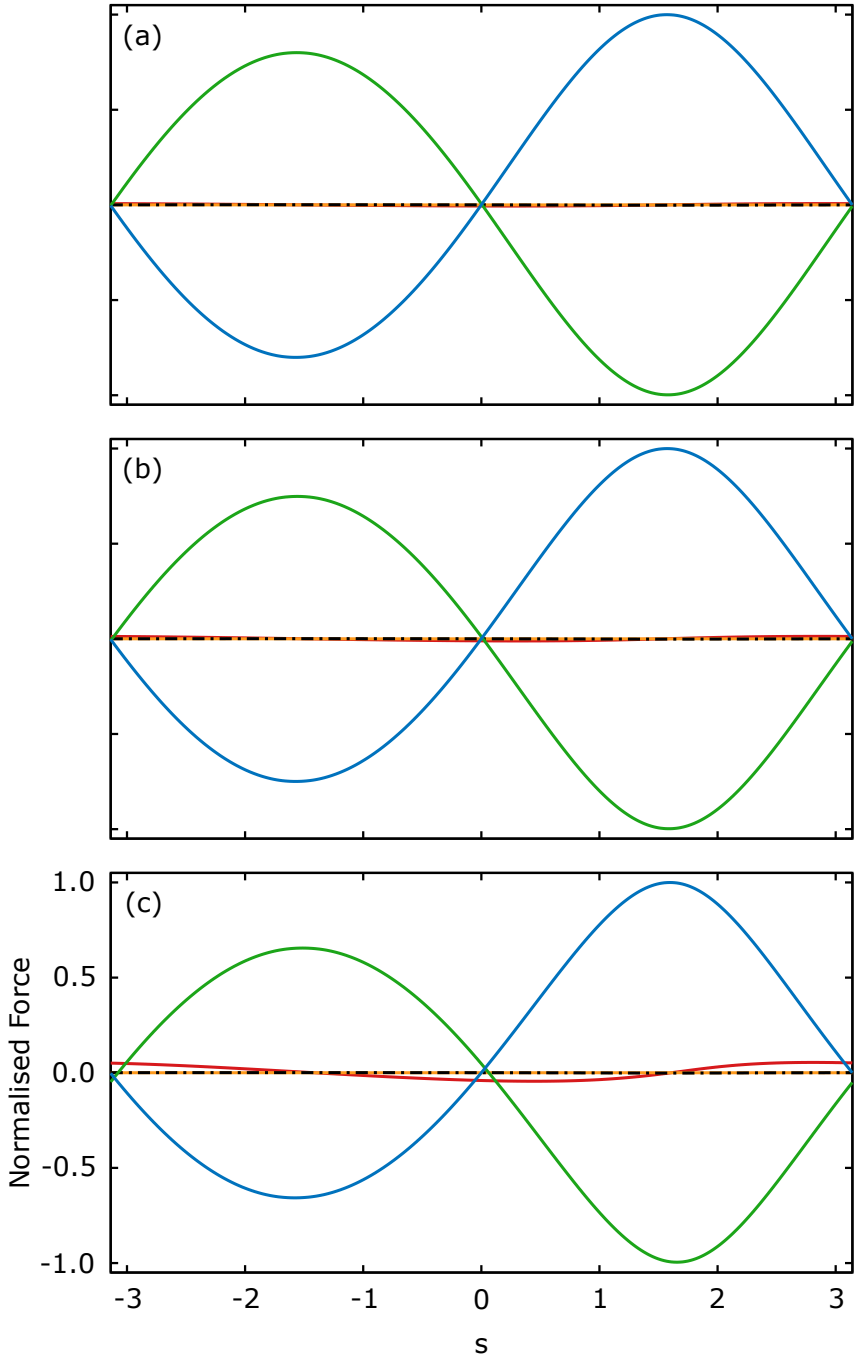


Figure 6.25: The effect of the five modelled forces of gravity (in *blue*), hydrostatic pressure (in *black*), inertia (in *red*), surface tension (in *orange*) and viscosity (in *green*) found in the films of figure 6.24. With $l_s^* = 0\,\mu m$ in (a), $l_s^* = 50\,\mu m$ in (b) and $l_s^* = 200\,\mu m$ in (c).

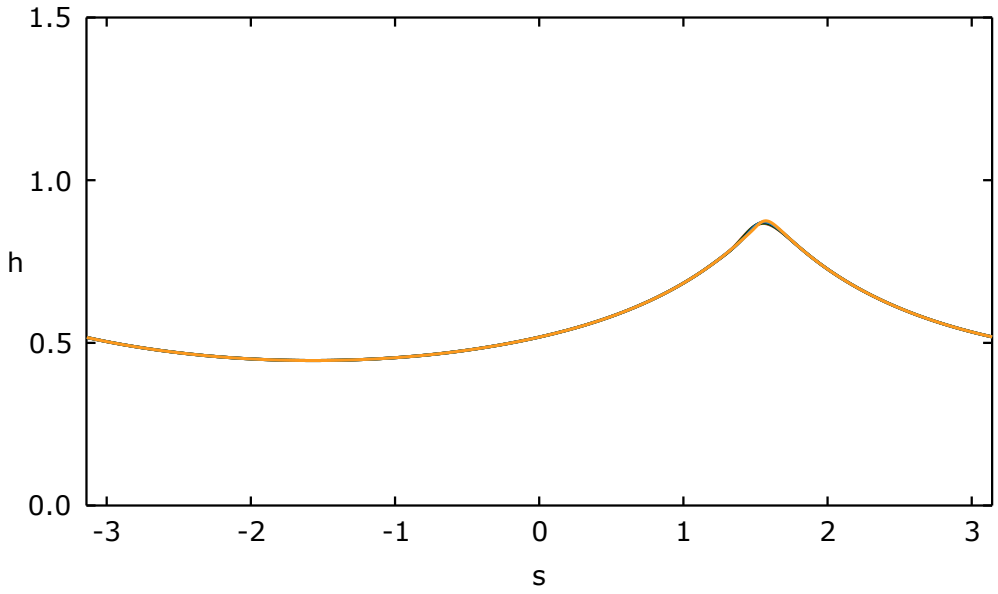


Figure 6.26: The effect of the surface tension coefficient, σ on the film profiles when a lower driving shear force of $\tau_a^* = 4.5\,N/m^2$, depicted for $\sigma = 0.0245\,N/m$ in *orange*, $0.25\,N/m$ in *blue*, $0.5\,N/m$ in *black*, $0.75\,N/m$ in *green* and $1\,N/m$ in *red*.

weaker at $\tau_a^* = 4.5\,N/m^2$.

6.4.1 Surface Stabilisation for Various Surface Tension Coefficients

As the driving shear has been reduced, the film peak has a sharper tip at the maximum depth. The film has a larger h' and means that the effect of surface tension is stronger on the film surface. Previously, changes in the surface tension coefficient had no change on the film surface, shown in figure 6.1. However, this is no longer the case with the weaker surface shear rate of $\tau_a^* = 4.5\,N/m^2$, shown in figure 6.26.

With the lowest surface tension coefficient, the maximum film depth is larger. This is because the smoothing effect from surface tension which would prevent the sharp tip is weaker. This higher peak also has a sharper point in the film as the inversion of the gravity and viscous forces occur over a smaller region of s, shown in figure 6.27. A very large surface tension coefficient causes the film surface to be smoother but is a relatively small change in the profile.

The change in σ is minor but is important when capillary ripples form. The lower surface tension coefficient of $\sigma = 0.0245\,N/m$ will hindered the ability to obtain stable solutions and increases the required simulation time of each film. Therefore, the remainder of this Section uses $\sigma = 0.5\,N/m$ which improves the

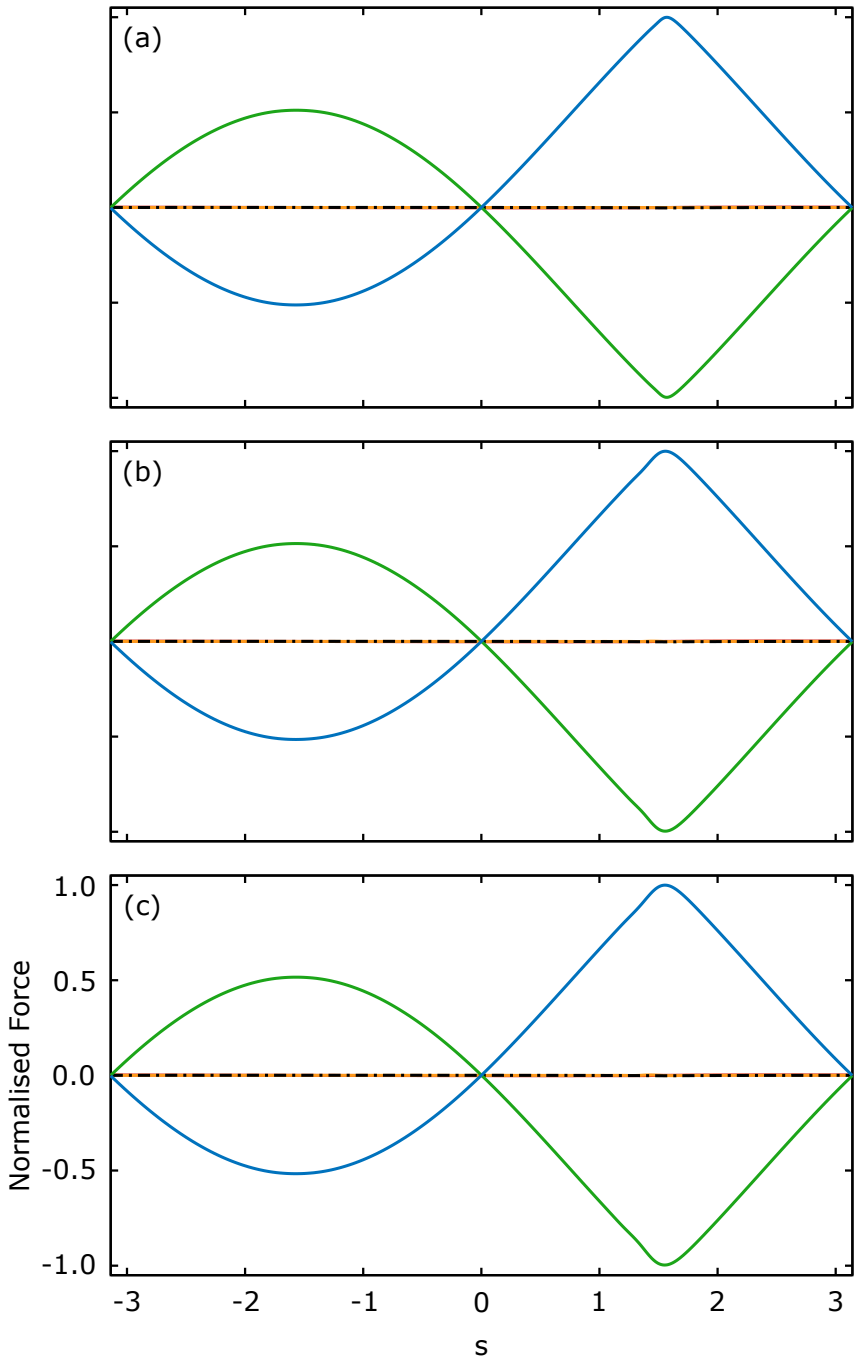


Figure 6.27: The typical forces found within a rimming flow, consisting of viscosity (*green*), surface tension (*orange*), inertia (*red*), hydrostatic pressure (*black*) and gravity (*blue*). The different panels represent new values of the surface tension coefficient, for $\sigma = 0.0245\,N/m$ in (a), $\sigma = 0.5\,N/m$ in (b) and $\sigma = 1\,N/m$ in (c) as shown in figure 6.26.

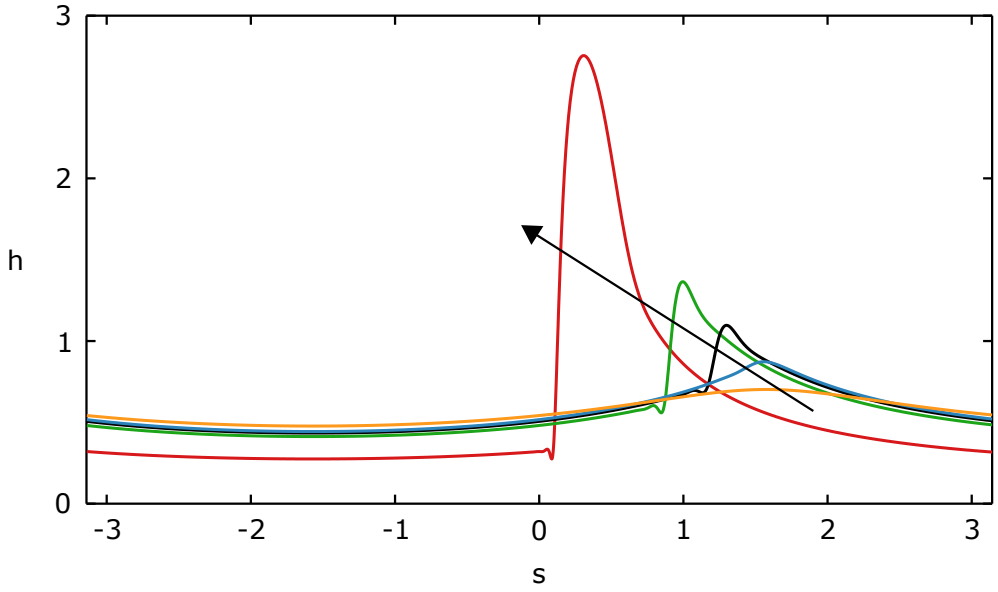


Figure 6.28: The effect of fluid density on the films now that a weaker driving shear force acts on the surface. The densities are equal to those of figure 6.12, with $\rho = 700\,kg/m^3$ given in *orange*, $\rho = 930\,kg/m^3$ in *blue*, $950\,kg/m^3$ coloured *black*, $1000\,kg/m^3$ in *green* and $1500\,kg/m^3$ in *red*.

numerical stability.

6.4.2 Importance of Fluid Density in Determining the Film Profile

Previously, the fluid density was found to have little effect on the film profiles unless the density was very high. By reducing driving shear force, this is no longer the case and density is now important. If the fluid density is reduced, the gravitational effects are decreased as the lighter fluid means the viscous effects are more dominant. This creates a more uniform film in the chamber, which is shown in figure 6.28.

When the fluid density is higher, there is a considerable change in the film behaviour. This was found for a small increase to the fluid density from $930\,kg/m^3$ to $950\,kg/m^3$ where the film developed into a narrow pool just before the middle of the rising wall. This accumulated fluid forms from the small reduction in the film height outside of the pool. There are capillary ripples that precede the pool due to surface tension smoothing. At large fluid densities the volume of fluid within the pool increases drastically with the effect of gravity and increases the film's maximum depth.

The uniform films are desirable for the bearing chamber as they lack any flow recirculation. However, a 2 % change in density can cause the smooth film to

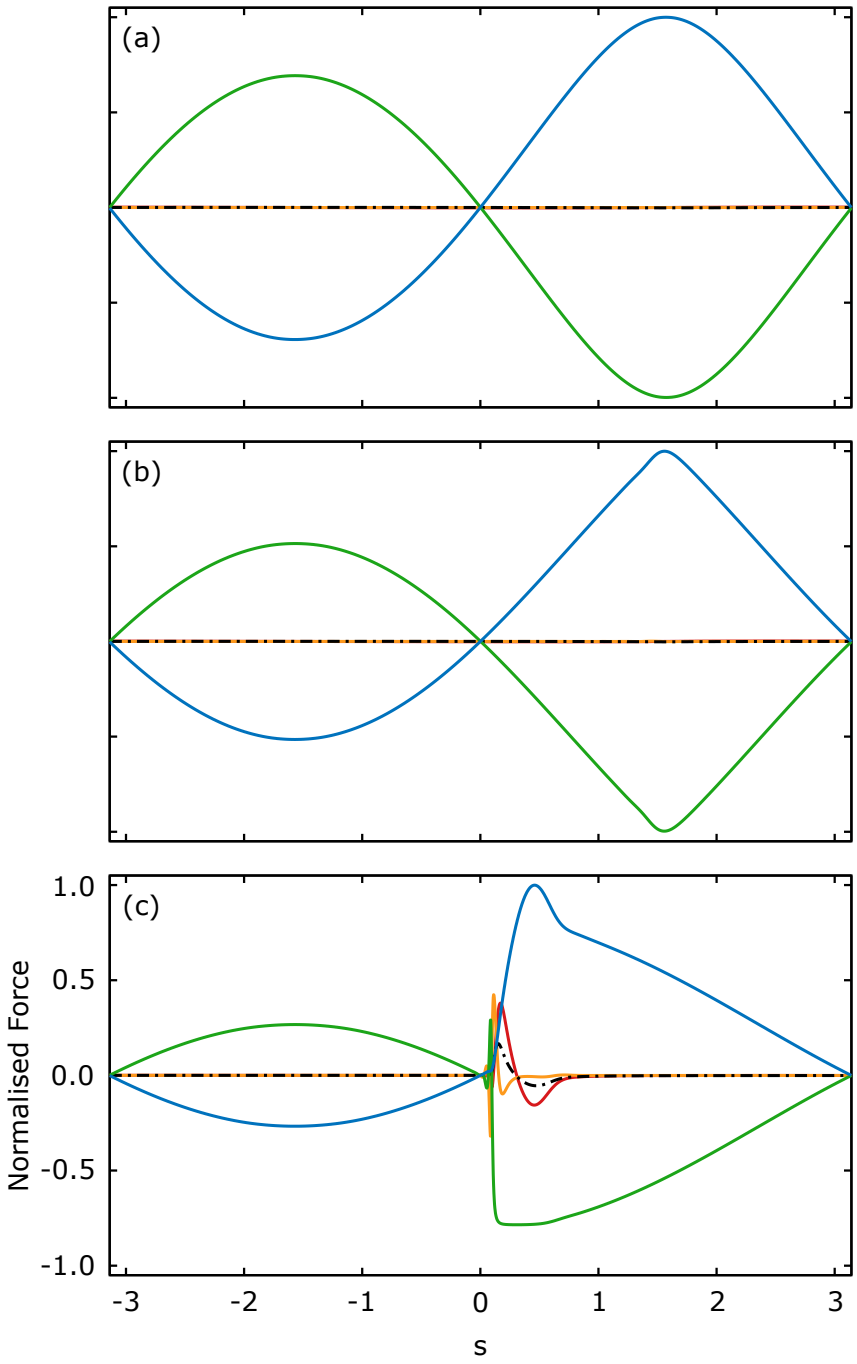


Figure 6.29: The developing forces within the films of figure 6.28 for increasing density, ρ, for $\rho = 700\,kg/m^3$, $930\,kg/m^3$ and $1500\,kg/m^3$ in (a), (b) and (c) respectively. The coloured lines depict the effective value of gravity, hydrostatic pressure, inertia, surface tension and viscosity as *blue*, *black*, *red*, *orange* and *green* colours respectively.

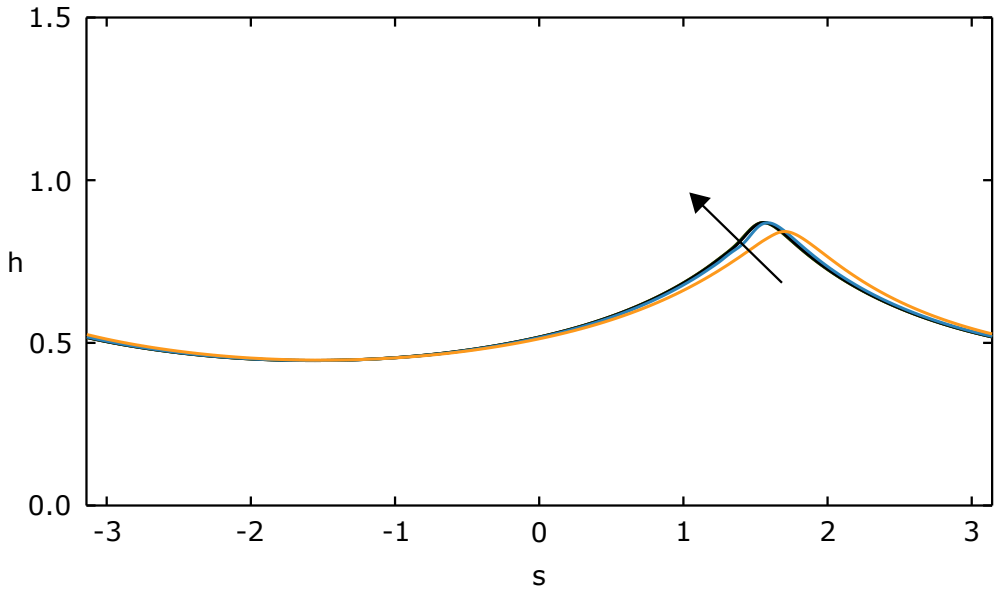


Figure 6.30: Profiles for changes to the fluid viscosity μ, with parameters defined in table 6.2 but the driving shear force is only $4.5\,N/m^2$. With *orange* for $0.001\,Ns/m^2$, *blue* for $0.002\,Ns/m^2$, *black* for $0.00483\,Ns/m^2$, *green* for $0.0075\,Ns/m^2$ and *red* for $0.01\,Ns/m^2$.

collapse into a pool and the higher order effects are now significant, as shown in figure 6.29.

6.4.3 The Effect of Viscosity with Weak Surface Shear

The fluid viscosity was found to have no significant change to the film profiles in Section 6.3. However, this was due to the strong air shear which is now weaker at $\tau_a^* = 4.5\,N/m$. The larger viscosity is found to have little change on the film surface and is because most of the parameters are inversely proportional to viscosity, shown in figure 6.30. This is also shown in figure 6.31 where the forces are zero in the domain, with the exception of gravity and viscosity. The film is found to be unchanged with $\mu \geq 0.002\,Ns/m^2$. If the viscosity is large with $\mu \gg 0.01\,Ns/m^2$, the effects of gravity will reduce and the flow will appear as a solid body due to the large viscous effects.

With $\mu = 0.001\,Ns/m^2$, the film has become smoother and the location of the maximum film depth is higher up the cylinder wall. This smoother film is attributed to the increase in inertia, shown in figure 6.17. This strong inertial effect reduces the fluid deceleration from gravity and the film is therefore smoother.

The characteristic value of μ has a linear relationship with the definitions of Re^*, Ca, λ and τ in (6.1). A pooled film may appear at very low values of μ, but this may be lower than any physical fluid. Therefore, the fluid viscosity is not a

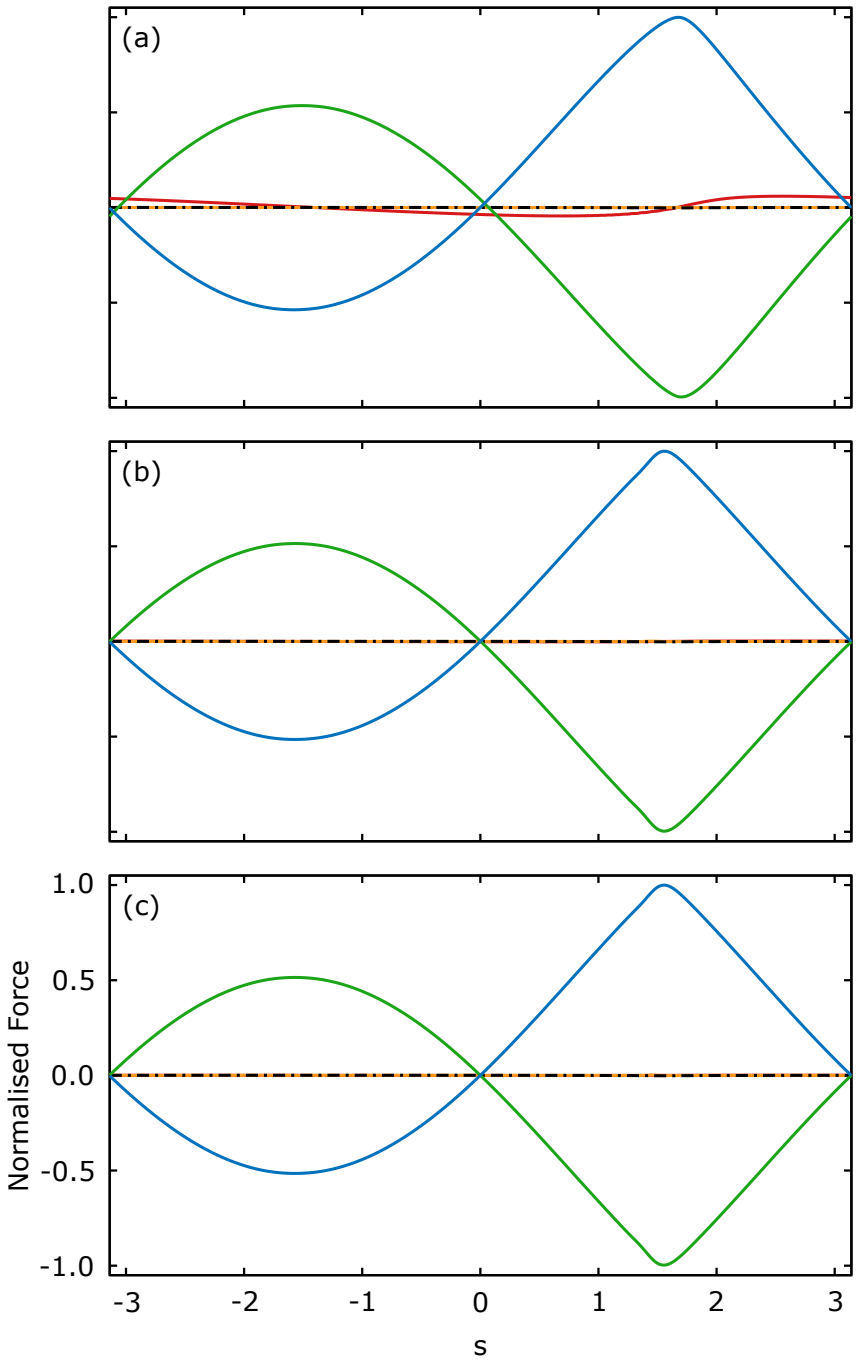


Figure 6.31: Outlines of five key forces found within the film profiles of figure 6.30, for changing dynamic viscosity, μ. With (a) mapping the forces for $\mu = 0.001\,Ns/m^2$, (b) for $\mu = 0.00483\,Ns/m^2$ and $\mu = 0.01\,Ns/m^2$ in (c). The five forces are denoted by the coloured lines, as surface tension in *orange*, inertia in *red*, gravity in *blue*, hydrostatic pressure in *black* and viscosity in *green*.

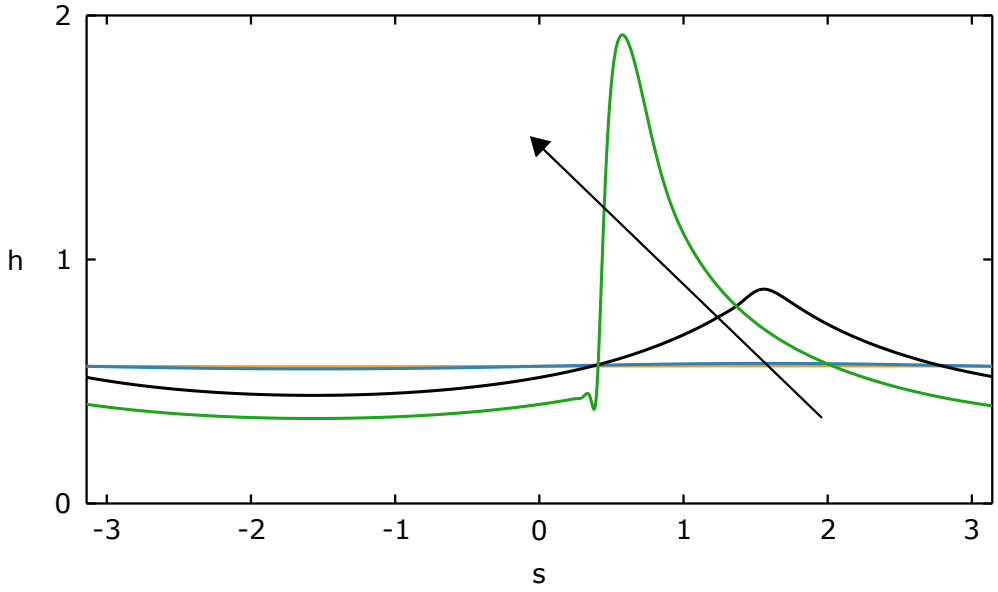


Figure 6.32: The effect of h_0 for the smooth solution defined in table 6.2 using the lower shear force of $\tau_a^* = 4.5\,N/m^2$. With the characteristic film heights h_0 given by a *green* line for $0.7\,mm$, *black* for $0.55\,mm$, *blue* for $0.05\,mm$ and *orange* for $h_0 = 0.01\,mm$.

significant characteristic for determining the flow.

6.4.4 Effect of Characteristic Thickness on Stable Film Structures

The method used in Section 6.3 to recalculate the filling fraction with changes in the film height has been used to ensure consistent fluid volumes for each film. These are presented in table 6.3.

The smaller film thicknesses reduce the values of the non-dimensional parameters of (6.1). The reduction in most of the higher order effects has a small impact on the film profile, specifically Re^*, τ and ε^3/Ca. However, the quadratic dependency in λ means the viscous effects are equal to or stronger than gravity with $h_0 \leq 0.05\,mm$. This is shown with the smooth films in figure 6.32, which have a uniform depth due to viscosity. The forces are symmetrical about the cylinder base with the viscous and gravitational effects on the rising and falling walls being equal, as shown in figure 6.33.

A larger characteristic height of $h_0 \geq 0.55\,mm$ leads to stronger gravitational effects which drains the fluid from the chamber walls. This creates a large pool in the cylinder which is shown in figure 6.32. The larger film height also reduces the effective shear rate acting on the film and a pool forms with a film height of $h_0 = 0.7\,mm$, which is lower than the previous Section where a pool will only form

at very large film depths. Another effect of increasing h_0 is the change in higher order terms as the value of ε increases. The pooled films feature a prominent surface wave preceding the pool and is due to the surface tension terms being an $O(\varepsilon^3)$ term. The reason the film develops a pool is a significant volume of fluid is pulled from the wall by gravity, where there has been a reduction of over 40 % in the minimum thickness for h_0 between $0.7\,mm$ and $0.1\,mm$, shown in figure 6.32.

The effect of surface tension is almost equal in strength to either viscosity or gravity in the local region around $s = 0.5$ where the capillary ripples form. Larger values of h_0 were investigated, however a stable film was not found with the current method. This has been because the iterative solver failed to converge to a stable solution.

6.4.5 Variation to the Cylinder Radius and Resulting Solutions

The film profiles for several cylinders have been simulated with the weaker surface shear of $\tau_a^* = 4.5\,N/m$. The filling fractions used for each film are presented in table 6.4 using the adjusted filling fraction equation to ensure an equal fluid volume for each film.

The effect of different sizes of cylinder are found to have minor changes in the film profiles. However, an interesting change has been found when the cylinder radius r_0 is very small. The smaller diameter cylinders have a shallower minimum depth and this fluid accumulates on the rising wall in an increasingly deeper and wider region. The wider pool is due to the increase in inertial and surface tension effects with the changes to ε and leads to a smoothing of the pool. This smoothing from surface tension occurs over a large area of the domain, when it is normally a localised effect in the surface waves in front of the pool. When the cylinder is large, the main change is the reduction in the effect of higher order terms. This is shown in figure 6.35 where the reduction in inertia at $r_0 = 1\,m$ means the effect is now zero.

While there are some changes to the film, the size of the cylinder is not found to be significant in determining the film profile. This is because the size of cylinder required to significantly change the flow is not realistic for the aero-engine bearing chambers.

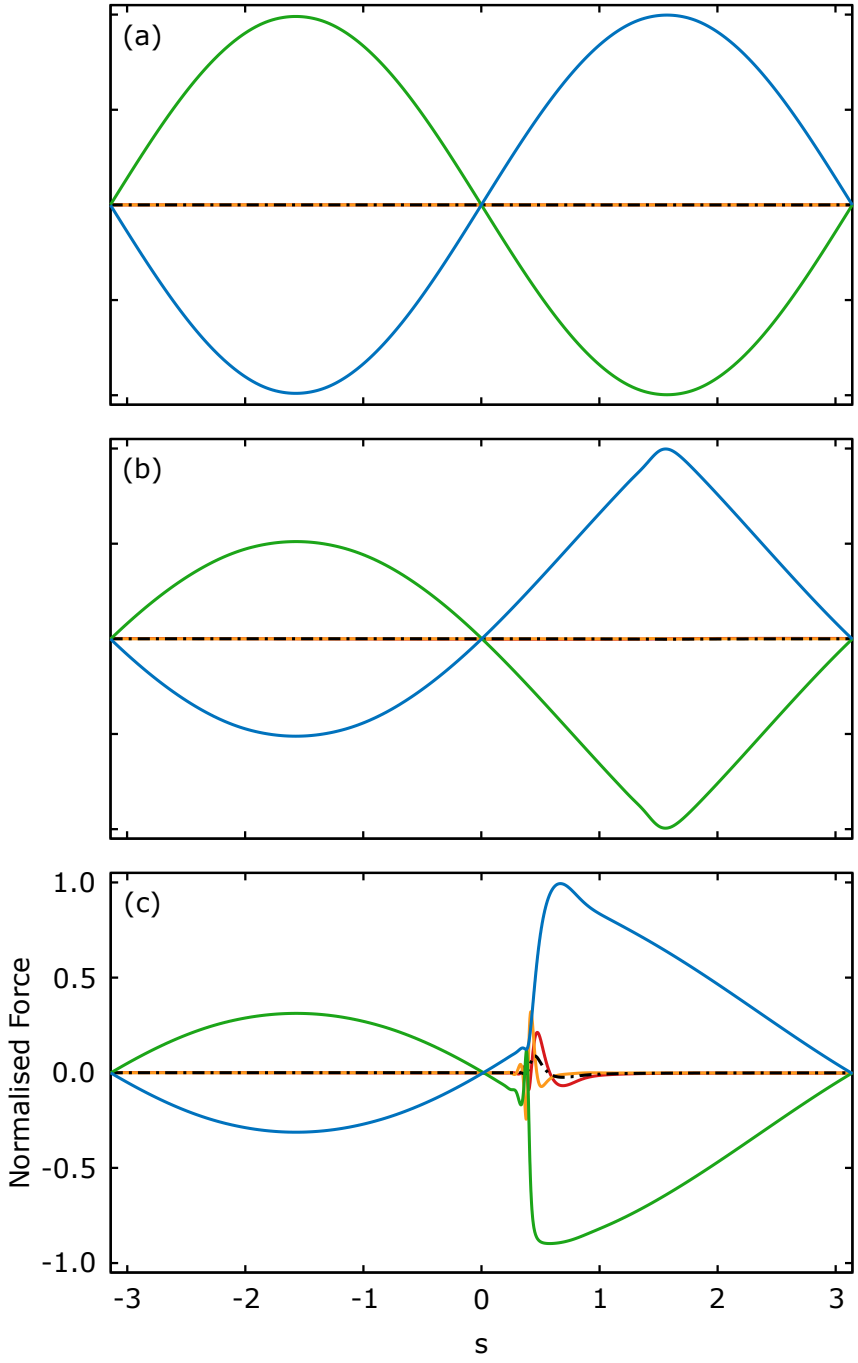


Figure 6.33: The forces of the key films defined as $h_0 = 0.01\,mm$, $h_0 = 0.55\,mm$ and $h_0 = 0.7\,mm$ shown in (a), (b) and (c) respectively as films from figure 6.32. The calculated forces are shown in *red* (inertia), *blue* (gravity), *green* (viscosity), *black* (hydrostatic pressure) and *orange* (surface tension).

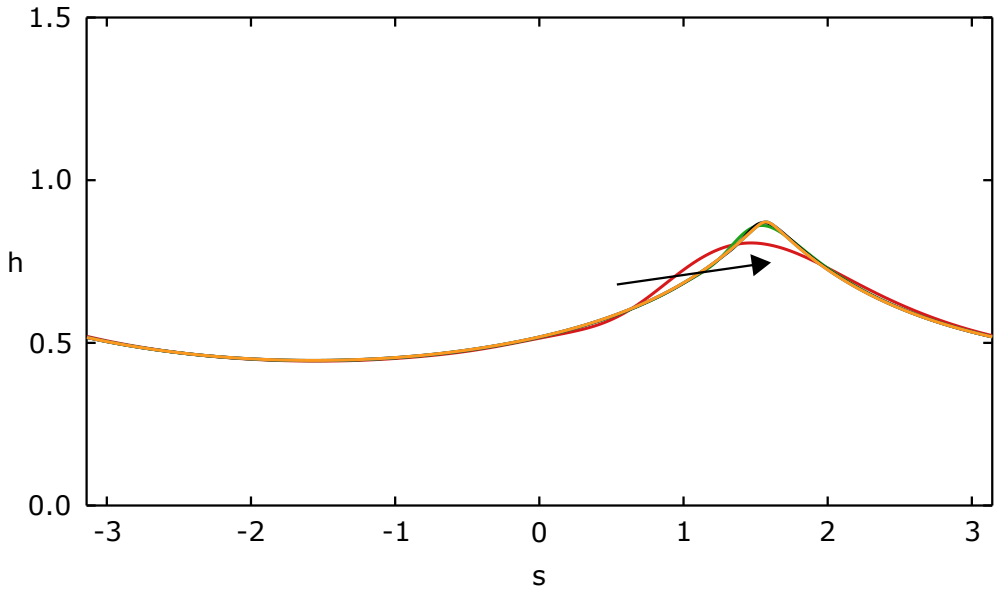


Figure 6.34: The changes to the film profiles with different cylinder radii, r_0 using $\tau_a^* = 4.5\,N/m^2$ and the other parameters of table 6.2, where *red* is for $r_0 = 0.01\,m$, *green* for $0.05\,m$, *black* for $0.11\,m$, *blue* for $r_0 = 0.5\,m$ and *orange* for $r_0 = 1\,m$.

6.4.6 The Effect of the Slip Condition on the Weakly Supported Film

The addition of both low and moderate slip lengths were shown to have only subtle changes to the thin films that develop in the cylinder in Section 6.3. This is contrary to most of the results shown in this thesis, where moderate slip has a significant impact on the film profile. If the driving shear is reduced, the effect of fluid slip is substantial. The case where there is no-slip establishes the control case of the expected film profiles. When the slip length of the cylinder is relatively small at $l_s^* = 10\,\mu m$, the smooth surface no longer exists. Instead, this has been replaced by a small pool in the chamber that is found high up on the rising wall. The fluid on the walls of the chamber has been thinned as a result of the slip condition. The creation of a pool may be thought of as a negative aspect for creating a bearing chamber which generates fluid slip. However, this pool only forms as the volume of fluid in the cylinder has not changed from the no-slip case.

This thinning of the film continues as the length of fluid slip increases up to the maximum value of $l_s^* = 200\,\mu m$. This large slip length has been reported in the literature and has the thinnest film by over 30 %. The volume of fluid contained within the recirculation region has increased because of this thinning and the pool is much larger in width and depth. This would be a negative feature in maintaining oil properties.

However, it must be understood that this negativity is because the volume of

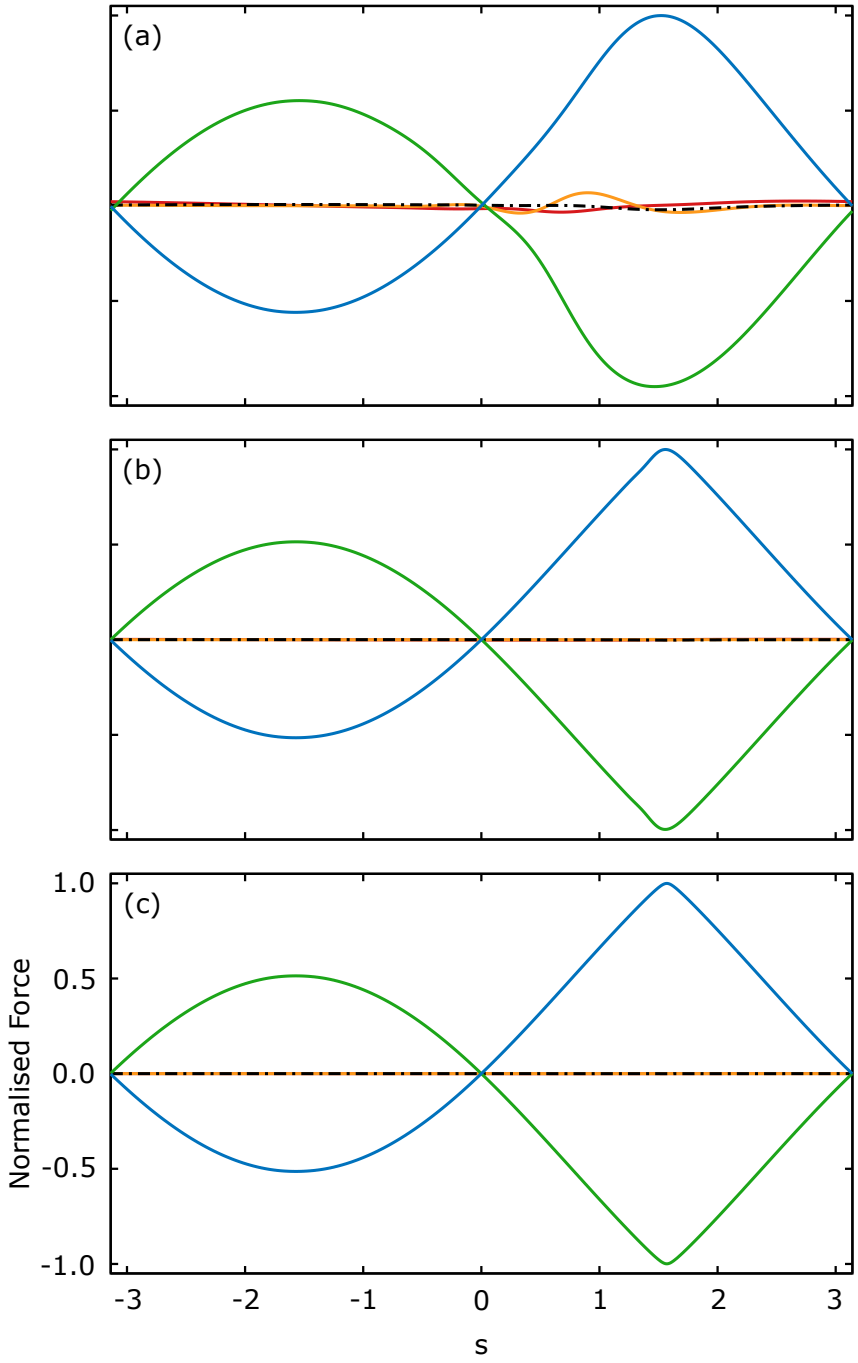


Figure 6.35: Visualisation of the forces found within films where $r_0 = 0.01\,m$, $r_0 = 0.11\,m$ and $r_0 = 1\,m$ in panels (a), (b) and (c) respectively for the films of figure 6.34, where the coloured lines are given as *black* for hydrostatic pressure, *blue* for gravity, *green* for viscosity, *red* for inertia and *orange* for surface tension.

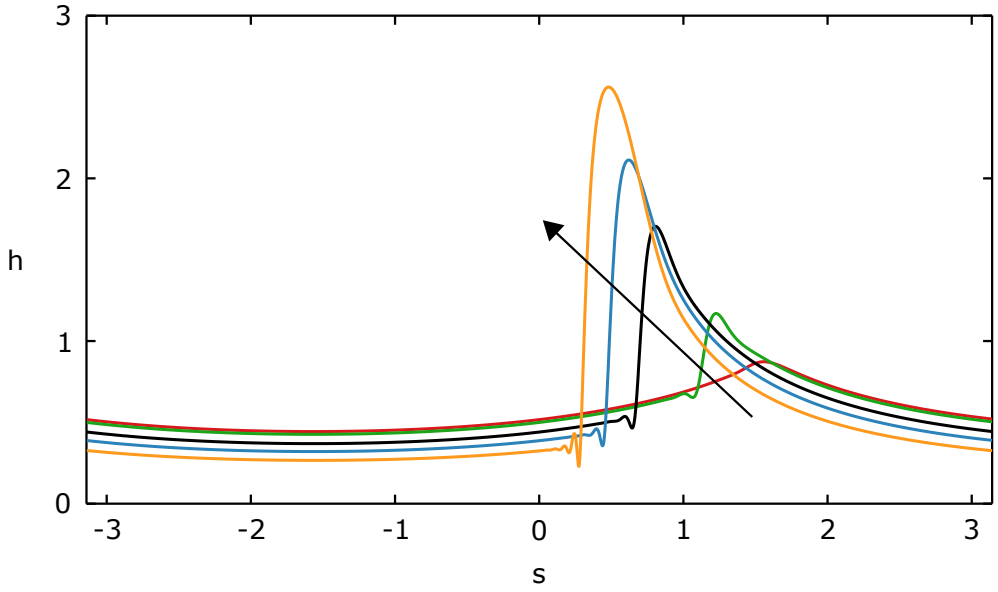


Figure 6.36: The effect that longer slip lengths, including the no-slip condition, have on the resulting film profiles. Where the parameters are defined in table 6.2 with the reduced shear rate of $\tau_a^* = 4.5\,N/m^2$, with $l_s^* = 0\,\mu m$ in *red*, $l_s^* = 10\,\mu m$ in *green*, $l_s^* = 50\,\mu m$ in *black*, $l_s^* = 100\,\mu m$ in *blue* and the largest slip length of $200\,\mu m$ in *orange*.

fluid has been kept constant. If fluid slip was to be created on the chamber walls, the amount of oil in the bearing chamber could be reduced to prevent this deeper pool. Interestingly, the increased fluid velocity at the wall reduces the amount of fluid needed to maintain a coated cylinder. This effect may also be used to encourage fluid to flow out of the chamber and into a sump.

Fundamentally, this finding is arguably the most important of the research in this thesis. These results have shown that slip has a dramatic effect of the film and may be exploited for the bearing chamber. The current knowledge on surfaces where fluid will slip is associated to either the use of chemical coatings that cause a hydrophobic effect or the use of small structures to create pockets of trapped air. The stability of these surfaces for long operating cycles, such as the bearing chamber, is not currently known. However, the use of surface structures seems to create the longest slip lengths and are likely to be the most reliable for the bearing chamber. This assumes that the pockets of air are stable during the various operating conditions and would require further research before commercial use. However, the effect of even small fluid slip is clearly substantial in some situations for rimming flows. It may be possible to modify the bearing chamber to have surfaces which can slip which will improve the oil flow through the system and therefore increase the efficiency of the engine.

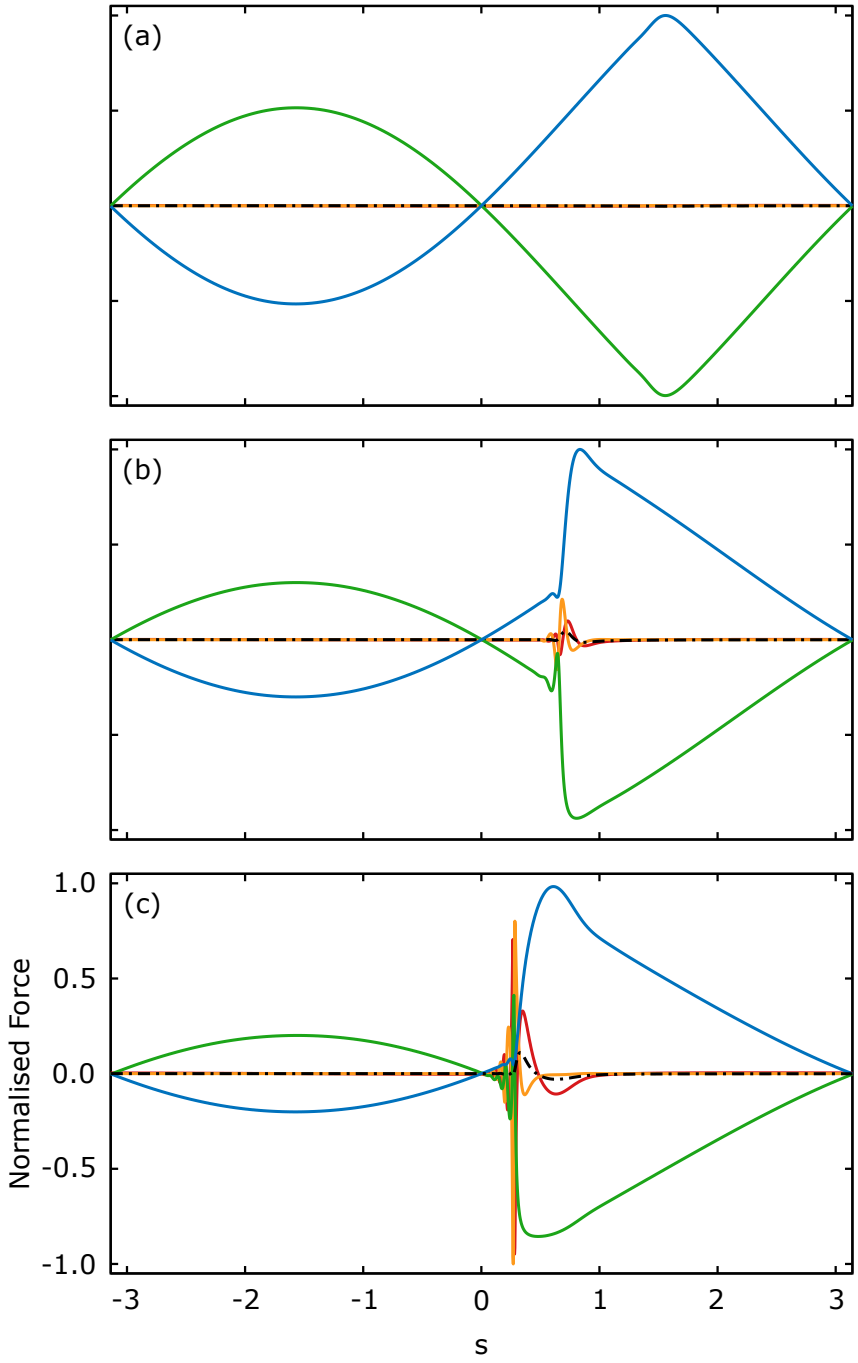


Figure 6.37: The forces found within the film profiles of figure 6.36, for the no-slip case in (a), $l_s^* = 50\,\mu m$ in (b) and $l_s^* = 200\,\mu m$ in (c). The forces are represented as surface tension in *orange*, viscosity in *green*, inertia in *red*, gravity in *blue* and hydrostatic pressure in *black*.

6.5 Chapter Summary

This Chapter details the importance of the physical parameters used to portray the bearing chamber and features the most significant finding of this thesis. The developed model is shown to be in good agreement with an alternative Eulerian thin-film model of Kakimpa et al. [1]. While there are some differences between the film profiles, these differences have been thoroughly explored and the two most probable causes have been identified. The first difference is the model of this thesis includes centrifugal inertia effects, while the study by Kakimpa et al. [1] excluded this effect. One of the findings in this Chapter is the centrifugal effects are not insignificant, especially when a recirculating pool occurs. Secondly, the Eulerian thin-film model includes a wall shear sub-model. This shear impedes the flow and causes the thickness around the cylinder to reduce, subsequently a deeper pool forms.

The numerical model is shown to be advantageous in solving the rimming flow problem, with the pseudo-spectral method being able to cluster nodes, which is particularly beneficial for resolving the capillary waves. The numerical method is also useful for other problems, especially for approximating continuous variables or if node clustering is needed, as there are numerous clustering functions which may be used.

The importance of the time-averaged characteristic values of the film are detailed in this Chapter, presenting a variety of films that form as a result of these parameters. The system of non-dimensional coefficients of Chapter 3 causes some parameters to be of greater importance; most notably the fluid density, applied surface shear coefficient and film height are key in determining if a smooth or pooling film forms. If there is a very strong surface shear inside the cylinder, only the characteristic film depth has a significant effect on the flow profile. There is, however, a slight change in the film with long slip lengths.

With a moderate shear rate applied to the film surface, the main finding of this research is presented for the effect of partial slip on the cylinder. Using slip lengths which have been documented in the background literature, the originally smooth film collapses and forms a deepening pool as slip increases. Even small slip lengths of 10 μm cause a significant change in the fluid dynamics of the problem, showing that modifications to the chamber surface that produce slip will be significant. This result, above all others in this thesis highlights the importance of developing surfaces which can cause fluid slip, resulting in substantial changes to the fluid profiles for the bearing chamber problem.

Chapter 7

Conclusions

This Chapter details the conclusions that are drawn throughout this thesis, along with suggestions on future works that may be undertaken to develop the novel contributions further.

The work of Chapter 2 presents a review of the current literature on the flows found within aero-engine bearing chambers. As well as the background literature on rimming flows which is frequently used as a comparable problem in similar studies. The previous findings have indicated that hydrostatic pressure, inertia and thermal convection are all important effects in modelling the thin films of the chamber. A review of the literature on fluid behaviour at very small scales has highlighted the idea that fluid may slip across a surface, an effect which can also be generated when using certain surfaces. There is a distinct lack of understanding on how these effects can have an impact at larger scales, especially those of rimming flows, this thesis aims to investigate the implications these may have for aero-engines, of which this thesis covers.

An approach to include the key effects highlighted from the literature has been developed for a two-dimensional flow around a horizontal cylinder, taking a depth-averaged method to reduce the equation dimensionality, a technique commonly associated with hydraulic theory. The resulting continuity, momentum and energy equations are presented in terms of mean values of the velocity, temperature and film height. Internal details of the flow are removed during depth-averaging, necessitating an a priori approximation of the complete flow velocity and temperature fields, which are calculated by quadratic functions. The fluid slip effect is included as a generalised Navier slip condition, with the results of the model shown to agree with previous studies without slip and has been inspected in detail.

An important result has been found in classical lubrication theory, where the imposed surface slip has substantially altered the mathematical limits, crucially, the maximum possible thickness that can be supported within the cylinder reduces

in correlation to longer slip lengths. A feature that occurs under adequately strong gravity is flow recirculation, which is strengthened with larger slip from the chamber wall. This strengthening arises when a significant volume of fluid is drained from the cylinder, as the driving shear force is unable to maintain the film's structure. As the volume of fluid is fixed, a deeper pool develops at the base. This shows one of main findings of this study where macro scale effects are observed because of micro scale slip lengths.

By including moderate inertia in the model formulation, the pool and smooth film types are connected by several transitional profiles with increasing inertia. These profiles typically have several capillary waves as a result of the surface tension terms which have been retained in the model. These surface waves are found to be larger across the transitional regime in the presence of slip, however the transition into smooth films appear at a lower Reynolds numbers and is another major finding from this thesis. Another significant finding is the existence of a non-unique solution branch in the parameter space for a given set of flow parameters, while typically the parameter space has only unique solutions in the absence of slip.

The film's internal temperatures are closely connected to the ease at which heat can transfer to the cold air flow, which is a significant limitation on the temperature as low heat transfer rates act as an insulating layer. The key effect of stronger thermal convection is to increase the temperature within a pool profile. A novel and important finding is how the effect of convection becomes amplified with greater fluid slip lengths, which is a consequence of the faster fluid velocities due to the non-zero velocity at the cylinder surface. When surface slip is present, the pool sees a greater amount of heat contained within, this is amplified by the cool surface region being moved around the cylinder and closer to the pool exit.

The transitional films as a result of including moderate inertia cause large regions of the film to be dominated by surface waves, these lead to a series of small peaks which each have a cool tip. The increase in amplitude of these surface waves by fluid slip mean these peaks are now colder, there is also a greater volume of fluid located on the rising wall which also has a colder film surface. Slip effects the thermal dynamics of the rimming flow and may be useful to engineers when designing aero-engine bearing chambers. This is further demonstrated when a local heating effect is being modelled where these effects are captured in detail, where slip has caused a cooling of the narrow film in front of the pool which is independent of thermal convective effects.

The method of depth-averaging the energy equation introduces a mean temperature function, from which the internal temperatures are reconstructed. In certain situations where there should be sudden fluctuations in the internal temperatures,

these changes are not always captured accurately in the mean temperature. This is because the depth-averaging method works best on constant variables, like the volume flux, whereas the mean temperature will vary across the domain. This may become a concern when there is strong thermal convection, weak inertial effects and a large volume of fluid inside the cylinder. This is an area for further improvement, with possible approaches detailed later in the thesis.

The numerical method has shown to be effective in accurately capturing small wavelength capillary effects, being compared in detail against similar models with surface tension coefficients which are representative of hydraulic oils. The Fourier spectral method in this thesis was modified with a clustering function to capture the surface waves around pooling films, though a different clustering function can be applied for other problems to help capture local effects. A detailed analysis showed that with moderate inertia, the centrifugal effects noticeably changes the fluid behaviour and is an important finding of this thesis.

The work of this thesis has detailed that there is no direct change in film temperatures as a result of fluid slip, although the changes to the velocities brought about by slip do help disperse heat through the film. It can therefore be suggested that slip is a secondary thermal effect, especially in comparison to convection or conduction. Fundamentally, it has been shown that even micro scale slip lengths have a dramatic impact on the fluid regime across a range of conditions. These changes are typically associated to a significant amount of both thinning and thickening of the film, emphasising the ability of boundary slip to control fluid flows. While the exact method of causing slip is not described in this thesis, several recommendations are offered later as avenues for engineers to achieve slip behaviour. Crucially, the ability to influence the large scale fluid behaviour by slip in the rimming flow problem presents an exciting aspect for engineers to include when designing bearing chambers.

Future Endeavours

This research has identified several areas for further experimental and theoretical investigations into the rimming flow problem and understanding and developing fluid slip.

The main idea of this thesis is that small scale surface features are important, these are typically chemical treatments or small geometric features as detailed in the literature. Therefore, the first recommendation is to perform a series of experimental investigations of a simple rimming flow problem to validate the effects of slip, where a rotating inner cylinder will create the necessary driving shear for fluid to coat the chamber. A series of inserts can then be used to test

different chemical and geometric patterns to determine which method will induce the largest fluid slip for the various hydraulic oils. These film profiles can be measured and compared to the steady profiles of this thesis to validate the use of slip to change the flow behaviour. The main aim will be to develop a stable platform for large scale slip that can be applied in the design of bearing chambers.

The behaviour of fluid slip is also found for flows over a porous material, which was touched upon in the supporting literature. Therefore, the second recommendation is to perform both experimental and numerical analysis of rimming flows where the cylinder walls have an attached layer of porous material which is infused with fluid. The use of porous materials has already been used in the context of bearing chambers by Chandra and Simmons [21] and will avoid some of the complex issues associated with sustaining fluid slip throughout an aero-engine life cycle.

The ability to include the mass and momentum transfer of the droplets in bearing chambers has been studied using boundary conditions. Normally the added mass from droplets is extracted from the cylinder by a simple radial velocity condition, where fluid is drawn out under the influence of gravity, however this can create a recirculation region adjacent to the sump. The third suggestion is to therefore develop a numerical model of the droplet impacts with a porous region around the sump, this may prevent recirculation regions from forming by controlling the flow. The porous region will also act as a slipping surface, which has been shown to change the film structure which may be used to improve the drainage from the cylinder. A later study could include thermal effects with the energy transfer of droplets into the film and the thermal effects of flow through a porous medium, which is expected to substantially change the fluid temperatures that has yet been studied.

The last recommendation is to extend the mathematical model of depth-averaging to include axial variations in completely modelling the three-dimensional problem. This is anticipated to be a substantial cost reduction and simplification of the rimming flow problem in comparison to full CFD analysis, meaning the unique flow features such as the “shark’s-teeth” can be found with the model and is a tantalising prospect for the aero-space industry.

Appendix A

Cylindrical Coordinate Identities

In this Appendix, a number of useful identities are given in correspondence to the cylindrical coordinate system outlined in Section 3.2.

The dimensional gradient, divergence and Laplacian operators in cylindrical coordinates, for $\mathbf{u}^* = \hat{r}u_r^* + \hat{\theta}u_\theta^*$ are

$$\nabla^*\mathbf{u}^* = \hat{r}\frac{\partial \mathbf{u}^*}{\partial r^*} + \frac{\hat{\theta}}{r^*}\frac{\partial \mathbf{u}^*}{\partial \theta^*}, \tag{A.1}$$

$$\nabla^* \cdot \mathbf{u}^* = \frac{1}{r^*}\frac{\partial}{\partial r^*}\left(r^* v^*\right) + \frac{1}{r^*}\frac{\partial}{\partial \theta^*}\left(u^*\right), \tag{A.2}$$

$$\begin{aligned}\nabla^{*2}\mathbf{u}^* = &\left[\frac{\partial^2 u_r^*}{\partial r^{*2}} + \frac{1}{r^*}\frac{\partial u_r^*}{\partial r^*} + \frac{1}{r^{*2}}\frac{\partial^2 u_r^*}{\partial \theta *^2} - \frac{u_r^*}{r^{*2}} - \frac{2}{r^{*2}}\frac{\partial u_\theta^*}{\partial \theta *}\right]\hat{r} \\ &+ \left[\frac{\partial^2 u_\theta^*}{\partial r^{*2}} + \frac{1}{r^*}\frac{\partial u_\theta^*}{\partial r^*} + \frac{1}{r^{*2}}\frac{\partial^2 u_\theta^*}{\partial \theta^{*2}} - \frac{u_\theta^*}{r^{*2}} + \frac{2}{r^{*2}}\frac{\partial u_r^*}{\partial \theta^*}\right]\hat{\theta}.\end{aligned} \tag{A.3}$$

The fluid contained within the cylinder has a unit tangential vector of the interface, defined by $l^* = l_r\hat{r} + l_\theta\hat{\theta}$ at the fluid interface, where the definitions of l_r^* and l_θ^* are

$$l_r^* = -\frac{\Pi^*}{H^*}\frac{\partial h^*}{\partial \theta^*}, \tag{A.4}$$

$$l_\theta^* = \Pi^*. \tag{A.5}$$

The components of Π^* and H^* at the interface are given as

$$\Pi^* = \left\{1 + \left(\frac{1}{H^*}\frac{\partial h^*}{\partial \theta^*}\right)^2\right\}^{-1/2}, \tag{A.6}$$

and

$$H^* = r_0 - h^*. \tag{A.7}$$

The unit normal vector of the interface, composed as $n^* = n_r\hat{r} + n_\theta\hat{\theta}$ is given with the components of

$$n_r^* = -l_\theta^* = -\Pi^*, \tag{A.8}$$

and

$$n_\theta^* = -l_r^* = -\frac{\Pi^*}{H^*}\frac{\partial h^*}{\partial \theta^*}. \tag{A.9}$$

With the coordinate system being defined in parts of r and θ, the typical stress tensor of the coordinate system is

$$\Gamma_{ij}^* = -P\delta_{ij} + 2\mu e_{ij}, \tag{A.10}$$

with $i, j = r, \theta$, δ_{ij} acting as the Dirac delta function and with tensor functions given as

$$e_{rr} = \frac{\partial u_r^*}{\partial r^*}, \tag{A.11}$$

$$e_{\theta\theta} = \frac{1}{r^*}\frac{\partial u_\theta^*}{\partial \theta^*} + \frac{u_r^*}{r^*}, \tag{A.12}$$

$$2e_{r\theta} = r^*\frac{\partial}{\partial r^*}\left(\frac{u_\theta^*}{r^*}\right) + \frac{1}{r^*}\frac{\partial u_r^*}{\partial \theta^*}. \tag{A.13}$$

Appendix B

The Free Surface Boundary Conditions

The equations of conservation at the two phase interface between the fluid and air are derived in this Appendix, notably those to ensure the energy, mass and momentum of fluid is maintained at the boundary. The current work has used an interface where there is no transfer of droplets into the fluid phase. However, these equations can be readily derived to account for the transfer of droplet mass and momentum and can be found in the works of Kay [6] and Williams [179]. The addition of energy transfer by droplets at an energy level different to the film can be found in the work of Kay [6]. Within this Appendix, all equations and variables have dimensions, with * denoting a dimensional variable in most cases.

To derive the conservation equations at the interface, a typical pillbox volume (where two distinct phases are encapsulated in adjoining boxes) is imagined to overlap the interface, as in figure B.1. With half of the volume within the pillbox contained within the continuous film around the chamber, and half within the core airflow (where droplets were included in Williams [179] and Kay [6]). The volumes denoted by $V_e\,(t)$ and $V_I\,(t)$ are for the internal and external volumes of the pillbox respectively, with the pillbox thickness given as δ. The internal and external volumes have surface normals $\tilde{n}_j^*$ pointing outwards from the interface. The interface also has an outwardly pointing normal n_j^* which is directed towards the core air flow.

B.1 Conservation of Interface Mass

To ensure that fluid mass is conserved at the interface, an integral expression of the convective derivatives of working fluid mass of both volumes of the pillbox, described in figure B.1 should be zero. This is given as

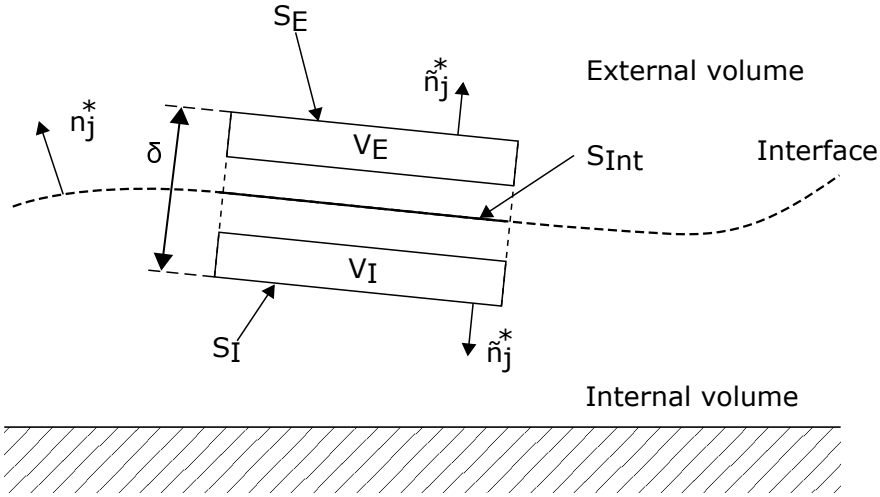


Figure B.1: A pillbox volume which encompasses a volume within and external to the film interface.

$$\frac{D^*}{D^*t^*}\int_{V_I(t)} \rho_I \, dV = 0, \tag{B.1}$$

$$\frac{D^*}{D^*t^*}\int_{V_E(t)} \rho_E \, dV = 0, \tag{B.2}$$

where the internal and external densities of fluid are given as ρ_I and ρ_E respectively. The fluid mass is the integral expressions. As the core airflow is assumed to be devoid of any fluid or droplets, an integral expression of only the internal pillbox volume is necessary in describing the conservation of fluid mass. This assumes that the volume of fluid in the cylinder is constant over time. The integral expression of the internal volume can be altered by the use of the Reynolds Transport theorem, which eloquently states that for a given quantity P defined within a volume V that

$$\frac{D^*}{D^*t^*}\int_{V(t)} P \, dV = \int_{V(t)} \frac{\partial P}{\partial t^*} \, dV + \int_{V(t)} \frac{\partial P u_j^*}{\partial x_j} \, dV, \tag{B.3}$$

with the fluid velocity denoted by u_j^*. The internal volume expression may be expressed as

$$\frac{d}{dt^*}\int_{V_I(t)} \rho_I \, dV + \int_{V_I(t)} \frac{\partial \left(\rho_I u_j^*\right)}{\partial x_j} \, dV = 0. \tag{B.4}$$

The divergence theorem states that for the general quantity P and volume surface S that

$$\int_{V(t)} \frac{\partial P}{\partial x_j}\, dV = \int_{S(t)} P n_j^*\, dS. \tag{B.5}$$

Therefore, with the surface bounding the internal volume, denoted by S_I, the integral of the differential can instead be expressed as

$$\int_{V_I(t)} \frac{\partial \rho_I}{\partial t^*}\, dV + \int_{S_I(t)} \left(\rho_I u_j^*\right) \tilde{n}_j^*\, dS = 0. \tag{B.6}$$

For the pillbox thickness of δ, the limit of $\delta \to 0$ can be used to change the size of volume V_I. With an infinitesimal thickness, it is reasonable to infer that the volume integral will vanish as the volume of the pillbox reduces, therefore

$$\lim_{\delta \to 0} \left(\int_{V_I(t)} \rho_I\, dV \right) = 0. \tag{B.7}$$

This means that the conservation of mass equation for the internal volume of the pillbox may be expressed as contributions from only the internal volume surface

$$\int_{S_I(t)} \left(\rho_I u_j^*\right) \tilde{n}_j^*\, dS = 0. \tag{B.8}$$

The conservation of mass for the internal volume may be expressed as functions of the interface surface, S_{int} instead of the internal volume surface S_I. The interface normal of n_j^* is replaced by the volume normal $\tilde{n}_j^*$ and the equation is given as

$$\int_{S_{int}(t)} \rho_I \left(U_j^* - u_{Ij}^*\right) n_j^*\, dS = 0, \tag{B.9}$$

where the velocity U_j, is the speed at the interface. The length of the interface is arbitrarily defined here, but leads to the velocity within the film being equal to that at the interface. The the conservation of liquid mass at the boundary may therefore be written as

$$u_{Ij}^* = U_j^*. \tag{B.10}$$

Following this same procedure for the external volume will derive the external velocity at the interface as $u_{Ej}^* = U_j^*$.

B.2 Conservation of Momentum at the Interface

Having established the conservation of fluid mass between the core airflow and film at the free surface in figure B.1. The same pillbox in figure B.1 can be used to

ensure that momentum is conserved at the interface. With the absence of liquid or droplets in the core gas flow within the cylinder, the airflow is assumed to be moving at a constant rate which imparts a surface shear on the fluid. There is also the atmospheric pressure P_a^*, from the airflow that acts on the interface.

The total momentum of the internal and the external volume are composed from the forces arising from gravity and viscosity (i.e. as the summation of body and surface forces respectively that act on the body). Looking at the volume outside of the film V_E and volume internal to the film V_I, the conservation of momentum is defined as

$$\frac{D^*}{D^*t^*}\int_{V_E(t)} \rho_E u_i^*\, dV = \int_{V_E(t)} \rho_E g_i\, dV + \int_{V_E(t)} \frac{\partial \Gamma^*_{Eij}}{\partial x_j}\, dV + \int_{V_E(t)} \frac{\partial \tilde{\Gamma}^*_{Eij}}{\partial x_j}\, dV, \tag{B.11}$$

$$\frac{D^*}{D^*t^*}\int_{V_I(t)} \rho_I u_i^*\, dV = \int_{V_I(t)} \rho_I g_i\, dV + \int_{V_I(t)} \frac{\partial \Gamma^*_{Iij}}{\partial x_j}\, dV + \int_{V_I(t)} \frac{\partial \tilde{\Gamma}^*_{Iij}}{\partial x_j}\, dV. \tag{B.12}$$

The new terms introduced are the stress tensors, with Γ^*_{Eij} and Γ^*_{Iij} being the external and internal stress tensors respectively. The external stress tensor is the stress of the air phase, now written as Γ^*_{aij} and the internal tensor is the stress tensor of the film, now written as Γ^*_{ij}. The limits of the stress tensors when approaching the interface from the internal and external volumes are given as $\tilde{\Gamma}^*_{ij}$ and $\tilde{\Gamma}^*_{aij}$ respectively.

Using the Reynolds Transport theorem, as outlined in equation (B.3), these integro-differential equations may be expressed as

$$\int_{V_E(t)} \frac{\partial\left(\rho_E u_i^*\right)}{\partial t^*}\, dV + \int_{V_E(t)} \frac{\partial\left(\rho_E u_i^* u_j^*\right)}{\partial x_j}\, dV = \int_{V_E(t)} \rho_E g_i\, dV + \int_{V_E(t)} \frac{\partial \Gamma^*_{aij}}{\partial x_j}\, dV + \int_{V_E(t)} \frac{\partial \tilde{\Gamma}^*_{aij}}{\partial x_j}\, dV, \tag{B.13}$$

$$\int_{V_I(t)} \frac{\partial\left(\rho_I u_i^*\right)}{\partial t^*}\, dV + \int_{V_I(t)} \frac{\partial\left(\rho_I u_i^* u_j^*\right)}{\partial x_j}\, dV = \int_{V_I(t)} \rho_I g_i\, dV + \int_{V_I(t)} \frac{\partial \Gamma^*_{ij}}{\partial x_j}\, dV + \int_{V_I(t)} \frac{\partial \tilde{\Gamma}_{ij}}{\partial x_j}\, dV, \tag{B.14}$$

The Divergence theorem may be used to express the volume integrals as surface integrals as shown in (B.5). The spatial derivatives may be expressed as functions of the surfaces, which gives the momentum equations as

$$\int_{V_E(t)} \frac{\partial\left(\rho_E u_i^*\right)}{\partial t^*}\, dV + \int_{S_E(t)} \left(\rho_E u_i^* u_j^*\right) \tilde{n}_j^*\, dS = \int_{V_E(t)} \rho_E g_i\, dV + \int_{S_E(t)} \left(\Gamma_{aij}^*\right) \tilde{n}_j^*\, dS + \int_{S_E(t)} \left(\tilde{\Gamma}_{aij}^*\right) \tilde{n}_j^*\, dS, \tag{B.15}$$

$$\int_{V_I(t)} \frac{\partial\left(\rho_I u_i^*\right)}{\partial t^*}\, dV + \int_{S_I(t)} \left(\rho_I u_i^* u_j^*\right) \tilde{n}_j^*\, dS = \int_{V_I(t)} \rho_I g_i\, dV + \int_{S_I(t)} \left(\Gamma_{ij}^*\right) \tilde{n}_j^*\, dS + \int_{S_I(t)} \left(\tilde{\Gamma}_{ij}^*\right) \tilde{n}_j^*\, dS. \tag{B.16}$$

The normals of the internal and external volumes may be expressed with the surface normals as

$$u_i^* u_j^* \tilde{n}_j^* = u_{Ei}^* \left(u_{Ej}^* n_j^* - U_j^* n_j^*\right) \tag{B.17}$$

$$u_i^* u_j^* \tilde{n}_j^* = u_{Ii}^* \left(U_j^* n_j^* - u_{Ij}^* n_j^*\right) \tag{B.18}$$

though, with equation (B.10), $u_i^* u_j^* n_j^* - u_i^* U_j^* n_j^* = 0$. The stress terms may also be expressed as functions of the interface surface as

$$\int_{S_E(t)} \left(\Gamma_{aij}^*\right) \tilde{n}_j^*\, dS + \int_{S_E(t)} \left(\tilde{\Gamma}_{aij}^*\right) \tilde{n}_j^*\, dS = \int_{S_{int}(t)} \Gamma_{aij}^* n_j^*\, dS - \int_{S_{int}(t)} \tilde{\Gamma}_{aij}^* n_j^*\, dS \tag{B.19}$$

$$\int_{S_I(t)} \left(\Gamma_{ij}^*\right) \tilde{n}_j^*\, dS + \int_{S_I(t)} \left(\tilde{\Gamma}_{ij}^*\right) \tilde{n}_j^*\, dS = -\int_{S_{int}(t)} \Gamma_{ij}^* n_j^*\, dS + \int_{S_{int}(t)} \tilde{\Gamma}_{ij}^* n_j^*\, dS. \tag{B.20}$$

The substitution of these stress tensor integrals and velocity definitions into the momentum conservation equations leads to

$$\int_{V_E(t)} \frac{\partial\left(\rho_E u_i^*\right)}{\partial t^*}\, dV = \int_{V_E(t)} \rho_E g_i\, dV + \int_{S_{int}(t)} \left(\Gamma_{aij}^* - \tilde{\Gamma}_{aij}^*\right) n_j^*\, dS, \tag{B.21}$$

$$\int_{V_I(t)} \frac{\partial\left(\rho_I u_i^*\right)}{\partial t^*}\, dV = \int_{V_I(t)} \rho_I g_i\, dV + \int_{S_{int}(t)} \left(\tilde{\Gamma}_{ij}^* - \Gamma_{ij}^*\right) n_j^*\, dS. \tag{B.22}$$

By taking the limit of $\delta \to 0$, as shown previously when deriving the conservation of mass, the volume integrals are shown to diminish for both internal and external volumes. This means that

$$\lim_{\delta\to 0}\left(\int_{V_E(t)}\frac{\partial\left(\rho_E u_i^*\right)}{\partial t^*}\,dV;\ \int_{V_E(t)}\rho_E g_i\,dV\right)=0, \tag{B.23}$$

$$\lim_{\delta\to 0}\left(\int_{V_I(t)}\frac{\partial\left(\rho_E u_i^*\right)}{\partial t^*}\,dV;\ \int_{V_I(t)}\rho_E g_i\,dV\right)=0. \tag{B.24}$$

Therefore, the conservation of momentum equations for the external and internal volumes are expressed as contributions from only the stress tensors,

$$\lim_{\delta\to 0}\left(\int_{S_{int}(t)}\left(\tilde{\Gamma}_{aij}^*-\Gamma_{aij}^*\right)n_j^*\,dS\right)=0, \tag{B.25}$$

$$\lim_{\delta\to 0}\left(\int_{S_{int}(t)}\left(\Gamma_{ij}^*-\tilde{\Gamma}_{ij}^*\right)n_j^*\,dS\right)=0. \tag{B.26}$$

At this stage, the internal and external equations are combined. Meaning the equation will represent the contributions at the interface from the internal and external stress components. This ensures the momentum is conserved both internally and externally and is given as

$$\left(\tilde{\Gamma}_{aij}^*-\tilde{\Gamma}_{ij}^*\right)n_j^*+\left(\Gamma_{ij}^*-\Gamma_{aij}^*\right)n_j^*=0. \tag{B.27}$$

The limiting stress tensors may be expressed with the Young-Laplace model for surface tension, $\left(\tilde{\Gamma}_{aij}^*-\tilde{\Gamma}_{ij}^*\right)n_j^*=\sigma\kappa^* n_i^*$, where κ^* is the surface curvature and σ is the surface tension coefficient. The conservation of momentum equation is defined as

$$\left(\Gamma_{ij}^*-\Gamma_{aij}^*\right)n_j^*=-\sigma\kappa^* n_i^*. \tag{B.28}$$

The expansion of this equation into its tangential and normal components is in Section B.4, using the definitions of the internal and external stress tensors from Appendix A.

B.3 Conservation of Energy at the Interface

If the film found in the chamber is subjected to a temperature differential between the wall and core airflow, it is necessary to ensure the energy at the interface is conserved. For a given volume V, the conservation of thermal energy is defined as

$$\int_{V(t)}\frac{\partial\left(\rho c_p T^*\right)}{\partial t^*}\,dV+\int_{V(t)}\frac{\partial\left(\rho c_p T^* u_j^*\right)}{\partial x_j}\,dV-\int_{V(t)}\phi^*\,dV=0; \tag{B.29}$$

where ϕ^* is the net heat flux into the volume. This equation is applied to the pillbox volumes of figure B.1, which leads to

$$\int_{V_E(t)} \frac{\partial\left(\rho_E c_p T^*\right)}{\partial t^*}\, dV + \int_{V_E(t)} \frac{\partial\left(\rho_E c_p T^* u_j^*\right)}{\partial x_j}\, dV - \int_{V_E(t)} \phi_E^*\, dV = 0, \tag{B.30}$$

$$\int_{V_I(t)} \frac{\partial\left(\rho_I c_p T^*\right)}{\partial t^*}\, dV + \int_{V_I(t)} \frac{\partial\left(\rho_I c_p T^* u_j^*\right)}{\partial x_j}\, dV - \int_{V_I(t)} \phi_I^*\, dV = 0. \tag{B.31}$$

Using the Divergence theorem (B.5), the spatial integrals are expressed as integrals of the bounding surfaces of the internal and external volumes

$$\int_{V_E(t)} \frac{\partial\left(\rho_E c_p T^*\right)}{\partial t^*}\, dV + \int_{S_E(t)} \left(\rho_E c_p T^* u_j^*\right) \tilde{n}_j^*\, dS - \int_{S_E(t)} \phi_E^*\, dS = 0, \tag{B.32}$$

$$\int_{V_I(t)} \frac{\partial\left(\rho_I c_p T^*\right)}{\partial t^*}\, dV + \int_{S_I(t)} \left(\rho_I c_p T^* u_j^*\right) \tilde{n}_j^*\, dS - \int_{S_I(t)} \phi_I^*\, dS = 0. \tag{B.33}$$

These equations can be thought of as a balance of the change to thermal energy over time, $\rho c_p T^*$, the thermal energy which is convected across the volume boundary, $\rho c_p T^* u_j^* \tilde{n}_j^*$ and the energy which is radiated across the boundary, ϕ^*. Similar to Sections B.1 and B.2, the integrals of the volume surfaces, S_I and S_E are expressed in terms of the interface surface S_{int} as

$$\int_{V_E(t)} \frac{\partial\left(\rho_E c_p T^*\right)}{\partial t^*}\, dV + \int_{S_{int}(t)} \left(\rho_E c_p T^* \left(u_{Ej}^* - U_j^*\right)\right) n_j^*\, dS - \int_{S_{int}(t)} \left(\phi_E^* - \tilde{\phi}_E^*\right)\, dS = 0, \tag{B.34}$$

$$\int_{V_I(t)} \frac{\partial\left(\rho_I c_p T^*\right)}{\partial t^*}\, dV - \int_{S_{int}(t)} \left(\rho_I c_p T^* \left(U_j^* - u_{Ij}^*\right)\right) n_j^*\, dS - \int_{S_{int}(t)} \left(\tilde{\phi}_I^* - \phi_I^*\right)\, dS = 0. \tag{B.35}$$

Two new parameters have been introduced at this stage. These are the limiting values of both the internal and external heat flux, given as $\tilde{\phi}_I^*$ and $\tilde{\phi}_E^*$ and are relatively similar to the limiting stresses of Section B.2 when approaching the interface. The conservation of mass (B.10) defines the velocity within each volume is equal to the interface velocity, $u_{Ej}^* = u_{Ij}^* = U_j^*$, which cancels the integrals with $\left(u_{Ej}^* - U_j^*\right)$ and $\left(U_j^* - u_{Ij}^*\right)$.

The thickness of the pillbox volumes is also assumed to be infinitesimal, so that

$$\lim_{\delta \to 0} \left(\int_{V_E(t)} \frac{\partial \left(\rho_E c_p T^* \right)}{\partial t^*} \right) = 0, \tag{B.36}$$

$$\lim_{\delta \to 0} \left(\int_{V_I(t)} \frac{\partial \left(\rho_I c_p T^* \right)}{\partial t^*} \right) = 0, \tag{B.37}$$

The remaining integral terms of the internal and external volumes are given as

$$\int_{S_{int}(t)} \left(\phi_E^* - \tilde{\phi}_E^* \right) \, dS = 0, \tag{B.38}$$

$$\int_{S_{int}(t)} \left(\tilde{\phi}_I^* - \phi_I^* \right) \, dS = 0. \tag{B.39}$$

These integral terms are valid for an arbitrary length of the interface. The equations are combined together to give

$$\left(\tilde{\phi}_E^* - \tilde{\phi}_I^* \right) + \left(\phi_I^* - \phi_E^* \right) = 0. \tag{B.40}$$

The internal and external heat flux limits of $\tilde{\phi}_E^*$ and $\tilde{\phi}_I^*$ vanish, as the assumption is there there is no heat generation capability in the interface. The external heat flux ϕ_E^* may be defined as the heat flux from convection at the fluid surface, given as $\phi_I^* = \gamma^* \left(T_a^* - T^* \right)$. The heat transfer coefficient at the surfaces γ^*, is the proportional constant value the temperature difference of the fluid at the surface T^* and the temperature of the air T_a^*. Within the film, the internal heat flux is given as $\phi_E^* = k^* \nabla^* T^* \cdot \mathbf{n}^*$, which is the Fourier law of conduction within the fluid. Therefore, the conservation of energy equation at the film free surface is defined as

$$k^* \nabla^* T^* \cdot \mathbf{n}^* = \gamma^* \left(T_a^* - T^* \right). \tag{B.41}$$

B.4 Expansion of Stress Boundary Condition

The conservation of momentum at the fluid and air phases (B.28) is expressed in terms of Newtonian stress tensors which are internal to the film Γ_{Iij}^* and external to the film Γ_{Eij}^*. These may be evaluated to form a set of boundary conditions at the film surface. A constant applied surface shear acts on the interface, τ_a^* so the external stress tensor is given as $\Gamma_{aij}^* n_j^* = -P_E \delta_{ij} n_j^* + \tau_a^* l_i^*$ and the internal stress tensor is defined as $\Gamma_{ij}^* n_j^* = -P_I \delta_{ij} n_j^* + 2\mu e_{ij} n_j^*$.

Several new terms have been introduced at this stage, the Dirac δ function, or Knronecker delta function states that if $i = j$ then $\delta_{ij} = 1$, otherwise $\delta_{ij} = 0$. For the cylindrical coordinate system used in this thesis, the exponents are given as

functions which are dependent on $(i,j) = (r,\theta)$

$$\begin{aligned} e_{rr} &= \frac{\partial u_r^*}{\partial r^*}, \\ e_{\theta\theta} &= \frac{1}{r^*}\frac{\partial u_\theta^*}{\partial \theta^*} + \frac{u_r^*}{r^*}, \\ 2e_{r\theta} &= r^*\frac{\partial}{\partial r^*}\left(\frac{u_\theta^*}{r^*}\right) + \frac{1}{r^*}\frac{\partial u_r^*}{\partial \theta^*}. \end{aligned}$$

The conservation of momentum equation of the interface (B.28) may be separated into normal and tangential forms. This can be done by using the normal, n_i^* and tangential, l_i^* vectors of the surface. The normal component of the conservation of momentum is

$$\left(\Gamma_{aij}^* - \Gamma_{ij}^*\right) n_j^* n_i^* = -\sigma\kappa^*, \tag{B.42}$$

with $n_i^* n_i^* = 1$. The tangential component is

$$\left(\Gamma_{aij}^* - \Gamma_{ij}^*\right) n_j^* l_i^* = 0, \tag{B.43}$$

with $n_i^* l_i^* = 0$. The definitions of the stress tensors mean the normal internal stresses of Γ_{ij}^* may be calculated by using a summation convention of the separate components. These components are defined as

$$\Gamma_{rr}^* n_r^* n_r^* = -P_I^* n_r^* n_r^* + 2\mu\left\{\frac{\partial u_r^*}{\partial r^*}\right\}\Pi^{*2}, \tag{B.44}$$

$$\Gamma_{r\theta}^* n_\theta^* n_r^* = -\mu\left\{r^*\frac{\partial}{\partial r^*}\left(\frac{u_\theta^*}{r^*}\right) + \frac{1}{r^*}\frac{\partial u_r^*}{\partial \theta^*}\right\}\left(\frac{1}{r^*}\frac{\partial h^*}{\partial \theta^*}\right)\Pi^{*2}, \tag{B.45}$$

$$\Gamma_{\theta r}^* n_r^* n_\theta^* = -\mu\left\{r^*\frac{\partial}{\partial r^*}\left(\frac{u_\theta^*}{r^*}\right) + \frac{1}{r^*}\frac{\partial u_r^*}{\partial \theta^*}\right\}\left(\frac{1}{r^*}\frac{\partial h^*}{\partial \theta^*}\right)\Pi^{*2}, \tag{B.46}$$

$$\Gamma_{\theta\theta}^* n_\theta^* n_\theta^* = -P_I^* n_\theta^* n_\theta^* + 2\mu\left\{\frac{1}{r^*}\frac{\partial u_\theta^*}{\partial \theta^*} + \frac{u_r^*}{r^*}\right\}\left(\frac{1}{r^*}\frac{\partial h^*}{\partial \theta^*}\right)^2\Pi^{*2}. \tag{B.47}$$

These may be summed into $i = \theta$ and $i = r$ components and then combined together to give the normal stress of the internal stress tensor, defined as

$$\begin{aligned} \Gamma_{ij}^* n_j^* n_i^* = -P_I^* + 2\mu\Bigg\{ &\left(\frac{1}{r^*}\frac{\partial u_\theta^*}{\partial \theta^*} + \frac{u_r^*}{r^*}\right)\left(\frac{1}{r^*}\frac{\partial h^*}{\partial \theta^*}\right)^2 + \frac{\partial u_r^*}{\partial r^*} \\ &- \left(\frac{\partial u_\theta^*}{\partial r^*} - \frac{u_\theta^*}{r^*} + \frac{1}{r^*}\frac{\partial u_r^*}{\partial \theta^*}\right)\left(\frac{1}{r^*}\frac{\partial h^*}{\partial \theta^*}\right)\Bigg\}\Pi^{*2}. \end{aligned} \tag{B.48}$$

Following this same procedure for summing the tensor components, the tangential stress of the internal stress tensor is given as

$$\Gamma^*_{ij}n^*_j l^*_i = \mu\Bigg\{ \left(\frac{\partial u^*_\theta}{\partial r^*} - \frac{u^*_\theta}{r^*} + \frac{1}{r^*}\frac{\partial u^*_r}{\partial \theta^*}\right)\left(\frac{1}{r^*}\frac{\partial h^*}{\partial \theta^*}\right)^2 - \left(r^*\frac{\partial}{\partial r^*}\left(\frac{u^*_\theta}{r^*}\right) + \frac{1}{r^*}\frac{\partial u^*_r}{\partial \theta^*}\right) + 2\left(\frac{1}{r^*}\frac{\partial u^*_\theta}{\partial \theta^*} + \frac{u^*_r}{r^*} - \frac{\partial u^*_r}{\partial r^*}\right)\left(\frac{1}{r^*}\frac{\partial h^*}{\partial \theta^*}\right)\Bigg\}\Pi^{*2}. \quad \text{(B.49)}$$

The external stress tensors follow a similar procedure. However, as the fluid only exists within the internal volumes, the stress tensors are expressed as the pressure at the interface P_a and the applied air shear τ^*_a for the normal and tangential components respectively

$$\Gamma^*_{aij}n^*_j n^*_i = -P^*_a, \quad \text{(B.50)}$$

$$\Gamma^*_{aij}n^*_j l^*_i = \tau^*_a. \quad \text{(B.51)}$$

Having defined the normal and tangential components from both the internal and external volumes of figure B.1, the normal stress condition is given as

$$P^*_a - P^* + 2\mu\Bigg\{ \left(\frac{1}{r^*}\frac{\partial u^*_\theta}{\partial \theta^*} + \frac{u^*_r}{r^*}\right)\left(\frac{1}{r^*}\frac{\partial h^*}{\partial \theta^*}\right)^2 + \frac{\partial u^*_r}{\partial r^*} - \left(\frac{\partial u^*_\theta}{\partial r^*} - \frac{u^*_\theta}{r^*} + \frac{1}{r^*}\frac{\partial u^*_r}{\partial \theta^*}\right)\left(\frac{1}{r^*}\frac{\partial h^*}{\partial \theta^*}\right)\Bigg\}\Pi^{*2} = -\sigma\kappa^*, \quad \text{(B.52)}$$

and the tangential stress boundary condition is

$$\tau^*_a + \mu\Bigg\{ \left(\frac{\partial u^*_\theta}{\partial r^*} - \frac{u^*_\theta}{r^*} + \frac{1}{r^*}\frac{\partial u^*_r}{\partial \theta^*}\right)\left(\frac{1}{r^*}\frac{\partial h^*}{\partial \theta^*}\right)^2 - \left(r^*\frac{\partial}{\partial r^*}\left(\frac{u^*_\theta}{r^*}\right) + \frac{1}{r^*}\frac{\partial u^*_r}{\partial \theta^*}\right) + 2\left(\frac{1}{r^*}\frac{\partial u^*_\theta}{\partial \theta^*} + \frac{u^*_r}{r^*} - \frac{\partial u^*_r}{\partial r^*}\right)\left(\frac{1}{r^*}\frac{\partial h^{*r}}{\partial \theta^*}\right)\Bigg\}\Pi^{*2} = 0. \quad \text{(B.53)}$$

Bibliography

[1] B. Kakimpa, H. Morvan, and S. Hibberd, "The depth-averaged numerical simulation of laminar thin-film flows with capillary waves," *Journal of Engineering for Gas Turbines and Power*, vol. 138, no. 11, p. 112501, 2016.

[2] S. AG, "Siemens achieves breakthrough with 3d printed gas turbine blades," 2017.

[3] S. Wittig, A. Glahn, and J. Himmelsbach, "Influence of high rotational speeds on heat transfer and oil film thickness in aero engine bearing chambers," in *ASME 1993 International Gas Turbine and Aeroengine Congress and Exposition*, vol. Volume 3A: General, p. V03AT15A060, 1993.

[4] A. Glahn and S. Wittig, "Two-phase air/oil flow in aero engine bearing chambers: Characterization of oil film flows," in *ASME 1995 International Gas Turbine and Aeroengine Congress and Exposition*, vol. 113, pp. 578–583, American Society of Mechanical Engineers, 1996.

[5] J. W. Chew, "Analysis of the oil film on the inside surface of an aero-engine bearing chamber housing," in *ASME 1996 International Gas turbine and Aeroengine Congress and Exhibition*, no. 96-GT-300, p. V001T01A082, American Society of Mechanical Engineers, 1996.

[6] E. D. Kay, *A depth-averaged model for non-isothermal rimming flow driven at the surface by droplet impact*. PhD thesis, The University of Nottingham, 2013.

[7] P. Gorse, S. Busam, and K. Dullenkopf, "Influence of operating condition and geometry on the oil film thickness in aeroengine bearing chambers," *Journal of Engineering for Gas Turbines and Power*, vol. 128, no. 1, pp. 103–110, 2004.

[8] C. J. Noakes, J. R. King, and D. S. Riley, "On three-dimensional stability of a uniform, rigidly rotating film on a rotating cylinder," *Quarterly Journal of Mechanics and Applied Mathematics*, vol. 58, no. 2, pp. 229–256, 2005.

[9] M. Farrall, K. Simmons, S. Hibberd, and P. Gorse, "A numerical model for oil film flow in an aeroengine bearing chamber and comparison to experimental data," *Journal of Engineering for Gas Turbines and Power*, vol. 128, no. 1, pp. 111–117, 2006.

[10] C. Guoding, S. Hengchao, and W. Jun, "Research into configuration and flow of wall oil film in bearing chamber based on droplet size distribution," *Chinese Journal of Aeronautics*, vol. 24, no. 3, pp. 355–362, 2010.

[11] C. J. Noakes, J. R. King, and D. S. Riley, "The effect of mass transfer on steady two-dimensional rimming flow," *Journal of Engineering Mathematics*, vol. 71, no. 2, pp. 223–236, 2011.

[12] C. Wang, H. P. Morvan, S. Hibberd, and K. A. Cliffe, "Thin film modelling for aero-engine bearing chambers," in *ASME 2011 Turbo Expo: Turbine Technical Conference and Exposition*, vol. Volume 1: Aircraft Engine; Ceramics; Coal, Biomass and Alternative Fuels; Wind Turbine, pp. 277–286, American Society of Mechanical Engineers, 2011.

[13] B. Chandra, S. H. Collicott, and J. H. Munson, "Scavenge flow in a bearing chamber with tangential sump off-take," *Journal of Engineering for Gas Turbines and Power*, vol. 135, no. 3, p. 032503, 2013.

[14] E. D. Kay, S. Hibberd, and H. Power, "Inertial effects at moderate Reynolds number in thin-film rimming flows driven by surface shear," *Physics of Fluids*, vol. 25, no. 10, p. 102108, 2013.

[15] E. D. Kay, S. Hibberd, and H. Power, "A depth-averaged model for non-isothermal thin-film rimming flow," *International Journal of Heat and Mass Transfer*, vol. 70, no. 1, pp. 1003–1015, 2014.

[16] E. D. Kay, S. Hibberd, and H. Power, "Non-isothermal rimming flow with the effects of surface shear and droplet impact," *Physics of Fluids*, vol. 27, no. 12, p. 122105, 2015.

[17] M. Tirumkudulu and A. Acrivos, "Coating flows within a rotating horizontal cylinder: Lubrication analysis, numerical computations, and experimental measurements," *Physics of Fluids*, vol. 13, no. 1, pp. 14–19, 2001.

[18] B. Kakimpa, H. P. Morvan, and S. Hibberd, "A coupled 1D film hydrodynamics and core gas flow model for air-oil flows in aero-engine bearing chambers," in *ASME Turbo Expo 2017: Turbomachinery Technical Conference and Exposition*, vol. Volume 2B: Turbomachinery, p. V02BT41A045, American Society of Mechanical Engineers, 2017.

[19] A. A. Adeniyi, H. Morvan, and K. Simmons, "A computational fluid dynamics simulation of oil-air flow between the cage and inner race of an aero-engine bearing," *Journal of Engineering for Gas Turbines and Power*, vol. 139, no. 1, pp. 012506 – 1 – 012506 – 8, 2017.

[20] H. Sun, G. Chen, Y. Zhang, and L. Wang, "Theoretical and experimental studies on the motion and thermal states of oil droplet in a bearing chamber," *Proceedings of the Institution of Mechanical Engineers, Part G: Journal of Aerospace Engineering*, vol. 230, no. 14, pp. 2596–2614, 2016.

[21] B. Chandra and K. Simmons, "Experimental investigation on aeroengine shallow pump performance," *Global Power and Propulsion Society*, p. 99, 2017.

[22] S. Chatterjee, G. Sugilal, and S. V. Prabhu, "Flow transitions in a partially filled rotating inclined pipe with continuous flow," *Experimental Thermal and Fluid Science*, vol. 83, no. 1, pp. 47–56, 2017.

[23] R. E. Johnson, "Steady-state coating flows inside a rotating horizontal cylinder," *Journal of Fluid Mechanics*, vol. 190, no. 1, pp. 321–342, 1988.

[24] Y. Agbessi, Y. Béreaux, J.-Y. Charmeau, R. Le Goff, and J. Biglione, "Modelling of an innovative liquid rotational moulding process," *International Journal of Material Forming*, 2018.

[25] V. Dyakova, V. Kozlov, and D. Polezhaev, "Pattern formation inside a rotating cylinder partially filled with liquid and granular medium," *Shock and Vibration*, vol. 2014, p. 9, 2014.

[26] O. Menekse, J. V. Wood, and D. S. Riley, "Investigation of Fe_2O_3–Al and Cr_2O_3–Al reactions using a high speed video camera," *Materials Science and Technology*, vol. 22, no. 2, pp. 199–205, 2006.

[27] H. T. Nguyen, B. Cosson, M.-F. Lacrampe, and T. A. Do, "Numerical simulation of reactive polymer flow during rotational molding using smoothed particle hydrodynamics method and experimental verification," *International Journal of Material Forming*, vol. 11, no. 4, pp. 583–592, 2017.

[28] K. O. Oglia, W. Yang, M. Shao, and J. Tan, "Surface quality of unsaturated polyester resin processed via continuous multi-shot rotational molding," in *AIP Conference Proceedings*, vol. 1846, p. 040001, AIP Publishing, 2017.

[29] K. J. Ruschak and L. E. Scriven, "Rimming flow of liquid in a rotating cylinder," *Journal of Fluid Mechanics*, vol. 76, no. 1, pp. 113–126, 1976.

[30] S. S. Singaram, H. Lodha, and R. J. Jachuck, "Experimental investigation of continuous single-phase rimming flow in a horizontal rotating cylinder," *Transport Phenomena and Fluid Mechanics*, vol. 60, no. 11, pp. 3939–3950, 2014.

[31] H. K. Moffatt, "Behaviour of a viscous film on the outer surface of a rotating cylinder," *Journal de Mécanique*, vol. 16, no. 5, pp. 651–973, 1977.

[32] F. M. Orr and L. E. Scriven, "Rimming flow: Numerical simulation of steady, viscous free-surface flow with surface tension," *Journal of Fluid Mechanics*, vol. 84, no. 1, pp. 145–165, 1978.

[33] L. Preziosi and D. D. Joseph, "The run-off condition for coating and rimming flows," *Journal of Fluid Mechanics*, vol. 187, pp. 99–113, 1988.

[34] S. B. G. O'Brien and E. G. Gath, "The location of a shock in rimming flow," *Physics of Fluids*, vol. 10, no. 4, pp. 1040–1042, 1998.

[35] E. S. Benilov, M. S. Benilov, and S. B. G. O'Brien, "Existence and stability of regularized shock solutions, with applications to rimming flows," *Journal of Engineering Mathematics*, vol. 63, no. 2–4, pp. 197–212, 2009.

[36] M. Villegas-Díaz, H. Power, and D. S. Riley, "On the stability of rimming flows to two-dimensional disturbances," *Fluid Dynamics Research*, vol. 33, no. 1, pp. 141–172, 2003.

[37] F. Melo, "Localized state in a film-dragging experiment," *Physical Review E: Statistical Physics, Plasmas, Fluids, and Related Interdisciplinary Topics*, vol. 48, no. 4, p. 2704, 1993.

[38] S. K. Wilson, R. Hunt, and B. R. Duffy, "On the critical solutions in coating and rimming flow on a uniformly rotating horizontal cylinder," *The Quarterly Journal of Mechanics and Applied Mathematics*, vol. 55, no. 3, pp. 357–383, 2002.

[39] A. Acrivos and B. Jin, "Rimming flows within a rotating horizontal cylinder: Asymptotic analysis of the thin-film lubrication equations and stability of their solutions," *Journal of Engineering Mathematics*, vol. 50, no. 2-3, pp. 99–121, 2004.

[40] E. S. Benilov, S. B. G. O'Brien, and I. A. Sazonov, "A new type of instability: Explosive disturbances in a liquid film inside a rotating horizontal cylinder," *Journal of Fluid Mechanics*, vol. 497, no. 1, pp. 201–224, 2003.

[41] E. S. Benilov, S. M. Lacey, and S. B. G. O'Brien, "Exploding solutions for three-dimensional rimming flows," *Quarterly Journal of Mechanics and Applied Mathematics*, vol. 58, no. 4, pp. 563–576, 2005.

[42] E. S. Benilov, N. Kopteva, and S. B. G. O'Brien, "Does surface tension stabilize liquid films inside a rotating horizontal cylinder?," *The Quarterly Journal of Mechanics and Applied Mathematics*, vol. 58, no. 2, pp. 185–200, 2005.

[43] M. Villegas-Díaz, H. Power, and D. S. Riley, "Analytical and numerical studies of the stability of thin-film rimming flow subject to surface shear," *Journal of Fluid Mechanics*, vol. 541, no. 1, pp. 317–344, 2005.

[44] E. S. Benilov, M. S. Benilov, and N. Kopteva, "Steady rimming flows with surface tension," *Journal of Fluid Mechanics*, vol. 597, no. 1, pp. 91–118, 2008.

[45] H. Aggarwal and N. Tiwari, "Generalized linear stability of non-inertial rimming flow in a rotating horizontal cylinder," *The European Physical Journal E*, vol. 38, no. 10, p. 111, 2015.

[46] E. S. Benilov, V. N. Lapin, and S. B. G. O'Brien, "On rimming flows with shocks," *Journal of Engineering Mathematics*, vol. 75, no. 1, pp. 49–62, 2012.

[47] P. L. Evans, L. W. Schwartz, and R. V. Roy, "Steady and unsteady solutions for coating flow on a rotating horizontal cylinder: Two-dimensional theoretical and numerical modeling," *Physics of Fluids*, vol. 16, no. 8, pp. 2742–2756, 2004.

[48] P. L. Evans, L. W. Schwartz, and R. V. Roy, "Three-dimensional solutions for coating flow on a rotating horizontal cylinder: Theory and experiment," *Physics of Fluids*, vol. 17, no. 7, p. 072102, 2005.

[49] J. Ashmore, A. E. Hosoi, and H. A. Stone, "The effect of surface tension on rimming flows in a partially filled rotating cylinder," *Journal of Fluid Mechanics*, vol. 479, no. 1, pp. 65–98, 2003.

[50] S. T. Thoroddsen and L. Mahadevan, "Experimental study of coating flows in a partially-filled horizontally rotating cylinder," *Experiments in Fluids*, vol. 23, no. 1, pp. 1–13, 1997.

[51] A. E. Hosoi and L. Mahadevan, "Axial instability of a free-surface front in a partially filled horizontal rotating cylinder," *Physics of Fluids*, vol. 11, no. 1, pp. 97–106, 1999.

[52] E. S. Benilov and S. B. G. O'Brien, "Inertial instability of a liquid film inside a rotating horizontal cylinder," *Physics of Fluids*, vol. 17, no. 5, p. 052106, 2005.

[53] E. S. Benilov, "Does surface tension stabilize liquid films inside a rotating horizontal cylinder? Part 2: Multidimensional disturbances," *Studies in Applied Mathematics*, vol. 116, no. 1, pp. 1–20, 2006.

[54] C. J. Noakes, J. R. King, and D. S. Riley, "On the development of rational approximations incorporating inertial effects in coating and rimming flows: A multiple-scales approach," *The Quarterly Journal of Mechanics and Applied Mathematics*, vol. 59, no. 2, pp. 163–190, 2006.

[55] K. Pougatch and I. Frigaard, "Thin film flow on the inside surface of a horizontally rotating cylinder: Steady state solutions and their stability," *Physics of Fluids*, vol. 23, no. 2, p. 022102, 2011.

[56] E. S. Benilov and V. N. Lapin, "Inertial instability of flows on the inside or outside of a rotating horizontal cylinder," *Journal of Fluid Mechanics*, vol. 736, no. 1, pp. 107–129, 2013.

[57] S. T. Thoroddsen and L. Mahadevan, "Shark-teeth pattern in coating flow inside a horizontally rotating cylinder," *Physics of Fluids*, vol. 8, no. 9, p. S10, 1996.

[58] R. T. Balmer, "The hygrocyst - a stability phenomenon in continuum mechanics," *Nature*, vol. 227, no. 5258, pp. 600–601, 1970.

[59] G. Seiden and P. J. Thomas, "Complexity, segregation, and pattern formation in rotating-drum flows," *Reviews of Modern Physics*, vol. 83, no. 4, pp. 1323–1365, 2011.

[60] A. v. B. Lopes, U. Thiele, and A. L. Hazel, "On the multiple solutions of coating and rimming flows on rotating cylinders," *Journal of Fluid Mechanics*, vol. 835, no. 1, pp. 540–574, 2018.

[61] G. A. Leslie, S. K. Wilson, and B. R. Duffy, "Three-dimensional coating and rimming flow: A ring of fluid on a rotating horizontal cylinder," *Journal of Fluid Mechanics*, vol. 716, no. 1, pp. 51–82, 2013.

[62] B. R. Duffy and S. K. Wilson, "Thin-film and curtain flows on the outside of a rotating horizontal cylinder," *Journal of Fluid Mechanics*, vol. 394, no. 1, pp. 29–49, 1999.

[63] M. A. Kelmanson, "On inertial effects in the Moffatt-Pukhnachov coating-flow problem," *Journal of Fluid Mechanics*, vol. 633, no. 1, pp. 327–353, 2009.

[64] A. K. Sahu and S. Kumar, "Thin-liquid-film flow on a topographically patterned rotating cylinder," *Physics of Fluids*, vol. 26, no. 4, p. 042102, 2014.

[65] C. Herschel, *115 experiment on the carrying capacity of large riveted, metal conduits, up to six feet in length.* Wiley, 1897.

[66] A. J. C. de Saint-Venant, "Théorie du mouvement non permanent des eaux, avec application aux crues des riviéres et á l'introduction de marées dans leurs lits," *Comptes rendus des seances de l'Academie des Sciences*, vol. 36, no. 1, pp. 154–174, 1871.

[67] D. J. Benney, "Long waves on liquid films," *Journal of Mathematics and Physics*, vol. 45, no. 1, pp. 150–155, 1966.

[68] L. T. Nguyen and V. Balakotaiah, "Modeling and experimental studies of wave evolution on free falling viscous films," *Physics of Fluids*, vol. 12, no. 9, pp. 2236–2256, 2000.

[69] B. Scheid, C. Ruyer-Quil, U. Thiele, O. A. Kabov, J. C. Legros, and P. Colinet, "Validity domain of the Benney equation including Marangoni effect for closed and open flows," *Journal of Fluid Mechanics*, vol. 527, no. 1, pp. 303–335, 2005.

[70] R. J. Gribben, R. Hunt, M. Abdelghaffar, and G. Wilks, "Evaluation of the approximate treatment of thin film flows," *Applied Mathematical Modelling*, vol. 14, no. 8, pp. 420–426, 1990.

[71] G. W. Recktenwald and P. Butler, "Depth-averaged modeling of convective heat transfer from printed circuit boards," in *The American Society of Mechanical Engineers Annual Meeting*, American Society of Mechanical Engineers Atlanta, GA, 1991. ASME Paper No. 91-WA-EEP-36.

[72] A. Costa and G. Macedonio, "Numerical simulation of lava flows based on depth-averaged equations," *Geophysical Research Letters*, vol. 32, no. 5, p. L05304, 2005.

[73] C. Ruyer-Quil and P. Manneville, "Modeling film flows down inclined planes," *The European Physical Journal B*, vol. 6, no. 2, pp. 277–292, 1998.

[74] C. Ruyer-Quil and P. Manneville, "Improved modeling of flows down inclined planes," *The European Physical Journal B*, vol. 15, no. 2, pp. 357–369, 2000.

[75] M. Sivapuratharasu, S. Hibberd, M. E. Hubbard, and H. Power, "Inertial effects on thin-film wave structures with imposed surface shear on an inclined plane," *Physica D: Nonlinear Phenomena*, vol. 325, no. 1, pp. 86–97, 2016.

[76] E. S. Benilov, "Depth-averaged model for hydraulic jumps on an inclined plate," *Physical Review E:*, vol. 89, no. 5, p. 053013, 2014.

[77] E. D. Kay, S. Hibberd, and H. Power, "A multi-layer integral model for locally-heated thin film flow," *Journal of Computational Physics*, vol. 336, no. 1, pp. 51–68, 2017.

[78] B. Reisfeld and S. G. Bankoff, "Non-isothermal flow of a liquid film on a horizontal cylinder," *Journal of Fluid Mechanics*, vol. 236, no. 1, pp. 167–196, 1992.

[79] Z. Ding, R. Liu, T. N. Wong, and C. Yang, "Absolute instability induced by Marangoni effect in thin liquid film flows on vertical cylindrical surfaces," *Chemical Engineering Science*, vol. 177, no. 1, pp. 261–269, 2018.

[80] O. A. Burmistrova, "Thermocapillary instability of a liquid layer on interior surface of a rotating cylinder," *Journal of Physics: Conference Series*, vol. 754, no. 3, p. 032004, 2016.

[81] G. A. Leslie, S. K. Wilson, and B. R. Duffy, "Non-isotheral flow of a thin film of fluid with temperature-dependent viscosity on a stationary horizontal cylinder," *Physics of Fluids*, vol. 23, no. 1, p. 062101, 2011.

[82] G. A. Leslie, S. K. Wilson, and B. R. Duffy, "Thermoviscous coating and rimming flow," *The Quarterly Journal of Mechanics and Applied Mathematics*, vol. 65, no. 4, pp. 483–511, 2012.

[83] T. C. Kumawat and N. Tiwari, "Stability analysis of the rimming flow inside a uniformly heated rotating horizontal cylinder," *Physics of Fluids*, vol. 29, no. 3, p. 032102, 2017.

[84] T. C. Kumawat and N. Tiwari, "Stability analysis of rimming flow inside a horizontally rotating cylinder in the presence of an insoluble surfactant," *Physics of Fluids*, vol. 29, no. 12, p. 122102, 2017.

[85] S. Chatterjee, G. Sugilal, and S. V. Prabhu, "Heat transfer in a partially filled rotating pipe with single phase flow," *International Journal of Thermal Sciences*, vol. 125, no. 1, pp. 132–141, 2018.

[86] S. Chatterjee, G. Sugilal, and S. V. Prabhu, "Impact of inclination on single phase heat transfer in a partially filled rotating pipe," *International Journal of Heat and Mass Transfer*, vol. 123, no. 1, pp. 867–878, 2018.

[87] T. C. Kumawat and N. Tiwari, "Hydrodynamic stability of thermoviscous liquid film inside a rotating horizontal cylinder: Heating and cooling effects," *Physics of Fluids*, vol. 30, no. 3, p. 032103, 2018.

[88] A. Oron, S. H. Davis, and S. G. Bankoff, "Long-scale evolution of thin liquid films," *Review of Modern Physics*, vol. 69, no. 3, pp. 931–980, 1997.

[89] R. V. Craster and O. K. Matar, "Dynamics and stability of thin liquid films," *Reviews of Modern Physics*, vol. 81, no. 3, pp. 1131–1198, 2009.

[90] N. H. Shuaib, H. Power, S. Hibberd, and K. Simmons, "A numerical study of wave structures developed on the free surface of a film flow on inclined planes subject to surface shear," *International Journal for Numerical Methods in Engineering*, vol. 68, no. 7, pp. 755–789, 2006.

[91] H. S. Tang, L. Z. Zhang, J. P.-Y. Maa, H. Li, C. B. Jiang, and R. Hussain, "Fluid driven by tangential velocity and shear stress: Mathematical analysis, numerical experiment, and implication to surface flow," *Mathematical Problems in Engineering*, vol. 2013, p. 12, 2013.

[92] S. Miladinova, S. Slavtchev, G. Lebon, and J.-C. Legros, "Long-wave instabilities of non-uniformly heated falling films," *Journal of Fluid Mechanics*, vol. 453, no. 1, pp. 153–175, 2002.

[93] S. Kalliadasis, A. Kiyashko, and E. A. Demekhin, "Marangoni instability of a thin liquid film heated from below by a local heat source," *Journal of Fluid Mechanics*, vol. 475, no. 1, pp. 377–408, 2003.

[94] S. Kalliadasis, E. A. Demekhin, C. Ruyer-Quil, and M. G. Velarde, "Thermocapillary instability and wave formation on a film falling down a uniform heated plane," *Journal of Fluid Mechanics*, vol. 492, no. 1, pp. 303–338, 2003.

[95] A. M. Frank, "3D Numerical simulation of regular structure formation in a locally heated falling film," *European Journal of Mechanics B: Fluids*, vol. 22, no. 5, pp. 445–471, 2003.

[96] U. Thiele and E. Knobloch, "Thin liquid films on a slightly inclined heated plate," *Physica D: Nonlinear Phenomena*, vol. 190, no. 3, pp. 213–248, 2004.

[97] R. Liu, Z. Ding, and Z. Zhu, "Thermocapillary effect on the absolute and convective instabilities of film flows down a fibre," *International Journal of Heat and Mass Transfer*, vol. 112, no. 1, pp. 918–925, 2017.

[98] Y. O. Kabova, V. V. Kuznetsov, and O. A. Kabov, "Shear-driven flow of locally heated viscous liquid film in a minichannel," *Microgravity Science and Technology*, vol. 23, no. 1, pp. S105–S112, 2011.

[99] P. M. J. Trevelyan and S. Kalliadasis, "Wave dynamics on a thin-liquid film falling down a heated wall," *Journal of Engineering Mathematics*, vol. 50, no. 2-3, pp. 177–208, 2004.

[100] A. M. Frank and O. A. Kabov, "Thermocapillary structure formation in a falling film: experiment and calculations," *Physics of Fluids*, vol. 18, no. 1, p. 032107, 2006.

[101] T. Gambaryan-Roisman, "Marangoni convection, evaporation and interface deformation in liquid films on heated substrate with non-uniform thermal conductivity," *International Journal of Heat and Mass Transfer*, vol. 53, no. 1-3, pp. 390–402, 2010.

[102] Y. Gatapova, Elizaveta and O. A. Kabov, "Shear-driven flows of locally heated liquid films," *International Journal of Heat and Mass Transfer*, vol. 51, no. 19-20, pp. 4797–4810, 2008.

[103] Z. Ding and T. N. Wong, "Stability of a localized heated falling film with insoluble surfactants," *International Journal of Heat and Mass Transfer*, vol. 67, no. 1, pp. 627–636, 2013.

[104] E. Lauga, M. P. Brenner, and H. A. Stone, *Springer Handbook of Experimental Fluid Mechanics*, ch. Microfluidics: The no-slip boundary condition, pp. 1219–1240. Springer Handbooks, Berlin, Heidelberg: Springer, 2006.

[105] C. Neto, D. R. Evans, E. Bonaccurso, H.-J. Butt, and V. S. J. Craig, "Boundary slip in Newtonian liquid: A review of experimental studies," *Reports on Progress in Physics*, vol. 68, no. 12, pp. 2859–2897, 2005.

[106] S. Granick, Y. Zhu, and H. Lee, "Slippery questions about complex fluids flowing past solids," *Nature Materials*, vol. 2, no. 4, pp. 221–227, 2003.

[107] J. C. T. Eijkel, "Liquid slip in micro- and nanofluidics: Recent research and its possible implications," *Lab on a Chip*, vol. 7, no. 3, pp. 299–301, 2007.

[108] C.-H. Choi, J. A. Westin, and K. S. Breuer, "Apparent slip flows in hydrophilic and hydrophobic microchannels," *Physics of Fluids*, vol. 15, no. 10, pp. 2897–2902, 2003.

[109] C. Cottin-Bizonne, S. Jurine, J. Baudry, J. Crassous, F. F. Restagno, and Charlaixé, "Nanorheology: an investigation of the boundary condition at hydrophobic and hydrophilic interfaces," *The European Physical Journal E*, vol. 9, no. 1, pp. 47–53, 2002.

[110] E. Schnell, "Slippage of water over nonwettable surfaces," *Journal of Applied Physics*, vol. 27, no. 10, pp. 1149–1152, 1956.

[111] T. A. Ho, D. V. Papavassiliou, L. L. Lee, and A. Striolo, "Liquid water can slip on a hydrophilic surface," *Proceedings of the National Academy of Sciences*, vol. 108, no. 39, pp. 16170–16175, 2011.

[112] C. Cottin-Bizonne, C. Barentin, and L. Bocquet, "Scaling laws for slippage on superhydrophobic fractal surfaces," *Physics of Fluids*, vol. 24, no. 1, p. 012001, 2012.

[113] E. Bonaccurso, H.-J. Butt, and V. S. J. Craig, "Surface roughness and hydrodynamic boundary slip of a Newtonian fluid in a completely wetting system," *Physical Review Letters*, vol. 90, no. 14, p. 144501, 2003.

[114] Y.-Z. Hu and S. Granick, "Microscopic study of thin film lubrication and its contributions to macroscopic tribology," *Chemical Engineering Communications*, vol. 197, no. 4, pp. 544–550, 2009.

[115] V. S. Ajaev, "Rupture of thin liquid films on structure surfaces," *Physical Review E: Statistical Physics, Plasmas, Fluids, and Related Interdisciplinary Topics*, vol. 84, no. 4, p. 041606, 2011.

[116] N. V. Priezjev, "Molecular dynamics simulation of oscillator Couette flows with slip boundary conditions," *Microfluidics and Nanofluidics*, vol. 14, no. 1-2, pp. 225–233, 2013.

[117] S. Richardson, "On the no-slip boundary condition," *Journal of Fluid Mechanics*, vol. 59, no. 4, pp. 707–719, 1973.

[118] Y. Zhu and S. Granick, "Rate-dependent slip of Newtonian liquid at smooth surfaces," *Physical Review Letters*, vol. 87, no. 9, p. 096105, 2001.

[119] Y. Zhu and S. Granick, "Limits of the hydrodynamic no-slip boundary condition," *Physical Review Letters*, vol. 88, no. 10, p. 106102, 2002.

[120] H. Spikes and S. Granick, "Equation for slip of simple liquid at smooth solid surfaces," *Langmuir*, vol. 19, no. 12, pp. 5065–5071, 2003.

[121] T. Lee, E. Charrault, and C. Neto, "Interfacial slip on rough, pattern and soft surfaces: A review of experiment and simulations," *Advances in Colloid and Interface Science*, vol. 210, no. 1, pp. 21–38, 2014.

[122] J. Ou, B. Perot, and J. P. Rothstein, "Laminar drag reduction in microchannels using ultrahydrophobic surfaces," *Physics of Fluids*, vol. 16, no. 12, pp. 4635–4643, 2004.

[123] D. C. Tretheway and C. D. Meinhart, "Apparent fluid slip at hydrophobic microchannel walls," *Physics of Fluids*, vol. 14, no. 3, pp. L9–L12, 2002.

[124] C. Nieto, H. Power, and M. Giraldo, "Boundary elements solution of Stokes flow between curved surfaces with nonlinear slip boundary condition," *Numerical Methods for Partial Differential Equations*, vol. 29, no. 3, pp. 757–777, 2013.

[125] P. A. Thompson and S. M. Troian, "A general boundary condition for liquid flow at solid surfaces," *Letters to Nature*, vol. 389, no. 6649, pp. 360–362, 1997.

[126] H. Power, J. Soavi, P. Kantachuvesiri, and C. Nieto, "The effect of Thompson and Troian's nonlinear slip condition on Couette flows between concentric rotating cylinders," *Zeitschrift für angewandte Mathematik und Physik*, vol. 66, no. 5, pp. 2703–2718, 2015.

[127] C. Nieto, M. Giraldo, and H. Power, "Boundary integral method for Stokes flow with linear slip flow conditions in curved surfaces," *Mesh Reduction Methods*, vol. 49, no. 10, pp. 353–362, 2009.

[128] C. Nieto, H. Power, and M. Giraldo, "Boundary integral equation approach for Stokes flow with non-linear slip boundary condition," in *AIP Conference Proceedings*, vol. 1281, pp. 123–126, American Institute of Physics, 2010.

[129] M. T. Matthews and J. M. Hill, "Newtonian flow with nonlinear Navier boundary condition," *Acta Mechanica*, vol. 191, no. 3-4, pp. 195–217, 2007.

[130] P. Zhou, C.-W. Wu, and G.-J. Ma, "Nonlinear boundary slip of fluid flowing over solid surface," *Journal of Central South University of Technology*, vol. 14, no. 1, pp. 30–33, 2007.

[131] R. Pit, H. Hervet, and L. Léger, "Friction and slip of a simple liquid at a solid surface," *Tribology Letters*, vol. 7, no. 2-3, pp. 147–152, 1999.

[132] R. Pit, H. Hervet, and L. Léger, "Direct experimental evidence of slip in hexadecane: Solid interfaces," *Physical Review Letters*, vol. 85, no. 5, pp. 980–983, 2000.

[133] J. Baudry, E. Charlaix, A. Tonck, and D. Mazuyer, "Experimental evidence for a large slip effect at a nonwetting fluid-solid interface," *Langmuir*, vol. 17, no. 17, pp. 5232–5236, 2001.

[134] E. Bonaccurso, M. Kappl, and H.-J. Butt, "Hydrodynamic force measurement: Boundary slip of water on hydrophilic surfaces and electrokinetic effects," *Physical Review Letters*, vol. 88, no. 7, p. 076103, 2002.

[135] C. Ybert, C. Barentin, C. Cottin-Bizonne, P. Joseph, and L. Bocquet, "Achieving large slip with superhydrophobic surfaces: Scaling laws for generic geometries," *Physics of Fluids*, vol. 19, no. 12, p. 123601, 2007.

[136] C.-H. Choi and C.-J. Kim, "Large slip of aqueous liquid flow over a nanoengineered superhydrophobic surface," *Physical Review Letters*, vol. 96, no. 6, p. 066001, 2006.

[137] G. R. Willmott and J. L. Tallon, "Measurement of Newtonian fluid slip using a torsional ultrasonic oscillator," *Physical Review E: Statistical Physics, Plasmas, Fluids, and Related Interdisciplinary Topics*, vol. 76, no. 6, p. 066306, 2007.

[138] O. I. Vinogradova, "Slippage of water over hydrophobic surfaces," *International Journal of Mineral Processing*, vol. 56, no. 1, pp. 31–60, 1999.

[139] O. I. Vinogradova, "Drainage of a thin liquid film confined between hydrophobic surfaces," *Langmuir*, vol. 11, no. 6, pp. 2213–2220, 1995.

[140] V. S. J. Craig, C. Neto, and D. R. M. Williams, "Shear-dependent boundary slip in an aqueous Newtonian liquid," *Physical Review Letters*, vol. 87, no. 5, p. 054504, 2001.

[141] C. D. F. Honig, J. E. Sader, P. Mulvaney, and W. A. Ducker, "Lubrication forces in air and accommodation coefficient measured by a thermal damping method using an atomic force microscope," *Physical Review E: Statistical Physics, Plasmas, Fluids, and Related Interdisciplinary Topics*, vol. 81, no. 5, p. 056305, 2010.

[142] J. P. Rothstein, "Slip on superhydrophobic surfaces," *Annual Review of Fluid Mechanics*, vol. 42, no. 1, pp. 89–90, 2010.

[143] N. V. Churaev, V. D. Sobolev, and A. N. Somov, "Slippage of liquid over lyophobic solid surfaces," *Journal of Colloid and Interface Science*, vol. 97, no. 2, pp. 574–581, 1984.

[144] A. Maali and B. Bhushan, "Measurement of slip length of superhydrophobic surfaces," *Philosophical Transations of the Royal Society A: Mathematical, Physical and Engineering Sciences*, vol. 370, no. 1967, pp. 230–2320, 2012.

[145] N. Y. Bailey, K. A. Cliffe, S. Hibberd, and H. Power, "Dynamics of a parallel, high-speed, lubricated thrust bearing with Navier slip boundary conditions," *IMA Journal of Applied Mathematics*, vol. 80, no. 1, pp. 1409–1430, 2015.

[146] N. Y. Bailey, K. A. Cliffe, S. Hibberd, and H. Power, "Dynamics of a high speed coned thrust bearing with a Navier slip boundary condition," *Journal of Engineering Mathematics*, vol. 97, no. 1, pp. 1–24, 2016.

[147] N. Y. Bailey, S. Hibberd, and H. Power, "Dynamics of a small gap gas lubricated bearing with Navier slip boundary conditions," *Journal of Fluid Mechanics*, vol. 818, pp. 68–99, 2017.

[148] J. Maureau, M. C. Sharatchandra, M. Sen, and M. Gad-el Hak, "Flow and load characteristics of microbearings with slip," *Journal of Micromechanics and Microengineering*, vol. 7, no. 2, pp. 55–64, 1997.

[149] F. Aurelian, M. Patrick, and H. Mohamed, "Wall slip effects in (elasto) hydrodynamic journal bearings," *Tribology International*, vol. 44, no. 7, pp. 868–877, 2011.

[150] R. W. Barber, Y. Sun, X. J. Gu, and D. R. Emerson, "Isothermal slip flow over curved surfaces," *Vacuum*, vol. 76, no. 1, pp. 73–81, 2004.

[151] R. S. Myong, J. M. Reese, R. W. Barber, and D. R. Emerson, "Velocity slip in microscale cylindrical Couette flow: The Langmuir model," *Physics of Fluids*, vol. 17, no. 8, p. 087105, 2005.

[152] D. Seo and W. A. Ducker, "In situ control of gas flow by modification of gas-solid interactions," *Physical Review Letters*, vol. 111, no. 17, p. 174502, 2013.

[153] S. Yuhong, R. W. Barber, and D. R. Emerson, "Inverted velocity profiles in rarefied cylindrical Couette gas flow and the impact of the accommodation coefficient," *Physics of Fluids*, vol. 17, no. 4, p. 047102, 2005.

[154] W.-M. Zhang, G. Meng, and X. Wei, "A review on slip models for gas microflows," *Microfluidics and Nanofluidics*, vol. 13, no. 6, pp. 845–882, 2012.

[155] A. P. Bowles and W. A. Ducker, "Gas flow near a smooth plate," *Physical Review E: Statistical Physics, Plasmas, Fluids, and Related Interdisciplinary Topics*, vol. 83, no. 5, p. 056328, 2011.

[156] F. Javadpour, M. McClure, and M. E. Naraghi, "Slip-corrected liquid permeability and its effect on hydraulic fracturing and fluid loss in shale," *Fuel*, vol. 160, no. 1, pp. 549–559, 2015.

[157] B. Alazmi and K. Vafai, "Analysis of fluid flow and heat transfer interfacial conditions between a porous medium and a fluid layer," *International Journal of Heat and Mass Transfer*, vol. 44, no. 9, pp. 1735–1749, 2001.

[158] S. Beavers, Gordon and D. D. Joseph, "Boundary conditions at a naturally permeable wall," *Journal of Fluid Mechanics*, vol. 30, no. 1, pp. 197–207, 1967.

[159] L. Zuo and Y. Hoi, "Numerical analysis for the mixed Navier-Stokes and Darcy problem with the Beavers-Joseph interface condition," *Numerical Methods for Partial Differential Equations*, vol. 31, no. 4, pp. 1009–1030, 2014.

[160] G. I. Taylor, "A model for the boundary condition of a porous material. Part 1," *Journal of Fluid Mechanics*, vol. 49, no. 2, pp. 319–326, 1971.

[161] D. B. Das, V. Nassehi, and R. J. Wakeman, "A finite volume model for the hydrodynamics of combined free and porous flow in sub-surface regions," *Advances in Environmental Research*, vol. 7, no. 1, pp. 35–58, 2002.

[162] L. M. de Socio, L. Marino, and G. Seminara, "Stability and admittance of a channel flow over a permeable interface," *Physics of Fluids*, vol. 17, no. 9, p. 094103, 2005.

[163] L. Shan and H. Zheng, "Partitioned time stepping method for fully evolutionary Stokes-Darcy flow with Beavers-Joseph interface conditions," *SIAM Journal on Numerical Analysis*, vol. 51, no. 2, pp. 813–839, 2013.

[164] S. M. Ross, "Theoretical model of the boundary condition at a fluid-porous interface," *American Institute of Chemical Engineers Journal*, vol. 29, no. 5, pp. 840–846, 1983.

[165] J.-L. Auriault, "About the Beavers and Joseph boundary condition," *Transport in Porous Media*, vol. 83, no. 2, pp. 257–266, 2010.

[166] D. A. Nield, "The Beavers-Joseph boundary condition and related matters: a historical and critical note," *Transport in Porous Media*, vol. 78, no. 3, pp. 537–540, 2009.

[167] I. P. Jones, "Low Reynolds number flow past a porous spherical shell," *Mathematical Proceedings of the Cambridge Philosophical Society*, vol. 73, no. 1, pp. 231–238, 1973.

[168] F. Valdés-Parada, C. G. Aguilar-Madera, J. Alberto Ochoa-Tapia, and B. Goyeau, "Velocity and stress jump conditions between a porous medium and a fluid," *Advances in Water Resources*, vol. 62, no. Part B, pp. 327–339, 2013.

[169] W. Jäger and A. Mikelić, "On the interface boundary condition of Beavers, Joseph, and Saffman," *SIAM Journal on Applied Mathematics*, vol. 60, no. 4, pp. 1111–1127, 2000.

[170] H. Tan, X.-M. Chen, K. M. Pillai, and T. D. Papathanasiou, "Evaluation of boundary conditions at the clear-fluid and porous-medium interface using the boundary element method," in *International Conference on Flow Processes in Composite Materials*, vol. 9, p. 10, 2008.

[171] S. Berg, A. W. Cense, J. P. Hofman, and R. M. M. Smits, "Flow in porous media with slip boundary condition," in *International Symposium of the Society of Core Analysts*, SCA2007-13, pp. 1–12, 2007.

[172] K. A. Nair and A. Sameen, "Experimental study of slip flow at the fluid-porous interface in a boundary layer flow," *Procedia IUTAM*, vol. 15, no. 1, pp. 293–299, 2015.

[173] G. Chun-Yuan and D. Qin-Feng, "Slip velocity model of porous walls absorbed by hydrophobic nanoparticles SiO_2," *Journal of Hydrodynamics*, vol. 19, no. 3, pp. 365–371, 2007.

[174] C.-H. Bruneau and I. Mortazavi, "Numerical modelling and passive flow control using porous media," *Computers & Fluids*, vol. 37, no. 5, pp. 488–498, 2008.

[175] J. Williams, S. Hibberd, H. Power, and D. S. Riley, "On the effects of mass and momentum transfer from droplets impacting on steady two-dimensional

rimming flow in a horizontal cylinder," *Physics of Fluids*, vol. 24, no. 5, p. 053103, 2012.

[176] L. N. Trefethen, *Spectral Methods in MATLAB*. Siam, 2000.

[177] J. P. Boyd, *Chebyshev and Fourier Spectral Methods*. Courier Corporation, 2001.

[178] J. M. P. Nicholson, H. Power, O. Tammisola, S. Hibberd, and E. D. Kay, "Fluid dynamics of the slip boundary condition for isothermal rimming flow with moderate inertial effects," *Physics of Fluids*, vol. 31, no. 033602, pp. 1–31, 2019.

[179] J. Williams, *Thin film rimming flow subject to droplet impact at the surface*. PhD thesis, The University of Nottingham, 2008.

[180] J. M. P. Nicholson, H. Power, O. Tammisola, S. Hibberd, and E. D. Kay, "On the non-isothermal thin film modelling of partial slip rimming flows.".